THE UNIVERSITY
OF BIRMINGHAM

3-D PRINTED MICROWAVE AND TERAHERTZ PASSIVE COMPONENTS

by

MILAN SALEK

A thesis submitted to the University of Birmingham for the degree of DOCTOR OF PHILOSOPHY

School of Electronic, Electrical and Systems Engineering

College of Engineering and Physical Sciences

The University of Birmingham

June 2019

ABSTRACT

This thesis presents the design of microwave and terahertz filters, fabricated using different types of 3-D printing technology. The work demonstrates the potential of using 3-D printing in the fabrication of microwave and terahertz passive components.

The first project introduces a compact coaxial cavity resonator filter which was fabricated using stereolithography 3-D printing process. The size and volume of this filter reduced by almost half, by fitting one resonator inside another resonator. This filter is ideal for fabrication by 3-D printing, as such a complex structure cannot be made easily by other methods. This project demonstrates the advantage of using 3-D printing in fabrication of components with complex structures.

The second project introduces three waveguide bandpass filters operating at centre frequency of 90 GHz, which were fabricated using the micro laser sintering process. The filters were the highest frequency metal 3-D printed filters reported at the time of publication. The third project introduces two waveguide filters operating at centre frequency of 180 GHz, which were also fabricated using the micro laser sintering process. These are the world highest frequency waveguide filters fabricated by a metal 3-D printing process. The capability of reproducibility of the micro laser sintering process is also discussed in this thesis.

The fourth project introduces a hybrid coaxial bandpass filter with two symmetrical transmission zeros, which was fabricated using stereolithography 3-D printing process. In this project the main-line couplings and input/ output coupling were realized using PCB lines, the idea of using PCB lines instead of coupling irises or probes is to allow different topologies to be designed easily by altering the PCB layout.

Finally, the fifth project introduces a terahertz waveguide bandpass filter with embedded H-plane waveguide bends. This filter is being fabricated using 3-D screen printing.

ACKNOWLEDGEMENTS

I would like to thank my supervisor Prof. Michael J. Lancaster, for his continuous support and guidance during my Ph.D. study in the Emerging Device Technology (EDT) Research Group at the University of Birmingham. It has been an honour to be his Ph.D. student. I appreciate all his contribution of time and ideas to complete my study.

I also would like to thank my co-supervisor Dr. Yi Wang for his support throughout my study. My appreciations go to all my colleagues in the Emerging Device Technology Research Group at the University of Birmingham for their support over these three years. In particular, I would like to thank Dr. Xiaobang Shang, who helped me on technical parts during my Ph.D. study.

I appreciate the Engineering and Physical Sciences Research Council (EPSRC) for the financial support. Finally, I would like to thank my father for his valuable support and encouragement.

TABLE OF CONTENTS

CHAPTER 1: INTRODUCTION

1.1 Research Motivation

Microwave and terahertz filters are used to perform a variety of functions in high frequency systems. Microwave filters can be found in any type of microwave systems such as satellite communication, radars, mobile systems, test and measurement systems and even electronic warfare. They provide frequency selectivity by selecting or rejecting one or more parts of the frequency spectrum. They are also used as building blocks for duplexers and diplexers to combine or separate multiple frequency bands. Terahertz filters are also used in a verity of terahertz systems such as terahertz communication systems, medical imaging and security imaging. Recently, additive manufacturing or 3-D printing has become an interesting technology for fabrication of microwave and terahertz components. Being able to fabricate complex 3-D structures with high resolution and accuracy using a variety of materials makes 3-D printing technologies an ideal fabrication process for fabrication of complex microwave and terahertz passive components. The additive manufacturing or 3-D printing technologies are also advancing as demand for these technologies is expanding. They are becoming increasingly common in industry and science [1]. Over the past decade many have used additive manufacturing to fabricate microwave components, where many high frequency passive components have been fabricated successfully using different 3-D printing technologies, examples of some of these components are reported in [2]-[12] and discussed in chapter 3.

Using 3-D printing technology for fabrication of passive microwave components has been investigated at the University of Birmingham over the past few years, where many microwave filters operating at a frequency range of 0.5 GHz to 90 GHz have been fabricated. Figure 1.1 shows some of these devices [13]-[17]. Figure 1.1 (a) shows a photograph of a fourth-order 0.5 GHz helical resonator bandpass filter fabricated using stereolithography 3-D printing process [13]. Figure 1.1 (b) shows a photograph of a fourth-order 3 GHz bandpass combline filter, which is fabricated using a stereolithography 3-D printing process [14]. Figure 1.1 (c) shows a photograph of a fifth-order X-band waveguide filter based on spherical resonators and figure 1.1 (d) shows a photograph of a fourth-order X-band bandpass filter based on spherical

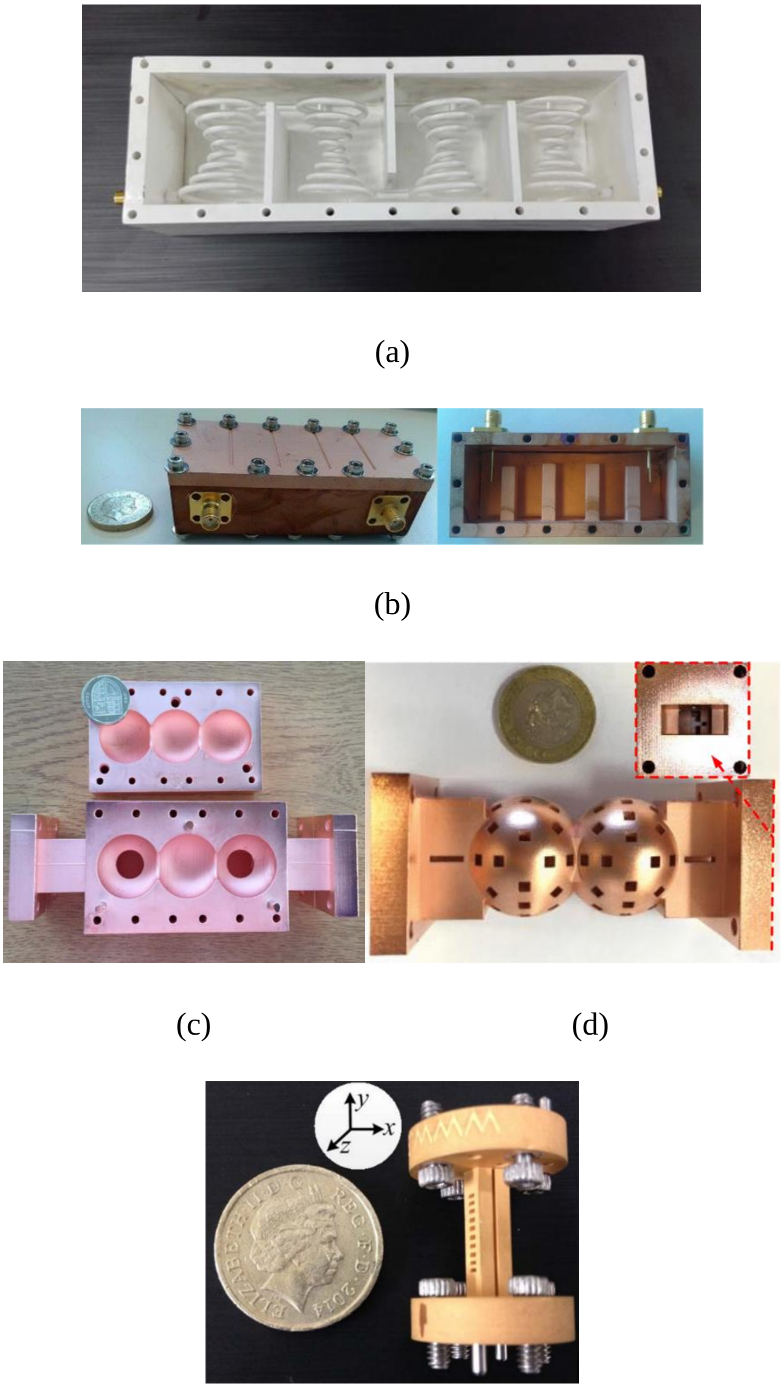

(a)

(b)

(c) (d)

(e)

Figure 1.1 Photographs of the 3-D printed microwave filters designed in the University of Birmingham. (a) Photograph of fourth-order helical resonator bandpass filter [13]. (b) Photograph of fourth-order bandpass combline filter [14]. (c) Photograph of fifth-order waveguide filter based on spherical resonators [15]. (d) Photograph of fourth-order bandpass filter based on spherical dual-mode resonators [16]. (e) Photograph of fifth-order waveguide filter [17].

dual-mode resonators, these filters are fabricated using stereolithography 3-D printing process [15, 16]. A fifth-order W-band waveguide filter is also fabricated using stereolithography 3-D printing process and reported in [17], and a photograph of this filter is shown in figure 1.1 (e).

The projects presented in this thesis focus on design and fabrication of several microwave filters, which are fabricated using different types of 3-D printing technology. All the projects are now completed except one which is still being fabricated at the time of writing. The work in thesis demonstrates the potential of using additive manufacturing or 3-D printing in fabrication of complex microwave and terahertz passive components. The work intends to explore 3-D printing as an additive manufacturing technology for the fabrication of high frequency microwave components, mainly filters using various 3-D printing technologies with metallic and non-metallic materials in fabrication process. Although some of the projects presented in this thesis operate at microwave frequencies, the goal is to push the 3-D printing to its limit for fabrication of complex high frequency passive components operating in the terahertz frequency range. As it will be explained later in the thesis, waveguide filters operating at 90 GHz and 180 GHz are successfully fabricated and tested, where good results are achieved. These are the highest frequency filters that have ever been fabricated using metallic 3-D printing process, showing the potential of using 3-D printing in fabrication of high frequency components. One of the projects is about the design of a terahertz waveguide filter operating with a centre frequency of 300 GHz, although this filter is not fabricated yet, it will demonstrate the possibility of using 3-D printing in fabrication of passive components at still higher frequencies.

1.2 Thesis Overview

This thesis is formed of nine chapters, which are intended to present 3-D printed microwave and terahertz filters, as well as the 3-D printing fabrication techniques used to fabricate them. These nine chapters are organised as follows.

- Chapter 1 presents the motivation and objectives of the work presented in this thesis. This chapter also provides an overview of the structure of this thesis.
- Chapter 2 provides the fundamental theory of filter networks, which used for the works presented in this thesis. This chapter begins by describing the basic concepts of the

microwave filter and filter transfer functions. This chapter introduces the coupling matrix synthesis of filter networks for both $N \times N$ and $N+2$ coupling matrices, as well as the technique for the reduction of the $N+2$ transversal coupling matrix to the folded coupling matrix. This chapter also provides several key concepts and equations related to rectangular and cylindrical cavity resonators, and rectangular and circular waveguides. Finally, as an example of the theory, the chapter describes the design and physical realization of a 300 GHz waveguide bandpass filter using coupling matrix theory and an EM simulation tool.

- Chapter 3 introduces additive manufacturing technologies, mainly focusing on 3-D printing technologies. This chapter describes the fabrication process of three main types of 3-D printing technology, which are stereolithography apparatus, fused deposition modelling and selective laser sintering. The chapter also introduces a recently developed 3-D printing technique, which is known as 3-D screen printing. Information about 3-D printing materials, metallization of 3-D printed microwave components and performance of 3-D printed microwave components are also provided in this chapter. Finally, the chapter explains some of the key design considerations for 3-D printing of microwave components.
- Chapter 4 presents the design of a compact fourth-order 3 GHz coaxial cavity resonator filter. In this project by fitting one resonator inside another resonator, the size and volume of the filter is reduced by almost half over conventional coaxial filters. This chapter provides the design procedure of the filter using coupling matrix theory. The filter presented in this chapter is fabricated by stereolithography 3-D printing process, where details of fabrication process are provided. Good agreement between the measured and simulated S parameter results demonstrates the accuracy of the fabrication process and validates the general concept. The work in this chapter was published in [18].
- Chapter 5 presents the design of metal 3-D printed fifth-order 90 GHz waveguide bandpass filters, which are fabricated using the micro laser sintering process. The filters are the highest frequency metal 3-D printed filters reported at the time they were published. Good agreement between measured and simulated S parameter results demonstrates the accuracy of the micro laser sintering process and its capability in fabrication of high frequency microwave components. Reproducibility of the fabrication process is also discussed in this chapter, and extremely close measured

results of the two identical filters demonstrates the capability of reproducibility of the fabrication process. It is also shown in this chapter that by electroplating the surface of the filter with copper, the insertion loss of the filter can be improved considerably. The quality of the filters is also discussed by comparing the measured results with simulated results, as well as providing the surface roughness measurements. The work in this chapter was published in [19] and [20].

- Chapter 6 presents the design of two identical fifth-order 180 GHz waveguide bandpass filters which are fabricated using the micro laser sintering process. The project in this chapter extends the work introduced in chapter 5, in order to show the capability of micro laser sintering process for fabricating filters that operate at much higher frequency. The filters presented in this chapter are the highest frequency waveguide filters which are fabricated using metal 3-D printing process. The chapter provides the design procedure and fabrication details of the filters. Good agreement between measured and simulated results demonstrates the accuracy of the micro laser sintering process, also the close measured results of the two waveguide filters demonstrates the capability of reproducibility of the micro laser sintering process. The work in this chapter demonstrates the potential of using micro laser sintering process for small to medium batch size production of high frequency waveguide filters.
- Chapter 7 presents the design of a fourth-order 2 GHz hybrid coaxial bandpass filter with two symmetrical transmission zeros, which is fabricated using stereolithography 3-D printing process. In this project PCB lines are used to realize the main-line couplings and input/ output coupling, and a capacitive gap is used to realize the cross coupling. The idea of using PCB lines instead of coupling irises or probes to achieve couplings, allows different topologies to be designed easily by altering the PCB layout, even a fully canonical filter which needs direct coupling between source and load could be possible. The design procedure of the filter is explained in this chapter, where a folded $N+2$ coupling matrix is used. Fabrication details of the filter are also provided in this chapter, and good agreement between the measured and simulated S parameter results demonstrates the accuracy of the fabrication process.
- Chapter 8 presents the design of a fifth-order 300 GHz waveguide bandpass filter with embedded H-plane waveguide bends. The filter is still being fabricated using 3-D screen printing technique. The project in this chapter demonstrates the possibility of using 3-D screen printing in fabrication of high frequency components. The design

procedure of the waveguide filter is provided in chapter 2, and in this chapter, the design of waveguide bends is explained. The chapter also provides discussion about insertion loss when using different metallic materials, dimensional tolerance analysis and effect of waveguide flange misalignment.

- Chapter 9 provides the conclusion of the thesis. Suggestions for future work are also discussed in this chapter.

References

[1] I. Gibson, D. W. Rosen, and B. Stucker, *Additive manufacturing technologies: 3D printing, rapid prototyping, and direct digital manufacturing*. New York: Springer, 2016.

[2] G. Venanzoni, C. Tomassoni, M. Dionigi, and R. Sorrentino, “Stereolitographic 3D printing of compact quasi-elliptical filters,” *2017 IEEE MTT-S International Microwave Workshop Series on Advanced Materials and Processes for RF and THz Applications (IMWS-AMP)*, Pavia, Italy, 2017, pp. 1-3.

[3] G. Venanzoni, M. Dionigi, C. Tomassoni, D. Eleonori, and R. Sorrentino, “3D printing of X band waveguide resonators and filters,” *2017 XXXIInd General Assembly and Scientific Symposium of the International Union of Radio Science (URSI GASS)*, Montreal, QC, Canada, 2017, pp. 1-2.

[4] J. Li, C. Guo, L. Mao, and J. Xu, “3D printed bandpass filters using compact high-Q hemispherical resonators with improved out-of-band rejection,” *Electronics Letters*, vol. 53, no. 6, pp. 413–415, Mar. 2017.

[5] C. Guo, J. Li, J. Xu, and H. Li, “An X-band lightweight 3-D printed slotted circular waveguide dual-mode bandpass filter,” *2017 IEEE International Symposium on Antennas and Propagation & USNC/URSI National Radio Science Meeting*, San Diego, CA, USA, 2017, pp. 2645-2646.

[6] J. Li, C. Guo, J. Xu, and L. Mao, “Lightweight low-cost Ka-band 3-D printed slotted rectangular waveguide bandpass filters,” *2017 IEEE International Symposium on Antennas and Propagation & USNC/URSI National Radio Science Meeting*, San Diego, CA, USA, 2017, pp. 2647-2648.

[7] M. Dauria, W. J. Otter, J. Hazell, B. T. W. Gillatt, C. Long-Collins, N. M. Ridler, and S. Lucyszyn, “3-D Printed Metal-Pipe Rectangular Waveguides,” *IEEE Transactions on Components, Packaging and Manufacturing Technology*, vol. 5, no. 9, pp. 1339–1349, Sept. 2015.

[8] B. Zhang and H. Zirath, “3D printed iris bandpass filters for millimetre-wave applications,” *Electronics Letters*, vol. 51, no. 22, pp. 1791–1793, Oct. 2015.

[9] M. V. D. Vorst and J. Gumpinger, “Applicability of 3D printing techniques for compact Ku-band medium/high-gain antennas,” *2016 10th European Conference on Antennas and Propagation (EuCAP),* Davos, Switzerland, 2016, pp. 1-4.

[10] F. Bongard, M. Gimersky, S. Doherty, X. Aubry, and M. Krummen, “3D-printed Ka-band waveguide array antenna for mobile SATCOM applications,” *2017 11th European Conference on Antennas and Propagation (EUCAP),* Paris, France, 2017, pp. 579-583.

[11] J. S. Silva, E. B. Lima, J. R. Costa, C. A. Fernandes, and J. R. Mosig, “Tx-Rx Lens-Based Satellite-on-the-Move Ka-Band Antenna,” *IEEE Antennas and Wireless Propagation Letters*, vol. 14, pp. 1408–1411, Mar. 2015.

[12] X. Shang, P. Klasmann, and M. J. Lancaster, “A compact Ka-band waveguide orthomode transducer fabricated by 3-D printing,” *2016 46th European Microwave Conference (EuMC),* London, UK, 2016, pp. 365-368.

[13] X. Shang, J. Li, C. Guo, M. J. Lancaster, and J. Xu, “3-D printed filter based on helical resonators with variable width,” *2017 IEEE MTT-S International Microwave Symposium (IMS),* Honololu, HI, USA, 2017, pp. 1587-1590.

[14] L. S. Araujo, X. Shang, M. J. Lancaster, A. J. B. de Oliveira, I. Llamas-Garro, J. M. Kim, M. Favre, M. Billod, and E. de Rijk, “3-D printed band-pass combline filter,” *Microwave and Optical Technology letters,* vol. 59, no. 6, pp. 1388-1390, Mar. 2017.

[15] C. Guo, X. Shang, M. J. Lancaster, and J. Xu, “A 3-D Printed Lightweight X-Band Waveguide Filter Based on Spherical Resonators,” *IEEE Microwave and Wireless Components Letters*, vol. 25, no. 7, pp. 442–444, July. 2015.

[16] C. Guo, X. Shang, J. Li, F. Zhang, M. J. Lancaster, and J. Xu, “A Lightweight 3-D Printed X-Band Bandpass Filter Based on Spherical Dual-Mode Resonators,” *IEEE Microwave and Wireless Components Letters*, vol. 26, no. 8, pp. 568–570, Aug. 2016.

[17] X. Shang, P. Penchev, C. Guo, M. J. Lancaster, S. Dimov, Y. Dong, M. Favre, M. Billod, and E. D. Rijk, “W-Band Waveguide Filters Fabricated by Laser Micromachining and 3-D Printing,” *IEEE Transactions on Microwave Theory and Techniques*, vol. 64, no. 8, pp. 2572–2580, Aug. 2016.

[18] M. Salek, X. Shang, and M. J. Lancaster, “Compact S-Band Coaxial Cavity Resonator Filter Fabricated By 3-D Printing,” *IEEE Microwave and Wireless Components Letters*, vol. 29, no. 6, pp. 382-384, June. 2019.

[19] M. Salek, X. Shang, R. C. Roberts, M. J. Lancaster, F. Boettcher, D. Weber, and T. Starke, “W-Band Waveguide Bandpass Filters Fabricated by Micro Laser Sintering,” *IEEE Transactions on Circuits and Systems II: Express Briefs*, vol. 66, no. 1, pp. 61–65, Jan. 2019.

[20] M. Salek, X. Shang, M. J. Lancaster, R. C. Roberts, T. Starke, F. Boettcher, and D. Weber, “90 GHz Micro Laser Sintered Filter: Reproducibility and Quality Assessment,” *2019 49th European Microwave Conference (EuMC),* Paris, France, 2019, pp. 1-4.

CHAPTER 2: FUNDAMENTAL THEORY OF FILTER NETWORKS

2.1 Basic Concepts of Microwave Filters

Microwave filters are crucial elements of every microwave system. They are the most vital components in many electronic systems such as satellite communication, radars, mobile systems and electronic warfare. Microwave filters provide frequency selectivity by selecting or rejecting one or more parts of the frequency spectrum [1, 2]. A microwave filter can be defined as a two-port network as presented in figure 2.1. Here I_1, I_2 and V_1, V_2 are the current and voltage variables at input and output ports respectively, Z_{01} and Z_{02} are the source and load impedances and E_S is the source voltage [3].

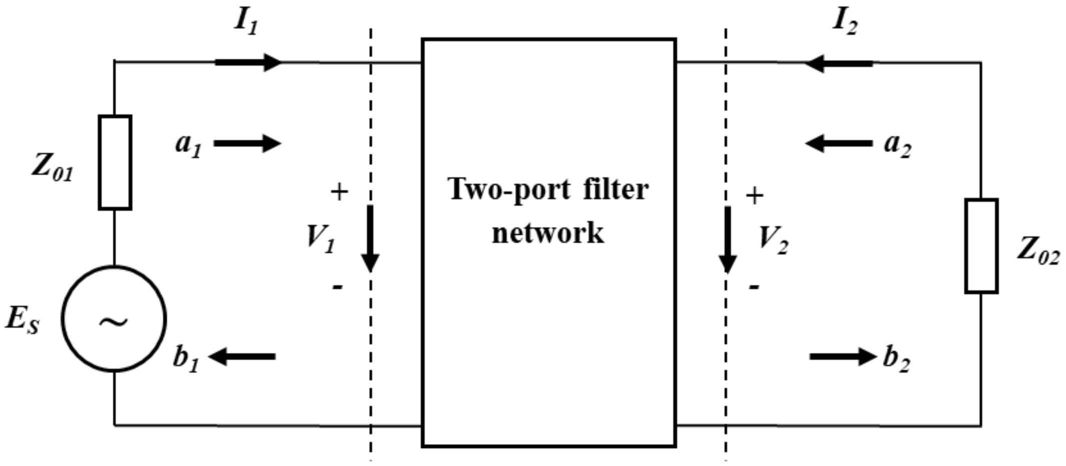

Figure 2.1 Two port filter network [3].

In figure 2.1, a and b represent the incident and reflected waves, respectively. They are introduced, because at microwave frequencies it is difficult to measure voltage and current [3]. Incident and reflected waves are defined as [3, 4]

$$a_n = \frac{1}{2}\left(\frac{V_n + Z_{0n}I_n}{\sqrt{Z_{0n}}}\right)$$

$$b_n = \frac{1}{2}\left(\frac{V_n - Z_{0n}I_n}{\sqrt{Z_{0n}}}\right) \qquad \text{for } n = 1 \text{ and } 2 \tag{2.1}$$

The scattering parameters also known as *S* parameters of the two-port network shown in figure 2.1 can be defined using wave variable as [3, 4]

$$S_{11} = \left.\frac{b_1}{a_1}\right|_{a_2=0} \qquad S_{12} = \left.\frac{b_1}{a_2}\right|_{a_1=0}$$

$$S_{21} = \left.\frac{b_2}{a_1}\right|_{a_2=0} \qquad S_{22} = \left.\frac{b_2}{a_2}\right|_{a_1=0} \tag{2.2}$$

where S_{12} and S_{21} are transmission coefficients and S_{11} and S_{22} are reflection coefficients. At microwave frequencies it is desirable to use *S* parameters, as they are directly measurable [3]. Return loss (L_R) and transmission loss (L_A) of any two-port network are related to *S* parameters by [3]

$$L_R = -20\log_{10}(|S_{11}|)$$

$$L_A = -20\log_{10}(|S_{21}|) \tag{2.3}$$

where logarithmic operation is to the base of 10. For a lossless two-port symmetrical filter network, the following relations between reflection and transmission coefficients exist, which shows the transmitted power must be equal to the incident power [3].

$$|S_{11}|^2 + |S_{21}|^2 = 1 \quad (S_{11}S_{11}^* + S_{21}S_{21}^* = 1)$$

$$|S_{22}|^2 + |S_{12}|^2 = 1 \quad (S_{22}S_{22}^* + S_{12}S_{12}^* = 1) \tag{2.4}$$

Also, for a lossless two-port filter network, return loss (L_R) and transmission loss (L_A) are related as [3]

$$L_R = -10\log_{10}\left(1 - 10^{-\frac{L_A}{10}}\right)$$

$$L_A = -10\log_{10}\left(1 - 10^{-\frac{L_R}{10}}\right) \tag{2.5}$$

2.2 Filter Transfer Functions

The response characteristics of a two-port lossless filter network can be mathematically described by its transfer function. The transfer function of a lossless filter network is defined as the ratio of the transmitted power to the available power, which can be expressed as [3]

$$|S_{21}(j\Omega)|^2 = \frac{1}{1+\varepsilon^2 F_N^2(\Omega)} \tag{2.6}$$

where ε is ripple constant, Ω is frequency variable and $F_N(\Omega)$ represents the filtering function. For a Chebyshev filter, which has a response that exhibits the equal ripple passband and maximally flat stopband, the amplitude square transfer function is given by [3]

$$|S_{21}(j\Omega)|^2 = \frac{1}{1+\varepsilon^2 T_N^2(\Omega)} \tag{2.7}$$

where the ripple constant ε, is related to passband ripple L_{Ar} (dB) and is expressed as [3]

$$\varepsilon = \sqrt{10^{\frac{L_{Ar}}{10}} - 1} \tag{2.8}$$

$T_N(\Omega)$ in equation (2.7) is the Chebyshev function of degree *N* and is expressed as [3]

$$T_N(\Omega) = \begin{cases} \cos(N\ \cos^{-1}\Omega) & |\Omega| \leq 1 \\ \cosh(N\ \cosh^{-1}\Omega) & |\Omega| \geq 1 \end{cases} \tag{2.9}$$

Figure 2.2 shows the amplitude response of a 6th order Chebyshev filter, which is normalised to have a unit cut-off frequency. The filter is designed to have a passband ripple L_{Ar} of 0.04 dB, corresponding to a passband return loss of 20 dB (which can be calculated using equation (2.5)). This type of filter is normally referred as all pole Chebyshev filter, since all the transmission zeros are located at infinity. There are many other different types of filters available with different transfer functions such as Butterworth, Elliptical and Bessel filter; full details of their transfer function can be found in [3] – [5].

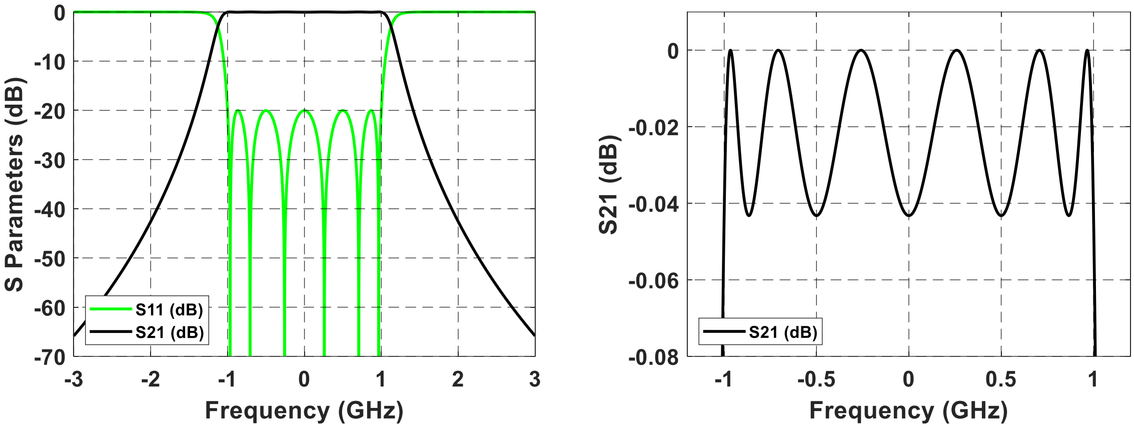

(a) (b)

Figure 2.2 Amplitude response of a 6th order Chebyshev filter. (a) The normalised *S* parameter response. (b) Expanded view of the S_{21} over normalised passband.

2.3 Filter Transfer Functions for Filters with Finite Transmission Zeros

For any two-port lossless bandpass filter network with finite transmission zeros and Chebyshev response, reflection and transfer polynomials are defined as [4]

$$S_{11}(\omega) = \frac{F(\omega)/\varepsilon_R}{E(\omega)} \tag{2.10}$$

$$S_{21}(\omega) = \frac{P(\omega)/\varepsilon}{E(\omega)} \tag{2.11}$$

where $S_{11}(\omega)$ and $S_{21}(\omega)$ are reflection and transfer functions of filter network, $F(\omega)$ and $E(\omega)$ are N^{th} degree polynomials, and $P(\omega)$ is an n_{fz} degree polynomial, which contains finite transmission zeros (N is the degree of filter and n_{fz} is the number of finite transmission zeros). Polynomials $F(\omega)$, $E(\omega)$ and $P(\omega)$ are all normalized to their highest degree coefficients such that their highest degree coefficient are unity.

The ε is a constant normalizing $S_{21}(\omega)$ to the chosen equiripple level at $\omega = 1$ (rad/s), and is expressed as [4]

$$\varepsilon = \frac{1}{\sqrt{10^{\frac{RL}{10}} - 1}} \left| \frac{P(\omega)}{F(\omega)/\varepsilon_R} \right|_{\omega=1} \tag{2.12}$$

where RL is prescribed return loss in dB, and ε_R is a constant normalizing nominator of $S_{11}(\omega)$, which has a value of unity for all cases except for fully canonical filters (where all transmission zeros are located at finite frequencies ($n_{fz} = N$)), it can be calculated as [4]

$$\varepsilon_R = \frac{\varepsilon}{\sqrt{\varepsilon^2 - 1}} \tag{2.13}$$

For a lossless bandstop filter network, reflection and transfer polynomials are exchanged to create a bandpass like filter configuration with bandstop filter characteristics, which are defined as [4]

$$S_{11}(\omega) = \frac{P(\omega)/\varepsilon}{E(\omega)} \tag{2.14}$$

$$S_{21}(\omega) = \frac{F(\omega)/\varepsilon_R}{E(\omega)} \tag{2.15}$$

For a bandpass filter, if $N - n_{fz}$ is an even number, the coefficients of polynomial $P(\omega)$ must be multiplied by *j* to preserve the unitary conditions, and for a bandstop filter, the coefficients of polynomial $F(\omega)$ must be multiplied by *j*, where N is degree of the filter and n_{fz} is the number of transmission zeros (reflection zeros for a bandstop filter) [4].

Using relations in equation (2.4), an alternative pole formula for a lossless filter network can be found as [4]

$$S_{21}(\omega)S_{21}^*(\omega) = \frac{P(\omega)P(\omega)^*}{\varepsilon^2 E(\omega)E(\omega)^*} = \frac{1}{\left[1 - j\frac{\varepsilon}{\varepsilon_R}C_N(\omega)\right]\left[1 + j\frac{\varepsilon}{\varepsilon_R}C_N(\omega)^*\right]} \tag{2.16}$$

where

$$C_N(\omega) = \frac{F(\omega)}{P(\omega)} \tag{2.17}$$

The $C_N(\omega)$ is filtering function of degree *N*, and for a general Chebyshev characteristic it can be defined as [4]

$$C_N(\omega) = \cosh\left[\sum_{n=1}^{N} \cosh^{-1}\big(x_n(\omega)\big)\right] \tag{2.18}$$

where

$$x_n(\omega) = \frac{\omega - \frac{1}{\omega_n}}{1 - \frac{\omega}{\omega_n}} \tag{2.19}$$

where, $\omega_n = s_n/j$ is the position of the n^{th} transmission zero in complex frequency plane and s_n is the complex frequency variable.

Using hyperbolic identities, equation (2.18) can be written as

$$C_N(\omega) = \frac{1}{2} \times \left[\prod_{n=1}^{N} \left(x_n(\omega) + \sqrt{x_n(\omega)^2 - 1} \right)) + \prod_{n=1}^{N} \left(x_n(\omega) - \sqrt{x_n(\omega)^2 - 1} \right)) \right] \tag{2.20}$$

By substituting $x_n(\omega)$ in equation (2.20), final form of the filter function $C_N(\omega)$ can be expressed as [4]

$$C_N(\omega) = \frac{1}{2} \times \left[\frac{[\prod_{n=1}^{N} (Y_n + Z_n) + \prod_{n=1}^{N} (Y_n - Z_n)]}{\prod_{n=1}^{N} (1 - \omega/\omega_n)} \right] \tag{2.21}$$

where

$$Y_n = \left(\omega - \frac{1}{\omega_n} \right)$$

$$Z_n = \sqrt{(\omega^2 - 1)} \times \sqrt{1 - \frac{1}{{\omega_n}^2}} \tag{2.22}$$

Comparing equation (2.21) to equation (2.17) reveals, that the numerator of $C_N(\omega)$ has the same zeros as polynomial $F(\omega)$, and denominator of $C_N(\omega)$ has the same zeros as polynomial $P(\omega)$. Polynomial $P(\omega)$ can be generated from zeros of denominator of $C_N(\omega)$ or from prescribed transmission zeros ω_n as [4]

$$P(\omega) = \prod_{n=1}^{n_{fz}} (\omega - \omega_n) \tag{2.23}$$

Polynomial $F(\omega)$ can be generated from zeros of numerator of $C_N(\omega)$ or by a recursive technique. Details of recursive technique is explained in [4].

Polynomial $E(\omega)$ is constructed, using alternating singularity principle by constructing complex polynomials $P(\omega)/\varepsilon - j\,F(\omega)/\varepsilon_R$, finding its zeros, and then taking conjugate of any zero that is in lower half of the ω plane, and finally reconstruct the $E(\omega)$ polynomial from the new zeros. Having obtained Polynomials $P(\omega)$, $F(\omega)$ and $E(\omega)$, reflection and transfer polynomials can be calculated, using equations (2.10) and (2.11) [4].

Figure 2.3 (a) shows the amplitude response of a 6th order Chebyshev filter with a pair of symmetrical finite transmission zeros, which is plotted using polynomial synthesis technique stated above. The response is normalised to have a unit cut-off frequency. The filter is designed to have a return loss of 20 dB and two transmission zeros at ± $j1.5$, which produce two attenuation lobes of 40.64 dB at ± $j1.76$. Introducing finite transmission zeros increase the selectivity of the filter response. This can be seen in figure 2.3 (b), where S_{21} responses of two 6th order Chebyshev filters with return loss of 20 dB is shown, one with no transmission zeros and the other with two transmission zeros at ± $j1.5$.

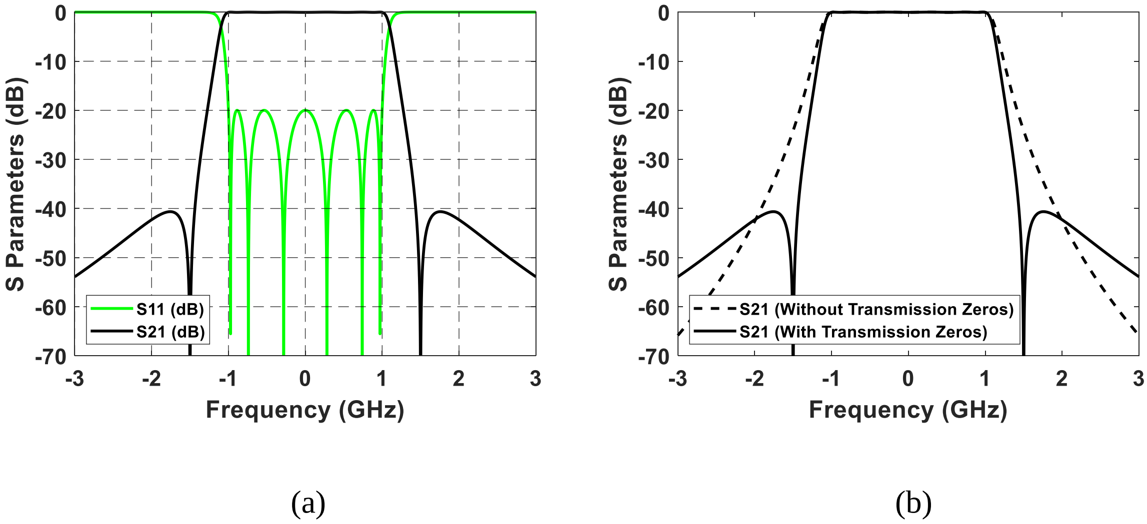

Figure 2.3 Amplitude response of 6th order Chebyshev filters. (a) The normalised S parameter response for a filter with a pair of symmetrical finite transmission zeros. (b) Comparison of the S_{21} response of a filter with no transmission zeros and a filter that has a pair of symmetrical transmission zeros.

2.4 Coupling Matrix Synthesis of Filter Networks

Prior to the development of coupling matrix theory, almost all filter synthesis techniques were based on the extraction of electrical elements from polynomials which represent the filter's electrical performance [6]. The concept of the coupling matrix theory was introduced by Atia and William in the early 1970s, they applied it to dual mode symmetric waveguide filters [7] – [9]. The coupling matrix of a filter network provides the real-world properties of the elements within the filter network. Each element in the coupling matrix represents an actual physical component of the filter network.

The advantage of modelling the filter network in matrix form is that, matrix operations such as similarity transformation, partitioning and inversion can be applied, which simplify the synthesis, reconfiguration of the topology and performance simulation of complex networks [4]. This section discusses two types of coupling matrix, the $N\times N$ coupling matrix and the $N+2$ coupling matrix.

2.4.1 The $N\times N$ Coupling Matrix

The equivalent circuit model of an N-coupled resonator filter network can be presented in two different ways, depending on the type of coupling between resonators. Figure 2.4 (a) shows equivalent circuit model with magnetic couplings and figure 2.4 (b) shows equivalent circuit model with electric couplings. Where R, G, L and C represent resistance, conductance, inductance and capacitance of components respectively. Loop current and node voltage in each resonator are denoted as i_N and v_N, respectively, and e_S and i_S are the voltage source and current source, respectively.

Both models in figure 2.4 can be analysed in similar way, where the normalized impedance matrix can be extracted from equivalent circuit model in figure 2.4 (a) and the normalized admittance matrix can be extracted from equivalent circuit model in figure 2.4 (b). Here only the magnetically coupled filter network in figure 2.4 (a) is going to be analysed, the discussion about electrically coupled filter network can be found in [3].

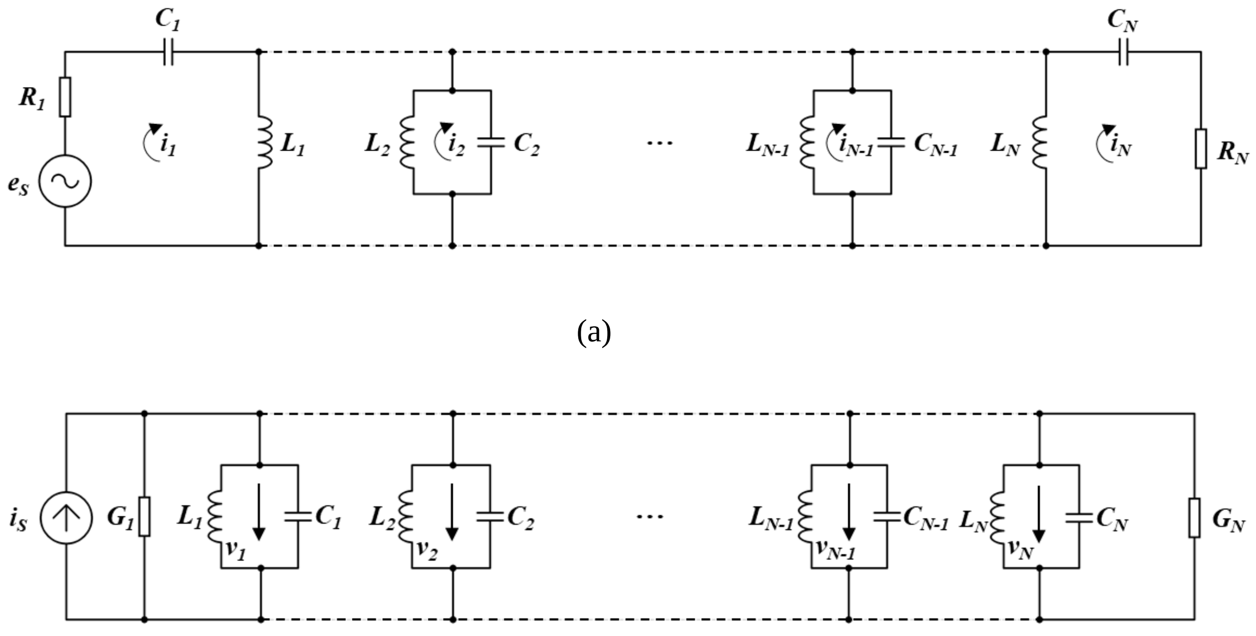

(a)

(b)

Figure 2.4 Equivalent circuit model of *N*-coupled resonators. (a) The resonators coupled by magnetic couplings [3]. (b) The resonators coupled by electric couplings [3].

Using Kirchhoff's voltage law which states that the algebraic sum of the voltages around any closed-circuit path is zero, loop equations for the circuit that is shown in figure 2.4 (a) can be written as [3]

$$
\begin{aligned}
&(R_1 + j\omega L_1 + \tfrac{1}{j\omega C_1}) i_1 - j\omega L_{12} i_2 \cdots - j\omega L_{1N} i_N = e_s \\
&-j\omega L_{21} i_1 + \left(j\omega L_2 + \tfrac{1}{j\omega C_2}\right) i_2 \cdots - j\omega L_{2N} i_N = 0 \\
&\vdots \\
&-j\omega L_{N1} i_1 - j\omega L_{N2} i_2 \cdots + \left(R_N + j\omega L_N + \tfrac{1}{j\omega C_N}\right) i_N = 0 \qquad (2.24)
\end{aligned}
$$

where $L_{ij} = L_{ji}$ denote mutual inductance between resonators i and j. The above loop equations can be represented in matrix form as [3]

$$\begin{bmatrix} R_1 + j\omega L_1 + \frac{1}{jwC_1} & -j\omega L_{12} & \cdots & -j\omega L_{1N} \\ -j\omega L_{21} & j\omega L_2 + \frac{1}{j\omega C_2} & \cdots & -j\omega L_{2N} \\ \vdots & \vdots & \ddots & \vdots \\ -j\omega L_{N1} & -j\omega L_{N2} & \cdots & R_N + j\omega L_N + \frac{1}{j\omega C_N} \end{bmatrix} \times \begin{bmatrix} i_1 \\ i_2 \\ \vdots \\ i_N \end{bmatrix} = \begin{bmatrix} e_s \\ 0 \\ \vdots \\ 0 \end{bmatrix} \tag{2.25}$$

which can also be represented as

$$[Z] \cdot [i] = [e] \tag{2.26}$$

where $[Z]$ is $N{\times}N$ impedance matrix, $[i]$ is current matrix and $[e]$ is voltage source matrix.

For a filter that is synchronously tuned, where all resonators of the filter resonate at the same frequency, the $N{\times}N$ impedance matrix in equation (2.25) can be normalised as [3]

$$[\overline{Z}] = \begin{bmatrix} \frac{R_1}{\omega_0\, L \cdot FBW} + p & -j\frac{\omega L_{12}}{\omega_0\, L \cdot FBW} & \cdots & -j\frac{\omega L_{1N}}{\omega_0\, L \cdot FBW} \\ -j\frac{\omega L_{21}}{\omega_0\, L \cdot FBW} & p & \cdots & -j\frac{\omega L_{2N}}{\omega_0\, L \cdot FBW} \\ \vdots & \vdots & \ddots & \vdots \\ -j\frac{\omega L_{N1}}{\omega_0\, L \cdot FBW} & -j\frac{\omega L_{N2}}{\omega_0\, L \cdot FBW} & \cdots & \frac{R_N}{\omega_0\, L \cdot FBW} + p \end{bmatrix} \tag{2.27}$$

which is normalised using [3]

$$[\overline{Z}] = \frac{[Z]}{\omega_0\, L \cdot FBW} \tag{2.28}$$

where $[\overline{Z}]$ is an $N{\times}N$ normalised impedance matrix, $FBW = \triangle\,\omega/\omega_0$ is fractional bandwidth, $\omega_0 = 1/\sqrt{LC}$ is centre frequency of the filter and p is the complex lowpass frequency variable given by [3]

$$p = j\frac{1}{FBW} \cdot \left(\frac{\omega}{\omega_0} - \frac{\omega_0}{\omega}\right) \tag{2.29}$$

Considering that $\omega/\omega_0 \approx 1$ for a narrow band filter, the $N{\times}N$ normalised impedance matrix (2.27) can be simplified as [3]

$$[\overline{Z}] = \begin{bmatrix} \frac{1}{q_{e1}} + p & -jm_{12} & \cdots & -jm_{1N} \\ -jm_{21} & p & \cdots & -jm_{2N} \\ \vdots & \vdots & \ddots & \vdots \\ -jm_{N1} & -jm_{N2} & \cdots & \frac{1}{q_{eN}} + p \end{bmatrix} \tag{2.30}$$

where $m_{ij} = m_{ji}$ is the normalised coupling coefficient between resonators i and j, and q_{e1} and q_{eN} are normalised quality factor of input and output resonators, which are defined as [3]

$$m_{ij} = \frac{L_{ij}}{L \cdot FBW} = \frac{M_{ij}}{FBW} \qquad i \neq j \tag{2.31}$$

$$q_{ei} = \frac{\omega_0 L}{R_i} \cdot FBW = Q_{ei} \cdot FBW \qquad \text{for } i = 1, N \tag{2.32}$$

M_{ij} and Q_{ei} are de-normalised coupling coefficient and external quality factor.

In case of asynchronously tuned filter, where resonators of the filter resonate at different frequencies, the normalised impedance matrix will be almost identical to matrix (2.30) with extra entries m_{ii} along the diagonal elements of the matrix to account for asynchronous tuning. That is [3],

$$[\overline{Z}] = \begin{bmatrix} \frac{1}{q_{e1}} + p - jm_{11} & -jm_{12} & \cdots & -jm_{1N} \\ -jm_{21} & p - jm_{22} & \cdots & -jm_{2N} \\ \vdots & \vdots & \ddots & \vdots \\ -jm_{N1} & -jm_{N2} & \cdots & \frac{1}{q_{eN}} + p - jm_{NN} \end{bmatrix} \tag{2.33}$$

Here it has been shown that normalised impedance matrix can be extracted, using loop equation formulation for *N*-coupled resonator filter with magnetic coupling. Similarly, in case of electrically coupled equivalent circuit model (Figure 2.4 (b)), Kirchhoff’s current law can be used to find node equation formulation to extract normalised admittance matrix, as is done in [3]. The normalised impedance matrix and normalised admittance matrix are both identical, this implies that a general matrix results, regardless of whether the couplings between resonators are: magnetic, electric or even combination of both, as follows [3]:

$$[A] = \begin{bmatrix} \frac{1}{q_{e1}} & 0 & \dots & 0 \\ 0 & 0 & \dots & 0 \\ \vdots & \vdots & \ddots & \vdots \\ 0 & 0 & \dots & \frac{1}{q_{eN}} \end{bmatrix} + p \begin{bmatrix} 1 & 0 & \dots & 0 \\ 0 & 1 & \dots & 0 \\ \vdots & \vdots & \ddots & \vdots \\ 0 & 0 & \dots & 1 \end{bmatrix} - j \begin{bmatrix} m_{11} & m_{12} & \dots & m_{1N} \\ m_{21} & m_{22} & \dots & m_{2N} \\ \vdots & \vdots & \ddots & \vdots \\ m_{N1} & m_{N2} & \dots & m_{NN} \end{bmatrix} \qquad (2.34)$$

which can also be presented as [3]

$$[A] = [q] + p[U] - j[m] \qquad (2.35)$$

where $[q]$ is $N\times N$ termination impedance matrix, which contains the values of $R_{11} = \frac{1}{q_{e1}}$ and $R_{NN} = \frac{1}{q_{eN}}$, that are the source and load impedances [4]. $[U]$ is $N\times N$ diagonal identity matrix with all entries at zero except for the diagonal entries that are equal to one [4]. $[m]$ is $N\times N$ general coupling matrix, which is a reciprocal matrix, containing the values of mutual couplings between resonators within the filter with zero diagonal entries for a synchronously tuned filter and nonzero diagonal entries m_{ii} for an asynchronously tuned filter [4].

The S parameters for a two-port filter network is given by [3]

$$S_{21} = 2 \times \frac{1}{\sqrt{q_{e1} \cdot q_{eN}}} [A]_{N1}^{-1}$$

$$S_{11} = \pm(1 - \frac{2}{q_{e1}} [A]_{11}^{-1}) \qquad (2.36)$$

For a Chebyshev filter, the normalised external quality factors and the general coupling matrix elements can be calculated from its lowpass prototype element values (g values) as [3]

$$q_{e1} = g_0 \, g_1 \qquad (2.37)$$

$$q_{eN} = g_N \, g_{N+1} \qquad (2.38)$$

$$m_{i,i+1} = \frac{1}{\sqrt{g_i \, g_{i+1}}} \qquad \text{for } i = 1 \text{ to } N-1 \qquad (2.39)$$

The lowpass g values for a Chebyshev lowpass porotype filter with passband ripple L_{Ar} (dB), return loss L_R and cut-off frequency of one (Ω_c = 1) is given by [3]

$$L_{Ar} = -10\log\left(1 - 10^{\frac{L_R}{10}}\right)$$

$$\beta = ln\left[coth\left(\frac{L_{Ar}}{17.37}\right)\right]$$

$$\gamma = \sinh\left(\frac{\beta}{2N}\right)$$

$$\mathrm{g}_0 = 1$$

$$\mathrm{g}_1 = \frac{2}{\gamma}\sin\left(\frac{\pi}{2N}\right)$$

$$\mathrm{g}_i = \frac{1}{\mathrm{g}_{i-1}}\frac{4\sin\left(\frac{(2i-1)\pi}{2N}\right)\cdot\sin\left(\frac{(2i-3)\pi}{2N}\right)}{\gamma^2 + \sin^2\left(\frac{(i-1)\pi}{N}\right)} \qquad \text{for } i = 2, 3, \cdots, N$$

$$\mathrm{g}_{\mathrm{N}+1} = \coth^2\left(\frac{\beta}{4}\right) \qquad \text{if } N \text{ is even}$$

$$\mathrm{g}_{N+1} = 1 \qquad \text{if } N \text{ is odd} \qquad (2.40)$$

For a specific maximum voltage standing wave ratio (*VSWR*), passband ripple L_{Ar} (dB) given by [3]

$$L_{Ar} = -10\log\left(1 - (\frac{VSWR-1}{VSWR+1})^2\right) \qquad (2.41)$$

The degree of a Chebyshev lowpass porotype N can be calculated, using following equation, if specific passband ripple L_{Ar} (dB) and minimum stopband attenuation L_{As} (dB) at $\Omega = \Omega_s$ (the equal ripple stopband starting frequency) required [3].

$$N \geq \frac{\cosh^{-1}\sqrt{\frac{10^{0.1\times L_{As}}-1}{10^{0.1\times L_{Ar}}-1}}}{\cosh^{-1}\Omega_s} \qquad (2.42)$$

2.4.2 The *N+2* Coupling Matrix

This section introduces $N+2$ coupling matrix, which overcome some of the shortcomings of the $N \times N$ coupling matrix. The $N+2$ coupling matrix has an extra pair of rows, one at the top and one at the bottom, as well as an extra pair of columns, one at the left and one at the right, which carry the input and output couplings from the source and load to the resonators.

The $N+2$ coupling matrix has the following advantages compared to conventional $N \times N$ coupling matrix [4]

- It allows a fully canonical filter functions to be synthesized.
- Multiple input/ output couplings become possible; that is, direct coupling between the source and load can be made, as well as coupling between source and load to the internal resonators.

The $N+2$ coupling matrix can be generated by synthesizing the transversal coupling matrix, which then can be transformed to a more convenient form, called folded coupling matrix by a transformation process, involving a series of matrix rotations.

The synthesis procedure of $N+2$ transversal coupling matrix of a Chebyshev filter begins with the generation of reflection and transfer polynomials, which explained in section 2.3 of this chapter. Having obtained reflection and transfer polynomials, the next step toward constructing the transversal coupling matrix is to convert both polynomials to complex frequency domain s, using $s = j\omega$, and then find the $y_{21}(s)$ and $y_{22}(s)$, which are elements of admittance matrix $[Y_N]$ for the overall network. The admittance matrix $[Y_N]$ is expressed as [4]

$$[Y_N] = \begin{bmatrix} y_{11}(s) & y_{12}(s) \\ y_{21}(s) & y_{22}(s) \end{bmatrix} = \frac{1}{y_d(s)} \times \begin{bmatrix} y_{11n}(s) & y_{12n}(s) \\ y_{21n}(s) & y_{22n}(s) \end{bmatrix} \tag{2.43}$$

$y_{21}(s)$ and $y_{22}(s)$ are obtained, using following equations for both bandpass filter and bandstop filter [4].

Consider a bandpass filter, if N (filter degree) is even:

$$y_{21}(s) = y_{21n}(s)/y_d(s) = (P(s)/\varepsilon)/m_1(s) \tag{2.44}$$

$$y_{22}(s) = y_{22n}(s)/y_d(s) = n_1(s)/m_1(s) \tag{2.45}$$

If *N* is odd:

$$y_{21}(s) = y_{21n}(s)/y_d(s) = (P(s)/\varepsilon)/n_1(s) \tag{2.46}$$

$$y_{22}(s) = y_{22n}(s)/y_d(s) = m_1(s)/n_1(s) \tag{2.47}$$

where

$$m_1(s) = Re(e_0 + f_0) + jIm(e_1 + f_1)s + Re(e_2 + f_2)s^2 + \cdots \tag{2.48}$$

$$n_1(s) = jIm(e_0 + f_0) + Re(e_1 + f_1)s + jIm(e_2 + f_2)s^2 + \cdots \tag{2.49}$$

e_i and f_i, $i = 0, 1, 2, 3, \cdots, N$ are the complex coefficients of $E(s)$ and $F(s)/\varepsilon_R$ respectively.

Now consider a bandstop filter, if *N* is even:

$$y_{21}(s) = y_{21n}(s)/y_d(s) = (F(s)/\varepsilon_R)/m_1(s) \tag{2.50}$$

$$y_{22}(s) = y_{22n}(s)/y_d(s) = n_1(s)/m_1(s) \tag{2.51}$$

If *N* is odd:

$$y_{21}(s) = y_{21n}(s)/y_d(s) = (F(s)/\varepsilon_R)/n_1(s) \tag{2.52}$$

$$y_{22}(s) = y_{22n}(s)/y_d(s) = m_1(s)/n_1(s) \tag{2.53}$$

where

$$m_1(s) = Re(e_0 + p_0) + jIm(e_1 + p_1)s + Re(e_2 + p_2)s^2 + \cdots \tag{2.54}$$

$$n_1(s) = jIm(e_0 + p_0) + Re(e_1 + p_1)s + jIm(e_2 + p_2)s^2 + \cdots \tag{2.55}$$

e_i and p_i, $i = 0, 1, 2, 3, \cdots, N$ are the complex coefficients of $E(s)$ and $P(s)/\varepsilon$ respectively.

After calculating the numerator and denominator of $y_{21}(s)$ and $y_{22}(s)$, partial fraction expansions can be used to find their residues r_{21k} and r_{22k} for $k = 1, 2, 3, \cdots, N$, and the eigenvalues λ_k of the network can be found by finding the roots of the denominator, which is common to both $y_{21}(s)$ and $y_{22}(s)$. By expressing obtained residues in matrix form, admittance matrix $[Y_N]$ in equation (2.43) can then be expressed as [4]

$$[Y_N] = j\begin{bmatrix} 0 & k_\infty \\ k_\infty & 0 \end{bmatrix} + \sum_{k=1}^{N} \frac{1}{(s - j\lambda_k)} \times \begin{bmatrix} r_{11k} & r_{12k} \\ r_{21k} & r_{22k} \end{bmatrix} \tag{2.56}$$

The constant k_∞ in matrix (2.56) is always zero except for a fully canonical filter, where the filter degree N is equal to the number of transmission zeros n_{fz}. Figure 2.5 (a) shows the general form of transversal array, which consists of a series of N individual first degree lowpass sections, which are connected in parallel between the source and load terminations, but not connected to each other. Figure 2.5 (b) shows that each first degree lowpass section consists of frequency invariant susceptance B_k and parallel connected capacitor C_k, which are connected through admittance inverters M_{Sk} and M_{Lk} to the source and load terminations, respectively [4]. Direct source to load coupling M_{SL} in figure 2.5 (a), shown as an inverter, which allows a fully canonical filter to be realized. Its value is equal to constant k_∞ in admittance matrix $[Y_N]$, and can be calculated by [4]

$$M_{SL} = k_\infty = \frac{\varepsilon \times (\varepsilon_R - 1)}{\varepsilon_R} \quad \text{or} \quad \sqrt{\frac{\varepsilon_R - 1}{\varepsilon_R + 1}} \tag{2.57}$$

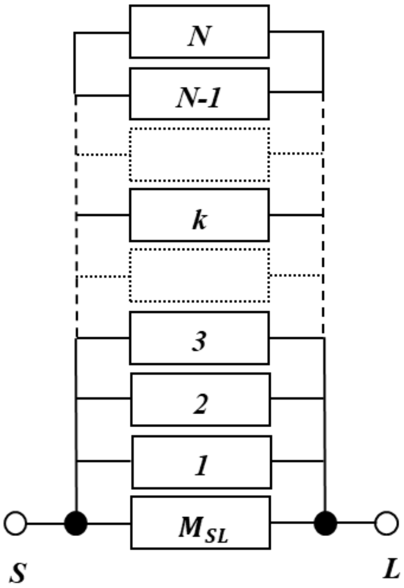

(a)

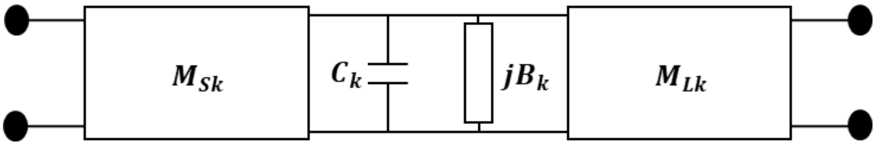

(b)

Figure 2.5 Canonical parallel transversal array. (a) *N*-resonator structure of transversal array [4]. (b) Equivalent circuit of the k^{th} lowpass resonator [4].

Admittance matrix of parallel connected lowpass resonators, which form a parallel transversal array, can be expressed in terms of the network elements as [4]

$$[Y_N] = j\begin{bmatrix} 0 & M_{SL} \\ M_{SL} & 0 \end{bmatrix} + \sum_{k=1}^{N} \frac{1}{(sC_k \; - \; jB_k)} \times \begin{bmatrix} {M_{Sk}}^2 & M_{Sk}M_{Lk} \\ M_{Sk}M_{Lk} & {M_{Lk}}^2 \end{bmatrix} \tag{2.58}$$

Admittance matrix in equation (2.58) is the sum of the y parameter matrices for N individual first degree lowpass sections, plus the y parameter matrix $[y_{SL}]$ to account for the direct source to load coupling M_{SL} [4].

Equating equations (2.56) and (2.58), results in set of equations which shows relationship between transversal circuit elements, and residues and eigenvalues, which are then can be used to construct the N+2 transversal coupling matrix [4].

$$C_k = 1$$

$$B_k = \; M_{kk} = \; -\lambda_k$$

$$M_{SL} = \; k_\infty$$

$${M_{Lk}}^2 = \; r_{22k}$$

$$M_{Sk}M_{Lk} = \; r_{21k}$$

$$M_{Lk} = \; \sqrt{r_{22k}}$$

$$M_{Sk} = \; \frac{r_{21k}}{\sqrt{r_{22k}}} \qquad\qquad k = 1, 2, 3, \cdots, N \tag{2.59}$$

where M_{Sk} is input coupling, M_{Lk} is output coupling, C_k is capacitor of the parallel networks that all are unity and B_k is frequency invariant susceptance which is representing the self-coupling. It is also obvious to see that direct source to load coupling M_{SL} is equal to k_∞.

Figure 2.6 shows the layout of the reciprocal N+2 transversal coupling matrix, which can be constructed using equation (2.59).

$$\begin{bmatrix} 0 & M_{S1} & M_{S2} & M_{S3} & \cdots & M_{Sk} & \cdots & M_{S,N-1} & M_{SN} & M_{SL} \\ M_{1S} & M_{11} & 0 & 0 & 0 & 0 & 0 & 0 & 0 & M_{1L} \\ M_{2S} & 0 & M_{22} & 0 & 0 & 0 & 0 & 0 & 0 & M_{2L} \\ M_{3S} & 0 & 0 & M_{33} & 0 & 0 & 0 & 0 & 0 & M_{3L} \\ \vdots & 0 & 0 & 0 & \ddots & 0 & 0 & 0 & 0 & \vdots \\ M_{kS} & 0 & 0 & 0 & 0 & M_{kk} & 0 & 0 & 0 & M_{kL} \\ \vdots & 0 & 0 & 0 & 0 & 0 & \ddots & 0 & 0 & \vdots \\ M_{N-1,S} & 0 & 0 & 0 & 0 & 0 & 0 & M_{N-1,N-1} & 0 & M_{N-1,L} \\ M_{NS} & 0 & 0 & 0 & 0 & 0 & 0 & 0 & M_{NN} & M_{NL} \\ M_{LS} & M_{L1} & M_{L2} & M_{L3} & \cdots & M_{LK} & \cdots & M_{L,N-1} & M_{LN} & 0 \end{bmatrix}$$

Figure 2.6 The N+2 transversal coupling matrix.

The frequency response of the transversal coupling matrix in terms of S parameters is given by [4]

$$S_{21} = -2j \times [A]^{-1}_{N+2,1}$$

$$S_{11} = 1 + 2j \times [A]^{-1}_{11} \tag{2.60}$$

where the matrix $[A]$ is given by

$$[A] = [m] + p[U] - j[q] \tag{2.61}$$

where $[q]$ is an N+2 matrix with all entries are zeros, except $[q]_{11} = [q]_{N+2,N+2} = 1$. $[U]$ is an identity matrix, except $[U]_{11} = [U]_{N+2,N+2} = 0$. $[m]$ is transversal coupling matrix and p is complex lowpass frequency variable, given by equation (2.29).

2.4.3 Coupling Matrix Reduction

Referring to figure 2.6 in previous section, there are N input and output couplings within the transversal coupling matrix, which makes it physically impractical or impossible for filter synthesis. The transversal coupling matrix can be transformed to a more convenient form, using a series of matrix rotations (similarity transforms) [10, 11], which annihilate unwanted coupling matrix entries from right to left along rows and from top to bottom in the columns.

The transformation process starts with first row on the top and last column on the right side of matrix, working inward toward the centre of matrix. The process continues until the remaining couplings can be realized in folded structure. The transformed matrix has the same reflection and transfer function characteristics as the original matrix, which indicates that matrix rotations ensures that eigenvalues and eigenvectors of the original matrix to be preserved [4].

The structure of folded N+2 coupling matrix can be seen in figure 2.7, where annihilated entries are shown in blue by numbers in sequence of transformations and nonzero couplings are denoted as

•	s	self-coupling
•	m	main line coupling
•	xa	asymmetric cross coupling
•	xs	symmetric cross coupling

Figure 2.8 shows the topology of folded canonical network of a 6th degree filter.

$$\begin{bmatrix} s & m & 5 & 4 & 3 & 2 & 1 & xa \\ . & s & m & 12 & 11 & 10 & xa & xs \\ . & . & s & m & 15 & xa & xs & 6 \\ . & . & . & s & m & xs & 13 & 7 \\ . & . & . & . & s & m & 14 & 8 \\ . & . & . & . & . & s & m & 9 \\ . & . & . & . & . & . & s & m \\ . & . & . & . & . & . & . & s \end{bmatrix}$$

Figure 2.7 6th degree folded N+2 coupling matrix structure.

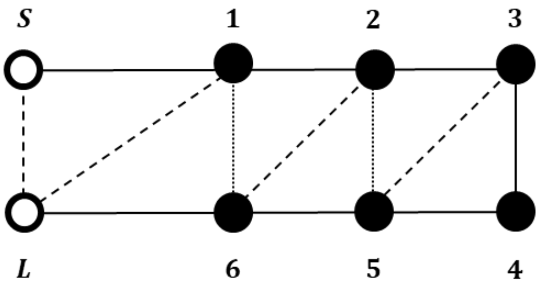

Figure 2.8 Folded canonical network coupling and routing schematic of a 6th degree filter.

Matrix rotation on an N+2 transversal coupling matrix M_0 is carried out by pre-multiplying by N+2 rotation matrix R_r, and post multiplying that by transpose of matrix R_r (R_r^t), as is expressed in the following equation for a complete series of transformations [4]

$$M_r = R_r \times M_{r-1} \times R_r^t \qquad \text{for } r = 1, 2, 3, \cdots, R \tag{2.62}$$

where, M_r is the matrix after rotation and R is the number of rotations which can be calculated by [4]

$$R = \sum_{i=1}^{(N+2)-3} i \tag{2.63}$$

Figure 2.9 shows a 6th degree N+2 rotation matrix with pivot of $[3, 4]$. The pivot $[i, j]$, indicates that elements R_{ii} and R_{jj} are equal to $\cos\theta_r$, and elements R_{ji} and $-R_{ij}$ are equal to $\sin\theta_r$, where θ_r is the angle of rotation.

$$\begin{bmatrix} 1 & 0 & 0 & 0 & 0 & 0 & 0 & 0 \\ 0 & 1 & 0 & 0 & 0 & 0 & 0 & 0 \\ 0 & 0 & 1 & 0 & 0 & 0 & 0 & 0 \\ 0 & 0 & 0 & R_{ii} & -R_{ij} & 0 & 0 & 0 \\ 0 & 0 & 0 & R_{ji} & R_{jj} & 0 & 0 & 0 \\ 0 & 0 & 0 & 0 & 0 & 1 & 0 & 0 \\ 0 & 0 & 0 & 0 & 0 & 0 & 1 & 0 \\ 0 & 0 & 0 & 0 & 0 & 0 & 0 & 1 \end{bmatrix}$$

$$R_{ii} = R_{jj} = \cos\theta_r \qquad\qquad R_{ji} = -R_{ij} = \sin\theta_r$$

Figure 2.9 6th degree N+2 rotation matrix.

Angle of rotation θ_r is calculated, using following equations for annihilating specific elements in an N+2 coupling matrix with rotation at pivot $[i, j]$ [4].

$$\theta_r = \tan^{-1}\left(\frac{M_{ik}}{M_{jk}}\right) \qquad \text{for elements in column } k$$

$$\theta_r = -\tan^{-1}\left(\frac{M_{kj}}{M_{ki}}\right) \qquad \text{for elements in row } k \tag{2.64}$$

Table 2.1 summarizes the entire rotation sequence for reduction of 6th degree N+2 transversal coupling matrix to folded coupling matrix, which is constructed based on folded N+2 coupling matrix in figure 2.7.

Table 2.1 6th degree rotation sequence for reduction of N+2 transversal coupling matrix to folded coupling matrix.

				$\theta_r = \tan^{-1}\left(c\frac{M_{kl}}{M_{mn}}\right)$				
Transform Number r	**Pivot $[i, j]$**	**Element to be Annihilated**	**Row/Column**	k	l	m	n	c
1	[5, 6]	M_{S6}	Row S	S	6	S	5	-1
2	[4, 5]	M_{S5}	Row S	S	5	S	4	-1
3	[3, 4]	M_{S4}	Row S	S	4	S	3	-1
4	[2, 3]	M_{S3}	Row S	S	3	S	2	-1
5	[1, 2]	M_{S2}	Row S	S	2	S	1	-1
6	[2, 3]	M_{2L}	Column L	2	L	3	L	1
7	[3, 4]	M_{3L}	Column L	3	L	4	L	1
8	[4, 5]	M_{4L}	Column L	4	L	5	L	1
9	[5, 6]	M_{5L}	Column L	5	L	6	L	1
10	[4, 5]	M_{15}	Row 1	1	5	1	4	-1
11	[3, 4]	M_{14}	Row 1	1	4	1	3	-1
12	[2, 3]	M_{13}	Row 1	1	3	1	2	-1
13	[3, 4]	M_{36}	Column 6	3	6	4	6	1
14	[4, 5]	M_{46}	Column 6	4	6	5	6	1
15	[3, 4]	M_{24}	Row2	2	4	2	3	-1

2.5 Microwave Waveguides and Resonators

2.5.1 Rectangular Waveguides

Rectangular waveguides are the simplest microwave structure, used to direct microwave signal with minimum loss. They provide good power handling and low loss and are easy to fabricate, but often bulky and difficult to integrate with active components [5]. Figure 2.10 shows a typical rectangular waveguide.

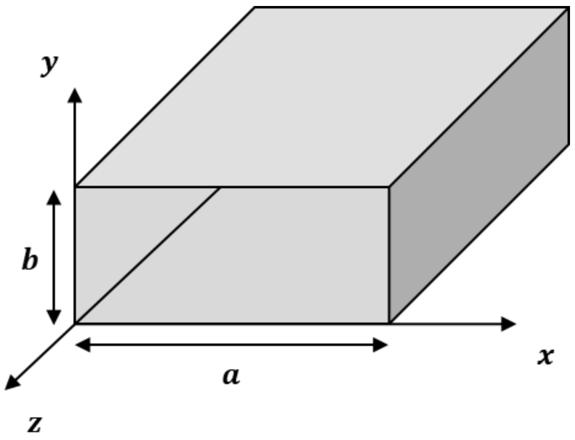

Figure 2.10 Rectangular waveguide.

A rectangular waveguide can propagate TM and TE modes, but not a TEM wave because rectangular waveguides only have one conductor [2]. Each mode in a rectangular waveguide has a cut-off frequency (f_{mnl}) given by [2]

$$f_{Cmn} = \frac{1}{2\pi\sqrt{\mu\epsilon}}\sqrt{\left(\frac{m\pi}{a}\right)^2 + \left(\frac{n\pi}{b}\right)^2} \tag{2.65}$$

where μ and ϵ are the permeability and permittivity of the material filling the waveguide, respectively. Indices m and n indicate the number of variations in x and y directions.

In a rectangular waveguide, the mode with the lowest cut-off frequency is called the dominant mode, which is TE_{10} mode with a cut-off frequency given by [2]

$$f_{C10} = \frac{1}{2a\sqrt{\mu\epsilon}} \tag{2.66}$$

Attenuation in rectangular waveguides can be caused by dielectric loss or conductor loss. The attenuation due to conductor loss in a hollow rectangular waveguide which operates in TE_{10} mode is given by [2]

$$\alpha_C = \frac{R_s}{a^3 b\beta k\eta}(2b\pi^2 + a^3k^2) \quad Np/m \tag{2.67}$$

where β is the propagation constant for the TE$_{10}$ mode, R_s is surface resistivity of the metallic walls, k is wave number and η is intrinsic impedance of the material filling the waveguide, and given by [2]

$$\beta = \sqrt{k^2 - \left(\frac{\pi}{a}\right)^2}$$

$$R_s = \sqrt{\frac{\omega\mu_0}{2\sigma}}$$

$$k = \omega\sqrt{\mu\epsilon}$$

$$\eta = \sqrt{\frac{\mu}{\epsilon}} \qquad (2.68)$$

σ is electrical conductivity of the metallic walls, μ_0 is permeability of vacuum and ω is angular frequency.

2.5.2 Rectangular Cavity Resonators

A rectangular cavity resonator is a section of rectangular waveguide terminated in a short circuit at both ends. Figure 2.11 illustrates a rectangular cavity resonator with length of *d*.

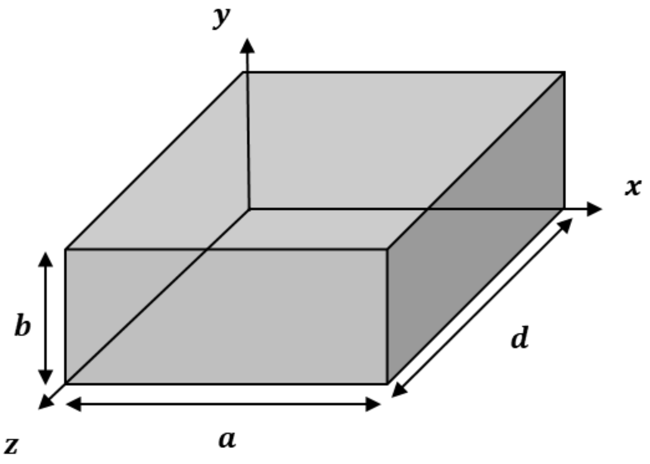

Figure 2.11 Rectangular cavity resonator.

A cavity resonator can be defined as a structure which can store both electric and magnetic fields. The resonant frequency of a cavity resonator is the frequency at which the energy stored in the electric field is equal to the energy stored in magnetic field [12].

In a rectangular cavity resonator, the electric field should be equal to zero at $z = 0$ and $z = d$, this implies that the length of cavity must be an integer multiple of half guided wavelength of the propagating wave. This condition can be expressed as [2]

$$d = \frac{l\pi}{\beta_{mn}} = \frac{l\lambda_g}{2} \qquad l = 1, 2, 3, \dots \dots \tag{2.69}$$

where λ_g is guided wavelength and β_{mn} is the propagation constant in a rectangular cavity resonator operating in TE or TM mode, which is given by [2]

$$\beta_{mn} = \sqrt{k^2 - \left(\frac{m\pi}{a}\right)^2 - \left(\frac{n\pi}{b}\right)^2} \tag{2.70}$$

a and b are width and height of the rectangular cavity resonator respectively. Indices m and n indicate the number of variations in x and y directions, and k is the wave number, which is defined in equation (2.68).

Using equation (2.69) and equation (2.70), the resonance wave number for a rectangular cavity resonator can be found, which is expressed as [2]

$$k_{mnl} = \sqrt{\left(\frac{m\pi}{a}\right)^2 + \left(\frac{n\pi}{b}\right)^2 + \left(\frac{l\pi}{d}\right)^2} \tag{2.71}$$

where d is length of the rectangular cavity resonator and indices l indicate the number of variations in z direction.

Using equation (2.71), the resonant frequency of a rectangular cavity resonator is expressed as follows [2]:

$$f_{mnl} = \frac{ck_{mnl}}{2\pi\sqrt{\mu_r\epsilon_r}} = \frac{c}{2\pi\sqrt{\mu_r\epsilon_r}}\sqrt{\left(\frac{m\pi}{a}\right)^2 + \left(\frac{n\pi}{b}\right)^2 + \left(\frac{l\pi}{d}\right)^2} \tag{2.72}$$

where μ_r and ϵ_r are relative permeability and permittivity of the material filling the cavity, and c is speed of light (2.99×10^8 m/s).

The unloaded quality factor for a cavity resonator is defined as the ratio of energy stored to the energy lost in the cavity resonator at the resonance frequency of the cavity resonator. It is important to calculate unloaded quality factor of rectangular cavity resonator, as it provides a sense of how much energy is lost in the cavity. The unloaded quality factor of a rectangular cavity resonator, for the TE_{101} mode, with lossy conducting walls and lossless dielectric, is given by [2]

$$Q_c = \frac{(kad)^3 b\eta}{2\pi^2 R_s} \frac{1}{[2l^2a^3b + 2bd^3 + l^2a^3d + ad^3]} \tag{2.73}$$

where Q_c represents the loss due to lossy conducting walls.

The unloaded quality factor of any cavity resonator with a lossy dielectric filling the cavity, but perfectly conductive walls, is given by [2]

$$Q_d = \frac{1}{\tan\delta} \tag{2.74}$$

where $\tan\delta$ is loss tangent of the material filling the cavity. If a cavity resonator has lossy conductive walls and filled with lossy dielectric, the total unloaded quality factor can be calculated using the following equation, which represents the total power loss [2].

$$Q_u = \frac{1}{\frac{1}{Q_c} + \frac{1}{Q_d}} \tag{2.75}$$

2.5.3 Circular Waveguides

Figure 2.12 shows a circular waveguide with cross section radius of a. A circular waveguide is a round metal pipe that supports TE and TM modes. Circular waveguides are mainly used in applications that required dual polarization capability. For example, a circularly polarized antenna must be able to propagate both vertically and horizontally polarized waves, and a circular waveguide is the most common form of dual polarization transmission line which can be used to be connected to such a component [1].

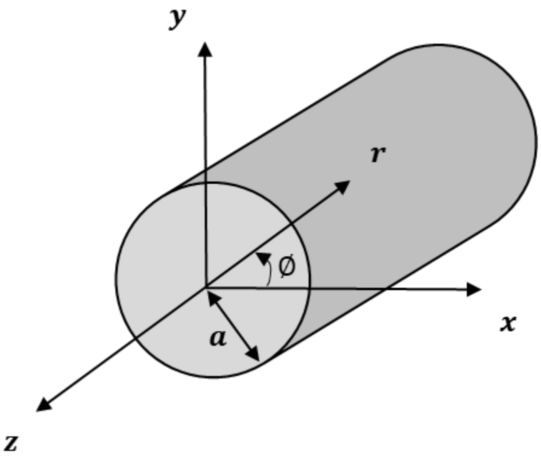

Figure 2.12 Circular waveguide.

The cut-off frequency of circular waveguide is given by [2]

$$f_{cnm} = \frac{p'_{nm}}{2\pi a\sqrt{\mu\epsilon}} \tag{2.76}$$

where μ and ϵ are permeability and permittivity of the material filling the waveguide respectively. Indices n and m indicate the number of circumferential ($\emptyset$) variations and radial (r) variations respectively. p'_{nm} is the root of Bessel functions, which can be found in table 2.2 for $m = 1 \cdots 3$ and $n = 0 \cdots 2$.

Looking at table 2.2, the smallest value is 1.841 which occurs when circular waveguide operates in TE_{11} mode, therefore TE_{11} mode is the dominant mode in a circular waveguide and has the lowest cut-off frequency [5].

Table 2.2 Roots of Bessel functions for TE modes [2].

n	p'_{n1}	p'_{n2}	p'_{n3}
0	3.832	7.016	10.174
1	1.841	5.331	8.536
2	3.054	6.706	9.970

The attenuation due to conductor loss in a hollow circular waveguide which operates in TE_{11} mode is given by [2]

$$\alpha_C = \frac{R_s}{ak\eta\beta}\left(k_c^2 + \frac{k^2}{p_{11}^2 - 1}\right) \quad Np/m \tag{2.77}$$

where R_s is surface resistivity of the metallic walls, β is the propagation constant, k is wave number, k_c is cut-off wave number and η is intrinsic impedance of the material filling the waveguide, and given by [2]

$$\beta = \sqrt{k^2 - k_c^2}$$

$$R_s = \sqrt{\frac{\omega\mu_0}{2\sigma}}$$

$$k = \omega\sqrt{\mu\epsilon}$$

$$k_c = \frac{p'_{nm}}{a}$$

$$\eta = \sqrt{\frac{\mu}{\epsilon}} \tag{2.78}$$

2.5.4 Cylindrical Cavity Resonators

Figure 2.13 shows a cylindrical cavity resonator, which is a section of circular waveguide with length of *d* and radius *a*, terminated in a short circuit at both ends.

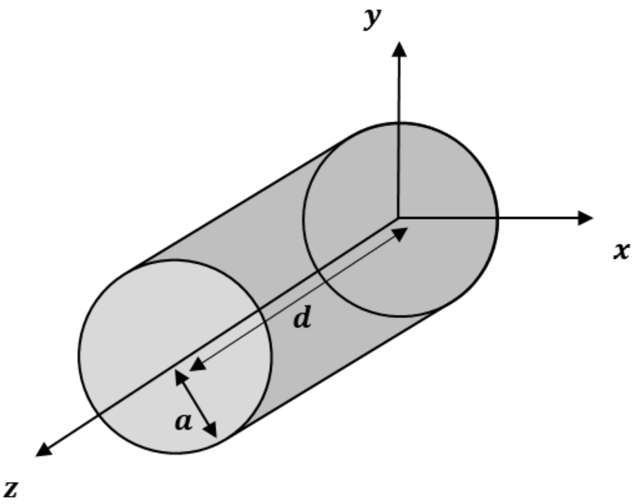

Figure 2.13 Cylindrical cavity resonator.

The resonant frequency of a cylindrical cavity resonator for TE and TM modes are given by [2]

For TE mode

$$f_{nml} = \frac{c}{2\pi\sqrt{\mu_r\epsilon_r}}\sqrt{\left(\frac{p'_{nm}}{a}\right)^2 + \left(\frac{l\pi}{d}\right)^2} \tag{2.79}$$

For TM mode

$$f_{nml} = \frac{c}{2\pi\sqrt{\mu_r\epsilon_r}}\sqrt{\left(\frac{p_{nm}}{a}\right)^2 + \left(\frac{l\pi}{d}\right)^2} \tag{2.80}$$

where μ_r and ϵ_r are relative permeability and permittivity of the material filling the cavity, c is speed of light, a and d are radius and length of the cylindrical cavity resonator, and indices m, n and l are the number of variations in x, y and z directions. p'_{nm} and p_{nm} are roots of the Bessel functions for TE and TM modes respectively, which are given in table 2.3 for $m = 1 \cdots 3$ and $n = 0 \cdots 2$ [5].

Table 2.3 Roots of Bessel functions for TE and TM modes [2].

n	p'_{n1}	p'_{n2}	p'_{n3}	p_{n1}	p_{n2}	p_{n3}
0	3.832	7.016	10.174	2.405	5.520	8.654
1	1.841	5.331	8.536	3.832	7.016	10.174
2	3.054	6.706	9.970	5.135	8.417	11.620

The quality factor due to lossy conducting wall of hollow cylindrical cavity resonator operating in TE mode, is given by [2]

$$Q_c = \frac{(ka)^3\eta ad}{4(p'_{nm})^2R_s}\frac{1-\left(\frac{n}{p'_{nm}}\right)^2}{\left\{\frac{ad}{2}\left[1+\left(\frac{\beta an}{(p'_{nm})^2}\right)^2\right]+\left(\frac{\beta a^2}{p'_{nm}}\right)^2\left(1-\frac{n^2}{\left(p'^{\,2}_{nm}\right)}\right)\right\}} \tag{2.81}$$

where R_s is surface resistivity of the metallic walls, β is propagation constant, k is wave number and η is intrinsic impedance of the material filling the cavity, which are given in equation (2.78). If the cylindrical cavity resonator filled with lossy dielectric, the unloaded quality factor due to lossy dielectric can be calculated, using equation (2.74), which then can be used to find total unloaded quality factor, using equation (2.75).

2.6 Design and Physical Realisation of Iris Coupled Waveguide Resonator Filter

The physical realization of microwave filters is based on coupling matrix theory [3, 4], where an electromagnetic simulator is used to determine the filter dimensions. Microwave filters consist of several resonators coupled by inductive or capacitive coupling elements. The inter resonator coupling between cavity resonators can be achieved with the use of an iris, and input/output coupling is realized by using a probe or iris.

The first step toward physical realization of a microwave filter is to identify the filter order and function based on the specification, which are then used to synthesis the coupling matrix. Having obtained the coupling matrix, the physical filter type needs to be identified, which depends on power handling capacity, losses and size requirements. The next step would be to find the filter physical dimensions based on coupling matrix elements, which involve extracting external quality factors and inter resonator couplings. Finally, by using advanced EM modelling techniques, the physical dimensions of the filter can be optimised.

Here, the design of a 5th order bandpass waveguide filter is used as an example, this is designed using coupling matrix theory and CST Microwave Studio [13]. The filter is specified in terms of the Chebyshev bandpass response with a centre frequency of 300 GHz, a bandwidth of 27 GHz and passband ripple of 0.04 dB, corresponding to return loss of 20 dB. The filter consists of five rectangular cavity resonators operating in the TE_{101} mode. The coupling between resonators and the input/output couplings are realized, using capacitive irises. Figure 2.14 shows the structure of the waveguide filter.

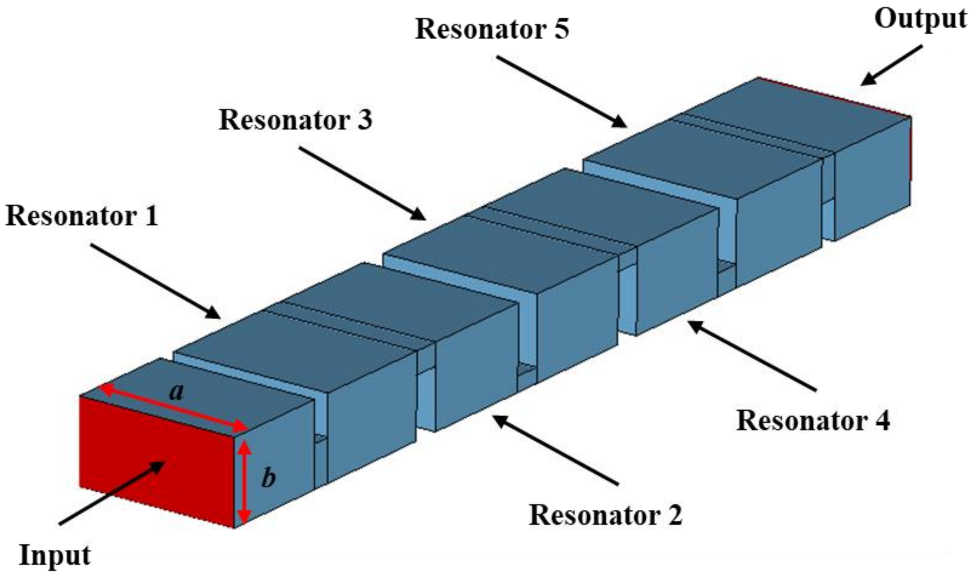

Figure 2.14 The structure of the waveguide filter, where a = 0.864 mm and b = 0.432 mm. Note that the blue area represents the vacuum, which is surrounded by PEC (perfect electric conductor).

Using equation (2.40), the g values (lowpass element values) corresponding to return loss of 20 dB are calculated as $g_0 = 1$, $g_1 = 0.9714$, $g_2 = 1.3721$, $g_3 = 1.8014$, $g_4 = 1.3721$, $g_5 = 0.9714$ and $g_6 = 1$. These are then used to determine the normalised external quality factors and coupling coefficients by using equations (2.37), (2.38) and (2.39) as $q_{e1} = q_{eN} = 0.9714$, $m_{12} = m_{45} = 0.8662$ and $m_{23} = m_{34} = 0.6361$. The coupling matrix of the filter is given as follows:

$$[m] = \begin{bmatrix} 0 & 0.8662 & 0 & 0 & 0 \\ 0.8662 & 0 & 0.6361 & 0 & 0 \\ 0 & 0.6361 & 0 & 0.6361 & 0 \\ 0 & 0 & 0.6361 & 0 & 0.8662 \\ 0 & 0 & 0 & 0.8662 & 0 \end{bmatrix} \tag{2.82}$$

Figure 2.15 shows ideal response of the filter, plotted using equation (2.36).

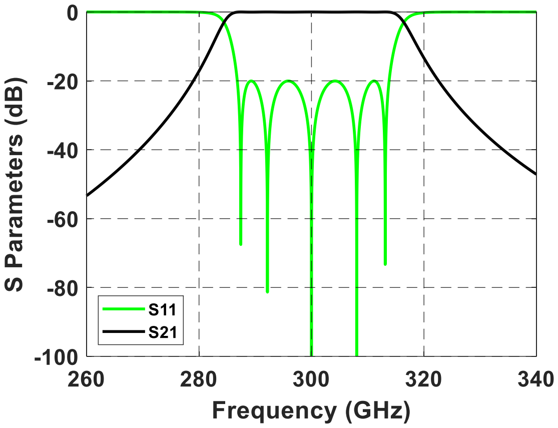

Figure 2.15 Ideal response of the 5th order Chebyshev filter.

To synthesis physical dimensions of the filter, un-normalised non-zero coupling coefficients and external quality factors need to be calculated, using the following relations [3, 4]:

$$Q_{e1} = \frac{q_{e1}}{FBW}$$

$$Q_{eN} = \frac{q_{eN}}{FBW}$$

$$M_{i,i+1} = \; FBW \cdot m_{i,i+1} \qquad \text{for } i \; = \; 1 \text{ to } N-1 \tag{2.83}$$

Table 2.4 provides calculated external quality factors and coupling coefficients of the waveguide filter.

Table 2.4 The external quality factors and coupling coefficients of the waveguide filter**.**

Q_{e1}	Q_{eN}	M_{12}	M_{23}	M_{34}	M_{45}
10.8	10.8	0.078	0.0573	0.0573	0.078

2.6.1 Extraction of External Quality Factor Using Simulation

The input/output coupling of the waveguide filter is realized with the use of an iris. The physical dimension of the input/ output irises is determined by using EM simulation tool, where the structure shown in figure 2.16 was used. Looking at figure 2.16, the input coupled by a capacitive iris with height of E and thickness of 0.1 mm, while the output is weakly coupled by reducing the iris height down to 5 μm with the same thickness, and the length of the waveguide cavity resonator denoted by L.

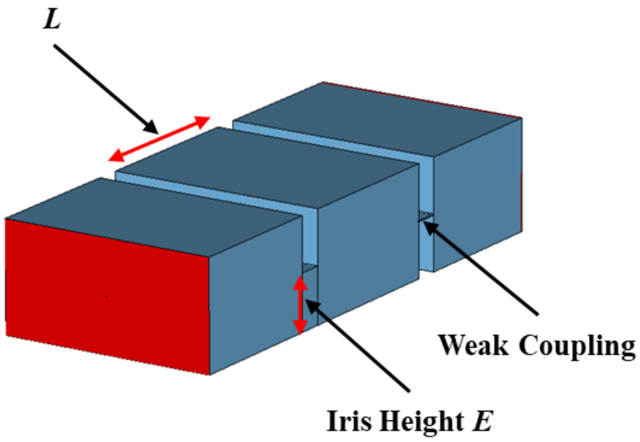

Figure 2.16 The structure of model used to extract external quality factor.

Figure 2.17 shows simulated S_{21} of the structure shown in figure 2.16, which can be used to extract the external quality factor Q_{e1}, using the following equation [3, 4].

$$Q_{e1} = \frac{f_0}{\Delta f} \tag{2.84}$$

f_0 is resonant frequency and Δf is 3 dB bandwidth.

By adjusting iris height E, a relation between external quality factor and iris height can be found as it is shown in figure 2.18. Using the relation, the height of iris can be found for the required external quality factor of $Q_{e1} = Q_{eN} = 10.8$. This is $E = 0.22$ mm and is denoted by red dot in figure 2.18. It is important to note that the length of cavity resonator L needs to be adjusted during each iteration of the simulation to keep the resonance frequency at 300 GHz. The red dot in figure 2.18 is therefore at the centre frequency of the waveguide filter and L found to be 0.668 mm for both resonator 1 and resonator 5 ($L_1 = L_5$), as the filter is symmetrical.

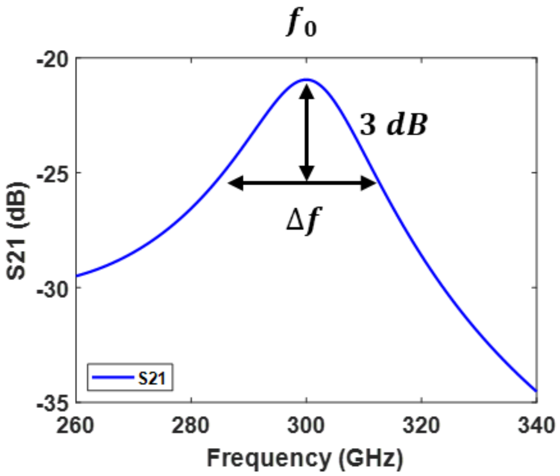

Figure 2.17 Simulated S_{21} of the structure shown in figure 2.16.

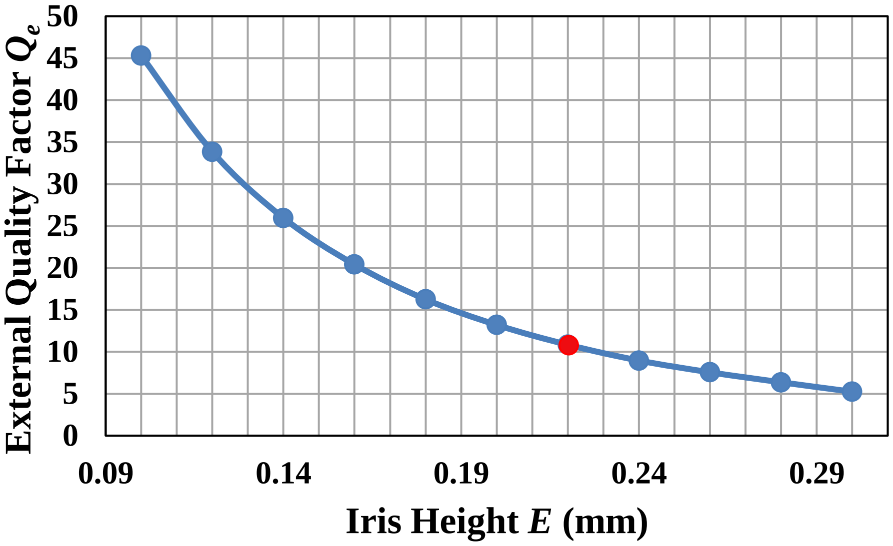

Figure 2.18 Relation between external quality factor and iris height.

2.6.2 Extraction of Inter Resonator Couplings

The coupling between resonators are also realized, using capacitive irises. The coupling coefficient k_c for each pair of resonators is extracted by using EM simulation tool. Figure 2.19 shows the structure of the model used to calculate inter resonator couplings, where the coupling between two resonators is controlled by adjusting iris height *D*. The iris thickness is kept fixed at 0.143 mm.

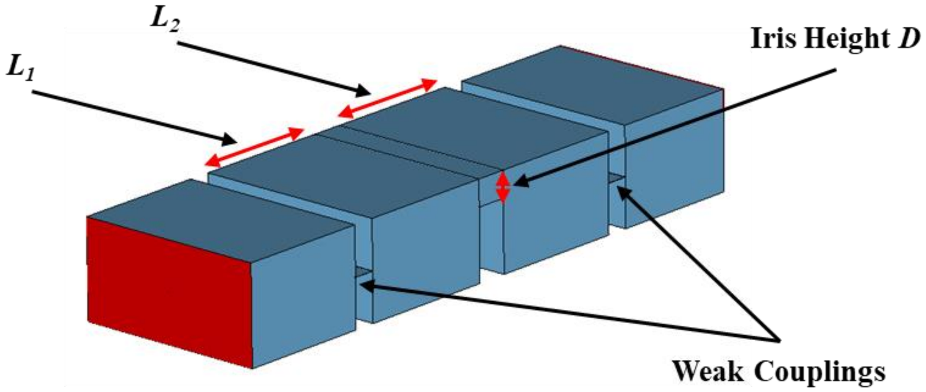

Figure 2.19 The structure of model used to extract inter resonator couplings.

The coupling coefficient between two resonators can be calculated by using electric and magnetic wall symmetry, which is difficult to implement experimentally and can only be calculated theoretically by using EM simulation software that has an eigenvalue calculation capability [4]. An alternative technique is to connect two resonators in a two-port structure as shown in figure 2.19, where both input and output ports are weakly coupled. Here the height of input and output irises are reduced to 0.8 µm to achieve weak coupling. The coupling coefficient can then be calculated from the centre frequency of the two coupled resonators (f_1 and f_2), which is shown in figure 2.20, where the coupling coefficient k_c is given by [4]

$$k_c = \pm\left(\frac{f_2^2 - f_1^2}{f_2^2 + f_1^2}\right) \tag{2.85}$$

By adjusting iris height D, a relation between inter resonator coupling coefficient and iris height can be found as shown in figure 2.21. This can be used to find iris height for the required coupling coefficient. The length of both resonators also needs to be adjusted in each iteration of the simulation to keep the middle frequency of the two peaks ($(f_1 + f_2) / 2$) at the centre frequency of the filter.

The iris heights corresponding to required coupling coefficients $M_{12} = M_{45} = 0.078$ and $M_{23} = M_{34} = 0.0573$, are obtained as $D_1 = D_4 = 0.116$ mm and $D_2 = D_3 = 0.08$ mm from the relation in figure 2.21, which are denoted by red and black dots respectively. The length of resonators is also found as $L_2 = L_4 = 0.628$ mm and $L_3 = 0.625$ mm.

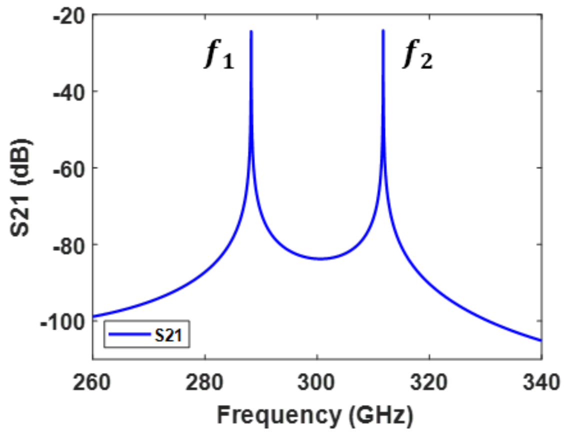

Figure 2.20 Simulated S_{21} of the structure shown in figure 2.19.

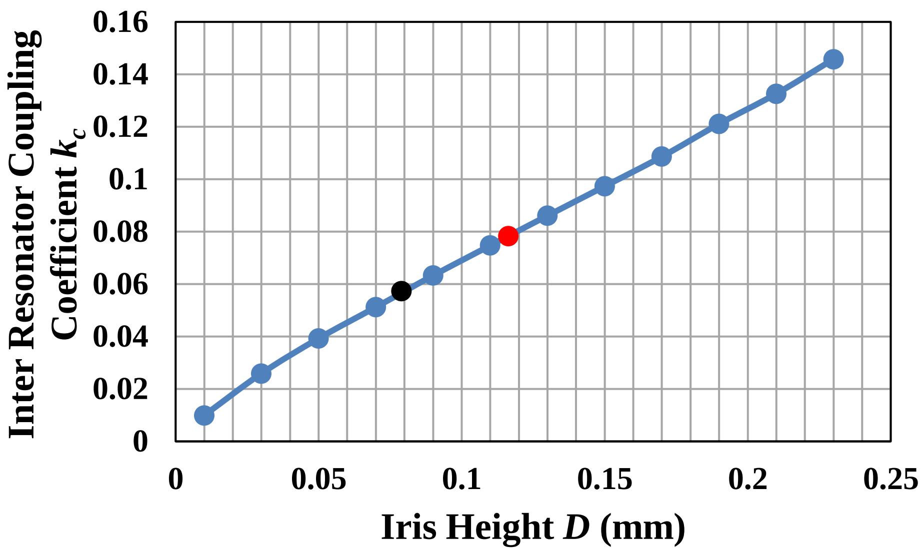

Figure 2.21 Relation between inter resonator coupling coefficient and iris height.

2.6.3 Final Physical Design of the Waveguide Filter

After extracting the initial physical dimensions of the waveguide filter, the last step involves connecting all five resonators in series to complete the filter. Figure 2.22 (a) shows the initial simulated response of the filter based on extracted physical dimensions in comparison with the ideal response. The results obtained can be considered as a reasonable initial response as it is close to the ideal response. A better solution can be obtained by optimising the waveguide filter, using advanced EM modelling technique such as finite element method (FEM).

During the optimisation process, optimisation goals are set to be: S11 under -20 dB for frequency range of 286.5 GHz to 313.5 GHz, S11 more than -20 dB for frequency range of 220 GHz to 286.5 GHz and S11 more than -20 dB for frequency range of 313.5 GHz to 330 GHz. The response of the filter after optimisation can be seen in figure 2.22 (b). During the optimisation, the height of irises and the length of the five resonators have been adjusted. The physical dimensions of the waveguide filter after optimisation are given in figure 2.23.

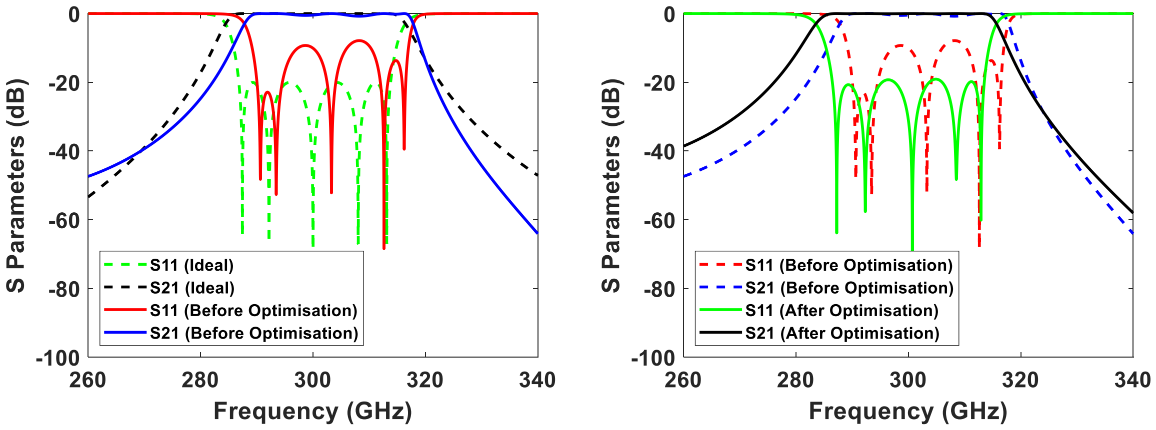

(a) (b)

Figure 2.22 Simulated response of the designed waveguide filter. (a) Simulated response of the filter before optimisation in comparison with ideal response. (b) Comparison between simulated response of the filter before optimisation and after optimisation.

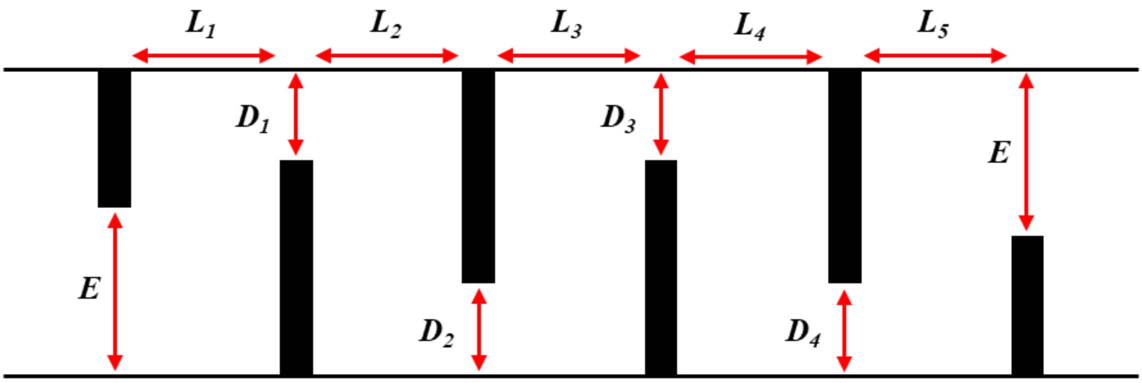

Figure 2.23 A side-view diagram of the waveguide filter. The dimensions of the waveguide filter after optimisation are given as $L_1 = L_5 = 0.694$ mm, $L_2 = L_4 = 0.644$ mm, $L_3 = 0.639$ mm, $E = 0.258$ mm, $D_1 = D_4 = 0.135$ mm and $D_2 = D_3 = 0.093$ mm.

2.7 Conclusion

The fundamental theory of microwave filter networks is explained in this chapter, starting by describing basic concepts of microwave filter and filter transfer function. The coupling matrix synthesis of filter networks introduced for both $N \times N$ and $N+2$ coupling matrices. The technique for reduction of the $N+2$ transversal coupling matrix to the folded coupling matrix was also described. This chapter introduced two standard cavity resonators, rectangular and cylindrical cavity resonators, as well as rectangular and circular waveguides, where several key concepts and equations related to both cavity resonators and waveguides reviewed. The final part of this chapter described the design and physical realization of an iris coupled waveguide resonator filter by using coupling matrix theory and EM simulation tool.

References

[1] P. A. Rizzi, *Microwave engineering: passive circuits*. Upper Saddle River, NJ: Prentice Hall, 2002.

[2] D. M. Pozar, *Microwave engineering*. Hoboken, NJ: Wiley, 2012.

[3] J.-S. Hong, *Microstrip filters for RF/microwave applications*. Hoboken, NJ: Wiley, 2011.

[4] R. J. Cameron, C. M. Kudsia, and R. R. Mansour, *Microwave filters for communication systems: fundamentals, design, and applications*. Hoboken, NJ, USA: John Wiley & Sons, Inc., 2018.

[5] P. Jarry and J. Beneat, *Advanced design techniques and realizations of microwave and RF filters*. Hoboken, NJ: Wiley, 2008.

[6] R. Cameron, “Advanced Filter Synthesis,” *IEEE Microwave Magazine*, vol. 12, no. 6, pp. 42–61, Oct. 2011.

[7] A. Atia and A. Williams, “New types of bandpass filters for satellite transponders,” COMSAT Tech, Rev. 1, pp. 21–43, Sept. 1971.

[8] A. Atia and A. Williams, “Nonminimum-Phase Optimum-Amplitude Bandpass Waveguide Filters,” *IEEE Transactions on Microwave Theory and Techniques*, vol. 22, no. 4, pp. 425–431, Apr. 1974.

[9] A. Atia, A. Williams, and R. Newcomb "Narrow-band multiple-coupled cavity synthesis," *IEEE Transactions on Circuits Systems*, CAS, vol. 1, no. 5, 21, pp. 649–655, Sept. 1974.

[10] F. R. Gantmacher, *The theory of matrices*. New York: Chelsea, 1959.

[11] C. E. Froberg, *Introduction to numerical analysis*. Reading: Addison-Wesley, 1965.

[12] M. J. Lancaster, *Passive Microwave Device Applications of High-temperature Superconductors*. Cambridge Univ Pr, 2006.

[13] Computer Simulated Technology (CST). (2017). Microwave Studio. [Online]. Available: http//www.cst.com/.

CHAPTER 3: ADDITIVE MANUFACTURING TECHNOLOGIES

Using additive manufacturing technologies to fabricate microwave components has become popular over the past decade. Many microwave components have been fabricated using additive manufacturing technologies such as microwave filters [1]-[15], antennas [16]-[22], waveguides [23]-[25], orthomode transducers (OMT) [26]-[29] and a diplexer [30]. Using additive manufacturing allows components with complex 3-D structures to be fabricated with high accuracy. It also allows rapid prototyping, which is an advantage as a way to inspect and visualise the structures of any complexity in a short period of time, usually before production [31]. Monoblock components can be fabricated by using additive manufacturing, which is very desirable for microwave components as it allows skipping the assembly of parts and prevents field leakage due to misalignments which results in poor performance.

3-D printing is an additive manufacturing technology to build three-dimensional objects and is based on the deposition of material, layer by layer [10]. There are many different types of 3-D printing technologies and are classified in three main categories:

- UV curing of resin, which includes stereolithography apparatus (SLA) technology and inkjet printing [32].
- Selective deposition of extruded material, which includes fused deposition modelling (FDM) [33].
- Powder binding, which includes selective laser sintering (SLS) [34].

Generally, both metallic and non-metallic materials can be used in 3-D printing process. Components made from non-metallic materials benefit from a much lighter weight due to the use of low-density materials. However, the downside of using non-metallic material is increasing the fabrication cost and complexity, as non-metallic microwave components require metal coating process to achieve a good electrical conductivity. Non-metallic materials also have lower working temperature. Using metallic material in fabrication of microwave components ensures higher working temperature, better thermal expansion properties, and increases the strength of components.

This chapter introduces different types of 3-D printing technologies, where details of fabrication process for each type is described. A recently developed 3-D printing technique will be introduced, which is known as 3-D screen printing, that allows complex metallic structures to be fabricated with high accuracy. Information about different types of materials that can be used in 3-D printing processes will be provided, as well as information about factors that could affect the performance of microwave components. A brief description about the metallization process of 3-D printed microwave components will also be given. Finally, some of the key design considerations for 3-D printing will be explained.

3.1 Stereolithography Apparatus

The stereolithography apparatus (SLA) process is a 3-D printing process, in which photo-curable liquid resin converts into solid objects using a 3-D printing machine known as stereolithograph apparatus. The process was first developed by Charles Hull and Raymond S. Freed in 1986 and it was the first commercial process in additive manufacturing [31].

Figure 3.1 shows how SLA process works. The process begins by filling the vat with photo-curable liquid resin, where the elevator platform is set just below the surface of liquid resin. The software converts 3-D model of the design into a series of cross section layers, typically with thickness of 0.025 to 0.5 mm. Each layer is built by scanning the ultraviolet laser beam on the surface of liquid resin, so that it cures and solidifies into a pattern corresponding to the structure of cross section layer. Once a layer is built, the elevator platform is then lowered by a distance equal to the thickness of a single layer, and a levelling wiper blade moves across the surface of the completed layer, re-coating it with new liquid. The ultraviolet laser beam then builds the next layer, as in previous step. The process continues until the whole structure is built. Once the part is completed, it is removed from the vat and cleaned of excess material by immersing it in a chemical bath [31].

Stereolithography apparatus technology creates a smooth surface due to small spot size of the laser beam and low viscosity of the photo-curable liquid resin. This makes the stereolithography apparatus technology to be one of the best 3-D printing processes for fabrication of microwave components. Microwave filters which are fabricated by the SLA technology have been reported in [1]-[10]. Other microwave components such as microwave antennas [16]-[20] and orthomode transducers (OMT) [27, 28] are also fabricated by SLA technology. The downsides of using SLA technology for fabricating microwave components are lower working temperature, low thermal expansion properties and decrease in the strength of components, as this technology uses non-conductive polymer or resin. The microwave components made by SLA technology require an additional metal coating process to achieve a good electrical conductivity which increases cost and complexity of the fabrication process.

3.2 Fused Deposition Modelling

Fused deposition modelling (FDM) also known as fused filament fabrication (FFF) is a solid-based additive manufacturing process in which a material is extruded layer by layer to build a structure. This technology was first developed by Scott Cramp in 1988, and then was patented in 1992 [31]. Figure 3.2 shows the FDM process, in which a filament material moves toward the printing head by drive wheels, where it is melted by heating elements within the printing head, the material is then extruded through the nozzle. As the material is extruded, the printing head moves over the build platform horizontally and vertically, drawing a cross section of a structure, where extruded material is cooled and solidified to form a layer. Once a layer is completed, the build platform is lowered, then the next layer is built. The process is continued until the whole structure is completed [31].

FDM is the cheapest additive manufacturing process, which is an advantage when high volume manufacturing is required. The downside of using FDM is restricted accuracy of parts built, due to nozzle aperture diameter (generally it is 400 µm wide). Another disadvantage of using FDM is unpredictable shrinkage. The FDM process extrudes heated material from the printing head and the material cools down rapidly once it is laid down, this rapid cooling introduces shrinkage and distortion into the model which is usually difficult to predict. The speed of the FDM process is also restricted by the low extrusion rate, because of high viscosities of plastic materials [31]. Despite low accuracy of FDM process, several microwave components have been successfully fabricated. Fabrication of microwave filters by FDM technology was reported in [14] and [15]. Other examples of microwave components, made by FDM technology are a waveguide to SMA adapter and a horn antenna [15, 21]. Microwave components that are fabricated by the FDM process require metal coating to achieve a good electrical conductivity, this increases the cost and complexity of the fabrication process.

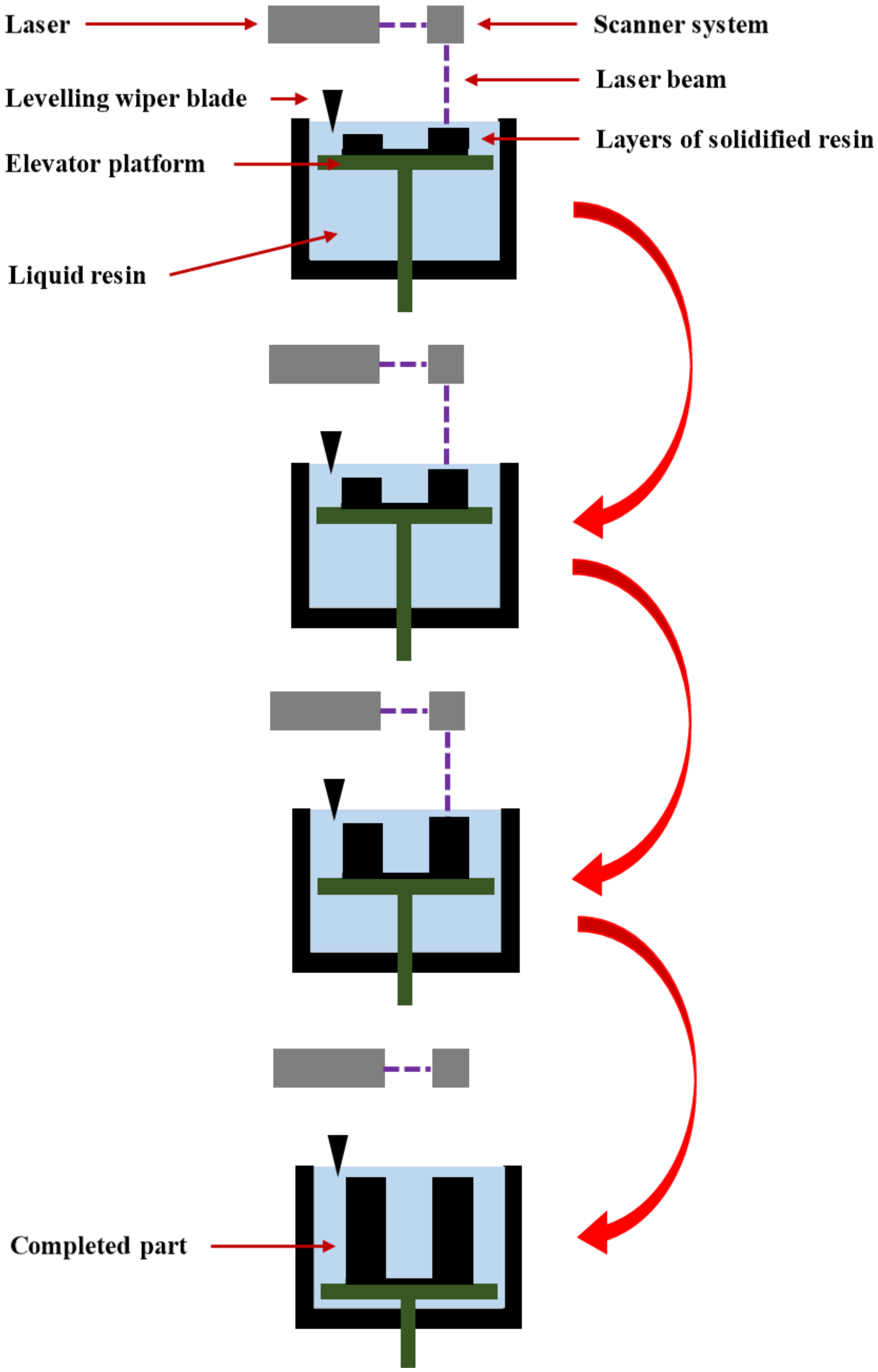

Figure 3.1 Stereolithography apparatus process.

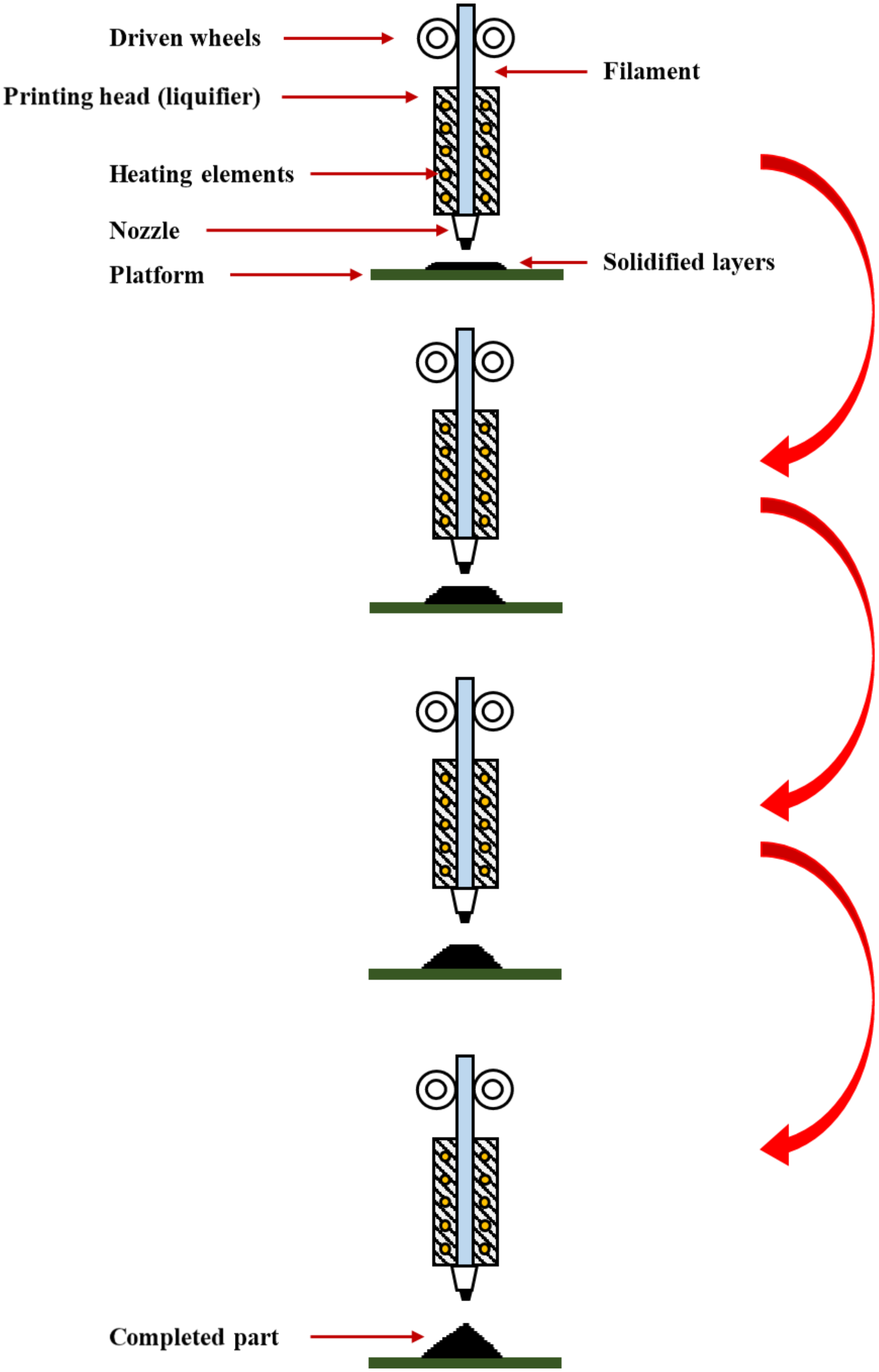

Figure 3.2 Fused deposition modelling process.

3.3 Selective Laser Sintering

Selective laser sintering (SLS) also known as selective laser melting (SLM) or micro laser sintering (MLS) is another type of additive manufacturing which is based on laser sintering of metal or plastic powders. The SLS technology was first developed by Carl Deckard, at the University of Texas in 1986 [31]. The SLS process is very similar to the SLA process, both techniques use a laser beam to trace out and build individual layers, although in the SLA process a liquid resin is cured by laser beam, but in the SLS process powder is selectively fused together by the laser beam to build a layer.

Figure 3.3 shows how SLS process works. The process begins by dividing the model structure into layers. Next, a thin layer of heat-fusible powder is deposited into the chamber where the part is going to be built. A laser beam (usually CO_2 laser) then selectively scans the layer of powder to create the bottom-most layer of the 3-D structure. The laser beam elevates the temperature of powder to the melting point, causing the powder particles to fuse and form a solid mass. Once a layer is completed, the building platform within the part-building chamber is lowered and another layer of powder is deposited on the top of the previously scanned layer. The laser then scans the newly deposited powder layer and creates the new solid layer of the model structure. The process is continued until the part is completed, which is then left to cool down gradually. Once the part is cooled, it is transferred to a cleaning station, where it is cleaned of the excess powder [31].

The SLS technology is the most accurate additive manufacturing to 3-D print solid metal structures. This is important for the fabrication of microwave components, as it enables components with complex structures to be directly fabricated from metallic materials, which results in high strength, wider working temperature range and better thermal expansion properties. Recent example of using SLS technology in fabrication of microwave components is reported in [13], where 90 GHz waveguide filters were fabricated using a micro laser sintering process; this will be explained further in chapter five.

High power consumption is one of the weaknesses of using the SLS process, which is due to the high wattage of the laser required to sinter the powder particles together. The dimensional accuracy of the fabrication is also limited by the laser beam spot size and powder particle dimensions.

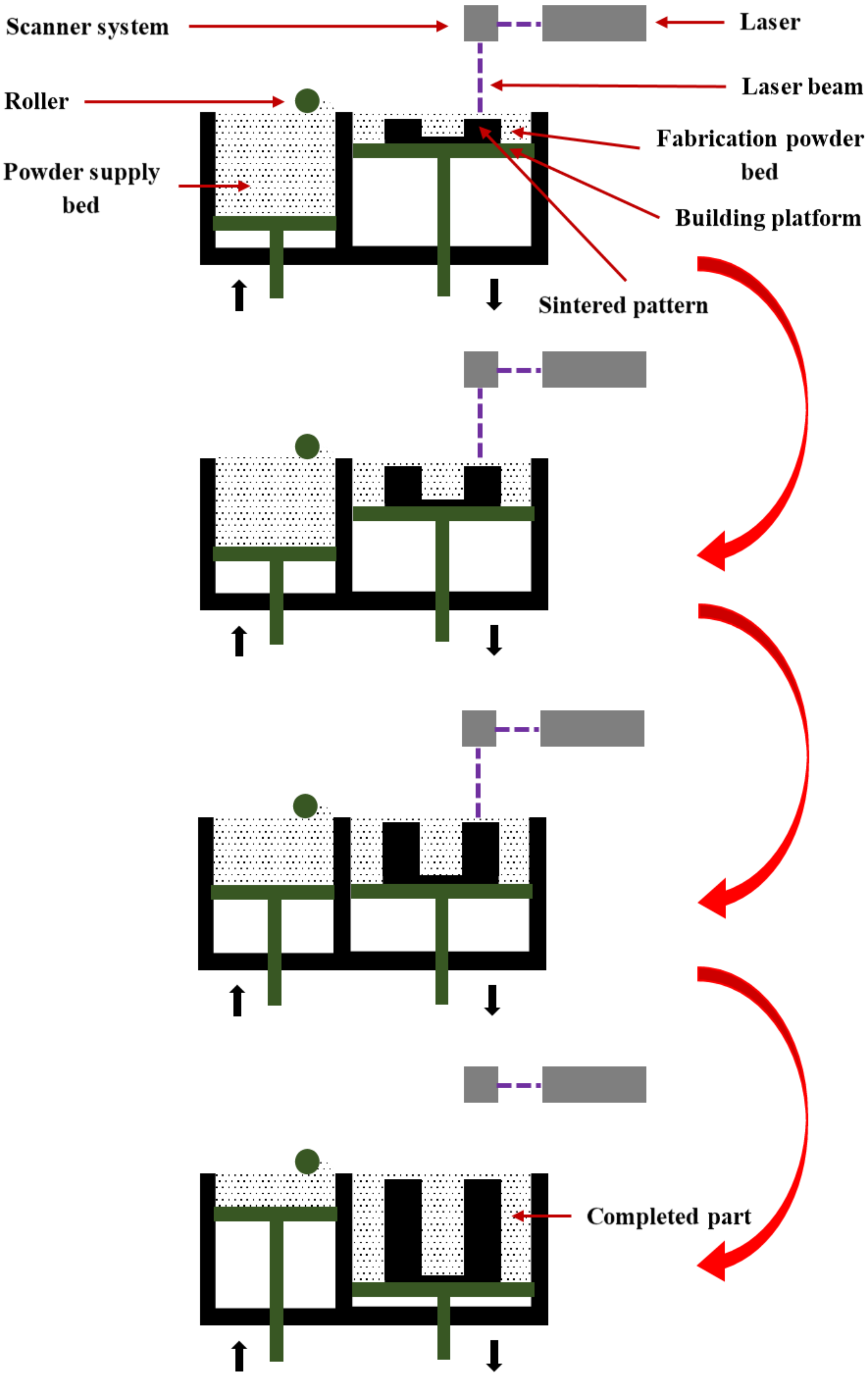

Figure 3.3 Selective laser sintering process.

3.4 3-D Printing Materials

3-D printing materials can be separated in two main groups: polymers and metals. Depending on which type of 3-D printing process is used, 3-D printing materials come in three different forms including; filament, resin and powder. Other types of material such as ceramics or composites are also used in 3-D printing technologies [35].

Polymers such as plastics come in three different forms including; filament, resin and powder. Generally, they can be divided in two different categories, thermosets and thermoplastics. Thermosets are those that come as a viscous fluid which can be cured and solidified via light exposure, heat or even by mixing with a catalyst. The stereolithography apparatus process uses photopolymer thermosets which harden during the fabrication process by exposing to an ultraviolet laser. Thermoplastics are those that come as a solid material which can be melted and solidified repeatably while their properties remain unchanged. Fused deposition modelling process uses thermoplastic polymers, where the solid thermoplastic polymer heated up to a malleable state and extruded onto a build platform where it can be solidified [35].

Metals are the other types of material that are used in 3-D printing, and exclusively come in powder form. Using metal in 3-D printing increases the strength of fabricated components, insures a wider working temperature range and better thermal expansion properties. Metal powders are used in the selective laser sintering process. A variety of metal powders are available for 3-D printing, which have their own unique properties. The most commonly used metal powders are copper, stainless steel, molybdenum, tungsten, titanium and aluminium [35].

Other materials that are used in 3-D printing, are ceramics or composites. A polymer that is filled with ceramic powder improves wear resistance and is used in stereolithography apparatus 3-D printing, here the liquid resin is filled with ceramic powders. Polymer powder with added aluminium, carbon, glass and graphite are also used in selective laser sintering, which results in static resistance, wear resistance and increase of strength. Composites such as filaments filled with fragments of graphite or metal nylon powder have also been used [35].

3.5 3-D Screen Printing

3-D screen printing is a new additive manufacturing technique which makes the use of the classical screen-printing technique. Fabrication of miniaturized parts by 3-D screen printing was first introduced by Fraunhofer IFAM Dresden in Germany [36]. This technique is a modified screen-printing process based on a powder-binder mixture that is printed layer by layer to build a desired structure then followed by de-binding and a conventional sintering step [37].

Figure 3.4 shows the principle of the 3-D screen printing process. The process starts by dividing the model structure into layers, where a screen layout is generated, resembling structure of each layer. Then powders, binder and additives are mixed to a homogenous printing paste, which is pressed through the screen with the help of a printing squeegee on a substrate to form the first layer of structure. After the first layer is dried, the second layer is printed on top of the first layer. The process continues until the required height is reached. Dimensional changes such as complex internal shapes or overhangs can be achieved by changing to different screens during the printing process. Once the entire structure is built and dried, the process is followed by a heat treatment which provides sintering and binder removal [37].

3-D screen printing enables production of complex structures down to micrometre scale. The technique is well suitable for mass production, where different parts with different structures can be made simultaneously. Easy upscaling for mass production, high accuracy and high reproducibly are among other advantages of 3-D screen printing [38, 39].

3-D screen printing process doesn’t need any supporting powder bed, which means there is no need to remove excess powder after production. 3-D screen printing allows variety of powder materials to be used in the fabrication process, such as titanium, copper, stainless steel, tungsten, molybdenum, nickel, cobalt, aluminium and carbides, as well as oxide ceramics. It is also possible to have a combination of materials, if they have similar heat treatment [38, 39].

This technology is potentially a good choice for fabrication of high frequency filters with complex structures, using a variety of metallic materials. The filter in chapter eight, which is a 300 GHz waveguide filter is designed for 3-D screen printing. This project demonstrates the possibility of using 3-D screen printing in fabrication of terahertz components.

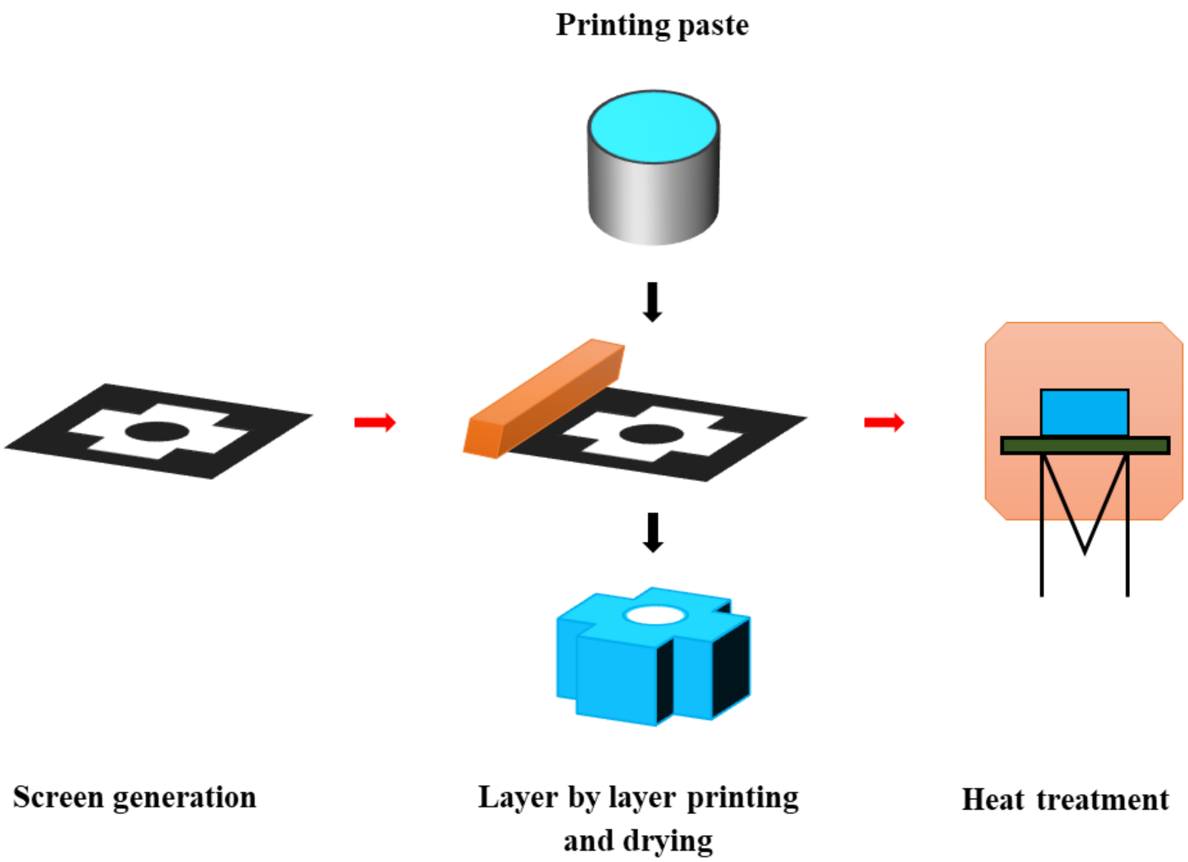

Figure 3.4 3-D Screen printing process.

3.6 Metallization of 3-D Printed Microwave Components

The metal coating process is an important part of the fabrication process for those microwave components that are fabricated with non-conductive materials. Microwave components that are made with metallic materials also might need metallization to achieve a better insertion loss performance. An improvement of insertion loss performance by electroplating the surface with copper is reported in [13].

For components made by the SLA or FDM process using non-conductive materials, a standard commercial electroless metal plating process can be employed. In the electroless metal plating process, the 3-D printed structure is sequentially immersed in a series of chemical baths for surface preparation, surface activation and metal deposition. The surface of the component is thus coated with a seed layer and can then be electroplated with the desired metal [40]. Components made with metallic materials such as those fabricated by SLS, can be metalized directly by electroplating.

The electroplating process involves coating a layer of metal onto an electrically conductive material, which offers wear resistance, corrosion protection and better conductivity, if the structure is plated with a higher conductive material [31]. In the process of electroplating, the object which is to be plated is connected to the cathode (negative terminal), and the metal which is to be plated onto the object is connected to the anode (positive terminal), and both are immersed into a chemical solution called the electrolyte. When the power is switched on, the ions from the metal move through the electrolyte, plating the object connected to the cathode. The thickness of the plated metal depends on the duration of the process and the area which is to be plated [31].

3.7 Performance of 3-D Printed Microwave Components

The performance of a 3-D printed microwave filter depends on many factors such as the electrical conductivity of the material, skin depth, surface roughness, dielectric loss of the material filling the cavities, accuracy of printing and misalignments between parts.

3.7.1 Skin Depth

For a filter that is fabricated with non-conductive materials such as those made by the SLA or FDM process, the metal coating is the critical part of the fabrication process to achieve a good electrical conductivity and insertion loss performance. The required thickness of the coated metal layer depends on the skin depth of the conductor at the operating frequency of the filter.

At high frequencies the current density is at the highest on the surface of conductor and decreases with depth. The current density of a semi-infinite plane conductor is given by [41]

$$J = J_{\text{surface}} \cdot e^{-\frac{d}{\delta}} \tag{3.1}$$

where J is the current density at depth d from the surface of the conductor, J_{surface} is surface current density and δ is the skin depth of the conductor. For a good conductor with electrical conductivity of σ, the skin depth δ can be calculated as [41]

$$\delta = \sqrt{\frac{1}{\pi f \mu_0 \mu_r \sigma}} \tag{3.2}$$

where f is the operating frequency, σ is the electrical conductivity of the conductive material, μ_0 is the permeability of vacuum and μ_r is the relative permeability of the conductive material.

Equation (3.2) shows that at a depth equal to the skin depth, the amplitude of current density is fallen to 36.8%, and at a depth equal to five times the skin depth, the current density is equal to 0.67% of the current density at the surface. Hence a good guide to the thickness of the coated metal layer is that it should be much larger than five times the skin depth to achieve low microwave loss. Figure 3.5 shows skin depth of four different metals as a function of frequency from 75 GHz to 750 GHz. As can be seen, the skin depth decreases as frequency increases and the metal with the highest electrical conductivity has the lowest skin depth. Looking at the red line in figure 3.5, the skin depth of copper at 100 GHz can be seen to be 0.206 μm, so a low microwave loss can be achieved with copper layer thickness of much larger than 1.03 μm, which is five times the skin depth.

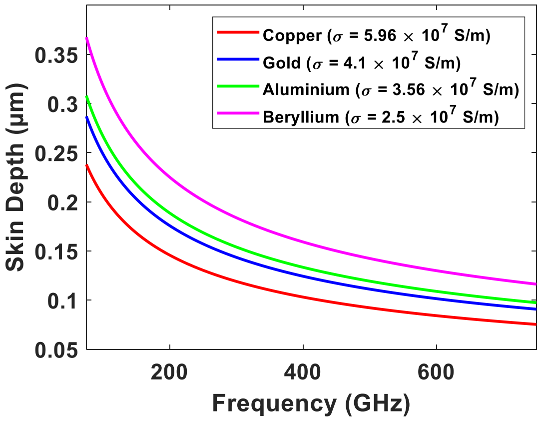

Figure 3.5 Skin depth of four different metals as a function of frequency from 75 GHz to 750 GHz.

3.7.2 Surface Roughness

Another factor that can affect performance of a 3-D printed microwave filter is the surface roughness. The surface roughness decreases the effective electrical conductivity, in other words it increases the conductor loss due to additional scattering of electrons. The effective electrical conductivity of rough metallic surfaces can be predicted using the Hammerstad-Bekkadal (HB) formula and given in [42]

$$\sigma_e = \sigma_0 \cdot \{K_{SR}\}^{-2} \tag{3.3}$$

where σ_0 is electrical conductivity of a conductor with a smooth surface and K_{SR} is Hammerstad surface roughness correction factor, which is given by [42]

$$K_{SR} = 1 + \frac{2}{\pi} tan^{-1}\left(1.4\left(\frac{\Delta}{\delta}\right)^2\right) \tag{3.4}$$

Here, δ is skin depth of conductor calculated from equation (3.2) and Δ is the RMS surface roughness.

Figure 3.6 shows the 2-D surface roughness profiles for triangular and rectangular grooves. For the purposes of simplicity, the surface roughness of 3-D printed components has been modelled using triangular and rectangular grooves. The RMS surface roughness (Δ), for an equilateral triangular profile is given by $\Delta = d/4$ and for a rectangular profile is given by $\Delta = b/d\sqrt{a(d-a)}$. This can also be used for square profile, when $a = b = d/2$, in which case $\Delta = d/4$. More details of calculation of Δ can be found in [43].

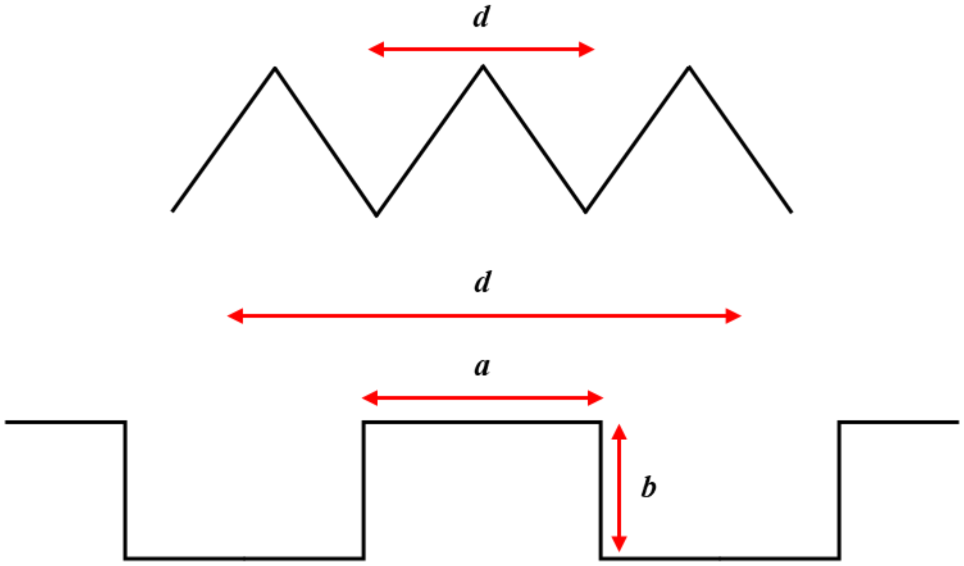

Figure 3.6 2-D surface roughness profiles for triangular and rectangular grooves.

It is important to mention that as the RMS surface roughness (Δ) increases, the value of surface roughness correction factor (K_{SR}) will also increase until it approaches to a value of 2, as shown in figure 3.7. This is the saturation point and shows the maximum effect of surface roughness on effective electrical conductivity of conductor. Figure 3.8 shows changes of the surface roughness correction factor (K_{SR}) over the frequency range of 75 GHz to 750 GHz for eight assumed RMS surface roughness values (0.8, 1, 1.2, 1.4, 1.6, 1.8, 2 and 2.2 μm). As the frequency increase, the surface roughness correction factor (K_{SR}) will also increase, for any given RMS surface roughness. This is because any increase in frequency will decrease the skin depth, resulting in an increase in the surface roughness correction factor (K_{SR}).

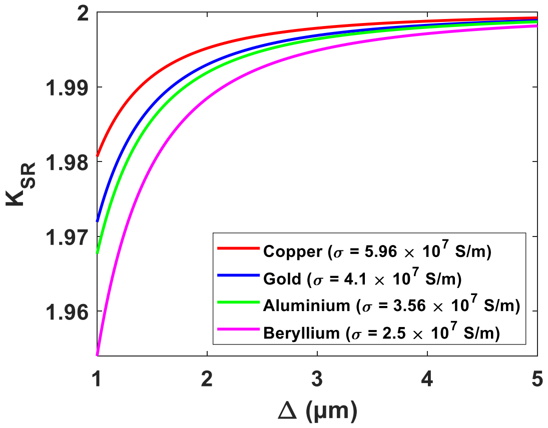

Figure 3.7 Calculated correction factor (K_{SR}) versus RMS surface roughness (Δ) for four different metals with square or equilateral triangular grooves at frequency of 100 GHz.

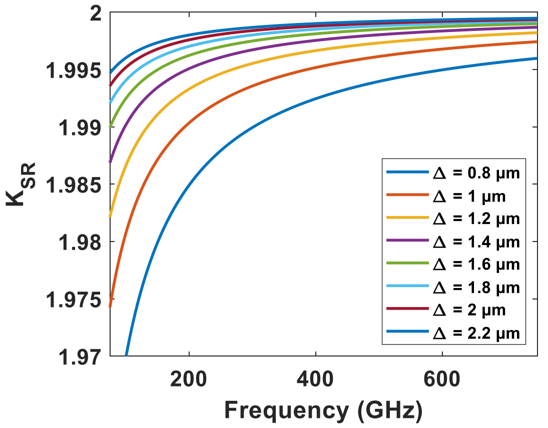

Figure 3.8 Calculated correction factor (K_{SR}) versus frequency from 75 GHz to 750 GHz for eight assumed RMS surface roughness (Δ). The material is copper with electrical conductivity of 5.96×10^7 S/m and with square or equilateral triangular grooves.

3.7.3 Misalignments and Accuracy of Parts

The other possible factors that could affect the performance of 3-D printed microwave filters are dielectric loss of the material filling the cavities, and misalignments and accuracy of parts. Here, all filters made with cavities are filled with air, and since the loss tangent is close to zero for the air-filled cavity, the dielectric loss will not affect the performance.

The misalignments between parts is a factor that can affect the performance of the filter depending on the structure of the filter and how parts are going to be assembled together. Using 3-D printing to make a microwave filter in one piece could reduce this effect. However, if the filter is fabricated with non-conductive materials like those made by SLA or FDM process, the filter might need to be made with two or more pieces to facilitate the metal coating process which requires access to the internal surfaces. This will be analysed further in the next chapters.

The accuracy of the 3-D printed parts is a factor that can also affect the performance of the filter. The accuracy of printed parts depends on the process, design and materials used. Variations in heating and cooling of materials during printing process results in internal stresses, which can lead to expansion or shrinkage of structures. Different 3-D processes have different capabilities, so it is important to choose the correct process to achieve a high dimensional accuracy [35].

3.8 Design Considerations for 3-D Printing of Microwave Components

There are number of rules that need to be followed when designing a microwave component that is going to be 3-D printed, these are dependent on which type of 3-D printing technology is going to be used. Different 3-D printing technologies have different capabilities and limitations which restrict the way components can be fabricated.

In 3-D printing process, components are built layer by layer, regardless of what type of 3-D printing technology is used. Each layer must be printed over a build platform, a support structure or a previously printed layer. There are situations when an area of a model is only partially supported by a layer below or not supported at all, this area is called overhang. Each type of 3-D printing process has its own limitation when it comes to dealing with overhangs. A partially supported structure can have a maximum angle of 45° degrees from the vertical, when using stereolithography apparatus or fused deposition modelling process [35]. When using a selective laser sintering process, such as micro laser sintering, a partially supported structure can have a maximum angle of 60° degrees from the vertical [44]. Figure 3.9 shows the maximum angle of overhangs for different types of 3-D printing processes. The limitation on overhangs can be overcome by using a support structure which can be removed during the post processing however, the complexity and the cost of fabrication is increased.

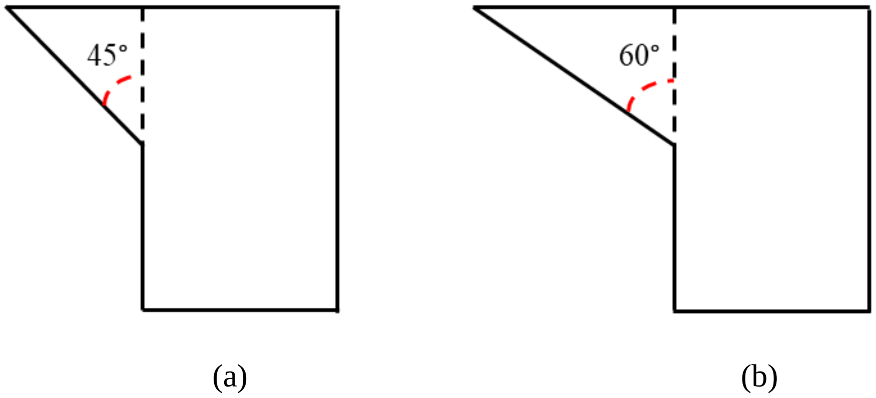

Figure 3.9 Maximum angle of overhang. (a) Maximum angle from vertical when using stereolithography apparatus or fused deposition modelling process. (b) Maximum angle from the vertical when using a selective laser sintering process, such as micro laser sintering.

Overhangs can also occur when there are horizontal holes within the structure. In such a situation, supports must be avoided, because removal of the support in horizontal holes is difficult and might be impossible when the dimension of holes is very small. The best solution is to change the build direction by 90° in a way to have vertical holes which eliminates the need for any support structure. For components with multiple holes in different directions, horizontal holes can be designed in a different shape rather than circular to prevent overhang. For example; use of hexagonal shape holes for waveguide flanges have been reported in [13], here the filters were fabricated using a micro laser sintering process; this will be explained further in chapter five.

When designing a component to be 3-D printed, it is important to choose the right thickness for walls. Different 3-D printing processes have different capabilities. However, the choice of right thickness for walls could be different in any kind of 3-D printing process. The thickness for walls also depends on the particular 3-D printing machine used in the process [35].

Warping is another issue that needs to be taken into consideration when designing a model that is to be 3-D printed. The materials used in 3-D printing processes will have physical changes, some are scanned with a laser and solidified as in stereolithography apparatus process, some are melted and cooled as in fused deposition modelling process and some are sintered as in selective laser sintering process. All this heating and cooling of materials can cause the components to distort during the fabrication process and this predominately occurs in large flat surfaces and large blocks. Warping can be avoided by calibrating the printer correctly, minimizing the size of flat surfaces and large blocks, and using adequate surface adhesion between the build platform and component [35].

Each type of 3-D printing process has its own limitations when it comes to printing small size features with intricate details. The minimum level of details is directly related to the mechanics and capability of each 3-D printing process, as well as the materials used and thickness of each layer. So, it is important to choose the right process, material and layer thickness as well as a suitable 3-D printer when designing a 3-D model with intricate details [35].

3.9 Conclusion

This chapter has provided a general introduction to additive manufacturing technologies. The focus was on 3-D printing which is an additive manufacturing technique that builds three dimensional objects by deposition of material, layer by layer. Details of the fabrication process for the three main types of 3-D printing technologies was described including: stereolithography apparatus, fused deposition modelling and selective laser sintering. An introduction to a recently developed 3-D printing technique, known as 3-D screen printing, that facilitates fabrication of complex structures with high accuracy using a variety of metallic materials was also discussed. This will be explained further in chapter eight.

This chapter also provided some information about materials that can be used in different types of 3-D printing process, as well as information about the factors that could affect the performance of 3-D printed microwave components. Metallization process of 3-D printed microwave components was briefly explained. As mentioned, non-metallic components go through an electroless plating process and metallic components can be metalized directly by electroplating. Finally, some of the key design considerations for 3-D printing were explained.

References

[1] X. Shang, J. Li, C. Guo, M. J. Lancaster, and J. Xu, “3-D printed filter based on helical resonators with variable width,” *2017 IEEE MTT-S International Microwave Symposium (IMS),* Honololu, HI, USA, 2017, pp. 1587-1590.

[2] G. Venanzoni, C. Tomassoni, M. Dionigi, and R. Sorrentino, “Stereolitographic 3D printing of compact quasi-elliptical filters,” *2017 IEEE MTT-S International Microwave Workshop Series on Advanced Materials and Processes for RF and THz Applications (IMWS-AMP),* Pavia, Italy, 2017, pp. 1-3.

[3] G. Venanzoni, M. Dionigi, C. Tomassoni, D. Eleonori, and R. Sorrentino, “3D printing of X band waveguide resonators and filters,” *2017 XXXIInd General Assembly and Scientific Symposium of the International Union of Radio Science (URSI GASS),* Montreal, QC, Canada, 2017, pp. 1-2.

[4] J. Li, C. Guo, L. Mao, and J. Xu, “3D printed bandpass filters using compact high-Q hemispherical resonators with improved out-of-band rejection,” *Electronics Letters*, vol. 53, no. 6, pp. 413–415, Mar. 2017.

[5] C. Guo, X. Shang, J. Li, F. Zhang, M. J. Lancaster, and J. Xu, “A Lightweight 3-D Printed X-Band Bandpass Filter Based on Spherical Dual-Mode Resonators,” *IEEE Microwave and Wireless Components Letters*, vol. 26, no. 8, pp. 568–570, Aug. 2016.

[6] C. Guo, J. Li, J. Xu, and H. Li, “An X-band lightweight 3-D printed slotted circular waveguide dual-mode bandpass filter,” *2017 IEEE International Symposium on Antennas and Propagation & USNC/URSI National Radio Science Meeting*, San Diego, CA, USA, 2017, pp. 2645-2646.

[7] C. Guo, X. Shang, M. J. Lancaster, and J. Xu, “A 3-D Printed Lightweight X-Band Waveguide Filter Based on Spherical Resonators,” *IEEE Microwave and Wireless Components Letters*, vol. 25, no. 7, pp. 442–444, July. 2015.

[8] J. Li, C. Guo, J. Xu, and L. Mao, “Lightweight low-cost Ka-band 3-D printed slotted rectangular waveguide bandpass filters,” *2017 IEEE International Symposium on Antennas and Propagation & USNC/URSI National Radio Science Meeting,* San Diego, CA, USA, 2017, pp. 2647-2648.

[9] X. Shang, P. Penchev, C. Guo, M. J. Lancaster, S. Dimov, Y. Dong, M. Favre, M. Billod, and E. D. Rijk, “W-Band Waveguide Filters Fabricated by Laser Micromachining and 3-D Printing,” *IEEE Transactions on Microwave Theory and Techniques*, vol. 64, no. 8, pp. 2572–2580, Aug. 2016.

[10] M. Dauria, W. J. Otter, J. Hazell, B. T. W. Gillatt, C. Long-Collins, N. M. Ridler, and S. Lucyszyn, “3-D Printed Metal-Pipe Rectangular Waveguides,” *IEEE Transactions on Components, Packaging and Manufacturing Technology*, vol. 5, no. 9, pp. 1339–1349, Sept. 2015.

[11] J. Saucourt, N. Jolly, A. Perigaud, O. Tantot, N. Delhote, S. Bila, and S. Verdeyme, “Design of 3D printed plastic modular filters,” *2016 46th European Microwave Conference (EuMC)*, London, UK, 2016, pp. 369-372.

[12] B. Zhang and H. Zirath, “3D printed iris bandpass filters for millimetre-wave applications,” *Electronics Letters*, vol. 51, no. 22, pp. 1791–1793, Oct. 2015.

[13] M. Salek, X. Shang, R. C. Roberts, M. J. Lancaster, F. Boettcher, D. Weber, and T. Starke, “W-Band Waveguide Bandpass Filters Fabricated by Micro Laser Sintering,” *IEEE Transactions on Circuits and Systems II: Express Briefs*, vol. 66, no. 1, pp. 61–65, Jan. 2019.

[14] J. Sence, W. Feuray, A. Périgaud, O. Tantot, N. Delhote, S. Bila, S. Verdeyme, J.-B. Pejoine, and R.-P. Gramond, “Plastic and metal additive manufacturing technologies for microwave passive components up to Ka band,” *International Journal of Microwave and Wireless Technologies*, vol. 10, no. 7, pp. 772–782, Sept. 2018.

[15] A. Perigaud, S. Bila, O. Tantot, N. Delhote, and S. Verdeyme, “3D printing of microwave passive components by different additive manufacturing technologies,” *2016 IEEE MTT-S International Microwave Workshop Series on Advanced Materials and Processes for RF and THz Applications (IMWS-AMP)*, Chengdu, China, 2016, pp. 1-4.

[16] M. V. D. Vorst and J. Gumpinger, “Applicability of 3D printing techniques for compact Ku-band medium/high-gain antennas,” *2016 10th European Conference on Antennas and Propagation (EuCAP)*, Davos, Switzerland, 2016, pp. 1-4.

[17] F. Bongard, M. Gimersky, S. Doherty, X. Aubry, and M. Krummen, “3D-printed Ka-band waveguide array antenna for mobile SATCOM applications,” *2017 11th European Conference on Antennas and Propagation (EUCAP)*, Paris, France, 2017, pp. 579-583.

[18] B. Liu, X. Gong, and W. Chappell, "Applications of Layer-by-Layer Polymer Stereolithography for Three-Dimensional High-Frequency Components," *IEEE Transactions on Microwave Theory and Techniques*, vol. 52, no. 11, pp. 2567–2575, Nov. 2004.

[19] J. S. Silva, E. B. Lima, J. R. Costa, C. A. Fernandes, and J. R. Mosig, "Tx-Rx Lens-Based Satellite-on-the-Move Ka-Band Antenna," *IEEE Antennas and Wireless Propagation Letters*, vol. 14, pp. 1408–1411, Mar. 2015.

[20] K. F. Brakora, J. Halloran, and K. Sarabandi, "Design of 3-D Monolithic MMW Antennas Using Ceramic Stereolithography," *IEEE Transactions on Antennas and Propagation*, vol. 55, no. 3, pp. 790–797, Mar. 2007.

[21] H. Yao, S. Sharma, R. Henderson, S. Ashrafi, and D. Macfarlane, "Ka band 3D printed horn antennas," *2017 Texas Symposium on Wireless and Microwave Circuits and Systems (WMCS)*, Waco, TX, USA, 2017, pp. 1-4.

[22] B. Zhang, P. Linner, C. Karnfelt, P. L. Tarn, U. Sodervall, and H. Zirath, "Attempt of the metallic 3D printing technology for millimeter-wave antenna implementations," *2015 Asia-Pacific Microwave Conference (APMC)*, Nanjing, China, 2015, pp. 1-3.

[23] J. Strycharz and P. Piasecki, "3D printed circular and rectangular waveguide mode converters," *2018 22nd International Microwave and Radar Conference (MIKON)*, Poznan, Poland, 2018, pp. 24-28.

[24] J. A. Byford and P. Chahal, "Ultra-wideband hybrid substrate integrated ribbon waveguides using 3D printing," *2016 IEEE MTT-S International Microwave Symposium (IMS)*, San Francisco, CA, USA, 2016, pp. 1-4.

[25] W. Otter, N. Ridler, H. Yasukochi, K. Soeda, K. Konishi, J. Yumoto, M. Kuwata-Gonokami, and S. Lucyszyn, "3D printed 1.1 THz waveguides," *Electronics Letters*, vol. 53, no. 7, pp. 471–473, Mar. 2017.

[26] H. Yukawa, Y. Ushijima, M. Abe, N. Yoneda, and M. Miyazaki, "A metal 3D-printed T-junction OMT with an offset stepped post," *2017 47th European Microwave Conference (EuMC)*, Nuremberg, Germany, 2017, pp. 444-447.

[27] H. Saeidi-Manesh, S. Saeedi, M. Mirmozafari, G. Zhang, and H. H. Sigmarsson, "Design and Fabrication of Orthogonal Mode Transducer Using 3D Printing Technology," *IEEE Antennas and Wireless Propagation Letters*, vol. 17, no. 11, pp. 2013–2016, Nov. 2018.

[28] X. Shang, P. Klasmann, and M. J. Lancaster, “A compact Ka-band waveguide orthomode transducer fabricated by 3-D printing,” *2016 46th European Microwave Conference (EuMC)*, London, UK, 2016, pp. 365-368.

[29] A. Bhutani, J. Schaefer, M. Pauli, S. Scherr, B. Goettel, M. Nierlich, and T. Zwick, “3D metal printed Ku/Ka Band modified turnstile junction Orthomode Transducer,” *2016 Asia-Pacific Microwave Conference (APMC),* New Delhi, India, 2016, pp. 1-4.

[30] E. Laplanche, O. Tantot, N. Delhote, A. Perigaud, S. Verdeyme, S. Bila, D. Baillargeat, and L. Carpentier, “A ku-band diplexer based on 3dB directional couplers made by plastic additive manufacturing,” *2017 47th European Microwave Conference (EuMC)*, Nuremberg, Germany, 2017, pp. 428-431.

[31] C. K. Chua, K. F. Leong, and C. S. Lim, *Rapid prototyping: principles and applications*. New Jersey: World Scientific, 2010.

[32] C. W. Hull, “Apparatus for production of three-dimensional objects by stereolithography,” U.S. Patent 4 575 330, Aug. 8, 1984.

[33] S. S. Crump, “Modeling apparatus for three-dimensional objects,” U.S. Patent 5 340 433, Jun. 8, 1992.

[34] C. R. Deckard, “Method and apparatus for producing parts by selective sintering,” U.S. Patent 4 863 538, Oct. 17, 1986.

[35] B. Redwood, F. Schöffer, and B. Garret, *The 3D printing handbook: technologies, design and applications*. Amsterdam, The Netherlands: 3D Hubs B.V., 2017.

[36] “Fraunhofer IFAM Dresden - Fraunhofer IFAM,” *Fraunhofer-Institut für Fertigungstechnik und Angewandte Materialforschung IFAM*. Accesses: Sept. 13, 2018. [Online]. Available: http://www.ifam-dd.fraunhofer.de/.

[37] M. Jurisch, T. Studnitzky, O. Andersen, and B. Kieback, “3D screen printing for the fabrication of small intricate Ti-6Al-4V parts,” *Powder Metallurgy*, vol. 58, no. 5, pp. 339–343, 2015.

[38] P. Brauer, M. Lindner, T. Studnitzky, B. Kieback, J. Rudolph, R. Werner, and G. Krause, “3D Screen Printing technology — Opportunities to use revolutionary materials and machine designs,” *2012 2nd International Electric Drives Production Conference (EDPC)*, Nuremberg, Germany, 2012, pp. 1-5.

[39] M. Dressler, T. Studnitzky, and B. Kieback, “Additive manufacturing using 3D screen printing,” *2017 International Conference on Electromagnetics in Advanced Applications (ICEAA)*, Verona, Italy, 2017, pp. 476-478.

[40] G. O. Mallory and J. B. Hajdu, *Electroless plating: fundamentals and applications*. Norwich, NY: Knoyes Publications/William Andrew Publishing, 2009.

[41] D. M. Pozar, *Microwave engineering*. Hoboken, NJ: Wiley, 2012.

[42] E. Hammerstad and O. Jensen, “Accurate Models for Microstrip Computer-Aided Design,” *MTT-S International Microwave Symposium Digest*, Washington DC, USA, 1980, pp. 407-409.

[43] S. P. Morgan, “Effect of Surface Roughness on Eddy Current Losses at Microwave Frequencies,” *Journal of Applied Physics*, vol. 20, no. 4, pp. 352–362, Oct. 1948.

[44] 3D Micro Print Gmbh. Accessed: Jan. 10, 2018. [Online]. Available: http://www.3dmicroprint.com/.

CHAPTER 4: DESIGN OF COMPACT 3 GHz COAXIAL CAVITY RESONATOR FILTER FABRICATED BY STEREOLITHOGRAPHY 3-D PRINTING

This chapter describes a compact 3 GHz coaxial cavity resonator filter which was fabricated by stereolithography 3-D printing. The filter is a fourth-order coaxial cavity resonator bandpass filter with a novel structure, where the first resonator is embedded inside the inner conductor of the second resonator and the fourth resonator is embedded inside the inner conductor of the third resonator to make the filter compact. Such an arrangement allows the size and volume of the filter to be reduced by approximately a factor of two. The filter was fabricated by stereolithography apparatus (SLA) 3-D printing process which allows such a filter with complex internal structure to be fabricated easily. The work has been published in [1].

4.1 Literature Review

Coaxial cavity resonator filters are widely employed in communication and radar systems. They offer a low manufacturing cost, a medium to high quality factor, a wide tuning range, a compact size and excellent spurious free performance [2, 3]. The significant challenge in the design of coaxial cavity resonator filters is reducing size and volume of the filter, whilst maintaining low loss. Generally, reducing the size of cavity resonator filters can be achieved by using dielectric resonators [4]-[6] or using dual-mode and multi-mode resonators [7]-[9]. However, these techniques cannot be applied directly to coaxial cavity resonator filters as they are based on different technologies and materials. There have been many studies since the 1980s in the field of design and analysis of coaxial cavity resonator filters [10]-[14], and recent studies mainly focusing on filter coupling topologies [15, 16]. Recently, several studies have also been conducted on how to reduce the size and volume of coaxial cavity resonator filters. In [17], two sixth-order orthogonal coaxial cavity filters are presented, in which the length of filters is reduced by changing the orientation of some of the coaxial cavity resonators. Some photographs of these filters are shown in figure 4.1 (a). Using this technique also allows multiple controllable transmission zeros to be generated because of the presence of cross coupling between nonadjacent resonators. Reducing the size and volume of coaxial cavity resonator filter by using inner conductive posts within a single cavity is reported in [18], where a quadruple-mode coaxial cavity resonator filter is presented. Here the coupling between posts is achieved by adjusting the post positions and dimensions instead of using coupling irises; having no metallic walls inside the cavity reduced the cavity size and volume. Figure 4.1 (b) shows a photograph of this filter. In [19], an inline coaxial cavity quasi-elliptic filter is introduced, where the size of the filter reduced by using controlled mixed electric and magnetic couplings to move the resonator closer. Figure 4.1 (c) shows a photograph of this filter. Altering the coupling properties can adjust the filter size to a certain extent by moving the resonators closer together, as done in [17]-[19], but the overall size of the filter is still limited as there is always a minimum distance between resonators. Increasing the open-end capacitance can also reduce the length of coaxial filter, but this also reduces the quality factor. Another technique that has been reported to reduce the length of resonators within the coaxial filter is to use stepped impedance resonators (SIR). The filter reported in [20] demonstrates this. Each resonator is formed of two coaxial structures that fitted into each other as shown in figure 4.1 (d). The length of such a filter can be reduced by adjusting the characteristic impedance of two-line sections in cascade. However, this will reduce the quality factor of the resonators.

4.2 The Filter Design Concept

The filter presented in this chapter is a novel fourth-order coaxial cavity resonator filter, where the coaxial resonators are embedded inside each other to make the filter compact. The filter is reported in [1]. Figure 4.2 shows the arrangement of the coaxial cavity resonator filter. Looking at figure 4.2 (a), it can be observed that each resonator is shorted at one end and open at the other end, forming quarter wavelength resonators operating in TEM mode. Figure 4.2 (b) and figure 4.2 (c) show the simplified diagram of the filter, where the central conductor of resonators one and four are represented by the red area, which are inserted inside resonators two and three, respectively. The blue area represents the metal of the inner conductor of resonators two and three, and the outer conductor of resonators one and four. The grey area represents the outer conductor of resonators two and three. This arrangement allows the size and volume of the filter to be reduced by approximately a factor of two. However, because of the complexity of internal structure, the filter couldn’t be easily fabricated by conventional fabrication techniques and the easiest way to fabricate found using 3-D printing techniques. The electric and magnetic fields in the resonators are shown in figure 4.2 (c), which is the same throughout the filter because all resonators are operating in TEM mode.

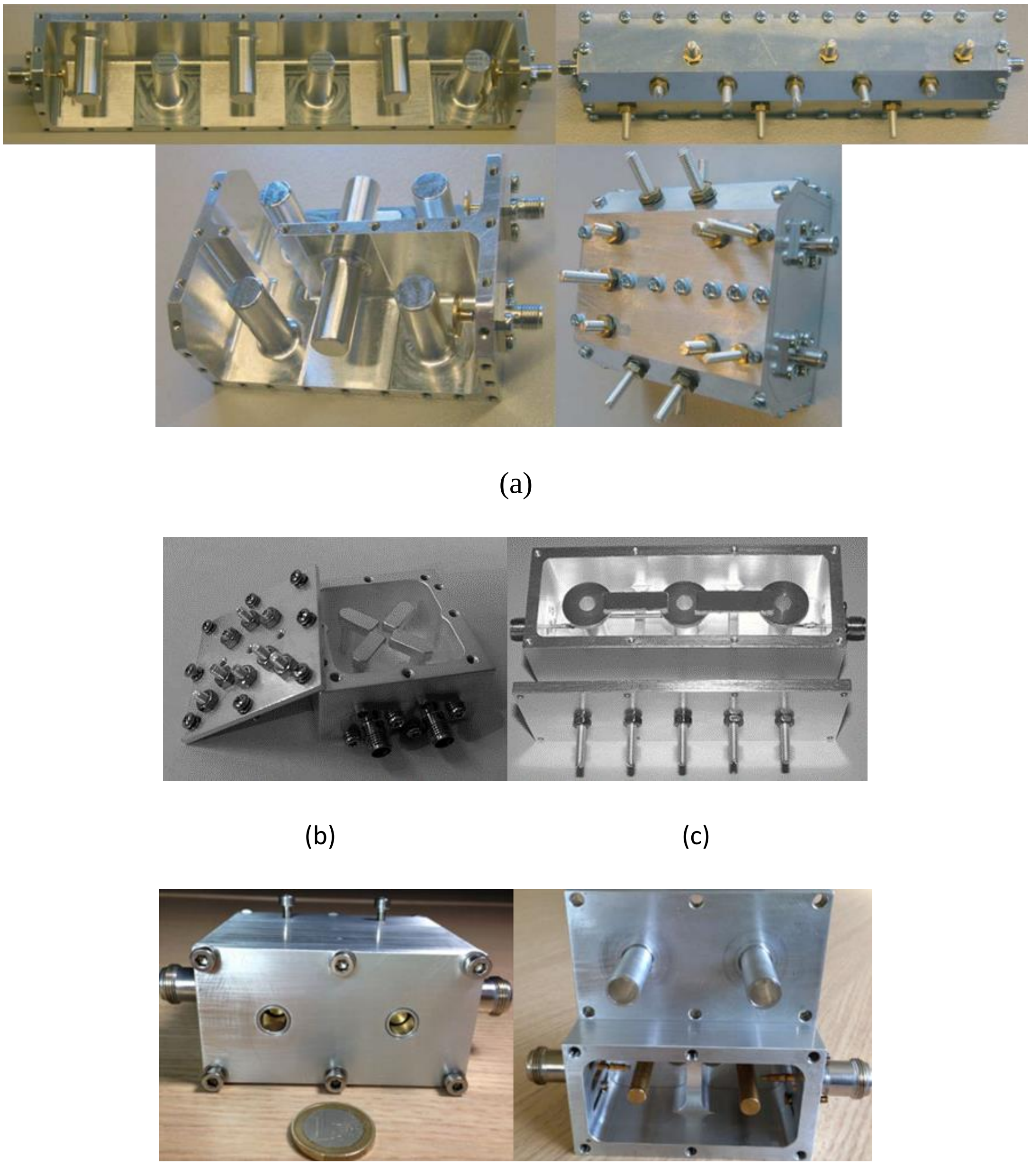

(a)

(b) (c)

(d)

Figure 4.1 Photographs of the reviewed compact coaxial cavity resonator filters. (a) Photograph of sixth-order orthogonal coaxial cavity filters [17]. (b) Photograph of quadruple-mode coaxial cavity resonator filter [18]. (c) Photograph of inline coaxial cavity quasi-elliptic filter [19]. (d) Photograph of second-order coaxial cavity filter based on SIR coaxial resonators [20].

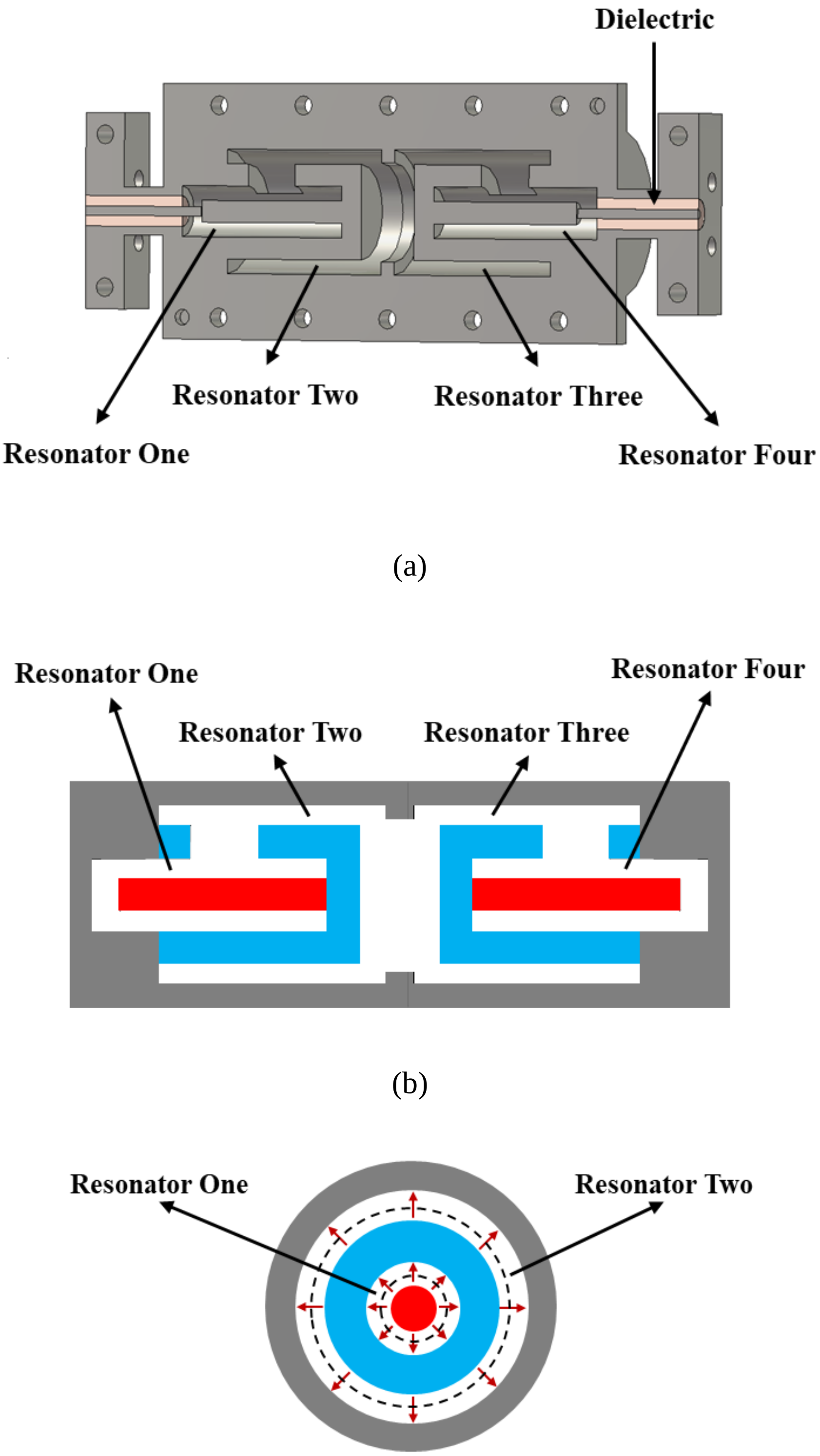

(a)

(b)

(c)

Figure 4.2 The configuration of the 3 GHz coaxial cavity resonator filter. (a) Cross section of the filter, showing resonators and internal couplings between resonators. (b) The simplified diagram of the filter. (c) Side view of the simplified diagram, showing electric field (solid red arrows) and magnetic field (dashed black lines).

4.3 Filter Design Using Coupling Matrix Theory

The coaxial cavity resonator filter is constructed with four quarter wavelength long coaxial resonators operating in TEM mode. The filter is specified in terms of Chebyshev bandpass response with a centre frequency of 3 GHz, a bandwidth of 90 MHz (fractional bandwidth of 3%) and a return loss of 20 dB over the passband. The coupling between resonators is realized, using irises and the input/output coupling is realized with the use of probes directly attached to SMA (sub miniature version A) connectors. The filter is designed using coupling matrix theory [21, 22]. From equation (2.40), the g values corresponding to return loss of 20 dB calculated as $g_0 = 1$, $g_1 = 0.9314$, $g_2 = 1.292$, $g_3 = 1.5775$, $g_4 = 0.7628$ and $g_5 = 1.221$. Then by using equations (2.37), (2.38) and (2.39), the elements of coupling matrix and the normalised external quality factors are determined as $q_{e1} = q_{eN} = 0.9314$, $m_{12} = m_{34} = 0.9116$ and $m_{23} = 0.7005$. The coupling matrix of the filter is given as

$$[m] = \begin{bmatrix} 0 & 0.9116 & 0 & 0 \\ 0.9116 & 0 & 0.7005 & 0 \\ 0 & 0.7005 & 0 & 0.9116 \\ 0 & 0 & 0.9116 & 0 \end{bmatrix} \tag{4.1}$$

The ideal response of the filter is plotted using equation (2.36) and shown in figure 4.3. The un-normalised non-zero coupling coefficients and the external quality factors calculated, using equation (2.83), which are provided in table 4.1. To find the physical dimensions of the filter, external quality factor and inter resonator couplings are extracted, which are then used to construct the filter and to find its initial response. Finally, dimensions of the filter optimised, using CST Microwave Studio [23]. The design procedure will be explained in the next sections.

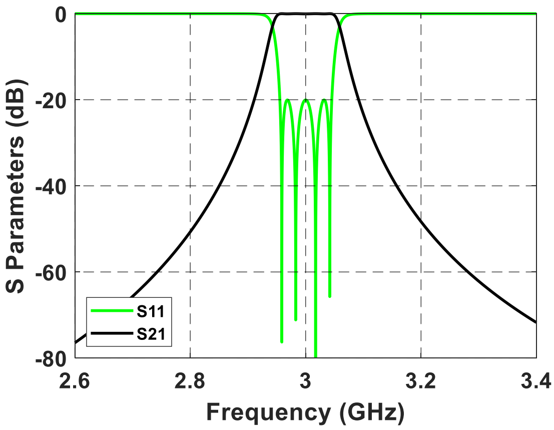

Figure 4.3 Ideal response of the Chebyshev filter.

Table 4.1 The external quality factors and coupling coefficients of the 3 GHz coaxial cavity resonator filter.

Q_{e1}	Q_{eN}	M_{12}	M_{23}	M_{34}
31.05	31.05	0.0274	0.021	0.0274

4.3.1 Extraction of External Quality Factor

The input/output coupling of the coaxial cavity resonator filter is realized with the use of probes directly attached to SMA connectors and it is extracted from the CST [23] simulation of a single cavity structure that is shown in figure 4.4. The value of the external quality factor Q_e is calculated with the use of simulated S_{21} and the formula, shown in figure 4.5.

By adjusting the probe penetration depth Z, on the end of the SMA connector, relation between external quality factor and probe penetration depth Z is found as shown in figure 4.6. This relation is used to find probe penetration depth for the required external quality factor of $Q_{e1} = Q_{eN} = 31.05$, and probe penetration depth Z is found as 2.86 mm, which is denoted by a red dot in figure 4.6. During the simulation process the length of coaxial cavity resonator L is also adjusted to keep the resonance frequency of the cavity resonator at 3 GHz and found to be 21.36 mm for resonators one and four ($L_1 = L_4$).

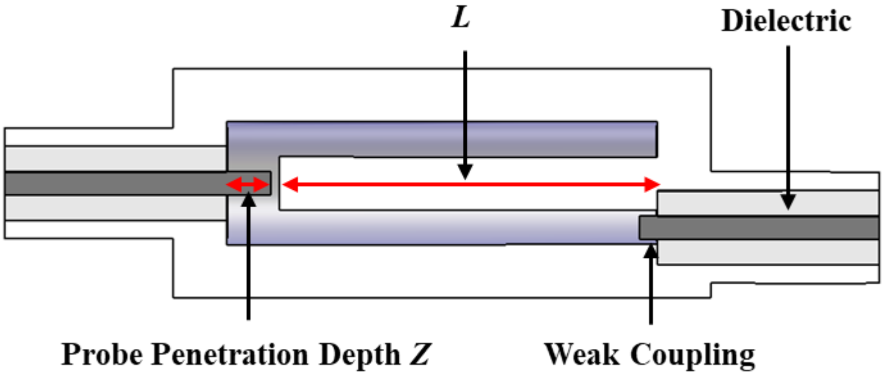

Figure 4.4 The structure of resonator used to extract external quality factor Q_e.

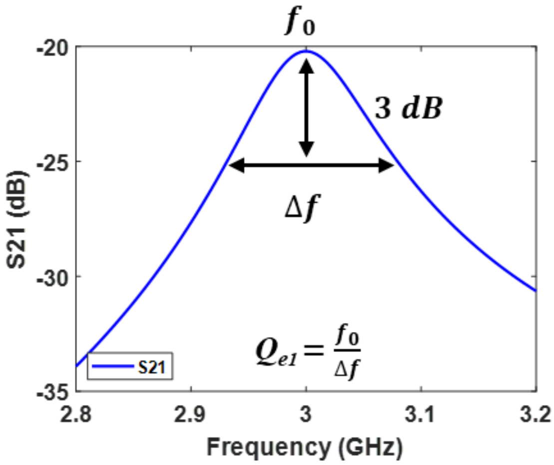

Figure 4.5 Simulated S_{21} of the structure shown in figure 4.4.

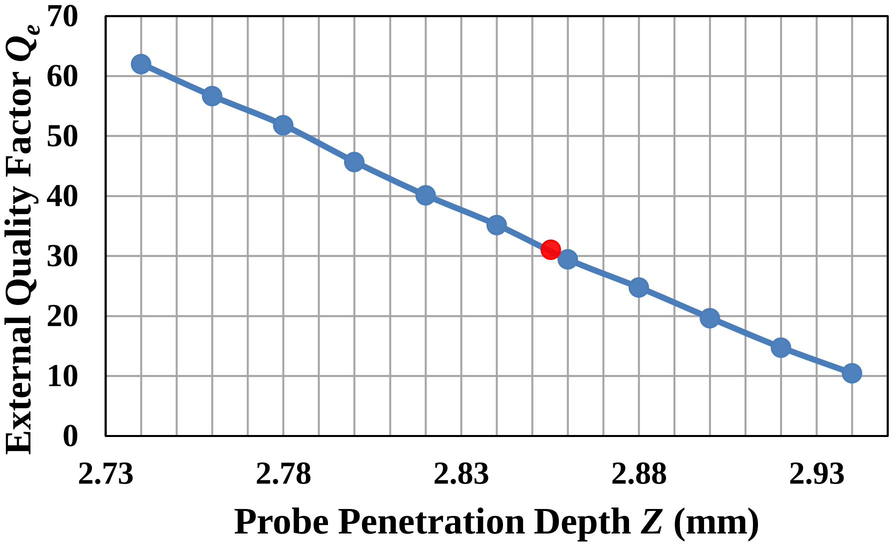

Figure 4.6 Relation between external quality factor Q_e and probe penetration depth Z.

4.3.2 Extraction of Inter Resonator Couplings

The couplings between resonators of the coaxial cavity resonator filter are realized with the use of irises. Figure 4.7 shows the structure of the model used to calculate the coupling between resonators 1 and 2, and resonators 3 and 4. The coupling between resonators is controlled by adjusting the width of iris, denoted by W.

The value of coupling coefficient is calculated by using the centre frequency of two resonators (f_1 and f_2) in simulated S_{21} and the formula, shown in figure 4.8, where the simulation was carried out in CST [23]. By adjusting the iris width W, the relation between the inter resonator coupling coefficient and iris width is found, which is shown in figure 4.9. Using the relation, the irises width corresponding to the required coupling coefficients $M_{12} = M_{34} = 0.0274$, are found to be $W_1 = W_2 = 7.34$ mm, which is denoted by a red dot in figure 4.9.

Similarly, to calculate the coupling between resonators 2 and 3, the structure shown in figure 4.10 is used. The coupling between resonators two and three is controlled by changing the radius of the iris, denoted by P. Figure 4.11 shows the simulated S_{21} of the structure shown in figure 4.10, and the formula to calculate the value of coupling coefficient. Adjusting the iris radius P results in achieving a relation between inter resonator coupling coefficient and iris radius, as shown in figure 4.12. Using this relation, the iris radius corresponding to the required coupling coefficient $M_{23} = 0.021$, is found to be $P = 6.84$ mm, which is denoted by a red dot in figure 4.12.

During the process of extraction of inter resonator couplings, the length of coaxial cavity resonators adjusted to keep the resonance frequency of the whole structure at 3 GHz. The length of resonators two and three was found to be $L_2 = L_3 = 20.32$ mm.

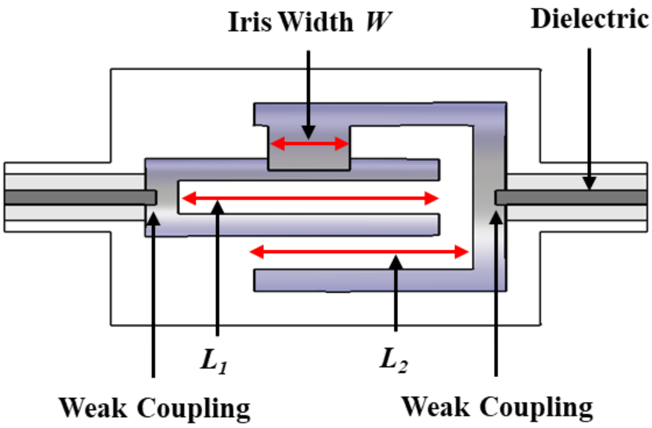

Figure 4.7 The structure of resonators one and two, used to extract inter resonator coupling coefficients M_{12} and M_{34}.

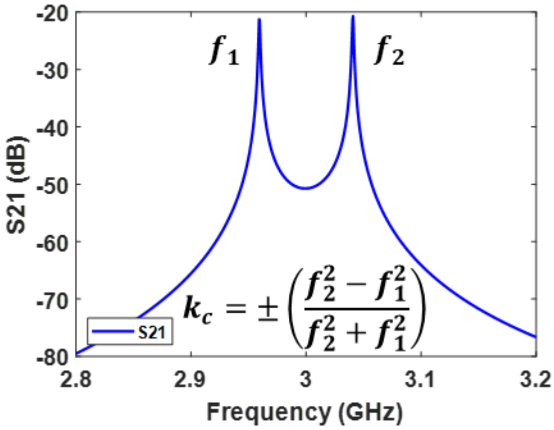

Figure 4.8 Simulated S_{21} of the structure shown in figure 4.7.

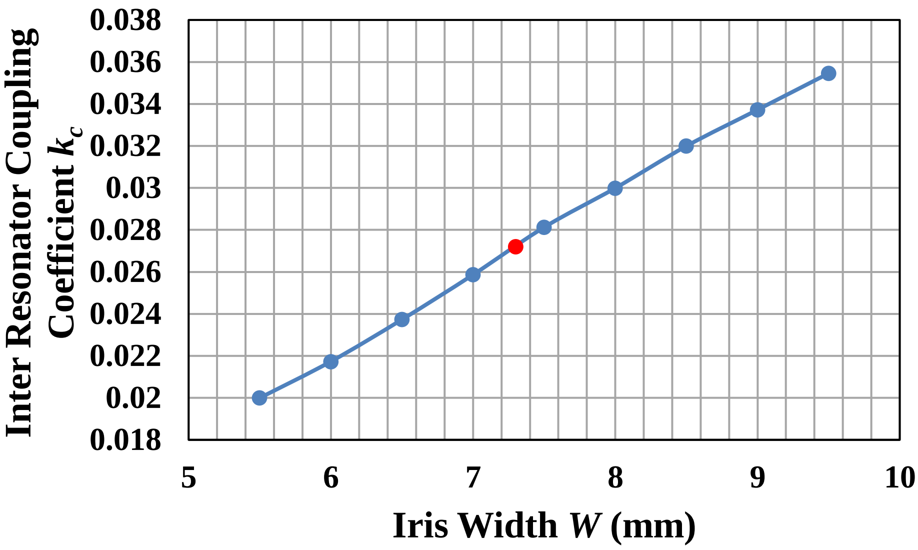

Figure 4.9 Relation between inter resonator coupling coefficient k_c and iris width W.

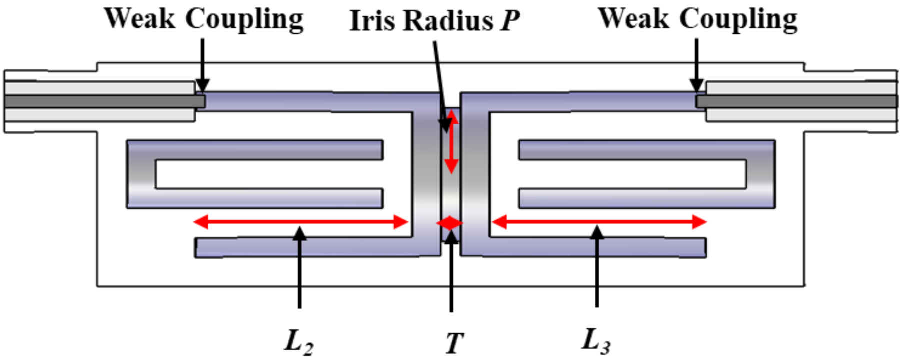

Figure 4.10 The structure of resonators two and three, used to extract inter resonator coupling coefficient M_{23}.

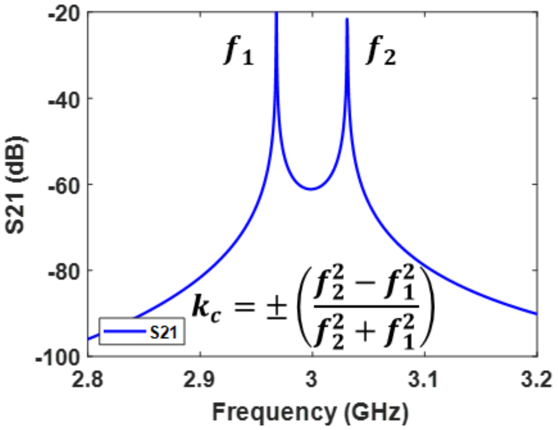

Figure 4.11 Simulated S_{21} of the structure shown in figure 4.10.

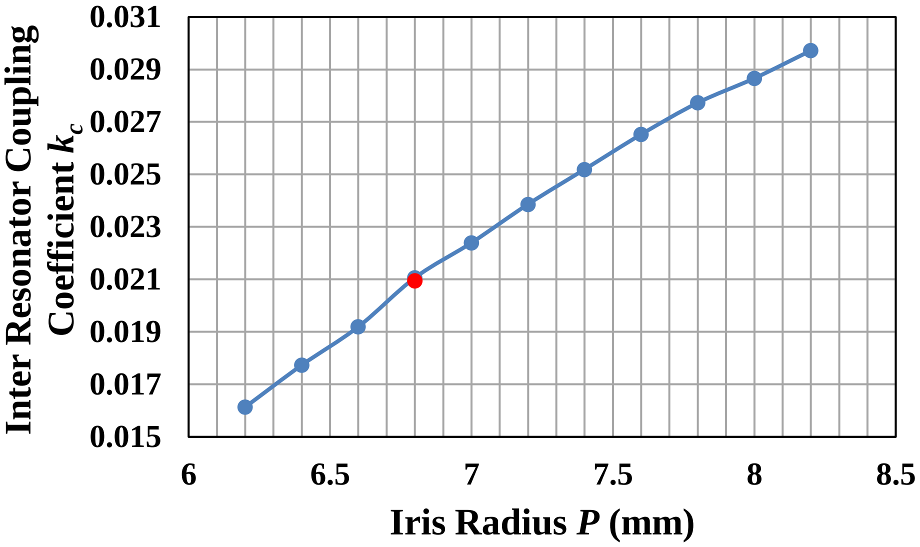

Figure 4.12 Relation between inter resonator coupling coefficient k_c and iris radius P.

4.3.3 Final Physical Design of the Filter

After extracting all physical dimensions of the coaxial cavity resonator filter, all four resonators were connected to each other to complete the filter as shown in figure 4.13 and then the whole structure was simulated in CST [23]. Figure 4.14 shows the simulated response of the filter before optimisation in comparison with the ideal response. The initial response of the filter is close to the ideal response and can be optimised to obtain a better solution. The initial dimensions of the filter optimised by CST [23] to get a response close to the ideal response. To optimise the filter, optimisation goals are set to be: S_{11} under -20 dB for frequency range of 2.955 GHz to 3.045 GHz, S_{11} more than -20 dB for frequency range of 2.6 GHz to 2.955 GHz and S_{11} more than -20 dB for frequency range of 3.045 GHz to 3.4 GHz. Figure 4.15 shows the response of the filter after optimisation in comparison with the response before optimisation. Figure 4.13 (a) provides the internal dimensions of the filter after optimisation and figure 4.13 (b) shows external structure of the filter along with all external dimensions.

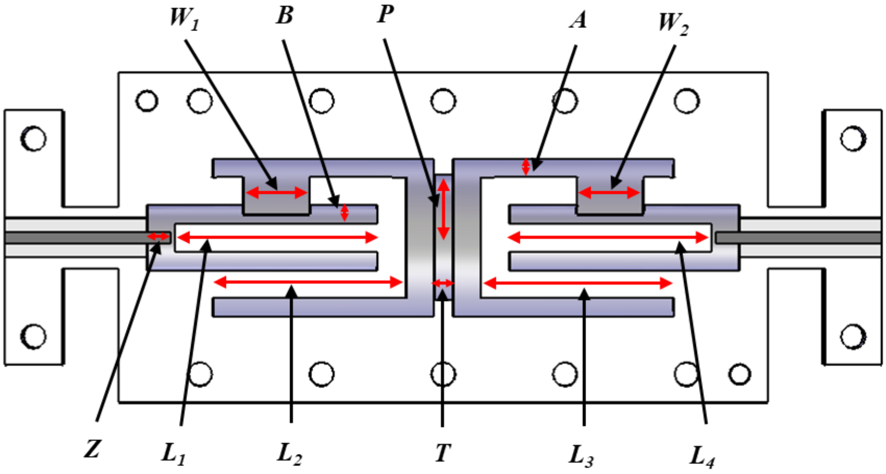

(a)

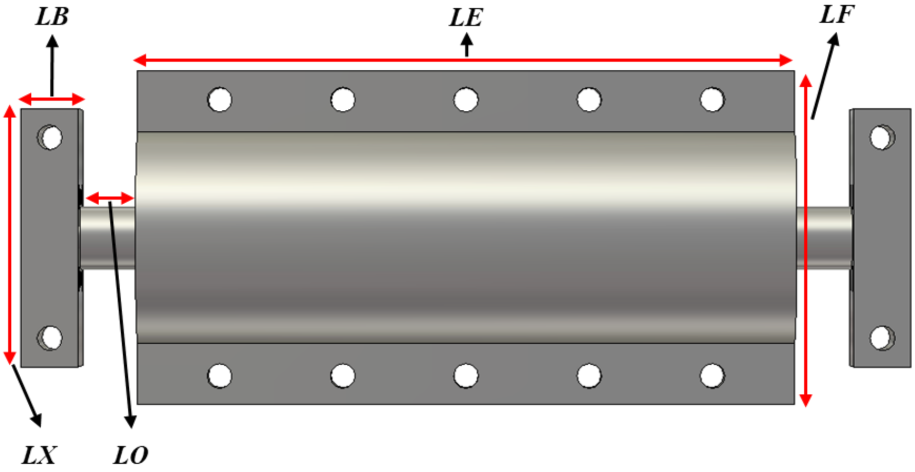

(b)

Figure 4.13 Illustration of the 3 GHz coaxial cavity resonator filter. (a) Internal structure of the filter showing internal dimensions. The dimensions after optimisation in millimetres are given as $P = 6.76$, $W_1 = W_2 = 7.11$, $L_1 = L_4 = 21.43$, $L_2 = L_3 = 20.5$, $A = B = 2$, $Z = 2.86$ and $T = 2$. (b) External structure of the filter showing external dimensions. The dimensions in millimetres are: $LX = 27$, $LB = 6$, $LO = 6.04$, $LE = 68.86$ and $LF = 35$.

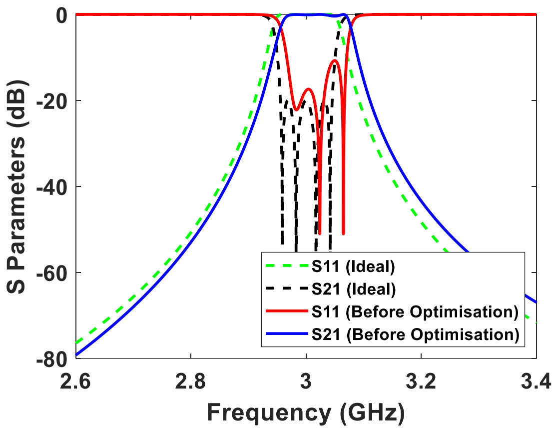

Figure 4.14 Simulated response of the 3 GHz coaxial cavity resonator filter before optimisation in comparison with the ideal response.

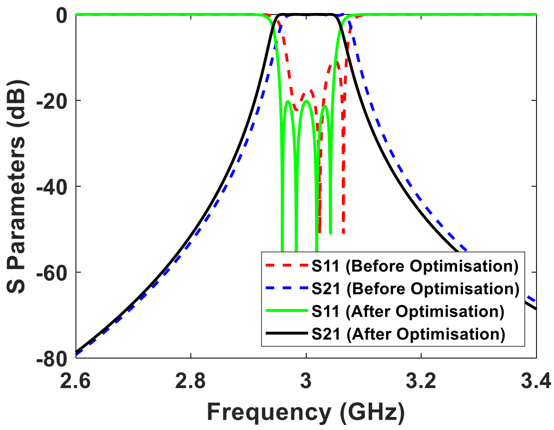

Figure 4.15 Comparison between simulated response of the 3 GHz coaxial cavity resonator filter before optimisation and after optimisation.

4.4 Fabrication Process

The coaxial cavity resonator filter presented in this chapter was fabricated, using stereolithography 3-D printing process with printing resolution of 0.1 mm. The stereolithography 3-D printing process was explained in chapter 3. In the process of 3-D printing, the filter was printed layer by layer. Each layer was built by scanning an ultraviolet laser beam across the surface of a non-conductive photo-curable polymer resin, which cured and solidified a pattern corresponding to the structure of the layer [24].

After the filter was 3-D printed, it was subsequently coated with 20 µm thick copper layer. The thickness of copper layer was compensated for in the 3-D model of the filter prior to fabrication. The skin depth at 3 GHz is calculated to be 1.119 µm by using equation (3.2) for copper with conductivity of 5.96×10^7 S/m. The specified thickness of copper layer was then chosen to be much larger than five times of the skin depth to achieve low microwave loss.

The material used in fabrication process was Accura Xtreme resin [25] with maximum working temperature range of 60^{o} C. Other types of materials can also be used in fabrication process if the filter is going to be used in high power applications, such as ceramic filled polymer materials. During the fabrication process supporting material was used whilst the parts were being built, using the same polymer material. The supporting material was removed during post processing once the parts are completed [25].

Figure 4.16 (a) shows a photograph of the fabricated filter after being copper plated and assembled. Looking at figure 4.16 (b), the filter is formed of two symmetrical pieces. Splitting into two pieces is to facilitate the copper plating process after printing, as it requires access to internal surfaces. The split is such that there is no current flow across the boundary, so it has little effect on the loss. In order to copper plate, a commercial electroless metal plating process was first employed, in which the surface of the filter was coated with a seed layer by sequentially immersing the filter in a series of chemical baths for surface preparation, surface activation and metal deposition. The filter then electroplated with copper [26]. This process was done by 3D-parts Ltd [25].

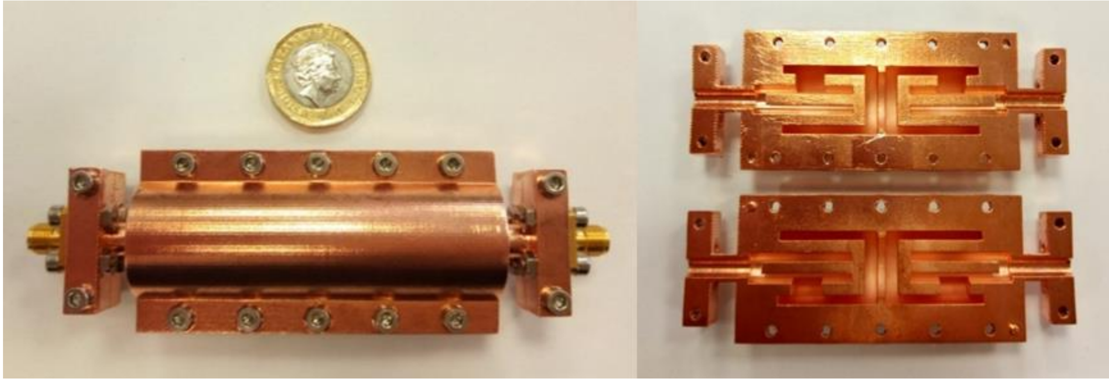

(a) (b)

Figure 4.16 Photograph of the fabricated 3 GHz coaxial cavity resonator filter after being copper plated. (a) Fabricated filter with both sides fixed together using nuts and bolts. (b) Left and right side of the fabricated filter.

Both pieces of the filter are assembled using seven nuts and bolts on each side as shown in figure 4.16 (a). The connectors used, are both standard 50 Ω female flange mount SMA connectors with a long straight centre conductor that is surrounded by a dielectric with dielectric constant of 2.1. Both connectors are placed on the flat ends of the filter and bolted onto the filter.

4.5 Measurement and Discussion

The *S* parameter measurements of the coaxial cavity resonator filter were carried out on an Agilent E8362C PNA network analyser. The network analyser was calibrated using SOLT (Short, Open, Load, Thru) method prior to the measurements. Figure 4.17 shows a photograph of the measurement setup, where the filter is placed between two probes of the network analyser. The measured and simulated results of the coaxial cavity resonator filter are shown in figure 4.18, where the measured results are denoted with solid lines and simulated results with dashed lines.

The *S* parameter results in figure 4.18 (a) shows that the measured centre frequency is shifted up by 19 MHz, which is almost 0.63% of simulated centre frequency. It can also be seen that the minimum return loss across the whole passband is about 13.5 dB.

The 19 MHz frequency shift is caused by small dimensional inaccuracies, as a result of small shrinkage in the length of structure of about 0.28 mm. This was confirmed by simulating a modified model in CST [23] considering the shrinkage. The results are shown in figure 4.19, where a good agreement between the re-simulated results and the measured results is achieved. The dimensional changes are due to final UV curing in SLA process and over plating the surface during copper plating process which could be corrected by remanufacturing the filter.

Looking at an expanded view of S_{21} in figure 4.18 (b), it can be observed that the minimum insertion loss is about 0.70 dB for the measured results. Based on simulation, the corresponding minimum insertion loss with perfectly smooth copper which has an electrical conductivity of 5.96×10^7 S/m is 0.46 dB [23]. The typical surface roughness values of these SLA structures are generally about 1 µm [27]. So, if the copper has a surface roughness of 1 µm, the effective electrical conductivity reduces to 2.66×10^7 S/m (based on equations (3.3) and (3.4)) and the minimum insertion loss becomes 0.63 dB as it is shown in figure 4.18 (b).

The simulated and measured insertion losses are very close and small additional loss not accounted for, could be caused by a combination of factors such as impurities in the copper, contamination of the copper surface, different surface roughness, joints and losses in the connectors. Here, minimum insertion losses are used, so the effect of the return loss is negligible given the return loss of the filter is about 50 dB at 3.04 GHz.

The insertion loss due to dissipation at the centre frequency of a Chebyshev bandpass filter can be estimated from its low pass g values by [28]

$$\Delta L_A = \frac{4.343 \cdot \Omega_c}{FBW} \sum_{i=1}^{N} \frac{\mathrm{g_i}}{Q_{ui}} \quad dB \tag{4.2}$$

where ΔL_A is insertion loss due to dissipation at the centre frequency of the filter, Ω_c is cut-off frequency of the lowpass prototype which is typically $\Omega_c = 1$ rad/s, g_i is low pass element values of Chebyshev lowpass prototype, FBW is fractional bandwidth of the filter, Q_{ui} is unloaded quality factor of the resonators and N is the filter degree.

Using the eigenmode solver of CST [23], unloaded quality factor of resonators one and four is found as $Q_{u1} = Q_{u4} = 1094$ and for resonators two and three as $Q_{u2} = Q_{u3} = 1238$. Substituting these unloaded quality factors into equation (4.2) yields an estimated insertion loss of 0.56 dB. Looking at expanded view of S_{21} in figure 4.18 (b), the average measured insertion loss is about 0.76 dB, shows that estimated insertion loss is 0.2 dB lower. This is a good estimation, but it cannot give a precise value as it doesn’t consider many factors that could affect the insertion loss, such as losses in the connectors, radiation loss at the interference between joints, impurities in the copper and contamination of the copper surface.

Figure 4.20 shows measured and simulated S_{21} over a wide frequency range of 2 – 15 GHz. As it can be seen, there is a spurious free window of about 10 GHz, as the first spurious mode appears at about 13 GHz. The spurious free performance of coaxial cavity resonator filters can be improved by capacitive loading the open end of the resonators however, this will reduce the quality factor [2].

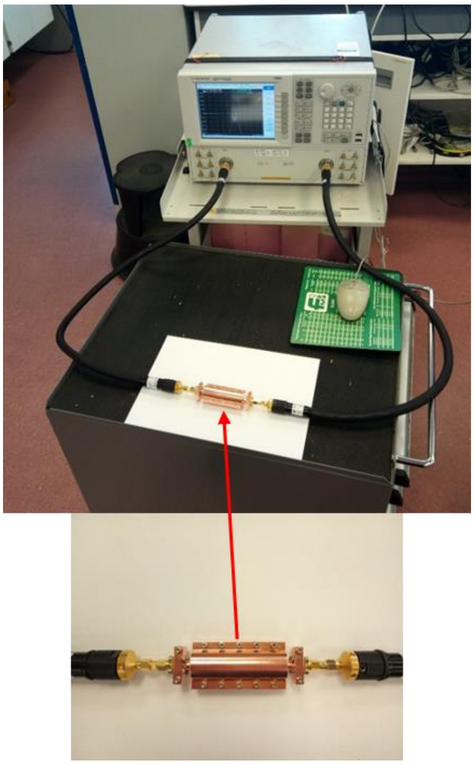

Figure 4.17 Photograph of the measurement setup with the 3 GHz coaxial cavity resonator filter connected to the two ports of the network analyser.

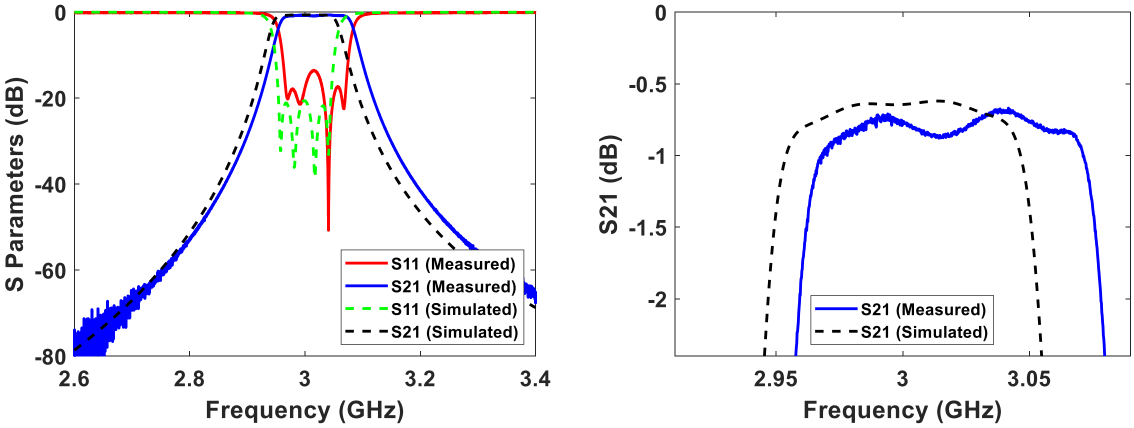

(a) (b)

Figure 4.18 Measured and simulated results of the 3 GHz coaxial cavity resonator filter. (a) Responses over the frequency range of 2.6 – 3.4 GHz. (b) Expanded view of S_{21} over the passband.

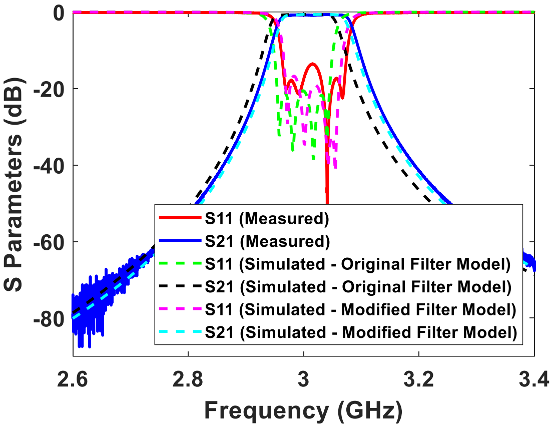

Figure 4.19 Comparison of measured and simulated results of the 3 GHz coaxial cavity resonator filter over the frequency range of 2.6 – 3.4 GHz. Simulated results of both original filter model and modified filter model provided.

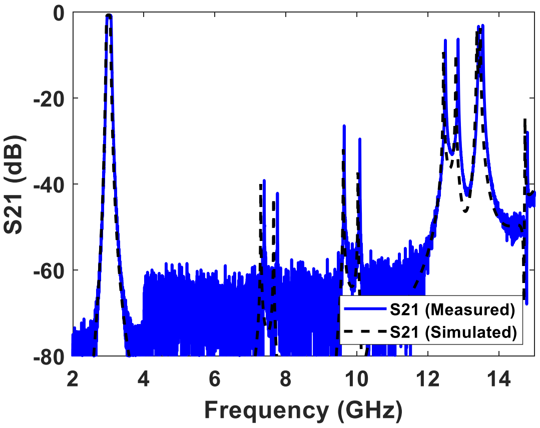

Figure 4.20 Measured and simulated S_{21} over a wide frequency range.

4.6 Conclusion

This chapter presented a compact coaxial cavity resonator filter with a novel structure. The idea proved that by fitting one resonator inside another resonator, the size and volume of the filter can be reduced by almost half. The design procedure of the filter using coupling matrix theory was explained and used to design other similar types of filter.

Because of the complexity of the internal structure of the filter, it was fabricated by stereolithography 3-D printing process. This project demonstrated the potential of using

3-D printing in the accurate fabrication of a complex microwave component. Finally, good agreement between the measured and simulated results validate the general concept and demonstrates the accuracy of the fabrication process.

References

[1] M. Salek, X. Shang, and M. J. Lancaster, “Compact S-Band Coaxial Cavity Resonator Filter Fabricated By 3-D Printing,” *IEEE Microwave and Wireless Components Letters*, vol. 29, no. 6, pp. 382-384, June. 2019.

[2] R. Mansour, “Filter technologies for wireless base stations,” *IEEE Microwave Magazine*, vol. 5, no. 1, pp. 68–74, Mar. 2004.

[3] C. Kudsia, R. Cameron, and W.-C. Tang, “Innovations in microwave filters and multiplexing networks for communications satellite systems,” *IEEE Transactions on Microwave Theory and Techniques*, vol. 40, no. 6, pp. 1133–1149, June. 1992.

[4] C. Wang and K. Zaki, “Dielectric resonators and filters,” *IEEE Microwave Magazine*, vol. 8, no. 5, pp. 115–127, Oct. 2007.

[5] S. Fiedziuszko, I. Hunter, T. Itoh, Y. Kobayashi, T. Nishikawa, S. Stitzer, and K. Wakino, “Dielectric materials, devices, and circuits,” *IEEE Transactions on Microwave Theory and Techniques*, vol. 50, no. 3, pp. 706–720, Mar. 2002.

[6] K. Zaki and C. Chen, “New Results in Dielectric-Loaded Resonators,” *IEEE Transactions on Microwave Theory and Techniques*, vol. 34, no. 7, pp. 815–824, July. 1986.

[7] S. Fiedziuszko, “Dual-Mode Dielectric Resonator Loaded Cavity Filters,” *IEEE Transactions on Microwave Theory and Techniques*, vol. 30, no. 9, pp. 1311–1316, Sept. 1982.

[8] V. Walker and I. Hunter, “Design of triple mode $TE_{01\delta}$ resonator transmission filters,” *IEEE Microwave and Wireless Components Letters*, vol. 12, no. 6, pp. 215–217, June. 2002.

[9] M. Memarian and R. Mansour, “Quad-mode and dual-mode dielectric resonator filters,” *IEEE Transactions on Microwave Theory and Techniques*, vol. 57, no. 12, pp. 3418–3426, Dec. 2009.

[10] A. Morini, G. Venanzoni, and T. Rozzi, “A new adaptive prototype for the design of side-coupled coaxial filters with close correspondence to the physical structure,” *IEEE Transactions on Microwave Theory and Techniques*, vol. 54, no. 3, pp. 1146–1153, Mar. 2006.

[11] H.-W. Yao, K. Zaki, A. Atia, and R. Hershtig, “Full wave modeling of conducting posts in rectangular waveguides and its applications to slot coupled combline filters,” *IEEE Transactions on Microwave Theory and Techniques*, vol. 43, no. 12, pp. 2824–2830, Dec. 1995.

[12] A. Harish and J. Raj, “A Direct Method to Compute the Coupling Between Nonidentical Microwave Cavities,” *IEEE Transactions on Microwave Theory and Techniques*, vol. 52, no. 12, pp. 2645–2650, Dec. 2004.

[13] Y. Rong and K. Zaki, “Full-wave analysis of coupling between cylindrical combline resonators,” *IEEE Transactions on Microwave Theory and Techniques*, vol. 47, no. 9, pp. 1721–1729, Sept. 1999.

[14] M. E. Sabbagh, K. Zaki, H.-W. Yao, and M. Yu, “Full-wave analysis of coupling between combline resonators and its application to combline filters with canonical configurations,” *IEEE Transactions on Microwave Theory and Techniques*, vol. 49, no. 12, pp. 2384–2393, Dec. 2001.

[15] R. Cameron, “Advanced Filter Synthesis,” *IEEE Microwave Magazine*, vol. 12, no. 6, pp. 42–61, Oct. 2011.

[16] J. Thomas, “Cross-coupling in coaxial cavity filters-a tutorial overview,” *IEEE Transactions on Microwave Theory and Techniques*, vol. 51, no. 4, pp. 1368–1376, Apr. 2003.

[17] M. Hoft and F. Yousif, “Orthogonal Coaxial Cavity Filters With Distributed Cross-Coupling,” *IEEE Microwave and Wireless Components Letters*, vol. 21, no. 10, pp. 519–521, Oct. 2011.

[18] X. Wang, G. Jang, B. Lee, and N. Park, “Compact Quad-Mode Bandpass Filter Using Modified Coaxial Cavity Resonator With Improved Q-Factor,” *IEEE Transactions on Microwave Theory and Techniques*, vol. 63, no. 3, pp. 965–975, Mar. 2015.

[19] H. Wang and Q.-X. Chu, “An Inline Coaxial Quasi-Elliptic Filter With Controllable Mixed Electric and Magnetic Coupling,” *IEEE Transactions on Microwave Theory and Techniques*, vol. 57, no. 3, pp. 667–673, Mar. 2009.

[20] H. Aouidad, E. Rius, J.-F. Favennec, A. Manchec, and Y. Clavet, “UHF second order bandpass filters based on miniature two-section SIR coaxial resonators,” *International Journal of Microwave and Wireless Technologies*, vol. 8, no. 08, pp. 1187–1196, Dec. 2016.

[21] J.-S. Hong, *Microstrip filters for RF/microwave applications*. Hoboken, NJ: Wiley, 2011.

[22] R. J. Cameron, C. M. Kudsia, and R. R. Mansour, *Microwave filters for communication systems: fundamentals, design, and applications*. Hoboken, NJ, USA: John Wiley & Sons, Inc., 2018.

[23] Computer Simulated Technology (CST). (2017). Microwave Studio. [Online]. Available: http//www.cst.com/.

[24] C. K. Chua, K. F. Leong, and C. S. Lim, *Rapid prototyping: principles and applications*. New Jersey: World Scientific, 2010.

[25] 3D-Parts Ltd. Accessed: Jan. 10, 2017. [Online]. Available: http://www.3dpartsltd.co.uk/.

[26] G. O. Mallory and J. B. Hajdu, *Electroless plating: fundamentals and applications*. Norwich, NY: Knoyes Publications/William Andrew Publishing, 2009.

[27] X. Shang, P. Penchev, C. Guo, M. J. Lancaster, S. Dimov, Y. Dong, M. Favre, M. Billod, and E. D. Rijk, “W-Band Waveguide Filters Fabricated by Laser Micromachining and 3-D Printing,” *IEEE Transactions on Microwave Theory and Techniques*, vol. 64, no. 8, pp. 2572–2580, Aug. 2016.

[28] S. Cohn, “Dissipation Loss in Multiple-Coupled-Resonator Filters,” *Proceedings of the IRE*, vol. 47, no. 8, pp. 1342–1348, Aug. 1959.

CHAPTER 5: DESIGN OF 90 GHz WAVEGUIDE BANDPASS FILTERS FABRICATED BY MICRO LASER SINTERING

This chapter introduces a fifth-order 90 GHz waveguide bandpass filter which is fabricated by a micro laser sintering process. The filter operates at a centre frequency of 90 GHz and has a fractional bandwidth of 11% (10 GHz bandwidth) with a Chebyshev response. The filter design procedure is based on coupling matrix theory which is explained in this chapter. The filter is fabricated by a powder bed based additive manufacturing technology, known as micro laser sintering, also known as selective laser sintering (SLS) or selective laser melting (SLM). The micro laser sintering technology allows microwave components such as microwave filters to be fabricated accurately with high resolution and good surface quality. It also allows the components to be made in a single piece from metal powders, resulting in better performance in terms of insertion loss.

Three filters are presented in this chapter which have the same structure and specification. Two of the filters made from stainless steel demonstrate the capability of the micro laser sintering process for reproducing microwave filters, and the other one made from stainless steel coated with copper shows the effect of copper plating on insertion loss performance. The quality of the filters will be discussed in this chapter by comparing the measured results with simulated results and providing the surface roughness measurements. The work was done in collaboration with Xiaobang Shang at the University of Birmingham and has been published in [1].

5.1 Introduction

As mentioned in chapter 3, additive manufacturing or 3-D printing allows complex 3-D structures to be fabricated accurately at a reasonable cost, where different types of materials can be used in the fabrication process. Different types of additive manufacturing technology introduced in chapter 3, among those selective laser sintering is capable of fabricating components directly from metals. Using metal in the fabrication process has many advantages such as increase in strength of components, wider working temperature range and better thermal expansion properties.

The filters reported in this chapter operate at a centre frequency of 90 GHz, with fractional bandwidth of 11% and are fabricated using the micro laser sintering process which is the same as the selective laser sintering process explained in chapter 3. The filters and the fabrication process are reported in [1], and reproducibility and quality assessment of the filters are reported in [2]. To the best of the author's knowledge, the filters are the highest frequency filters fabricated by a metal 3-D printing process at the time of publication.

5.2 Waveguide Bandpass Filter Design Using Coupling Matrix Theory

The filter that is presented in this chapter is designed with a centre frequency of 90 GHz, a bandwidth of 10 GHz (fractional bandwidth of 11%) and a return loss of 20 dB over the passband. The filter has a Chebyshev bandpass response and is constructed with five rectangular resonators operating in the TE_{101} mode. The coupling between the resonators and input/output coupling are realized using inductive irises. The design procedure was based on coupling matrix theory [3, 4], in which the filter specification was translated into coupling matrix elements, which are then used to find physical dimensions of the filter.

By using equation (2.40), the g values corresponding to a specified return loss of 20 dB are calculated as $g_0 = 1$, $g_1 = 0.9714$, $g_2 = 1.3721$, $g_3 = 1.8014$, $g_4 = 1.3721$, $g_5 = 0.9714$ and $g_6 = 1$. These are then used to calculate the normalised external quality factors and coupling coefficients using equations (2.37), (2.38) and (2.39) as $q_{e1} = q_{eN} = 0.9714$, $m_{12} = m_{45} = 0.8662$ and $m_{23} = m_{34} = 0.6361$. The coupling matrix of the filter is given as

$$[m] = \begin{bmatrix} 0 & 0.8662 & 0 & 0 & 0 \\ 0.8662 & 0 & 0.6361 & 0 & 0 \\ 0 & 0.6361 & 0 & 0.6361 & 0 \\ 0 & 0 & 0.6361 & 0 & 0.8662 \\ 0 & 0 & 0 & 0.8662 & 0 \end{bmatrix} \tag{5.1}$$

The ideal response of the filter is shown in figure 5.1, which is plotted using equation (2.36). The un-normalised non-zero coupling coefficients and the external quality factors are provided in table 5.1, which are calculated using equation (2.83). The initial physical dimensions of the filter found by extracting the external quality factor and inter resonator couplings, which are then optimised by using CST Microwave Studio [5] to get a response close to the ideal response. The design procedure of the filter will be explained in the next sections.

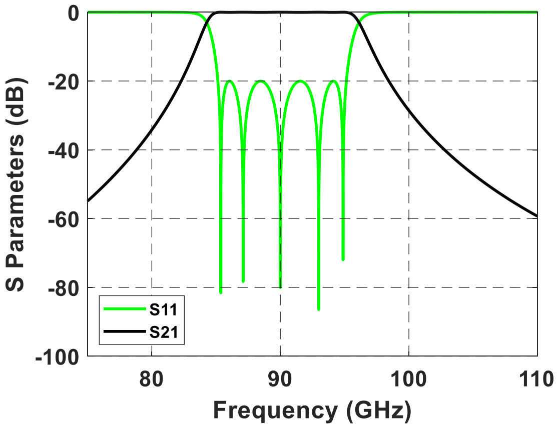

Figure 5.1 Ideal response of the Chebyshev filter.

Table 5.1 The external quality factors and coupling coefficients of the 90 GHz waveguide bandpass filter.

Q_{e1}	Q_{eN}	M_{12}	M_{23}	M_{34}	M_{45}
8.76	8.76	0.0961	0.0706	0.0706	0.0961

5.2.1 Extraction of External Quality Factor

The input/output coupling of the 90 GHz waveguide bandpass filter is realized using inductive irises. Figure 5.2 shows the structure of the model used to calculate the external quality factor, where the width of input iris denoted by E, the length of resonator by L and the iris thickness is kept at 0.5 mm. By simulating the model in CST [5], S_{21} can be found as shown in figure 5.3. The external quality factor then can be calculated by using simulated S_{21} and the formula, shown in figure 5.3. The relation between external quality factor and the iris width is found by adjusting the iris width E, which is shown in figure 5.4. The initial dimension of the iris width is found from this relation as E = 1.75 mm, which corresponds to the required external quality factor of $Q_{e1} = Q_{eN} = 8.76$. This is denoted by a red dot in figure 5.4. The length of resonator L was also adjusted during the simulation process in order to keep the resonance frequency at 90 GHz, which is found to be $L_1 = L_5$ = 1.29 mm.

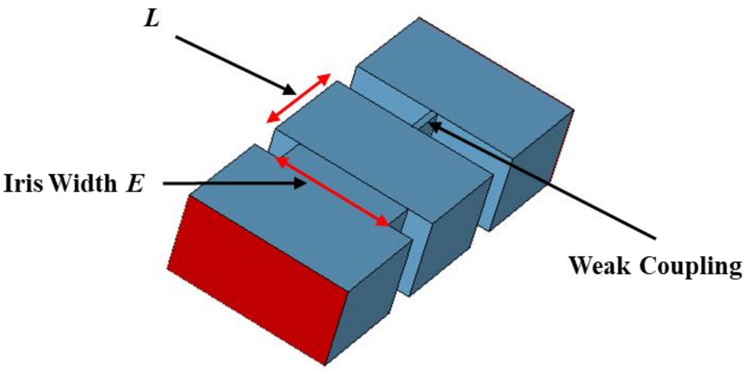

Figure 5.2 The structure of model used to extract external quality factor Q_e.

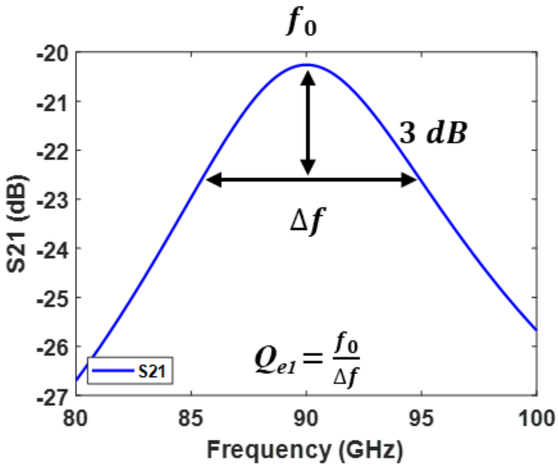

Figure 5.3 Simulated S_{21} of the structure shown in figure 5.2.

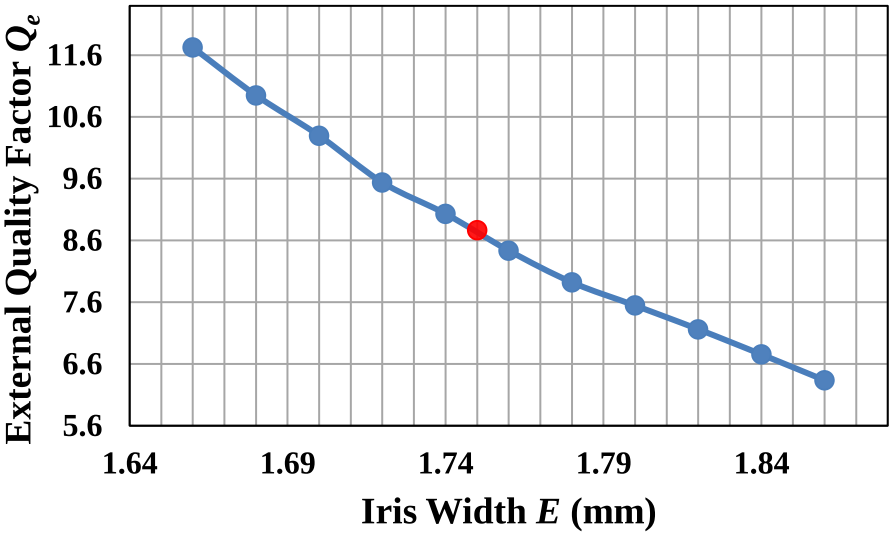

Figure 5.4 Relation between external quality factor Q_e and iris width E.

5.2.2 Extraction of Inter Resonator Couplings

The couplings between resonators of the 90 GHz waveguide bandpass filter are realized using inductive irises. To calculate inter resonator couplings, the model shown in figure 5.5 was used, where the width of iris between two resonators is denoted by *D*, the length of resonators by L_1 and L_2, and the iris thickness is kept at 0.5 mm. The coupling between two resonators is calculated by using the centre frequency of two resonators (f_1 and f_2) from the simulated S_{21} and the formula, shown in figure 5.6, where the simulation was carried out in CST [5].

Figure 5.7 shows the relation between inter resonator coupling coefficient and the iris width, which is found by adjusting the iris width *D*. The iris width corresponding to coupling coefficients $M_{12} = M_{45} = 0.0961$ and $M_{23} = M_{34} = 0.0706$, are found from the relation as $D_1 = D_4 = 1.42$ mm and $D_2 = D_3 = 1.31$ mm, which are denoted by red and black dots in figure 5.7. The length of both resonators is also adjusted during the process to keep the resonance frequency of the model at 90 GHz. The length of resonators is found as $L_2 = L_4 = 1.58$ mm and $L_3 = 1.64$ mm.

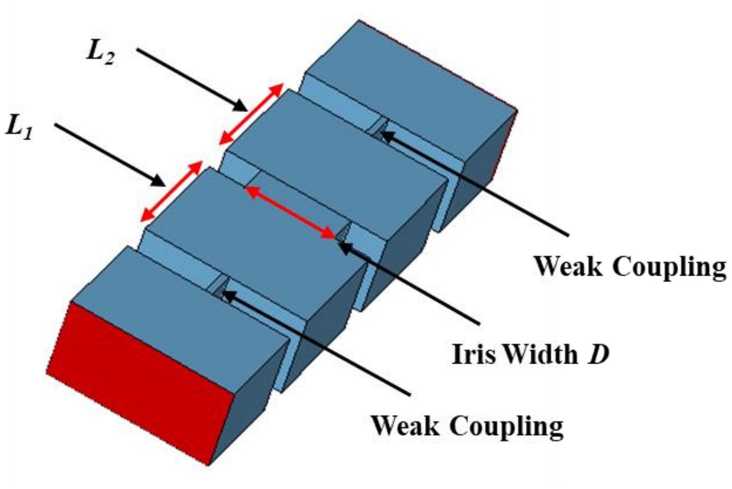

Figure 5.5 The structure of model used to extract inter resonator couplings.

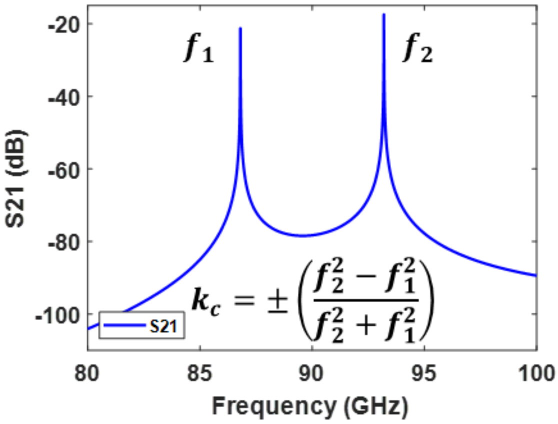

Figure 5.6 Simulated S_{21} of the structure shown in figure 5.5.

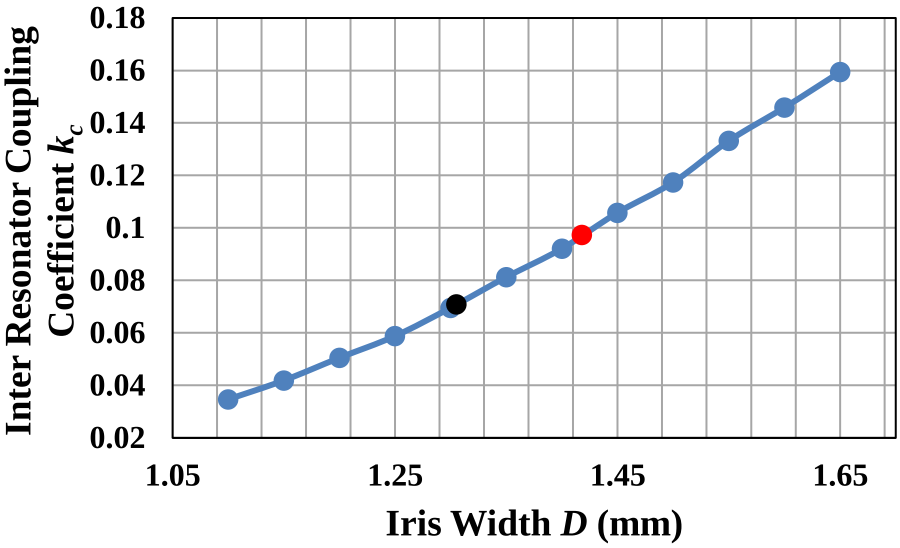

Figure 5.7 Relation between inter resonator coupling coefficient k_c and iris width D.

5.2.3 Final Physical Design of the Filter

The final step of design procedure was to connect all resonators together based on extracted initial physical dimensions to complete the filter. Figure 5.8 shows internal structure of the 90 GHz waveguide bandpass filter, where all five resonators are connected in series using inductive irises. Figure 5.9 shows initial response of the 90 GHz waveguide bandpass filter before optimisation in comparison with the ideal response. The filter was optimised by CST [5] to achieve a good response, close to the ideal response. During the optimisation process, the length of the resonators and the width of irises is adjusted. Optimisation goals are set to be: S_{11} under -20 dB for frequency range of 85 GHz to 95 GHz, S_{11} more than -20 dB for frequency range of 75 GHz to 85 GHz and S_{11} more than -20 dB for frequency range of 95 GHz to 110 GHz. Figure 5.10 shows the response of the filter after optimisation in comparison with the response before optimisation. The internal dimensions of the filter after optimisation are given in figure 5.8.

External design of the 90 GHz waveguide bandpass filter is shown in figure 5.11 (a), along with its external dimensions. Figure 5.11 (b) shows a cross section view of the filter with all internal couplings and resonators. Figure 5.11 also shows that the standard UG387/U flanges are included in the design, so the waveguide filter and flanges could be fabricated in a single piece which enables accurate connection to the measurement system. The alignment pin holes, precision alignment pin holes and screw holes are also included in both input and output UG387/U flanges and they all are designed in hexagonal shape to prevent overhang during the fabrication process as explained in chapter 3.

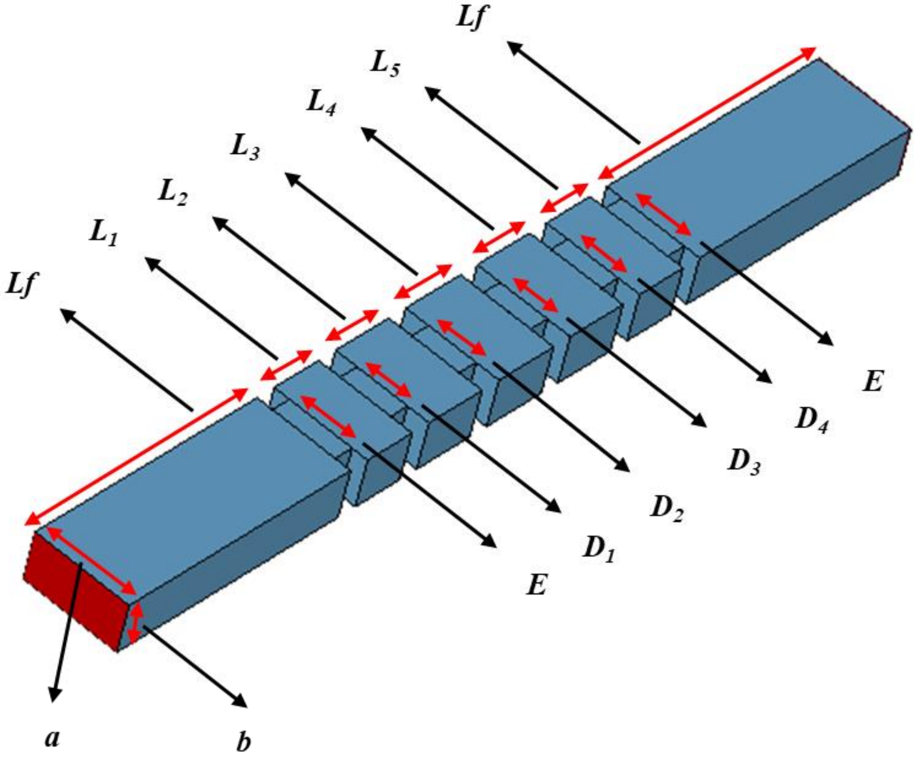

Figure 5.8 Internal structure of the 90 GHz waveguide bandpass filter showing internal dimensions. The dimensions after optimisation in millimetres are: $Lf = 6.48$, $L_1 = L_5 = 1.317$, $L_2 = L_4 = 1.582$, $L_3 = 1.636$, $E = 1.7$, $D_1 = D_4 = 1.374$, $D_2 = D_3 = 1.291$, $a = 2.54$ and $b = 1.27$.

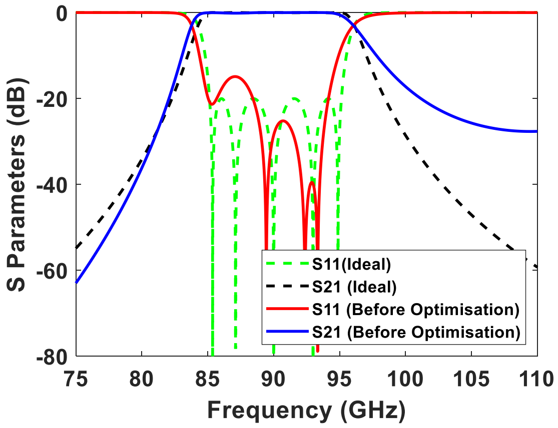

Figure 5.9 Simulated response of the 90 GHz waveguide bandpass filter before optimisation in comparison with ideal response.

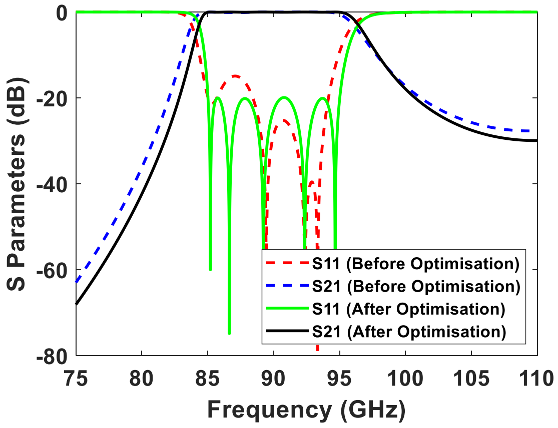

Figure 5.10 Comparison between simulated response of the 90 GHz waveguide bandpass filter before optimisation and after optimisation.

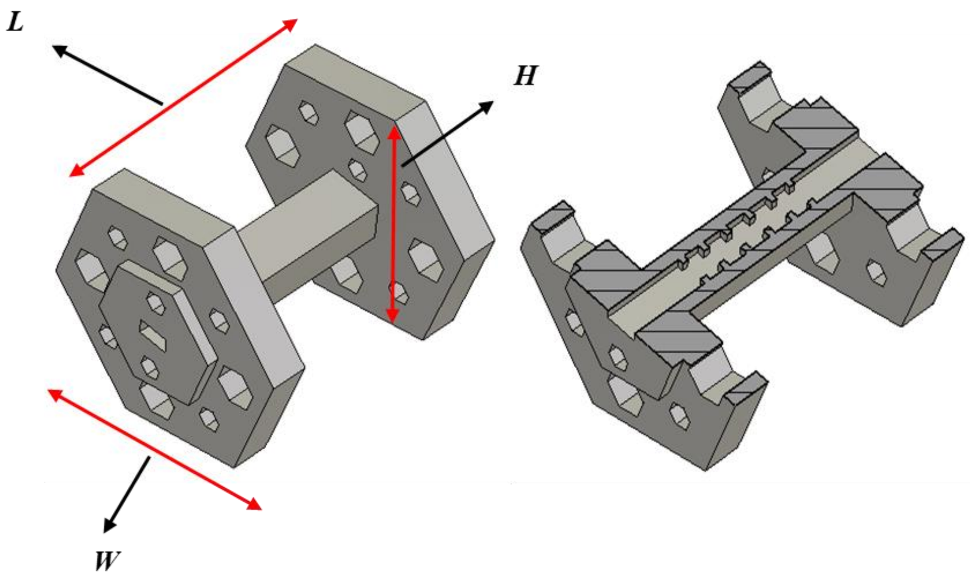

(a) (b)

Figure 5.11 Illustration of the 90 GHz waveguide bandpass filter. (a) Completed filter, showing external dimensions. The dimensions in millimetres are: $L = 21.4$, $H = 19.05$ and $W = 22$. (b) A cross section view of the waveguide filter showing internal couplings and resonators.

5.3 Micro Laser Sintering Fabrication Process

The filters that are presented in this chapter were fabricated by 3D Micro Print GmbH [6], using a micro laser sintering process in an inert argon atmosphere. The micro laser sintering process is the same as selective laser sintering process (SLS), which was explained in chapter 3. All three filters are made from stainless steel powder material, where one of the filters coated with a 5 µm thick copper layer with electrical conductivity of 5.96×10^7 S/m, which is done by electroplating the surface. The powder particle sizes were smaller than d_{80} 5 µm (d_{80} is particle size distribution) and had an electrical conductivity of 1.25×10^7 S/m. The type of stainless steel was 1.4542 (17-4PH), which is a chromium nickel copper alloyed stainless steel, containing 17% chromium, 4% nickel, 4% copper and 0.3% niobium. The thickness of each layer in the process was set at 5 µm. The laser source was an IR fiber laser with an average laser power of 50 W, and the laser spot diameter was focused down to 30 µm, which was operated in continuous wave mode. The printing process of each filter took about 16 hours which could be reduced by optimising the build process further. Figure 5.12 (a) shows photograph of the 90 GHz waveguide bandpass filter on the support structure after the fabrication process. The filters were constructed on a support structure in order to be printed at 60° from the vertical, which prevents any overhang during printing process as explained in chapter 3. The support structure was cut off by an Electrical Discharge Machine (EDM) wire during post processing. Figure 5.12 (b) shows a photograph of one of the two filters made from stainless steel and not coated with copper. Figure 5.12 (c) shows a photograph of the third filter, after being electroplated with 5 µm thick copper layer. A Bruker SkyScan 1076 MicroCT system was used to obtain a view of the internal structure of the fabricated filter non-destructively in order to detect any defects, voids or cracks. Figure 5.13 shows the CT scan image, with figure 5.13 (a) showing the cross section of the waveguide filter, and figure 5.13 (b) showing the end on view of the input waveguide.

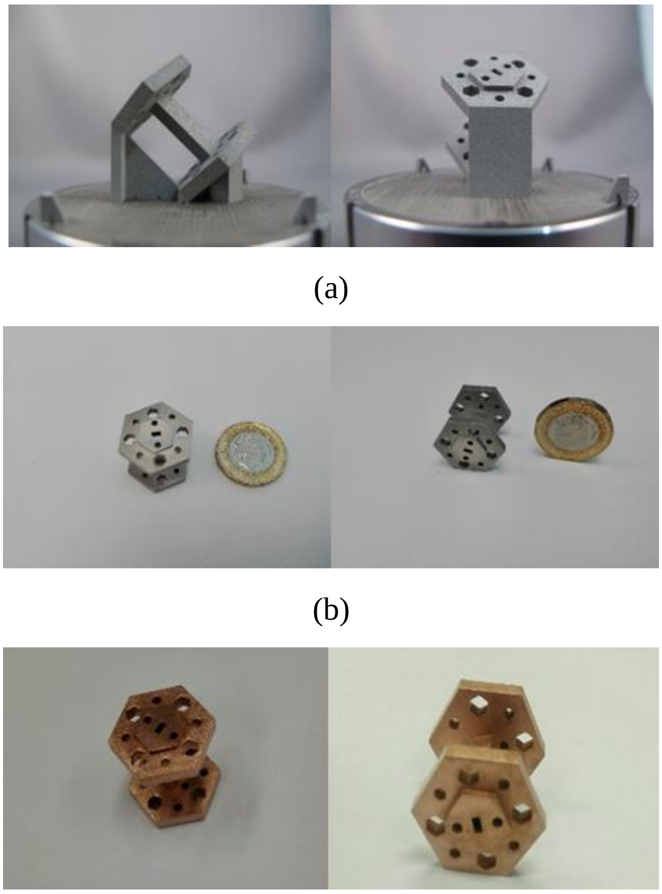

(a)

(b)

(c)

Figure 5.12 Photograph of the fabricated 90 GHz waveguide bandpass filters. (a) Filter on support structure after fabrication process. (b) One of the two filters made from stainless steel and not coated with copper. (c) The filter made from stainless steel, coated with 5 µm thick copper layer.

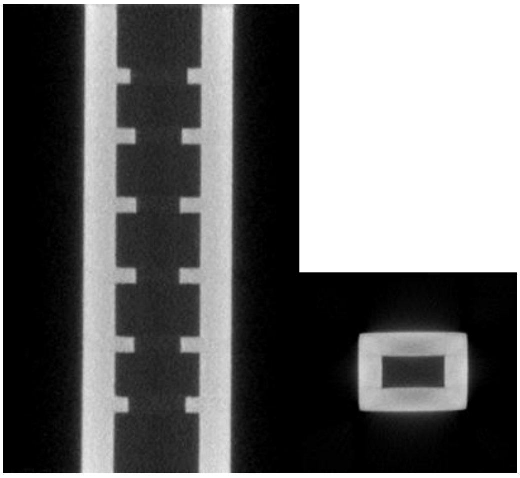

(a) (b)

Figure 5.13 CT scan image of the fabricated 90 GHz waveguide bandpass filter. (a) Cross section of the waveguide bandpass filter. (b) End on view of the input waveguide.

5.4 Measurement and Discussion

The *S* parameter measurements of the 90 GHz waveguide bandpass filters were performed on a Keysight E8361C PNA network analyser. The network analyser was calibrated using TRL (Thru, Reflect, Line) method prior to the measurements. Figure 5.14 shows photograph of the measurement setup, where the 90 GHz waveguide bandpass filter is placed between two waveguide flanges of the network analyser, aligned using four alignment pins and tightened with four screws on each side. The *S* parameter measurement results along with simulated results of the filters are shown in figure 5.15, figure 5.16 and figure 5.17, where the measured results are denoted with solid lines and simulated results with dashed lines.

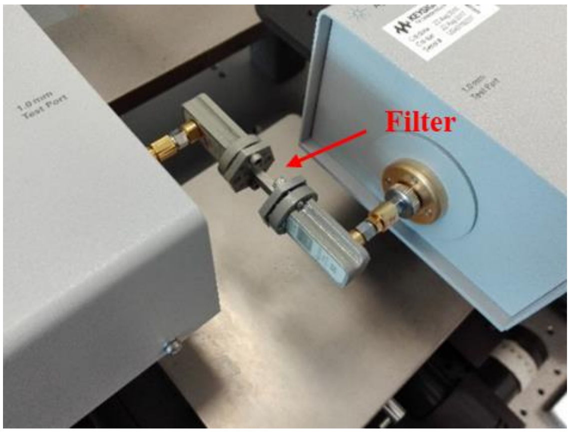

Figure 5.14 Photograph of the measurement setup with the 90 GHz waveguide bandpass filter placed between the two waveguide flanges of the network analyser.

Looking at the measured and simulated results of the first sample made from stainless steel in figure 5.15 (a), it can be observed that the measured centre frequency is shifted down by 1.66 GHz (1.84% of the simulated centre frequency) and the minimum return loss is about 24.41 dB across the whole passband. Measured and simulated results of the second sample made from stainless steel in figure 5.16 (a) shows the frequency shift is about 1.68 GHz (1.87% of the simulated centre frequency) and the minimum return loss is about 28 dB across the whole passband. By looking at measured and simulated results of the copper plated filter in figure 5.17 (a), the frequency shift is only 0.9 GHz (1% of the simulated centre frequency) and the minimum return loss is about 26.56 dB across the whole passband. The small unwanted frequency shifts in the filters is believed to be caused by dimensional inaccuracy, as a result of expansion in the length of resonators during manufacturing, which could be corrected by remanufacturing. It is interesting to notice that such an expansion of dimensions is repeatable, where the two filters made from stainless steel have a very similar frequency shift, this repeatable frequency shift could be corrected by remanufacturing the filter and adjusting the model accordingly to compensate for frequency shift during the remanufacturing. It is possible to investigate the frequency shift by simulating the filter with measured dimensions, however the CT scan image in figure 5.13 is not accurate enough.

Figure 5.18 illustrates the measured results of both samples made from stainless steel on the same plot. The results show that both filters have very close results, indicating the capability of reproducibility of the micro laser sintering process. The return loss of the filters made from stainless steel is slightly different, however their return losses are very close to the designed return loss of 20 dB. Having five poles in measured results indicates excellent accuracy of the manufacturing process. It is worth mentioning that return loss is a very sensitive measurement of the dimensional accuracy and the errors can be attributed to small dimensional inaccuracies.

A modified model of the filter is simulated in CST [5] by considering dimensional changes of 10 µm. Figure 5.19 shows variation in S_{11} and S_{21} with a selection of random changes in the size by 10 µm. The results show that if dimensions are changed by 10 µm during the manufacturing process, still good results will be achieved.

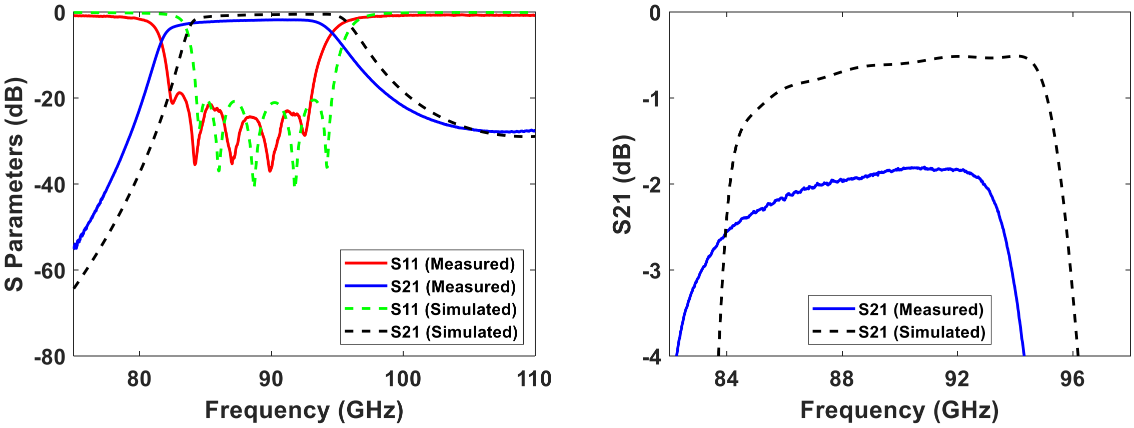

(a) (b)

Figure 5.15 Measured and simulated results of the first sample of 90 GHz waveguide bandpass filter made from stainless steel. (a) Measured and simulated results over the whole W-band. (b) Expanded view of S_{21} over passband.

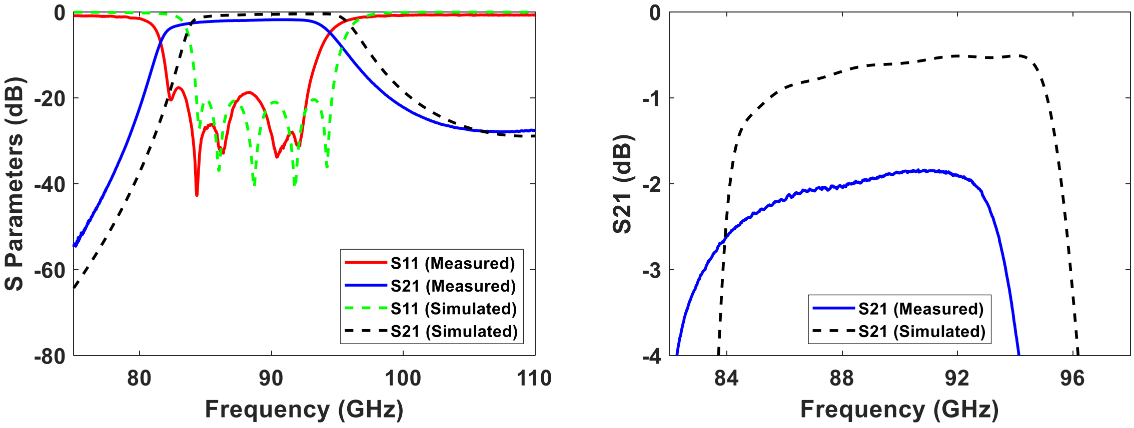

(a) (b)

Figure 5.16 Measured and simulated results of the second sample of 90 GHz waveguide bandpass filter made from stainless steel. (a) Measured and simulated results over the whole W-band. (b) Expanded view of S_{21} over passband.

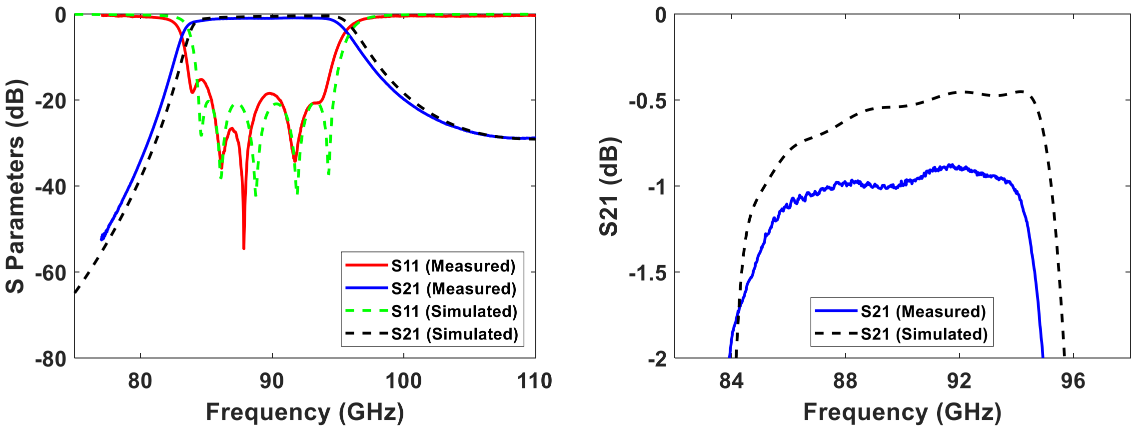

(a) (b)

Figure 5.17 Measured and simulated results of the 90 GHz waveguide bandpass filter made from stainless steel, coated with 5 µm thick copper layer. (a) Measured and simulated results over the whole W-band. (b) Expanded view of S_{21} over passband.

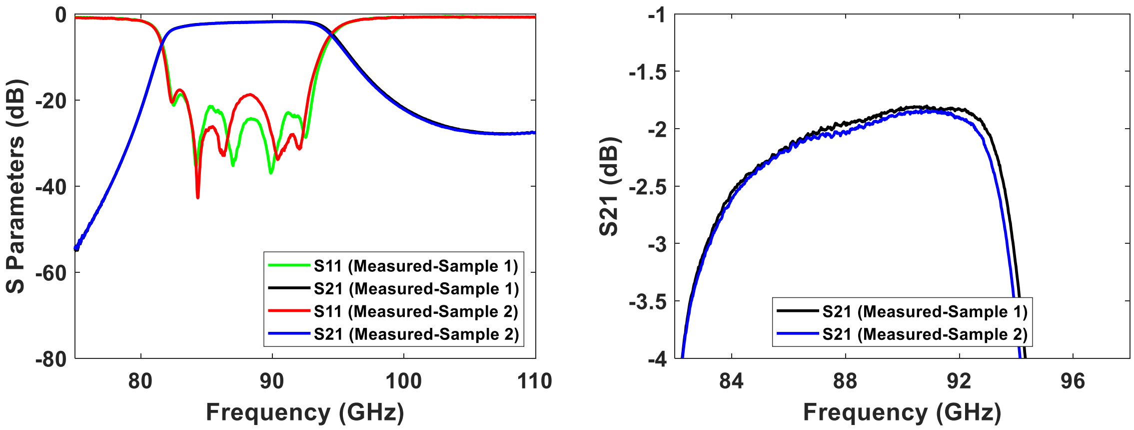

(a) (b)

Figure 5.18 Measured results of both samples of the 90 GHz waveguide bandpass filters made from stainless steel. (a) Measured results over the whole W-band. (b) Expanded view of S_{21} over passband.

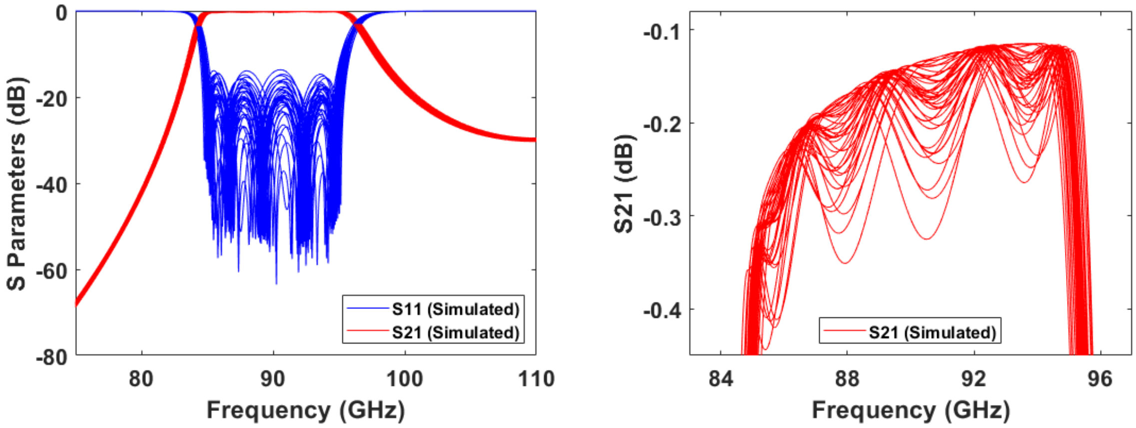

(a) (b)

Figure 5.19 Simulated tolerance analysis of the 90 GHz waveguide bandpass filter. Simulated results are with a selection of random changes in the size by 10 µm. (a) Simulated results over the whole W-band. (b) Expanded view of S_{21} over passband.

The expanded view of S_{21} in figure 5.15 (b) shows an average measured insertion loss of around 1.94 dB over the passband for the first sample made from stainless steel, this is 1.34 dB higher than the simulated results. Looking at expanded view of S_{21} in figure 5.16 (b), the average measured insertion loss is about 2 dB over the passband for the second sample made from stainless steel which is higher only by 0.06 dB from the results of first sample. The maximum difference between measured insertion losses is at the frequency of 88.19 GHz and it is accounted for by the difference in S_{11} of the two filters. The close insertion loss is another indication of capability of reproducibility of the micro laser sintering process.

The expanded view of S_{21} in figure 5.17 (b) shows an average measured insertion loss of 1 dB over the passband for the copper plated filter, which is 0.47 dB higher than simulated results. The results show that the copper plated filter has about 1 dB lower measured insertion loss in comparison to the filters made from stainless steel and not coated with copper, showing the effect of copper plating on insertion loss.

Detailed surface roughness measurements of the filters carried out, using a Mitutoyo SurfTest SV-3000 CNC surface roughness tester at Hong Kong University. Figure 5.20 shows a photograph of the surface roughness measurement setup. Figure 5.21 shows surface roughness measurements at various position on the structure. The side 4 shows the support structure with the filter printed vertically which was cut by an Electrical Discharge

Machine (EDM) wire. The side 4 has a very low Ra surface roughness of about 0.6 µm. The other vertical sides (2, 3, 5 and 6) have a roughness value of between 1.8 - 5 µm. The flange face in figure 5.21 has a roughness value of about 1 µm, and it is not vertically grown. The roughness values are very small, but still larger than the skin depth (0.475 µm for stainless steel with electrical conductivity of 1.25×10^7 S/m and 0.217 µm for copper with electrical conductivity of 5.96×10^7 S/m).

From the surface roughness measurement results in figure 5.21, the average typical surface roughness values of the filters found to be about 2.1 µm. This reduces effective conductivity of stainless steel to 3.19×10^6 S/m and copper to 14.97×10^6 S/m (based on equations (3.3) and (3.4)), and according to calculation in CST [5] resulting in additional loss of 0.46 dB for the stainless steel filters and 0.45 dB for the copper coated filter. However, this loss is already reflected in simulated results of the filters. The loss caused by conduction loss of the 12.96 mm long waveguides joining the filter to flanges is also included in the simulated results, which is about 0.08 dB for stainless steel filters and 0.03 dB for copper plated filter. Small misalignments during measurements also contributed to the difference in insertion loss, however this shows up in the return loss, and 20 dB return loss contributes about 0.04 dB to the insertion loss.

Because of high operating frequency and small skin depth, the additional loss is highly dependent on the surface effects. The additional difference between the simulated and measured insertion loss is caused by a combination of factors including: surface oxidation, contamination of the surface, impurities of powder material used, the effect of the granular nature of the surface which is formed from the powder and changes in the specified conductivity of the stainless steel and copper due to manufacturing process. The insertion loss can be improved by electroplating the surface with a good conductor, using chemical polishing or laser polishing to reduce the surface roughness and even using higher conductivity powder materials.

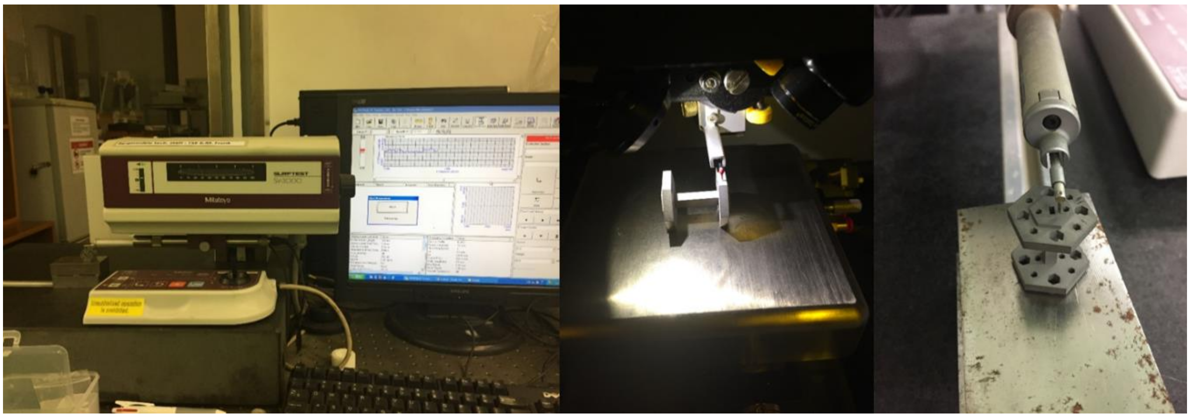

Figure 5.20 Photograph of the surface roughness measurement setup, using a Mitutoyo SurfTest SV-3000 CNC surface roughness tester.

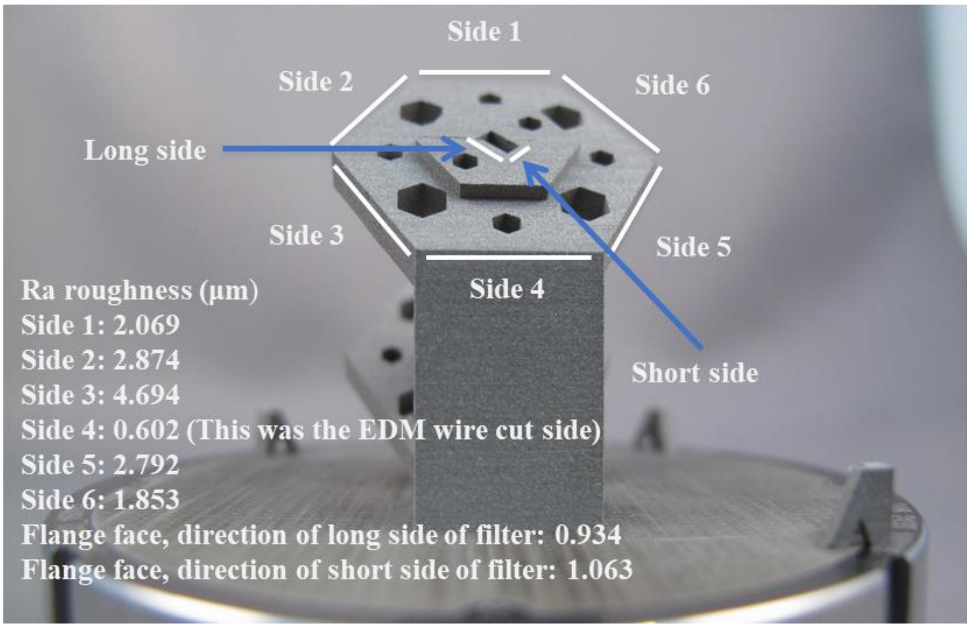

Ra roughness (µm)
Side 1: 2.069
Side 2: 2.874
Side 3: 4.694
Side 4: 0.602 (This was the EDM wire cut side)
Side 5: 2.792
Side 6: 1.853
Flange face, direction of long side of filter: 0.934
Flange face, direction of short side of filter: 1.063

Figure 5.21 The surface roughness measurements at various position on the 90 GHz waveguide bandpass filter.

5.5 Conclusion

This chapter presented metal 3-D printed W-band waveguide bandpass filters which were fabricated by a micro laser sintering process. These are the highest frequency metal 3-D printed filters reported at the time when they were published. The design procedure of the filters using coupling matrix theory was explained as well as the fabrication process. Good agreement between the measured and simulated *S* parameter results demonstrated that the micro laser sintering process can be used to fabricate high frequency microwave components such as filters with complex structures accurately. Also, extremely close measured results of the two identical filters demonstrated the capability of reproducibility of the micro laser sintering process, which makes this process suitable for small to medium batch size production of high frequency filters. Micro laser sintering technique also allows the components to be made in a single piece, and as it is shown in this chapter, the waveguide filter and flanges are made in a single structure. It is also shown that the insertion loss of the filter can be improved considerably by electroplating the surface with copper. Finally, measurements of the surface roughness showed that in the micro laser sintering process the surface roughness is very low and around 1 – 5 µm.

References

[1] M. Salek, X. Shang, R. C. Roberts, M. J. Lancaster, F. Boettcher, D. Weber, and T. Starke, "W-Band Waveguide Bandpass Filters Fabricated by Micro Laser Sintering," *IEEE Transactions on Circuits and Systems II: Express Briefs*, vol. 66, no.1 pp. 61–65, Jan. 2019.

[2] M. Salek, X. Shang, M. J. Lancaster, R. C. Roberts, T. Starke, F. Boettcher, and D. Weber, "90 GHz Micro Laser Sintered Filter: Reproducibility and Quality Assessment," *2019 49th European Microwave Conference (EuMC)*, Paris, France, 2019, pp. 1-4.

[3] J.-S. Hong, *Microstrip filters for RF/microwave applications*. Hoboken, NJ: Wiley, 2011.

[4] R. J. Cameron, C. M. Kudsia, and R. R. Mansour, *Microwave filters for communication systems: fundamentals, design, and applications*. Hoboken, NJ, USA: John Wiley & Sons, Inc., 2018.

[5] Computer Simulated Technology (CST). (2017). Microwave Studio. [Online]. Available: http//www.cst.com/.

[6] 3D Micro Print Gmbh. Accessed: Jan. 10, 2018. [Online]. Available: http://www.3dmicroprint.com/.

CHAPTER 6: 180 GHz WAVEGUIDE BANDPASS FILTERS FABRICATED BY MICRO LASER SINTERING

This chapter presents a fifth-order waveguide bandpass filter, operating at a centre frequency of 180 GHz with a fractional bandwidth of 11% (20 GHz bandwidth) and a Chebyshev response. The filter is fabricated by micro laser sintering process and it is the highest frequency waveguide filter that has ever been fabricated using additive manufacturing. In order to show the reproducibility of the fabrication process, two identical filters are presented in this chapter with the same structure and specification; both are made from stainless steel. This project extends the work introduced in chapter 5, which shows the capability of the micro laser sintering process for fabricating filters, but in this case operating at much higher frequency. It also shows that the process is still capable of reproducing filters, even though the dimensions are reduced by almost a half.

6.1 Introduction

Additive manufacturing or 3-D printing has already shown its potential in fabrication of microwave components, as explained in chapter 3. As mentioned, numerus microwave devices are fabricated using different types of additive manufacturing, where many have been fabricated using non-metallic materials such as plastics. As discussed previously, non-metallic materials such as plastics are inexpensive and lightweight, but the downside of using them are their thermal and mechanical sensitivity.

Metal 3-D printing technique such as selective laser sintering (SLS) has been used in the past to fabricate microwave filters [1], and as mentioned in chapter 5, high frequency waveguide bandpass filters operating at centre frequency of 90 GHz were fabricated by micro laser sintering process using metallic materials [2]. Here, Micro laser sintering process is used again to fabricate waveguide bandpass filters operating at centre frequency of 180 GHz. These are the highest frequency 3-D printed filters fabricated, which show the capability of micro laser sintering process in producing high frequency components. Having almost identical results with both filters also shows the excellent reproducibility of the process at this frequency.

6.2 Waveguide Bandpass Filter Design

The waveguide bandpass filter presented in this chapter has the same structure as the filters introduced in chapter 5 but operating at different centre frequency. The filter is designed using the same procedure, using coupling matrix theory [3, 4]. Here the filter design procedure is going to be explained briefly and full details of design procedure can be found in chapter 5. The filter is designed with a centre frequency of 180 GHz, a bandwidth of 20 GHz (fractional bandwidth of 11%) and a return loss of 20 dB over the passband. The filter is specified in terms of Chebyshev response and is constructed with five rectangular resonators operating in the TE_{101} mode.

The coupling between resonators and input/ output coupling are realized using inductive irises. The design procedure began by translating the filter specification into coupling matrix elements, which are then translated into physical dimensions following the procedure explained in [3, 4]. Based on coupling matrix theory [3, 4], the un-normalised none-zero coupling coefficients between resonators and external quality factor of the first (Q_{e1}) and the last (Q_{eN}) resonators are calculated as $M_{12} = M_{45} = 0.0961$, $M_{23} = M_{34} = 0.0706$ and $Q_{e1} = Q_{eN} = 8.76$. Figure 6.1 shows the ideal response of the Chebyshev filter, which is plotted using equation (2.36).

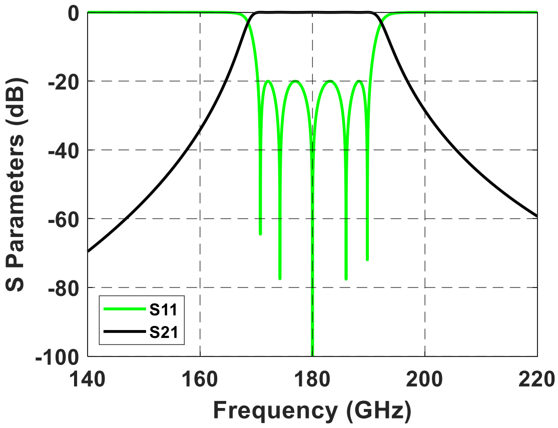

Figure 6.1 Ideal response of the Chebyshev filter.

Figure 6.2 shows internal structure of the filter. The couplings between resonators 1 and 2 and resonators 4 and 5 are realized by adjusting the width of irises denoted by W_1 and W_4, which is set by coupling coefficients M_{12} and M_{45}. The couplings between resonators 2 and 3 and resonators 3 and 4 are realized by adjusting the width of irises denoted by W_2 and W_3 and set by coupling coefficients M_{23} and M_{34}. The input/ output coupling is realized by adjusting the width of iris denoted by *Ext* and set by external quality factor $Q_{e1} = Q_{eN}$. Internal dimensions of the filter are given in figure 6.2. Simulations and optimisation of the filter are carried out in CST Microwave Studio [5].

Figure 6.3 (a) shows the external design of the filter and its external dimensions. Figure 6.3 (b) shows a cross section view of the filter with all the resonators visible. As it can be seen in figure 6.3, both input and output UG387/U waveguide flanges are included in the design and they both have alignment pin holes and screw holes. Fabricating the waveguide filter and waveguide flanges in one piece allows accurate connection to measurement system. The UG387/U waveguide flanges are designed in octagonal shapes, and alignment pin holes and screw holes are designed in pentagonal shapes, this is to prevent overhang during the fabrication process as explained in chapter 3.

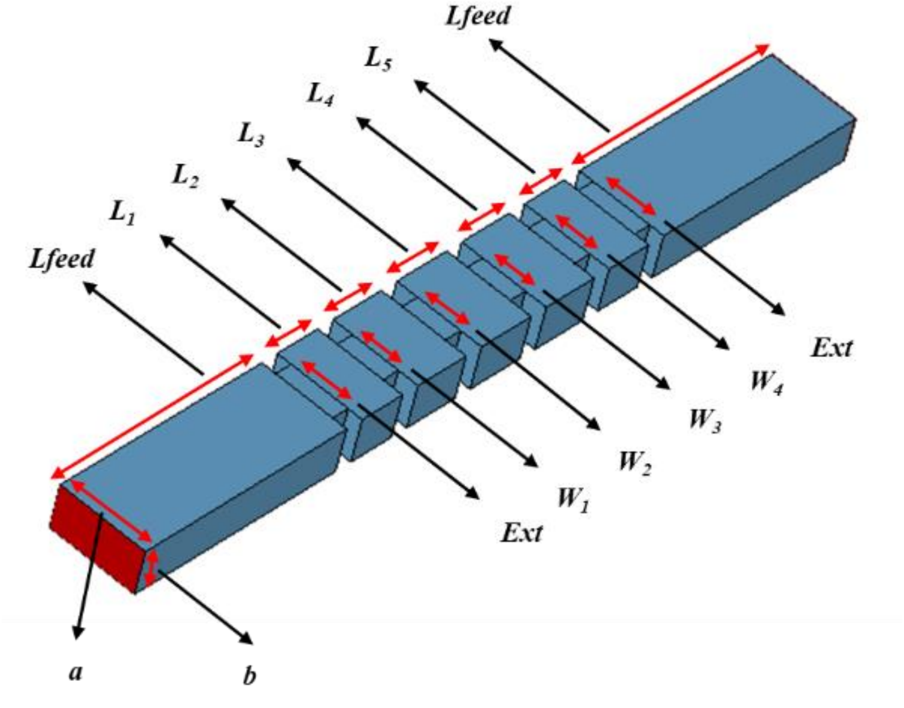

Figure 6.2 Internal structure of the 180 GHz waveguide bandpass filter showing internal dimensions. The dimensions in millimetres are: $Lfeed = 9.095$, $L_1 = L_5 = 0.648$, $L_2 = L_4 = 0.782$, $L_3 = 0.809$, $Ext = 0.857$, $W_1 = W_4 = 0.688$, $W_2 = W_3 = 0.645$, $a = 1.295$ and $b = 0.648$.

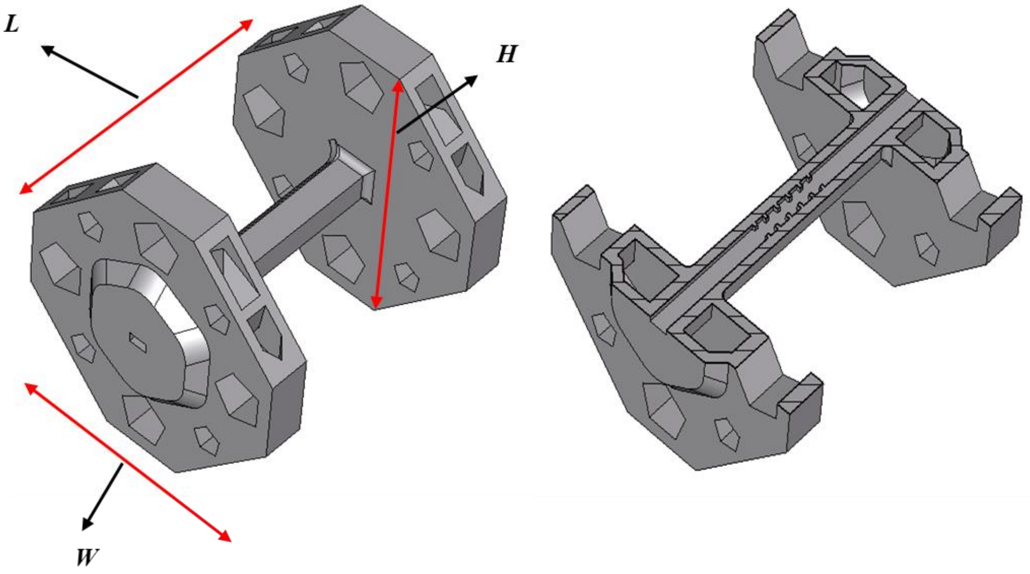

(a) (b)

Figure 6.3 Illustration of the 180 GHz waveguide bandpass filter. (a) External design of the filter showing external dimensions. The dimensions in millimetres are: *L = 21.36*, *H = 19.23* and *W = 19.23*. (b) A cross section view of the filter showing internal couplings between resonators.

6.3 Fabrication Process

The filters presented in this chapter were fabricated by 3D Micro Print GmbH [6] using the micro laser sintering process. Details of micro laser sintering process was provided in chapter 3. As mentioned in chapter 3, the model structure is printed layer by layer, where the powders are selectively fused using a laser beam. Here an IR fiber laser with 50 W average power is used, where the laser is focused down to a spot size of 30 µm and operated in continuous wave mode during the fabrication process. The thickness of each layer in the process was set to 5 µm and the printing time was about 10 hours for each filter. Both filters were made from stainless steel powders with electrical conductivity of 1.25×10^7 S/m. The powder particle size was about d_{80} 5 µm (d_{80} is particle size distribution). The type of stainless steel was 1.4542 (17-4PH), which is a chromium nickel copper alloyed stainless steel. After the filters were printed, the entire structure of the filters was slightly blasted with Corundum and the flange surfaces were mechanically polished in order to achieve a smooth surface.

Figure 6.4 shows photograph of the fabricated waveguide bandpass filters. Both input and output waveguide flanges have empty internal cavities, this is to make the filters lighter and reduce the stress on walls during the fabrication process. Figure 6.5 shows the structure of these empty cavities.

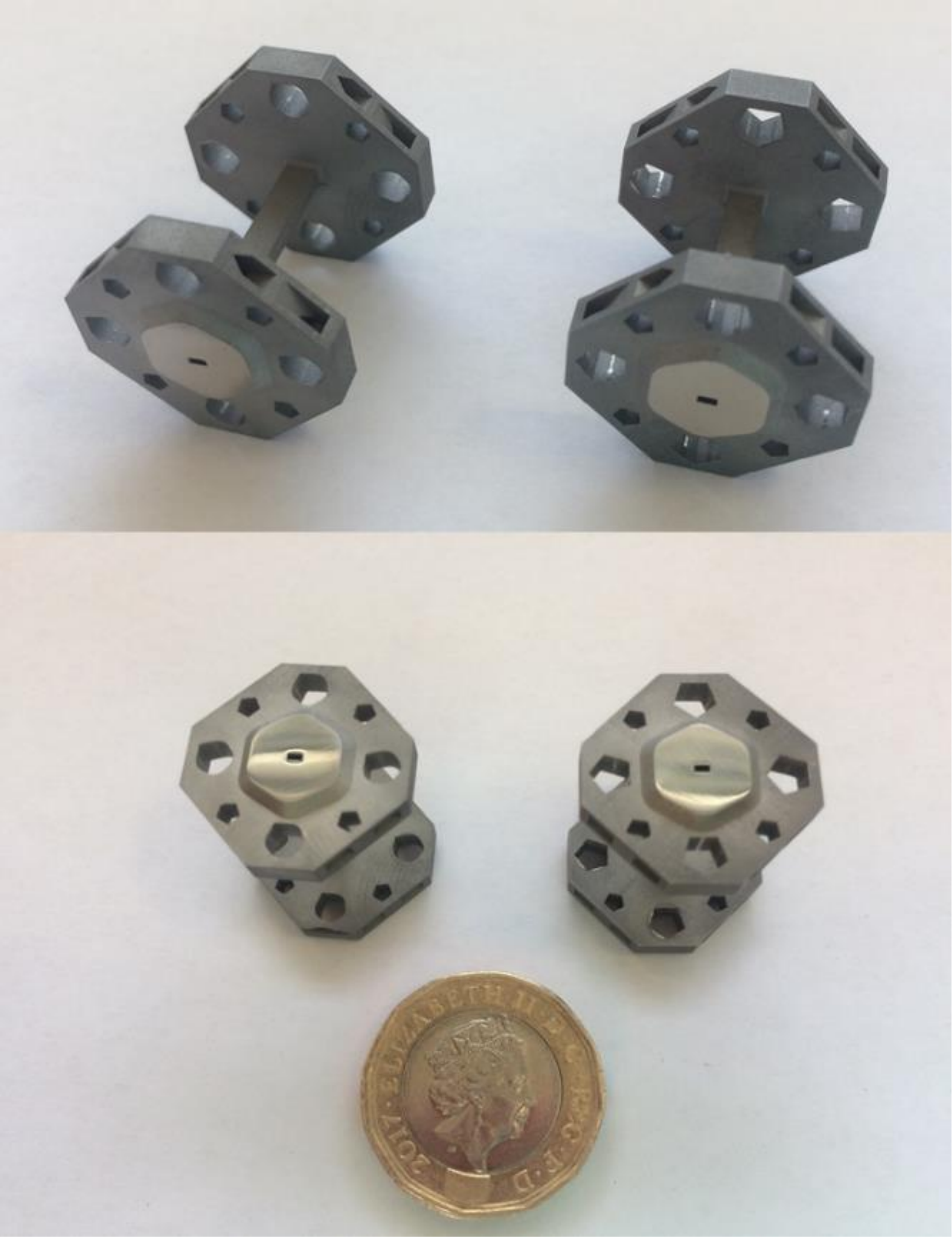

Figure 6.4 Photograph of the fabricated 180 GHz waveguide bandpass filters. The photograph shows sample 1 on the left and sample 2 on the right.

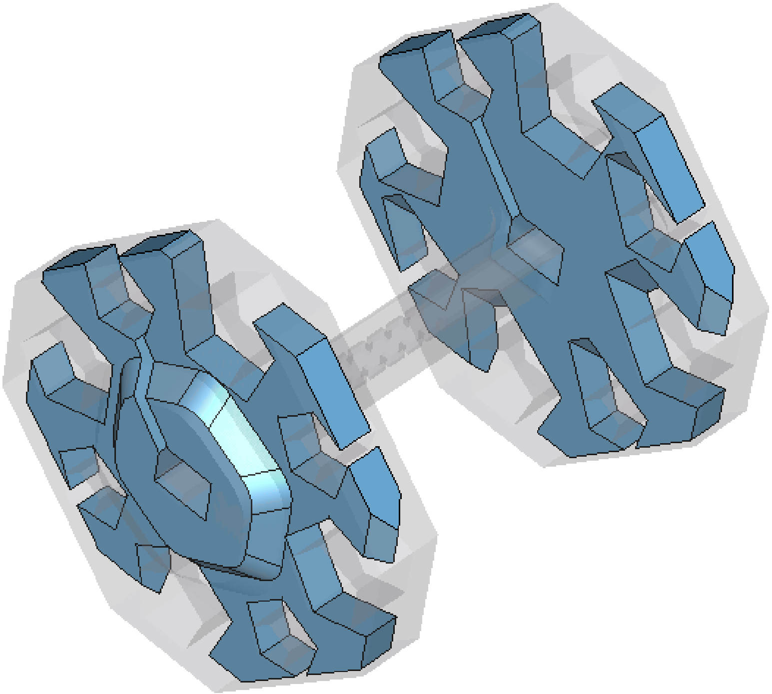

Figure 6.5 Structure of the empty cavities within the waveguide flanges of the filter. The blue areas represent empty cavities.

6.4 Measurement and Discussion

The *S* parameter measurements of the 180 GHz waveguide bandpass filters were performed on Keysight N5247B PNA-X network analyser. The network analyser was calibrated using TRL (Thru, Reflect, Line) method prior to the measurements. Figure 6.6 shows a photograph of the measurement setup with the filter placed between two waveguide flanges of the network analyser. They were aligned using four alignment pins of the waveguide flanges and tightened using four bolts on each side. Figure 6.7 and figure 6.8 show the measured and simulated results of both filters, where the measured results are denoted with solid lines and simulated results with dashed lines.

Looking at measured and simulated results of the first sample in figure 6.7 (a), the measured centre frequency is shifted down by 2.75 GHz (1.53% of the simulated centre frequency) and the minimum measured return loss is about 18.34 dB across the whole passband. Measured and simulated results of the second sample in figure 6.8 (a) shows the measured centre frequency is shifted down by 2.4 GHz (1.33% of the simulated centre frequency) and the minimum measured return loss is about 17.25 dB across the whole passband. The unwanted frequency shifts in the filters are believed to be caused by dimensional inaccuracies during the manufacturing process and could be corrected by remanufacturing the filters. The results show that the frequency shifts in both filters are very close and repeatable, so the model could be adjusted accordingly to compensate during the remanufacturing.

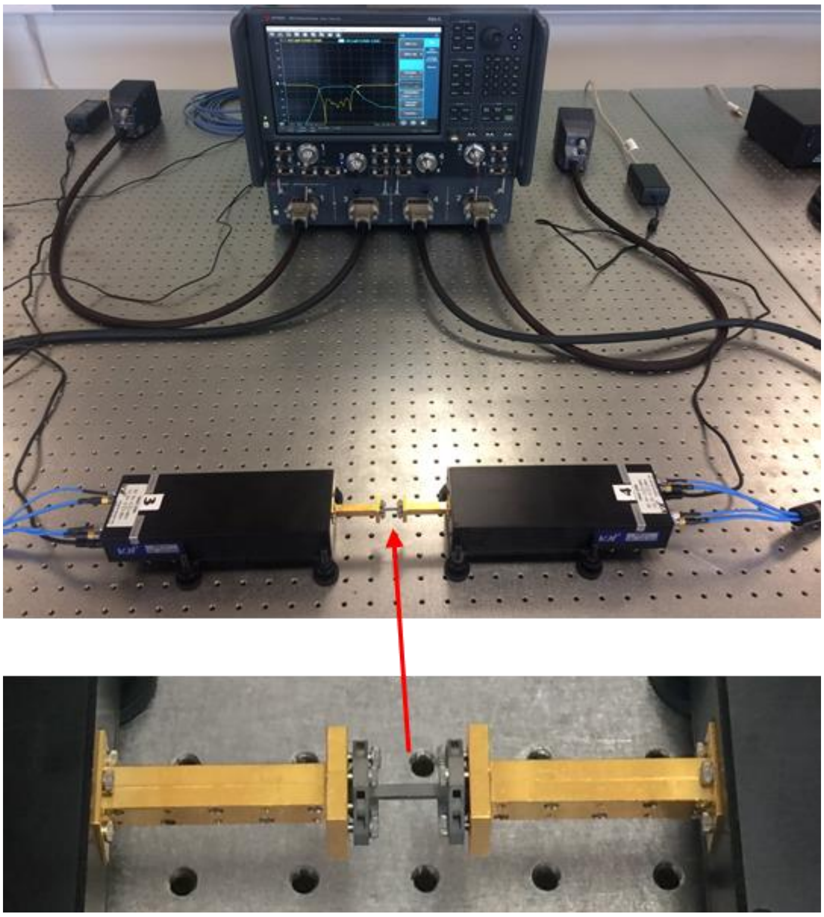

Figure 6.6 Photograph of the measurement setup with the 180 GHz waveguide bandpass filter placed between two waveguide flanges of the network analyser.

The expanded view of S_{21} in figure 6.7 (b) shows an average measured insertion loss of 3.26 dB over the passband for the first sample, this is 1.94 dB higher than the simulated results. Also, looking at the expanded view of S_{21} in figure 6.8 (b), the average measured insertion loss is about 3.19 dB over the passband for the second sample, which is 1.87 dB higher than the simulated results.

The average typical surface roughness values of the filters measured using a Keyence VHX 6000 optical microscope at 3D Micro Print GmbH [6], which was about 7 µm. This reduces effective conductivity of stainless steel to 3.13 $\times 10^6$ S/m (based on equations (3.3) and (3.4)). Based on calculation in CST [5], this results in additional loss of 0.64 dB. This loss is already reflected in simulated results. The loss due to conduction loss of 18.19 mm long stainless steel waveguides joining the filter to flanges is also included in the simulated results, which is about 0.29 dB.

The additional difference between the simulated and measured insertion loss is mainly attributed to a combination of factors including: contamination of the surface, impurities of powder material, changes in the specified conductivity of the stainless steel due to manufacturing process, effect of granular nature of the surface formed from the powder and different surface roughness within the cavities. Small misalignment of the waveguide flanges during measurements also contributed to the additional insertion loss, but also affects the return loss. The 20 dB return loss contributes about 0.04 dB to the insertion loss.

Figure 6.9 shows the measured results of both filters on the same plot. The results show that both samples have very close results, this indicates the capability of reproducibility of the micro laser sintering process. Table 6.1 summarises the measured results of both samples. Looking at the results, the difference between measured centre frequencies is only 0.35 GHz, average measured insertion losses are very close, and the difference is only 0.08 dB, and the return losses are very close to the designed return loss of 20 dB.

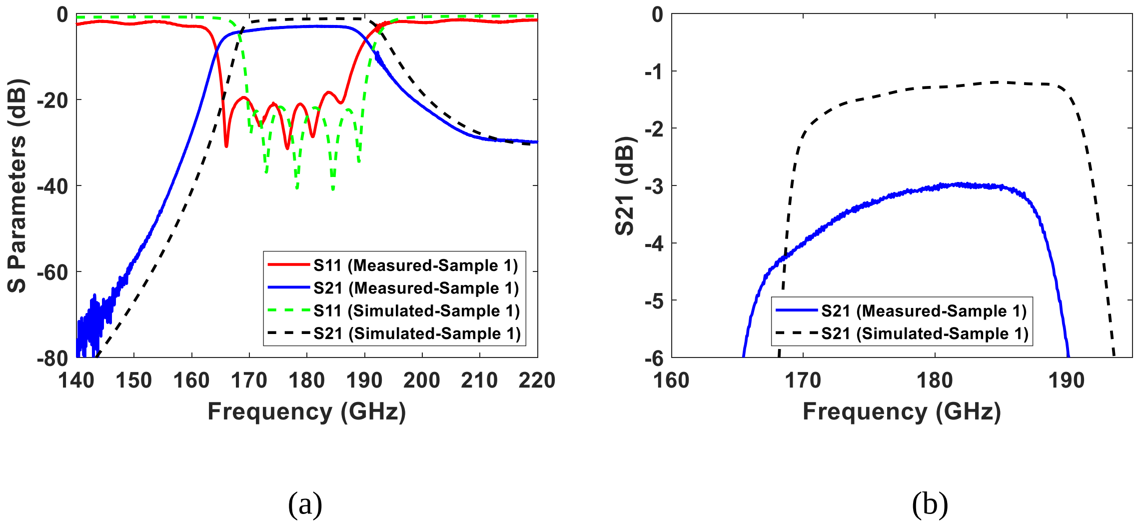

(a) (b)

Figure 6.7 Measured and simulated results of the first sample. (a) Responses over the frequency range of 140 – 220 GHz. (b) Expanded view of S_{21} over passband.

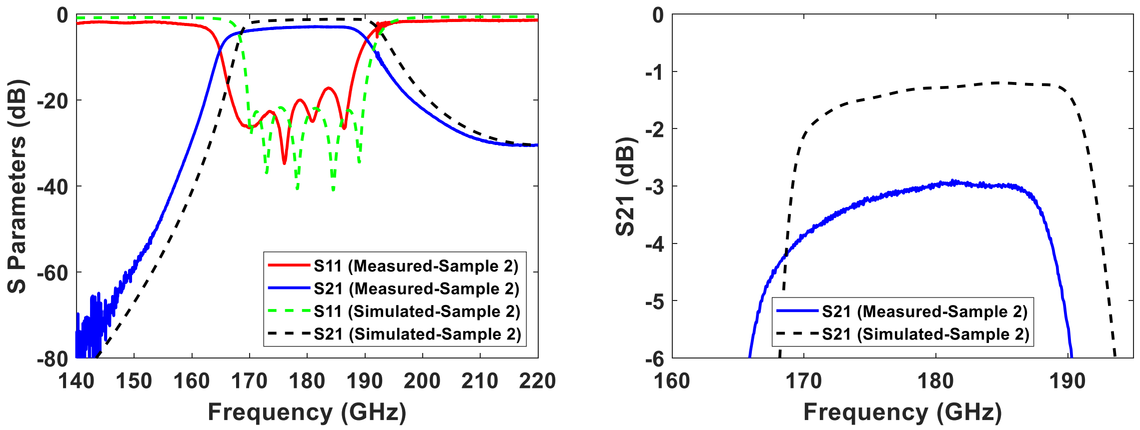

(a) (b)

Figure 6.8 Measured and simulated results of the second sample. (a) Responses over the frequency range of 140 – 220 GHz. (b) Expanded view of S_{21} over passband.

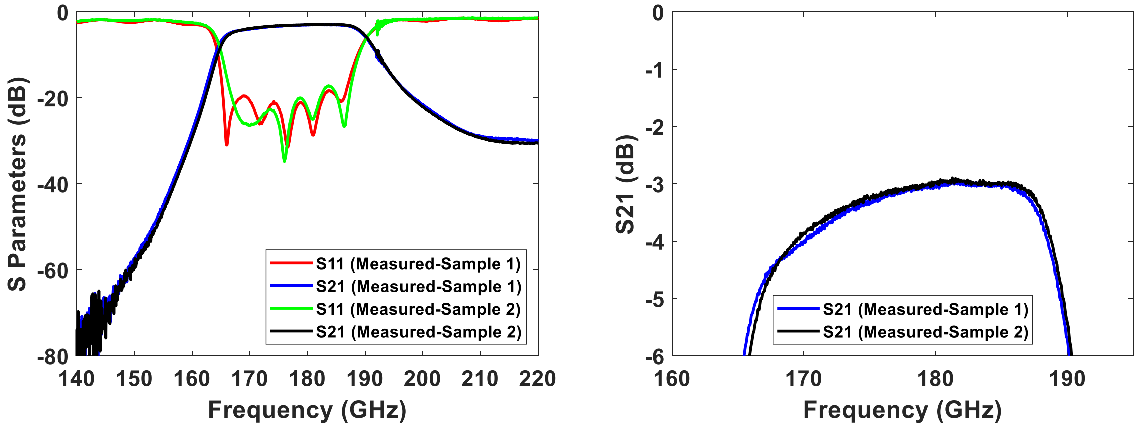

(a) (b)

Figure 6.9 Measured results of the both samples. (a) Responses over the frequency range of 140 – 220 GHz. (b) Expanded view of S_{21} over passband.

Table 6.1 Measured results of the both samples.

	Sample 1	**Sample 2**
Measured centre frequency	177.25 GHz	177.6 GHz
Average measured insertion loss	3.26 dB	3.19 dB
Minimum measured return loss	18.34 dB	17.25 dB

6.5 Conclusion

This chapter presented two identical 180 GHz waveguide bandpass filters which were fabricated using micro laser sintering process. These are the highest frequency waveguide filters which were fabricated using metal 3-D printing. The design procedure and fabrication details of the filters were briefly explained. The measured results had good agreement with the simulated results which demonstrated the accuracy of the micro laser sintering process. The close measured results of the two filters demonstrated the capability of reproducibility of the micro laser sintering process. The project demonstrates the potential of using micro laser sintering process for small to medium batch size production of high-quality waveguide filters operating at high frequencies. The filters will be electroplated in gold in order to learn more about the losses.

References

[1] B. Zhang and H. Zirath, “3D printed iris bandpass filters for millimetre-wave applications,” *Electronics Letters*, vol. 51, no. 22, pp. 1791–1793, Oct. 2015.

[2] M. Salek, X. Shang, R. C. Roberts, M. J. Lancaster, F. Boettcher, D. Weber, and T. Starke, “W-Band Waveguide Bandpass Filters Fabricated by Micro Laser Sintering,” *IEEE Transactions on Circuits and Systems II: Express Briefs*, vol. 66, no. 1, pp. 61–65, Jan. 2019.

[3] J.-S. Hong, *Microstrip filters for RF/microwave applications*. Hoboken, NJ: Wiley, 2011.

[4] R. J. Cameron, C. M. Kudsia, and R. R. Mansour, *Microwave filters for communication systems: fundamentals, design, and applications*. Hoboken, NJ, USA: John Wiley & Sons, Inc., 2018.

[5] Computer Simulated Technology (CST). (2017). Microwave Studio. [Online]. Available: http//www.cst.com/.

[6] 3D Micro Print Gmbh. Accessed: Jan. 10, 2018. [Online]. Available: http://www.3dmicroprint.com/.

CHAPTER 7: DESIGN OF 2 GHz HYBRID COAXIAL BANDPASS FILTER FABRICATED BY STEREOLITHOGRAPHY 3-D PRINTING

This chapter presents a fourth-order 2 GHz hybrid coaxial bandpass filter, which is fabricated using stereolithography 3-D printing. The filter consists of four coaxial resonators, where main-line couplings between resonators are realized using PCB (printed circuit board) lines, instead of using coupling irises or probes. The input/output coupling is also realized using PCB lines. The idea allows different topologies to be designed easily by altering the PCB, even a fully canonical filter could be considered. Here, to demonstrate the idea, a fourth-order coaxial bandpass filter is designed with one cross coupling in order to have two transmission zeros, which provide higher passband skirt selectivity. The quality factor of each of the coaxial resonators in the filter is increased by introducing base rounding in the resonator, this is explained in this chapter. The filter is designed to operate at a centre frequency of 2 GHz, with a fractional bandwidth of 2% (40 MHz bandwidth), a Chebyshev response and two transmission zeros at 1.96 GHz and 2.04 GHz. The design procedure is based on coupling matrix theory, where a folded $N+2$ coupling matrix is used. The design procedure of the filter is explained in this chapter, and the fabrication details of the filter is also provided.

7.1 Introduction

Coaxial bandpass filters are used in various communication systems, particularly in communication satellites and earth stations, because of their high-power capability, low loss, high selectivity, compact size, low manufacturing cost and easy tuning [1, 2]. With rapid development in microwave technology, the frequency spectrum resources become scarce and higher skirt selectivity of passband is required to overcome the demand. To obtain a sharp passband response, transmission zeros can be located near the passband by introducing cross couplings between resonators of the filter. Theoretically this is achievable, but in practice it might not be easy and will increase cost and complexity of the fabrication. Different types of cross coupled coaxial cavity filters with new features and topologies have been designed and reported in [3]-[9], where cross couplings have been used to get better frequency selectivity. However, the main-line couplings and cross couplings are realized using coupling irises and probes or by changing the position and dimension of resonators. The coaxial bandpass filter presented in this chapter uses PCB lines for main-line couplings and a capacitive gap for cross coupling. The idea allows multiple cross couplings to be included in the PCB layout if different topology is going to be implemented. The input/output coupling is also realized using PCB lines, this way the input and output can be easily coupled directly if a fully canonical filter is going to be designed. Here to demonstrate the idea, a fourth-order coaxial bandpass filter with two transmission zeros is presented, however same technique can be used to implement different topologies. The filter is fabricated using stereolithography 3-D printing, and a good agreement between measured and simulated results is achieved.

7.2 Design of Hybrid Coaxial Bandpass Filter

The hybrid coaxial bandpass filter is designed with a centre frequency of 2 GHz, a bandwidth of 40 MHz (factional bandwidth of 2%), a return loss of 20 dB and two transmission zeros at 1.96 GHz and 2.04 GHz ($\pm j1.96$), which produce two attenuation lobes of 31 dB on the lower and upper sides of the passband. The filter is specified in terms of the general Chebyshev bandpass response and constructed with four quarter wavelength long coaxial resonators operating in TEM mode.

The filter is designed using coupling matrix theory [10, 11], where a folded $N+2$ coupling matrix is used. The physical dimensions of the filter are found by extracting external quality factor and inter resonator couplings, which are then used to construct the filter. The dimensions of the filter then optimised, using CST Microwave Studio [12]. The next sections will give details of the design procedure.

7.2.1 Determining the Folded $N+2$ Coupling Matrix

The first step in order to determine the folded $N+2$ coupling matrix is to generate the transversal coupling matrix, which is then transformed to a folded coupling matrix, using a series of matrix rotations. Based on the technique explained in section 2.3 (chapter 2), the coefficients of the numerator and denominator of polynomials $S_{11}(s)$ and $S_{21}(s)$ computed and are shown in table 7.1. Here, the coefficients of polynomial $P(s)$ have been multiplied by j to preserve the unitary conditions, because (N - n_{fz}) is an even number (note N is degree of the filter and n_{fz} is the number of transmission zeros) [11].

Table 7.1 Coefficients of polynomials $E(s)$, $F(s)$ and $P(s)$ for the fourth-order filter with two transmission zeros (note polynomials are converted to complex frequency domain s, using $s = j\omega$).

S^i i =	Coefficients of $S_{11}(s)$ and $S_{21}(s)$ denominator polynomial $E(s)$	Coefficients of $S_{11}(s)$ numerator polynomial $F(s)$	Coefficients of $S_{21}(s)$ numerator polynomial $P(s)$
0	$1.4452 + j9.18355 \times 10^{-4}$	0.14452	$j3.8416$
1	2.82057	0	0
2	3.22867	1.03762	$j1$
3	$2.09335 - j1.06342 \times 10^{-4}$	$-j2.32742 \times 10^{-4}$	
4	1	1	
		$\varepsilon_R = 1$	$\varepsilon = 2.671624$

The numerator and denominator polynomials of $y_{21}(s)$ ($=y_{21n}(s)/y_d(s)$) and $y_{22}(s)$ ($= y_{22n}(s)/y_d(s)$) are then constructed using the coefficients of polynomials $E(s)$, $F(s)$ and $P(s)$ in table 7.1 and equations (2.44) and (2.45). The coefficients of polynomials $y_{21n}(s)$, $y_{22n}(s)$ and $y_d(s)$ are summarised in table 7.2, which are normalised to the highest degree coefficient of polynomial $y_d(s)$.

Table 7.2 Coefficients of numerator and denominator polynomials of $y_{21}(s)$ and $y_{22}(s)$.

S^i i =	Coefficients of denominator polynomial of $y_{21}(s)$ and $y_{22}(s)$ ($y_d(s)$)	Coefficients of numerator polynomial of $y_{22}(s)$ ($y_{22n}(s)$)	Coefficients of numerator polynomial of $y_{21}(s)$ ($y_{21n}(s)$)
0	0.79485	$j4.59178 \times 10^{-4}$	$j0.71897$
1	0	1.4103	0
2	2.13315	0	$j0.1872$
3	0	1.0467	
4	1		

By using the coefficients of numerator and denominator polynomials of $y_{21}(s)$ and $y_{22}(s)$ in table 7.2, $y_{21}(s)$ and $y_{22}(s)$ are obtained. Partial fraction expansions then used to find their residues r_{21k} and r_{22k} for $k = 1, 2, 3, 4$. Also, by finding the roots of the denominator $y_d(s)$, the eigenvalues λ_k of the network for $k = 1, 2, 3, 4$ found. Residues, eigenvalues and eigenvectors for the fourth-order filter are given in table 7.3.

Table 7.3 Residues, eigenvalues and eigenvectors for the fourth-order filter.

	Eigenvalues	Residues		Eigenvectors	
k	λ_k	r_{22k}	r_{21k}	$T_{Nk} = \sqrt{r_{22k}}$	$T_{1k} = r_{21k}/\sqrt{r_{22k}}$
1	-1.2853	0.1362	0.1362	0.3689	0.3689
2	-0.6936	0.3872	-0.3872	0.6222	-0.6222
3	0.6936	0.3872	0.3872	0.6222	0.6222
4	1.2853	0.1362	-0.1362	0.3689	-0.3689

The direct source to load coupling M_{SL} can be calculated, using equation (2.57) and constants ε and ε_R in table 7.1, however, because the filter is not a fully canonical filter, the constant ε_R has a value of unity, which makes the coupling between source and load to be zero.

The elements of transversal coupling matrix are calculated using equation (2.59). Table 7.4 provides calculated elements of transversal coupling matrix, which are used to construct the transversal coupling matrix.

Table 7.4 Elements of transversal coupling matrix.

M_{Sk} (Input couplings)	M_{Lk} (Output couplings)	M_{kk} (Self couplings)
$M_{S1} = 0.3689$	$M_{L1} = 0.3689$	$M_{11} = 1.2853$
$M_{S2} = -0.6222$	$M_{L2} = 0.6222$	$M_{22} = 0.6936$
$M_{S3} = 0.6222$	$M_{L3} = 0.6222$	$M_{33} = -0.6936$
$M_{S4} = -0.3689$	$M_{L4} = 0.3689$	$M_{44} = -1.2853$

The transversal coupling matrix of the hybrid coaxial bandpass filter is given as

$$[m] = \begin{bmatrix} 0 & 0.3689 & -0.6222 & 0.6222 & -0.3689 & 0 \\ 0.3689 & 1.2853 & 0 & 0 & 0 & 0.3689 \\ -0.6222 & 0 & 0.6936 & 0 & 0 & 0.6222 \\ 0.6222 & 0 & 0 & -0.6936 & 0 & 0.6222 \\ -0.3689 & 0 & 0 & 0 & -1.2853 & 0.3689 \\ 0 & 0.3689 & 0.6222 & 0.6222 & 0.3689 & 0 \end{bmatrix} \tag{7.1}$$

Using the coupling matrix reduction technique described in section 2.4.3 (chapter 2), the transversal coupling matrix is reduced to a folded form with a series of six rotations, where the elements M_{S4}, M_{S3}, M_{S2}, M_{2L}, M_{3L} and M_{13} are annihilated in the sequence shown in table 7.5. The folded coupling matrix of the hybrid coaxial bandpass filter after the reduction process is given in matrix (7.2).

$$[m] = \begin{bmatrix} 0 & 1.02307 & 0 & 0 & 0 & 0 \\ 1.02307 & 0 & 0.868202 & 0 & -0.178806 & 0 \\ 0 & 0.868202 & 0 & 0.770468 & 0 & 0 \\ 0 & 0 & 0.770468 & 0 & 0.868202 & 0 \\ 0 & -0.178806 & 0 & 0.868202 & 0 & 1.02307 \\ 0 & 0 & 0 & 0 & 1.02307 & 0 \end{bmatrix} \tag{7.2}$$

Table 7.5 4th degree rotation sequence for reduction of *N+2* transversal coupling matrix to folded coupling matrix.

				$\theta_r = \tan^{-1}\left(c\frac{M_{kl}}{M_{mn}}\right)$				
Transform Number *r*	**Pivot [*i, j*]**	**Element to be Annihilated**	**Row/Column**	***k***	***l***	***m***	*N*	***c***
1	[3, 4]	M_{S4}	Row *S*	*S*	4	*S*	3	-1
2	[2, 3]	M_{S3}	Row S	*S*	3	*S*	2	-1
3	[1, 2]	M_{S2}	Row *S*	*S*	2	*S*	1	-1
4	[2, 3]	M_{2L}	Column *L*	2	*L*	3	*L*	1
5	[3, 4]	M_{3L}	Column *L*	3	*L*	4	*L*	1
6	[2, 3]	M_{13}	Row 1	1	3	1	2	-1

Figure 7.1 shows ideal response of the Chebyshev filter, which is plotted using equation (2.60). Figure 7.2 shows the topology of the hybrid coaxial bandpass filter.

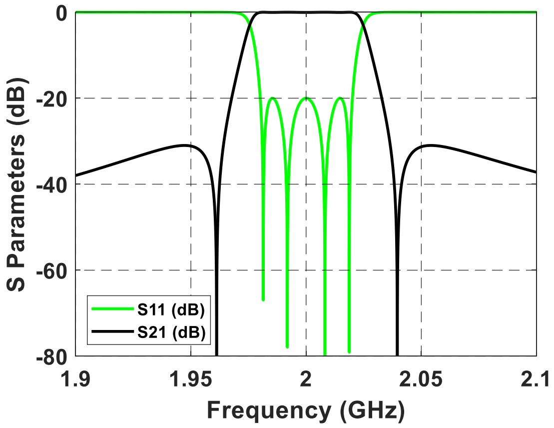

Figure 7.1 Ideal response of the Chebyshev filter.

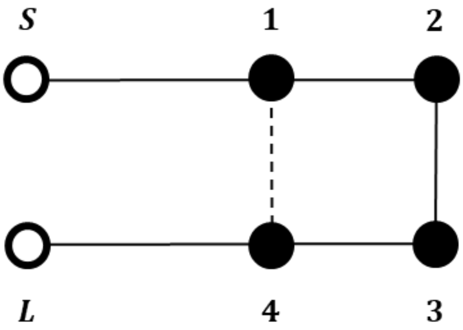

Figure 7.2 Coupling and routing schematic of the 2 GHz hybrid coaxial bandpass filter.

To calculate external quality factors and coupling coefficients, the normalised external quality factor of the folded *N+2* coupling matrix should be calculated first, which can be calculated by [11]

$$q_{e1} = q_{eN} = \frac{1}{{m_{S1}}^2} \quad or \quad \frac{1}{{m_{1S}}^2} \quad or \quad \frac{1}{{m_{LN}}^2} \quad or \quad \frac{1}{{m_{NL}}^2} \tag{7.3}$$

The normalised external quality factor calculated as $q_{e1} = q_{eN} = 0.9554$. The un-normalised non-zero coupling coefficients and the external quality factors of the 2 GHz hybrid coaxial bandpass filter are calculated using equation (2.83), provided in table 7.6, which are used to find physical dimensions of the hybrid coaxial bandpass filter.

Table 7.6 The external quality factors and coupling coefficients of the 2 GHz hybrid coaxial bandpass filter.

Q_{e1}	Q_{eN}	M_{12}	M_{23}	M_{34}	M_{14}
47.77	47.77	0.017364	0.01541	0.017364	-0.003576

7.2.2 Quality Factor Improvement of Coaxial Resonator

The cross section of coaxial resonator used in the hybrid coaxial bandpass filter is shown in figure 7.3. The resonator is a quarter wavelength long which operates in TEM mode. As it is shown in figure 7.3, the maximum current is flowing at the bottom of the resonator, which contributes a large part of the ohmic losses and results in lower unloaded quality factor. In order to reduce the ohmic losses, the base rounding is introduced into the resonator, which spreads the current and minimises this power loss. Using base rounding in coaxial resonator to increase the unloaded quality factor is already reported in [13, 14], where details are provided. It is also reported in [13, 14], that the optimal unloaded quality factor for a coaxial resonator can be obtained by making the ratio of inner diameter of outer conductor to outer diameter of inner conductor as $b/a = 3.59$.

The radius of the base for rounding is R_b and the maximum unloaded quality factor can be found by simulating the resonator in CST [12], here the radius of base is adjusted in order to get maximum unloaded quality factor by considering $b/a = 3.59$ ($b = 35.9$ mm and $a = 10$ mm). Figure 7.4 shows relation between unloaded quality factor per volume and the radius of base rounding R_b, which is plotted by adjusting the radius of base rounding. During the simulation process, the open-end capacitive gap of the resonator is kept fixed at $h = 20$ mm and only the length of inner conductor of resonator is adjusted to keep the resonance frequency of the resonator at 2 GHz. Using the relation in figure 7.4, the radius of base rounding is found as $R_b = 4.8$ mm for maximum unloaded quality factor per volume of 0.10648, this is denoted by a red dot in figure 7.4. Figure 7.5 shows relation between unloaded quality factor and the radius of base rounding R_b, this relation shows when $R_b = 4.8$ mm, the unloaded quality factor of the resonator is 5878, as it is denoted by a red dot. The relation in figure 7.5 also shows the unloaded quality factor of the resonator can be increased further by increasing the radius of base rounding, but based on relation in figure 7.4 this will cause the unloaded quality factor per volume to decrease, and in this project the intension was to increase the unloaded quality factor while maintaining small volume. The small rounding R_a at the top of inner conductor of the resonator is introduced to improve high power handling, as it is reported in [13, 14].

For the filter presented here, the ratio b/a is kept at 3 as b = 30 mm and a = 10 mm, because of minimum distance of 4 mm between resonators and minimum diameter of 10 mm for inner conductor of each resonator, which is required in order to 3-D print the filter. The relation between unloaded quality factor per volume and the radius of base rounding R_b is plotted using the same technique explained above by considering b/a = 3, this relation is shown in figure 7.6. Using the relation in figure 7.6, the radius of base rounding is found as R_b = 3.4 mm for maximum unloaded quality factor per volume of 0.12655, which is denoted by a red dot in figure 7.6. The relation between unloaded quality factor and the radius of base rounding R_b is shown in figure 7.7, showing unloaded quality factor of 4926 when R_b = 3.4 mm (this is denoted by a red dot in figure 7.7). Looking at the relation in figure 7.7, the unloaded quality factor can be increased further by increasing the radius of base rounding R_b. However, referring to the relation in figure 7.6, it can be seen the unloaded quality factor per volume will decrease.

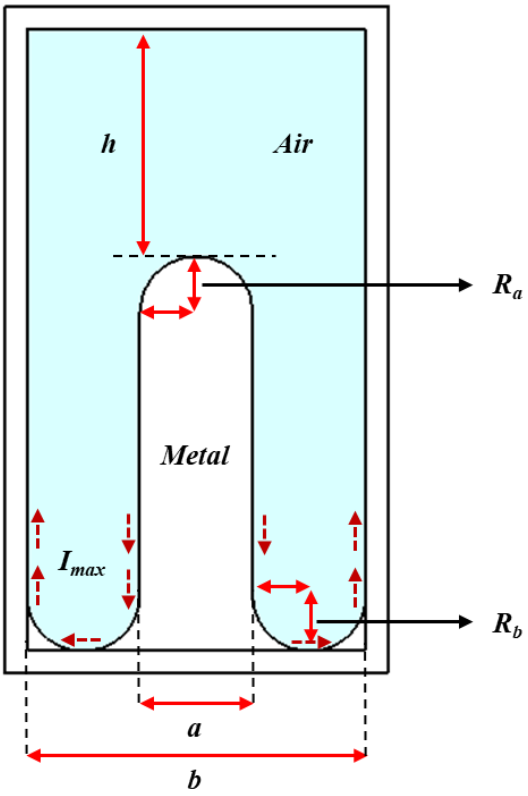

Figure 7.3 Cross section of the coaxial resonator with base rounding. Here, the coaxial resonator is rotationally symmetric.

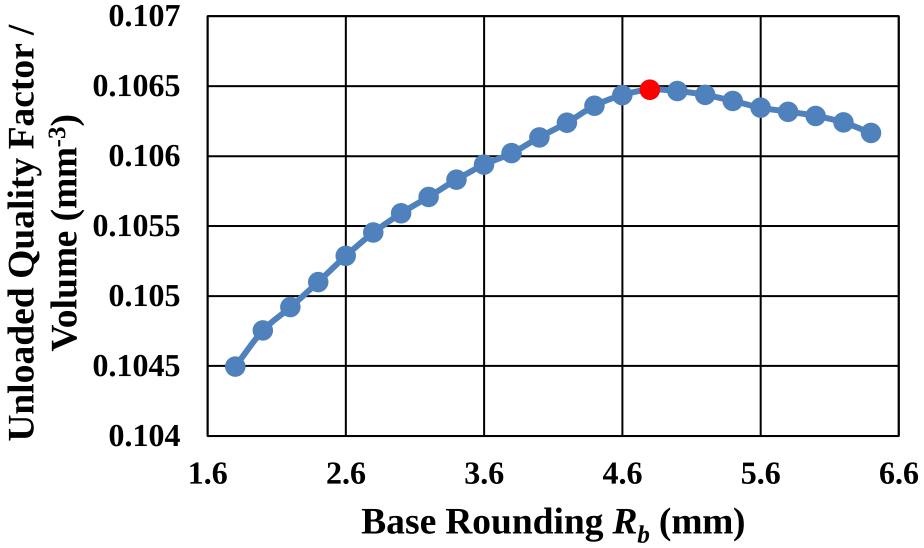

Figure 7.4 Relation between unloaded quality factor per volume and radius of base rounding R_b, considering $b/a = 3.59$.

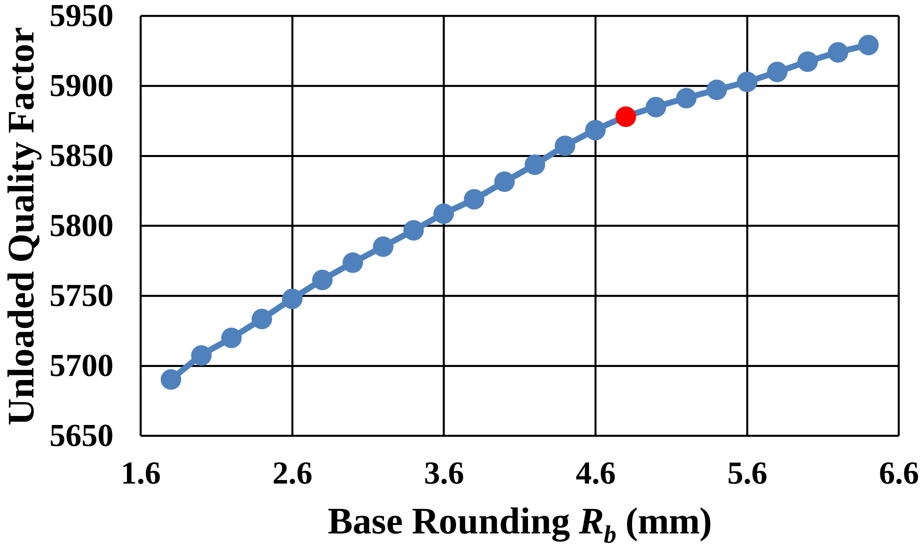

Figure 7.5 Relation between unloaded quality and radius of base rounding R_b, considering $b/a = 3.59$.

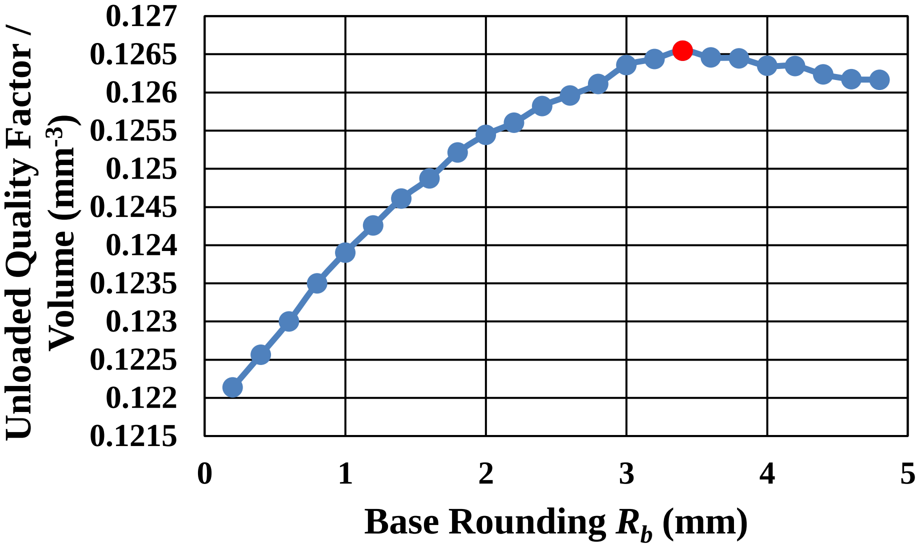

Figure 7.6 Relation between unloaded quality factor per volume and radius of base rounding R_b, considering *b*/*a* = 3.

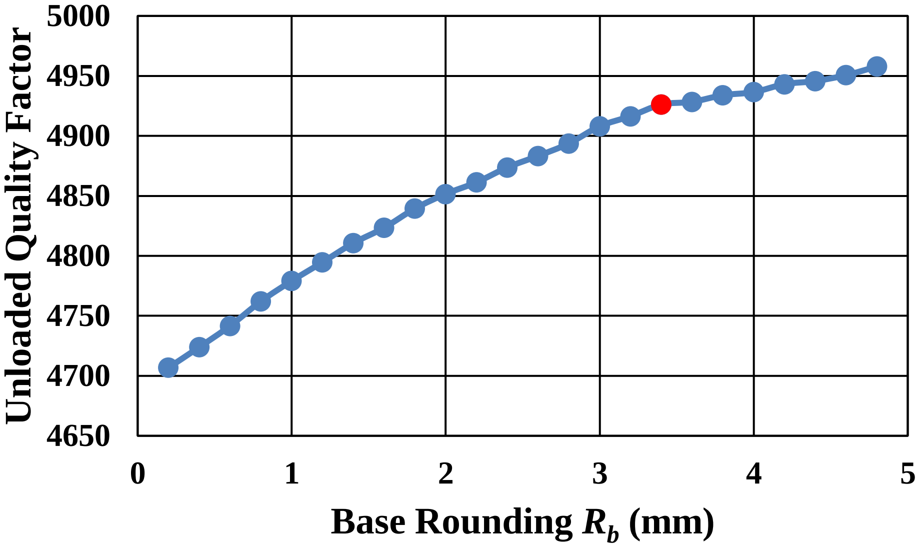

Figure 7.7 Relation between unloaded quality factor and radius of base rounding R_b, considering *b*/*a* = 3.

7.2.3 Extraction of External Quality Factor

The input/output coupling of the hybrid coaxial bandpass filter is realized with the use of PCB lines attached to SMA connectors. Figure 7.8 shows the structure of resonator used to extract external quality factor, with figure 7.8 (a) showing internal structure of the resonator and figure 7.8 (b) showing PCB layout. The PCB is placed just above the centre conductor of coaxial resonator (0.9 mm), here the PCB doesn't have ground. The gap above the PCB is 3 mm, which is denoted by *T* in figure 7.8 (a).

Looking at figure 7.8 (b) the PCB lines are connected to SMA connectors through a wider PCB line, having a width of 1.565 mm and a length of 2.5 mm, which has a characteristic impedance of $Z_0 = 50\ \Omega$. The rest of PCB lines have a width of 0.6 mm. The PCB is RT/duroid 5880 with dielectric thickness of 508 µm, dielectric constant of 2.2, dielectric loss tangent of 0.0009 and copper thickness of 18 µm [15]. By simulating the structure in CST [12], S_{21} can be obtained as shown in figure 7.9. The value of the external quality factor Q_e then can be calculated by using the simulated S_{21} and the formula, shown in figure 7.9.

The value of external quality factor can be controlled by adjusting rotation angle of PCB line, denoted by *E* in figure 7.8 (b). By adjusting the rotation angle of PCB line *E*, a relation between external quality factor and rotation angle of PCB line is found as shown in figure 7.10. The rotation angle of PCB line for the required external quality factor of $Q_{e1} = Q_{eN} = 47.77$ is found using the relation in figure 7.10 as $E = 88.32°$, this is denoted by a red dot in figure 7.10.

The length of coaxial resonator *L* is also adjusted during the simulation process to keep the resonance frequency of the resonator at 2 GHz, which is found to be $L = 29.17$ mm when $E = 88.32°$.

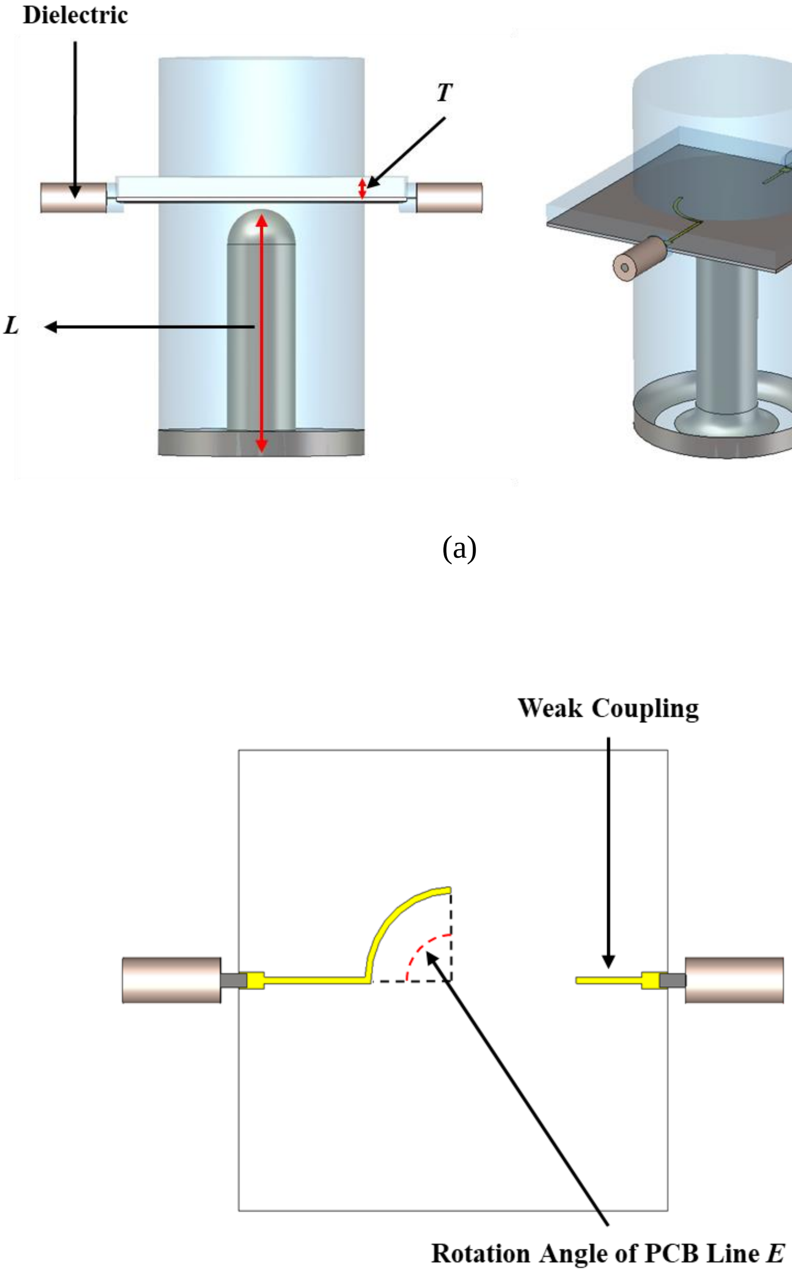

(a)

(b)

Figure 7.8 The structure of resonator used to extract external quality factor Q_e. (a) Internal structure of the resonator. (b) PCB layout.

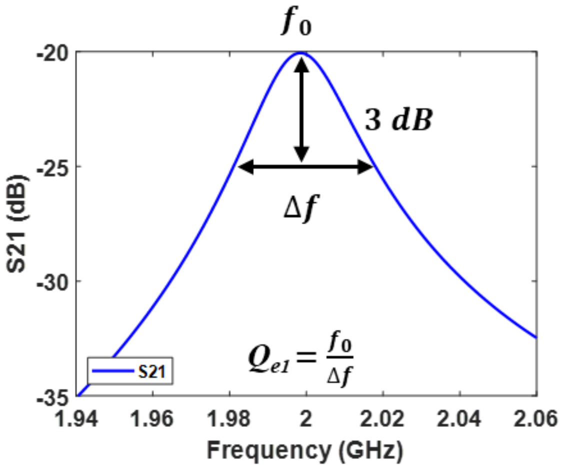

Figure 7.9 Simulated S_{21} of the structure shown in figure 7.8.

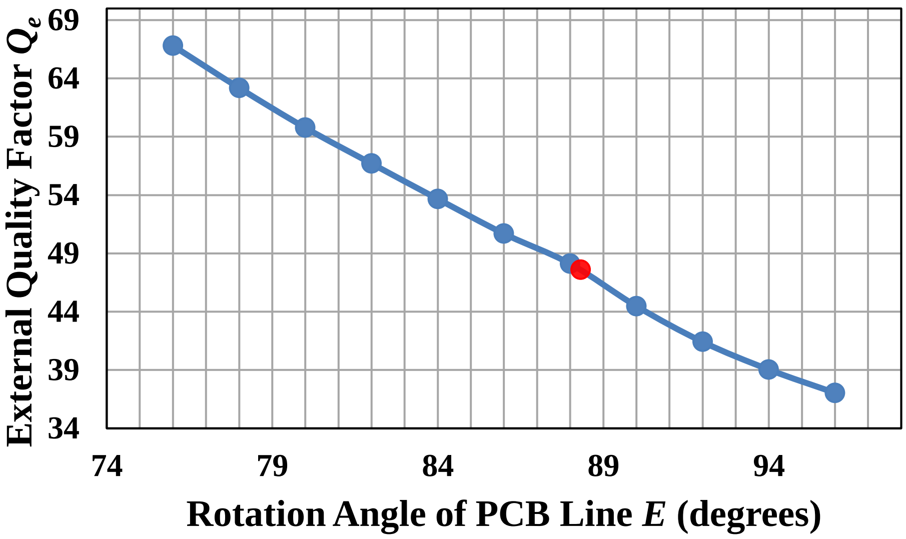

Figure 7.10 Relation between external quality factor Q_e and rotation angle of PCB line E.

7.2.4 Extraction of Inter Resonator Couplings

The couplings between resonators of the hybrid coaxial bandpass filter are realized with the use of PCB lines. Figure 7.11 shows the structure of the model used to calculate the inter resonator couplings, with figure 7.11 (a) showing internal structure of the model and figure 7.11 (b) showing PCB layout. The coupling between resonators is controlled by adjusting the rotation angle of PCB line, denoted by D in figure 7.11 (b). The coupling between two resonators is calculated by using the centre frequency of resonators (f_1 and f_2) of the simulated S_{21} and the formula, shown in figure 7.12. Here, the simulation was carried out in CST [12].

Figure 7.13 shows the relation between inter resonator coupling coefficient and the rotation angle of PCB line D. Using the relation, the rotation angle of PCB line corresponding to the required coupling coefficients $M_{12} = M_{34} = 0.017364$ and $M_{23} = 0.01541$, are found as $D_1 = D_3 = 89.27°$ and $D_2 = 81.71°$, which are denoted by red and black dots in figure 7.13.

To calculate the cross coupling between resonators 1 and 4, the structure shown in figure 7.14 is used, with figure 7.14 (a) showing internal structure of the model and figure 7.14 (b) showing PCB layout. Referring to the table 7.6, the value of coupling coefficient M_{14} is negative, which is a capacitive coupling. The cross coupling between resonators 1 and 4 is controlled by adjusting the capacitive gap, denoted by T in figure 7.14 (a). Here, the final size of PCB is used, because the capacitive gap goes across the middle of the filter.

Figure 7.15 shows the simulated S_{21} of the structure shown in figure 7.14, and the formula to calculate the value of the cross coupling. By adjusting the capacitive gap T, the relation between cross coupling coefficient and the capacitive gap can be found, as shown in figure 7.16. The capacitive gap corresponding to the required cross coupling coefficient $M_{14} = -0.003576$ is found from this relation as $T = 5$ mm, this is denoted by a red dot in figure 7.16.

During the simulation process the length of coaxial resonators is adjusted to keep the resonance frequency of the model at 2 GHz. The length of resonators found as $L_1 = L_4 = 28.86$ mm and $L_2 = L_3 = 28.91$ mm.

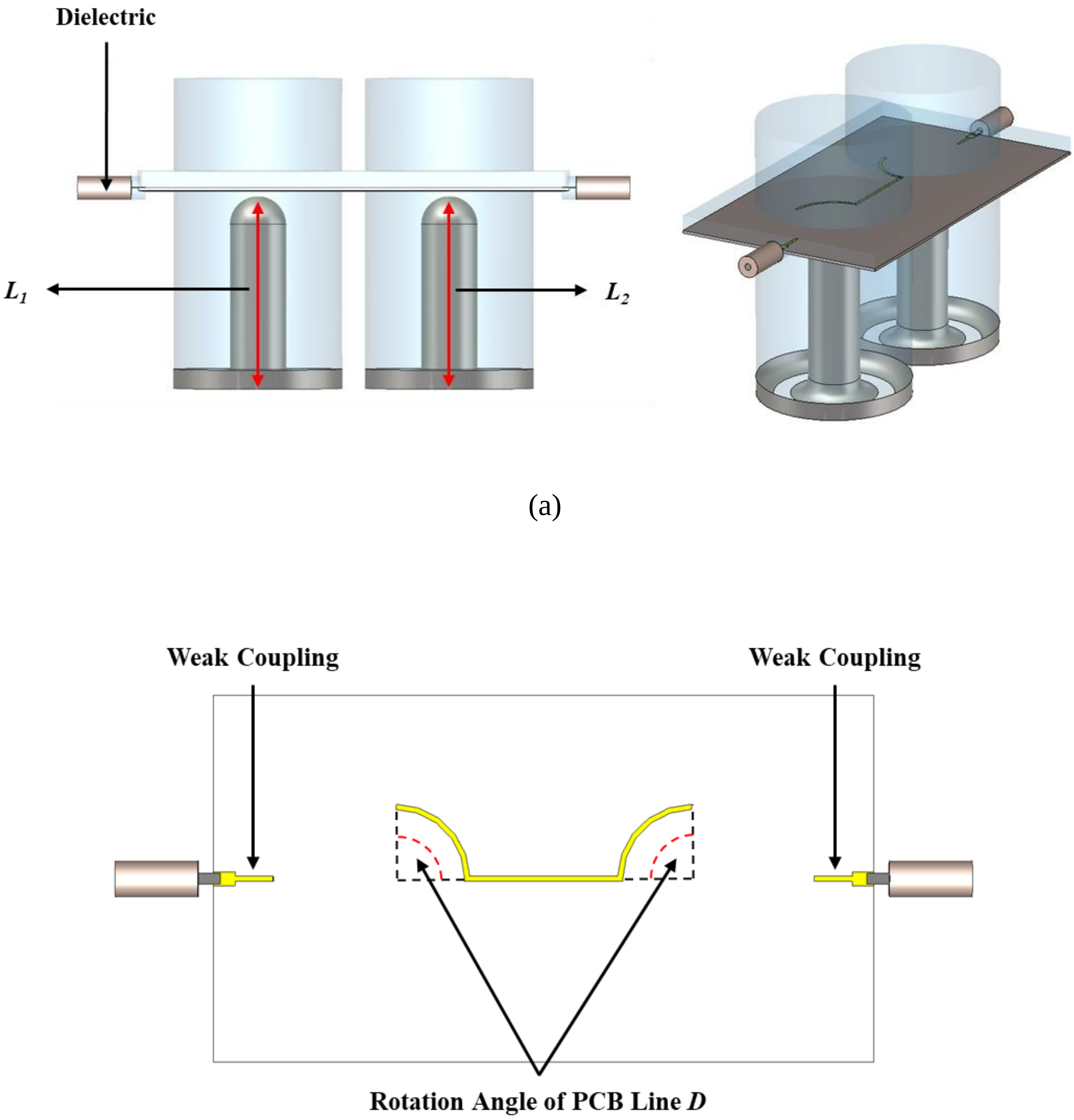

(a)

(b)

Figure 7.11 The structure of the model used to extract inter resonator couplings. (a) Internal structure of the model. (b) PCB layout.

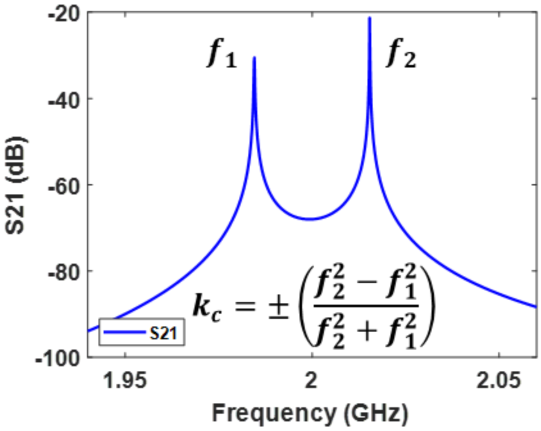

Figure 7.12 Simulated S_{21} of the structure shown in figure 7.11.

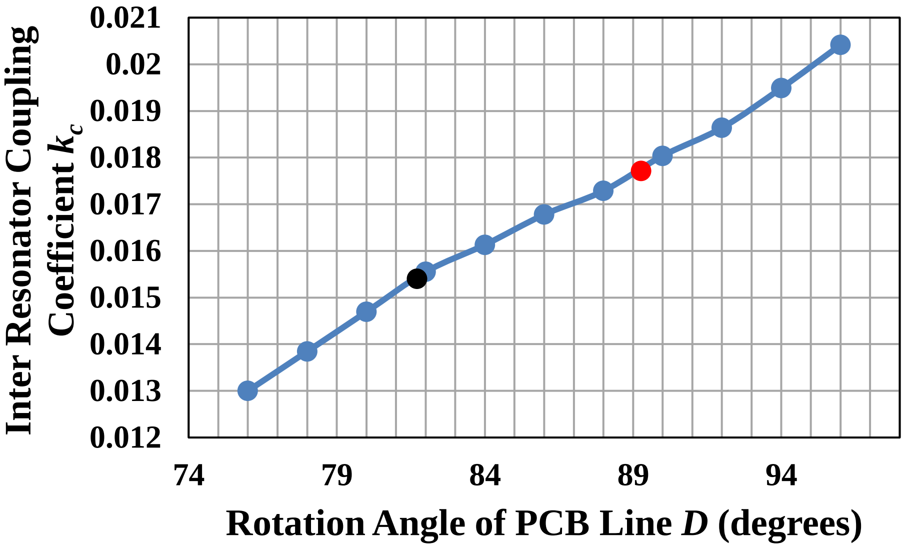

Figure 7.13 Relation between inter resonator coupling coefficient k_c and rotation angle of PCB line *D*.

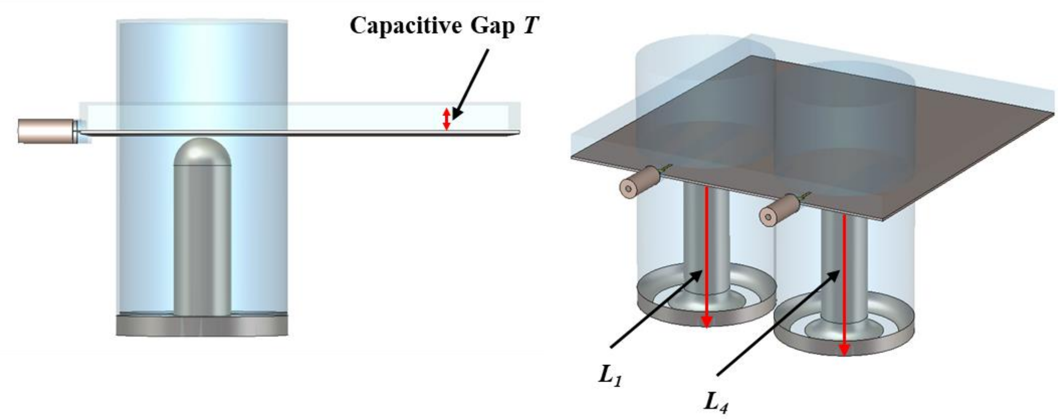

(a)

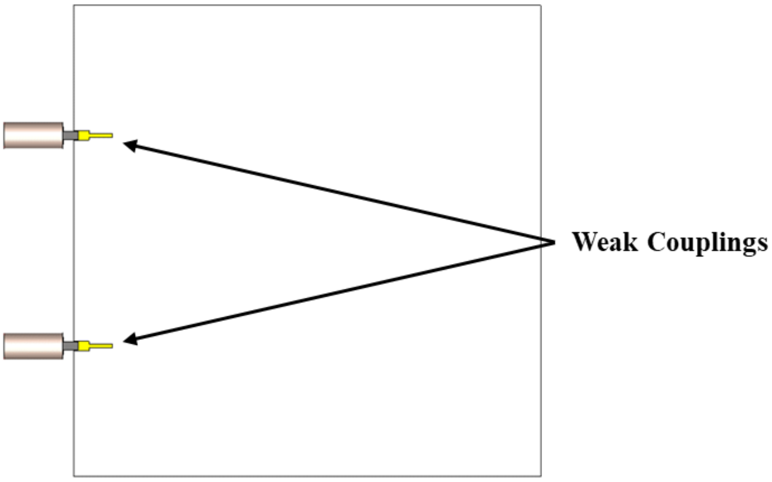

(b)

Figure 7.14 The structure of the model used to extract cross coupling. (a) Internal structure of the model. (b) PCB layout.

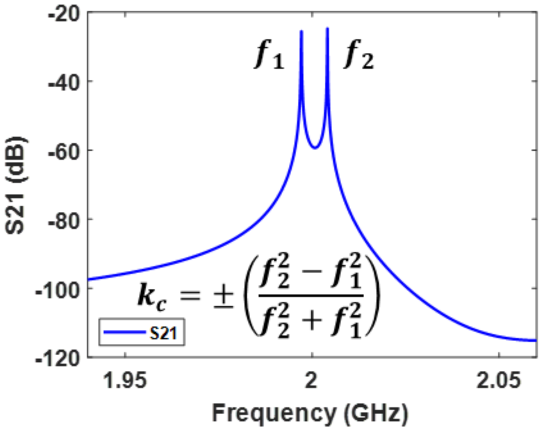

Figure 7.15 Simulated *S21* of the structure shown in figure 7.14.

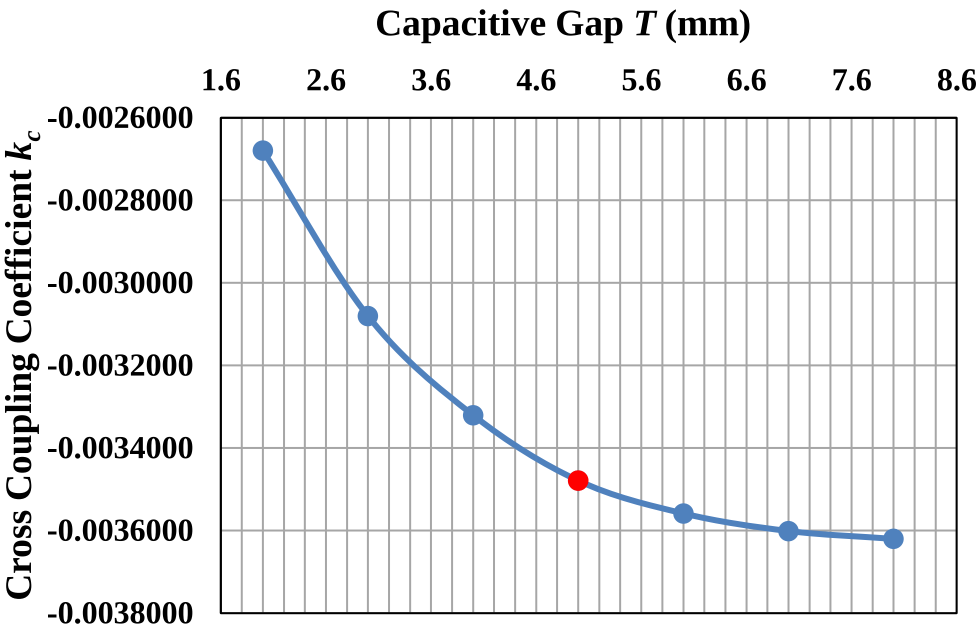

Figure 7.16 Relation between cross coupling coefficient k_c and capacitive gap *T*.

7.2.5 Final Physical Design of the Filter

After obtaining all physical dimensions of the hybrid coaxial bandpass filter, all resonators were connected to each other in a folded form to complete the filter. Figure 7.17 (a) shows internal structure of the filter and figure 7.17 (b) shows PCB layout of the filter. The filter was then simulated in CST [12] in order to find initial response before optimisation. Figure 7.18 shows this simulated response of the filter before optimisation in comparison with the ideal response. The initial dimensions of the filter are then optimised by CST [12] to obtain a better response, close to the ideal response.

During the optimisation process, optimisation goals are set to be: S_{11} under -20 dB for frequency range of 1.98 GHz to 2.02 GHz, S_{11} more than -20 dB for frequency range of 1.9 GHz to 1.98 GHz, S_{11} more than -20 dB for frequency range of 2.02 GHz to 2.1 GHz, S_{21} under -50 dB at frequency of 1.96 GHz and S_{21} under -50 dB at frequency of 2.04 GHz. Figure 7.19 shows the response of the filter after optimisation process in comparison with the response before optimisation. The internal dimensions of the filter after optimisation are provided in figure 7.17 (a) and the dimensions of PCB layout are given in figure 7.17 (b).

The external design of the hybrid coaxial bandpass filter is shown in figure 7.20, where all external dimensions are provided. As it can be seen, the filter consists of three pieces; the bottom part, the PCB, and the top part which can be bolted to the bottom part with the PCB in between.

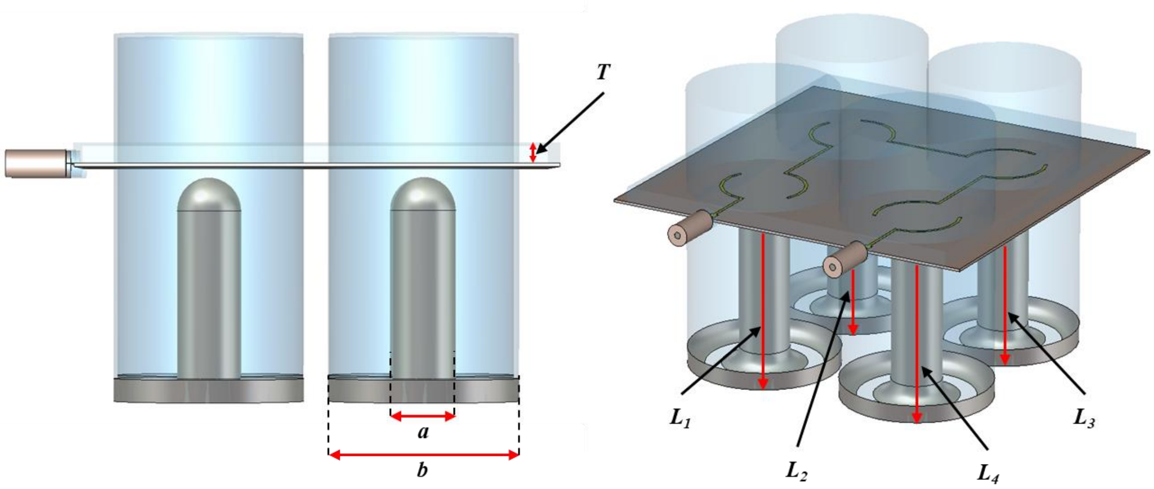

(a)

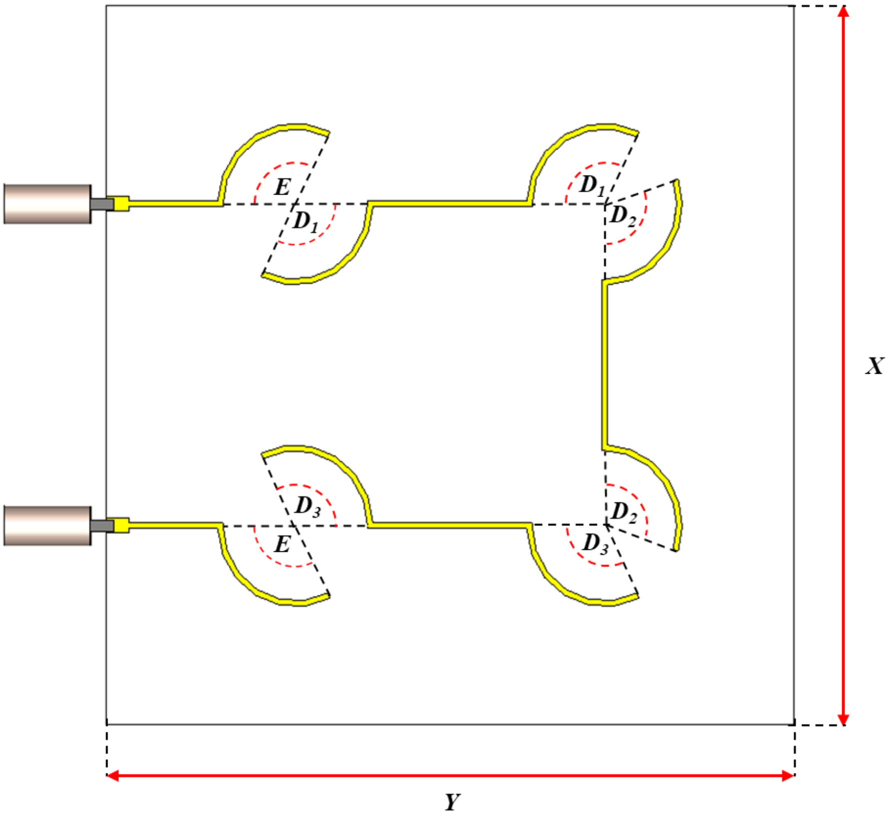

(b)

Figure 7.17 Internal structure of the 2 GHz hybrid coaxial bandpass filter, showing internal dimensions. (a) Internal structure of the filter. The dimensions after optimisation in millimetres are: $a = 10$, $b = 30$, $T = 3$, $L_1 = L_4 = 28.54$ and $L_2 = L_3 = 28.62$. (b) PCB layout of the filter. The dimensions of PCB in millimetres and the rotation angle of PCB lines in degrees are: $X = 76$, $Y = 75.6$, $E = 116.58°$, $D_1 = D_3 = 116.38°$ and $D_2 = 108.29°$.

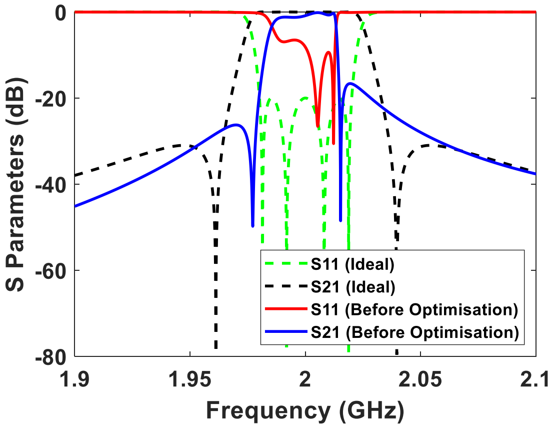

Figure 7.18 Simulated response of the 2 GHz hybrid coaxial bandpass filter before optimisation in comparison with the ideal response.

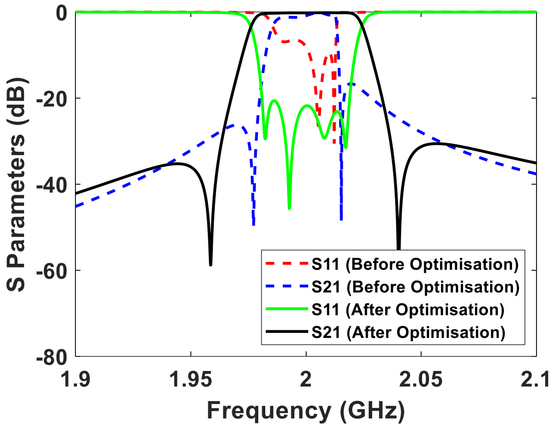

Figure 7.19 Comparison between simulated response of the 2 GHz hybrid coaxial bandpass filter before optimisation and after optimisation.

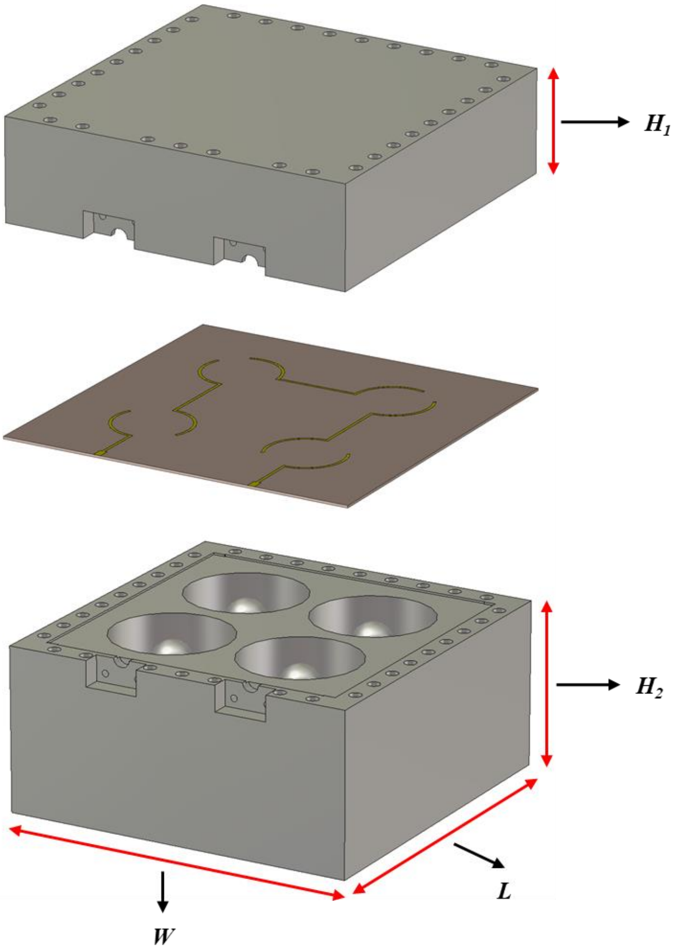

Figure 7.20 External design of the 2 GHz hybrid coaxial bandpass filter, showing external dimensions. The dimensions in millimetres are: H_1 = 25.61, H_2 = 41.69, L = 88.28 and W = 88.28.

7.3 Fabrication Process

The filter presented in this chapter was fabricated using stereolithography apparatus (SLA) process, however the PCB was fabricated separately using a conventional PCB manufacturing technique. The printing resolution in the SLA process was 0.1 mm and the printing material used in the process was Accura Xtreme White 200 resin, which offers high strength, stiffness and durability [16].

The filter was fabricated layer by layer, where each layer was built by scanning an ultraviolet laser beam across the surface of polymer resin, details of SLA process was provided in chapter 3. The filter was subsequently coated with a 20 µm thick copper layer after it was 3-D printed. The 20 µm thick copper layer was compensated from the 3-D model of the filter prior to printing process. A commercial electroless metal plating process was employed to coat the surface of the filter with a seed layer, and the filter was then electroplated with copper [17]. Here, the thickness of copper layer chosen to be much larger than five times the skin depth in order to achieve a low microwave loss as explained in section 3.7 (chapter 3). Note that the skin depth at 2 GHz is calculated to be 1.458 µm, using equation (3.2) for copper with electrical conductivity of 5.96×10^7 S/m. During the fabrication process the supporting material used was only on the outer base of the parts. The supporting material was built from the same polymer material that used to build the parts and was removed during post processing. The entire fabrication process was done by 3DDC Ltd [16].

Figure 7.21 (a) shows a photograph of the fabricated filter after being copper plated and assembled, where the PCB is placed between top part and bottom part. The position of the PCB on the bottom part is shown in figure 7.21 (b), where both SMA connectors are soldered to the PCB. Figure 7.21 (c) shows the top and bottom parts of the filter individually, and figure 7.21 (d) shows the fabricated PCB before being soldered to SMA connectors. Both top and bottom parts of the filter are assembled using thirty-four nuts and bolts, where the PCB is placed in between, as shown in figure 7.21 (a). The connectors are both straight 50 Ω female flange mount SMA connectors with a solderable termination connected to the centre conductor, where the centre conductor is surrounded by a dielectric with dielectric constant of 2.1. Both connectors are soldered to the PCB and bolted onto the filter walls.

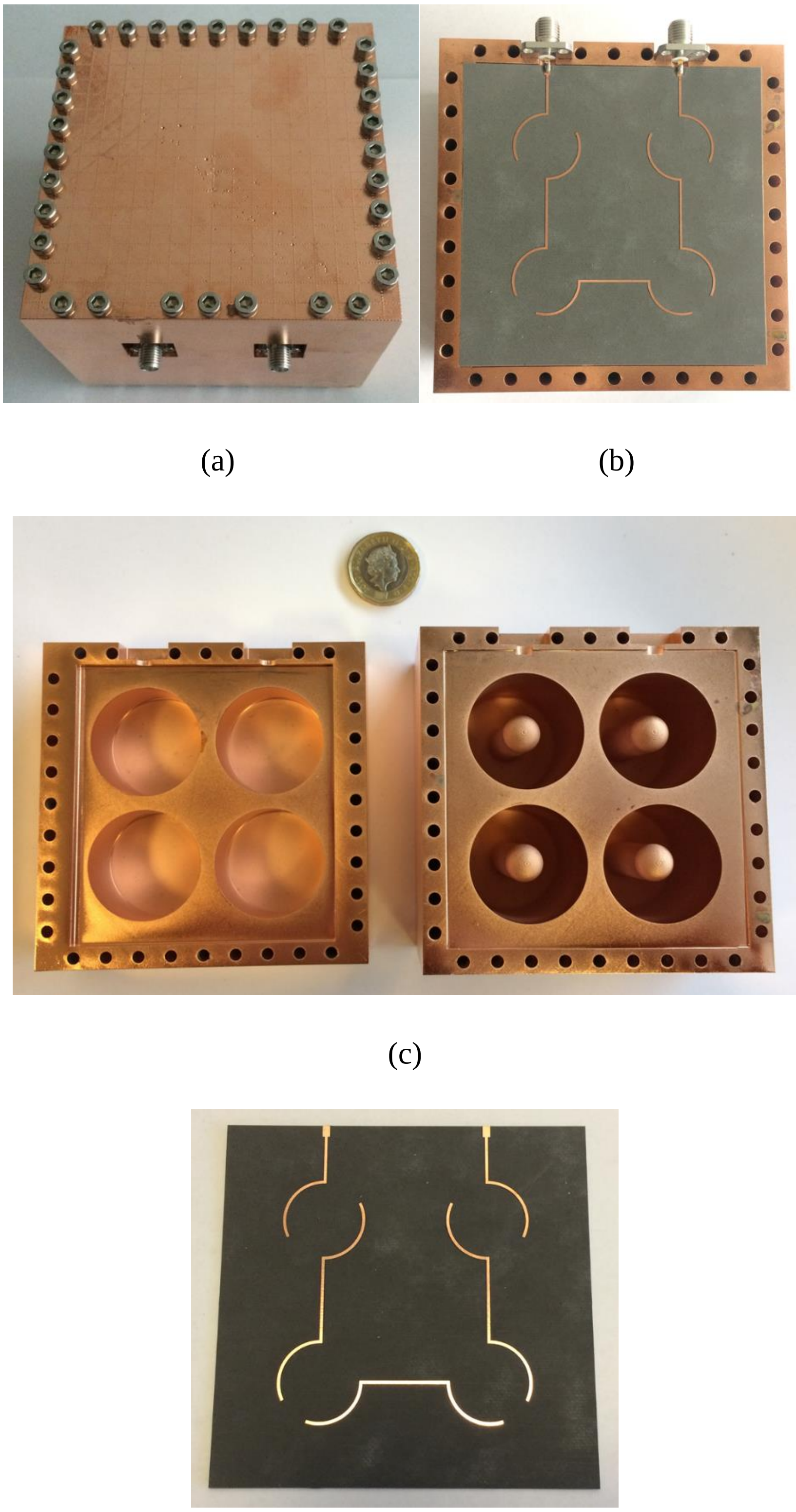

(a) (b)

(c)

(d)

Figure 7.21 Photograph of the fabricated 2 GHz hybrid coaxial bandpass filter after being copper plated. (a) Fabricated filter with all parts assembled together using nuts and bolts. (b) Position of the PCB on the bottom part. (c) Top and bottom parts of the filter. (d) Fabricated PCB.

7.4 Measurement and Discussion

The *S* parameter measurements of the hybrid coaxial bandpass filter were performed on an Agilent E8362C PNA network analyser. The network analyser was calibrated using SOLT (Short, Open, Load, Thru) method prior to the measurements. Figure 7.22 shows a photograph of the measurement setup, where the filter is placed between two probes of the network analyser. The measured and simulated results of the hybrid coaxial bandpass filter are shown in figure 7.23. Here, the measured results are denoted with solid lines and simulated results with dashed lines.

Looking at the *S* parameter results in figure 7.23, the measured results have good agreement with simulated results. The *S* parameter results in figure 7.23 (a) shows that the measured centre frequency is shifted up only by 2 MHz (0.1% of the simulated centre frequency) and the minimum return loss is about 22.55 dB, which are close to the designed specifications. The 2 MHz frequency shift is caused by dimensional inaccuracies and it is believed to be caused by final UV curing. The frequency shift can be corrected by remanufacturing the filter; however, the frequency shift is very small.

The expanded view of S_{21} in figure 7.23 (b) shows a minimum insertion loss of around 0.47 dB over the passband, which is 0.05 dB higher than the simulated results. As mentioned in section 4.5 (chapter 4), the typical surface roughness values of these SLA structures are generally about 1 µm [18]. This reduces the effective conductivity of copper to 3.17×10^7 S/m (here the effective conductivity is calculated using equations (3.3) and (3.4)). According to calculation in CST [12], this results in additional loss of 0.05 dB, however this loss is already reflected in the simulated results of the filter. The 20 dB return loss also contributes about 0.04 dB to the insertion loss which is also taken into account.

The small additional difference between measured insertion loss and simulated insertion loss is believed to be caused by a combination of factors, including: losses in connectors, contamination of the copper surface, impurities in the copper, different surface roughness, losses in PCB lines and radiation loss at the interference between joints.

Figure 7.24 shows measured and simulated S_{21} over a wide frequency range of 1 – 7 GHz. Generally, coaxial filters have good spurious free performance compare to other type of filters, and the coaxial filter in chapter 4 has proved this, which had a spurious free window of about 10 GHz. However, the coaxial filter presented here hasn’t got a good spurious free performance, this is because the PCB lines act as resonators. The length of PCB lines that couple resonators 1 and 2, and resonators 3 and 4 is 51.02 mm each, the length of PCB line that couple resonators 2 and 3 is 48.63 mm, and the length of PCB lines that couple first and last resonators to the source and load is 26.83 mm. If we assume the PCB lines act like half wavelength resonators in free space, their resonance frequencies can be estimated. The resonance frequency of PCB lines that couple resonators 1 and 2, and resonators 3 and 4 is estimated as 2.9 GHz, the resonance frequency of PCB line that couple resonators 2 and 3 is estimated as 3 GHz, and the resonance frequency of PCB lines that couple first and last resonators to the source and load is estimated as 5.6 GHz. These estimations show that the length of PCB lines is probably the main cause of poor spurious free performance of the filter. In order to achieve a better spurious free performance, the length of PCB lines could be design shorter by reducing the wall thickness between the resonators, this could be implemented in future work.

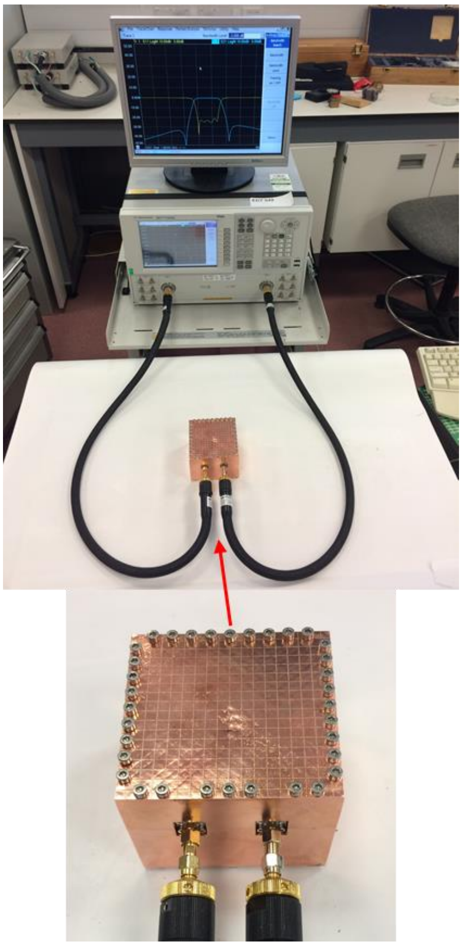

Figure 7.22 Photograph of the measurement setup with the 2 GHz hybrid coaxial bandpass filter placed between two probes of the network analyser.

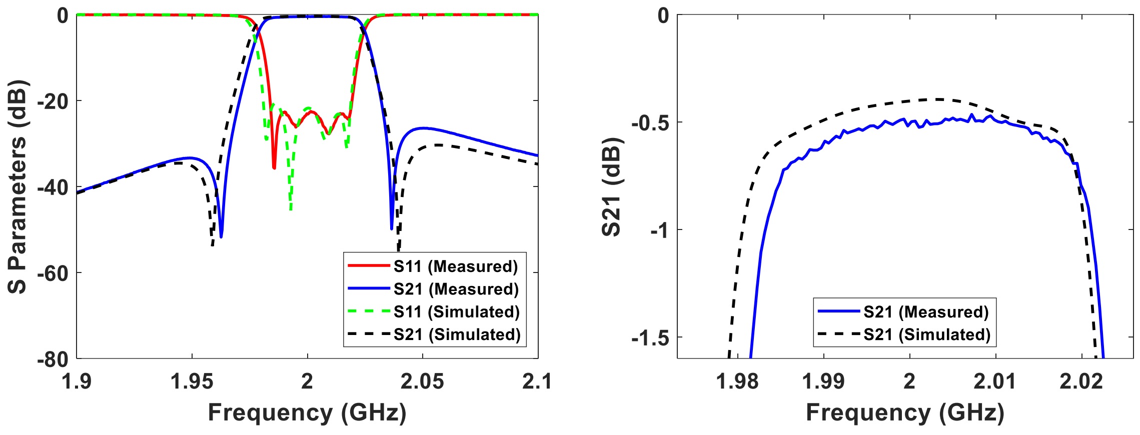

(a) (b)

Figure 7.23 Measured and simulated results of the 2 GHz hybrid coaxial bandpass filter. (a) Measured and simulated results over the frequency range of 1.9 – 2.1 GHz. (b) Expanded view of S_{21} over passband.

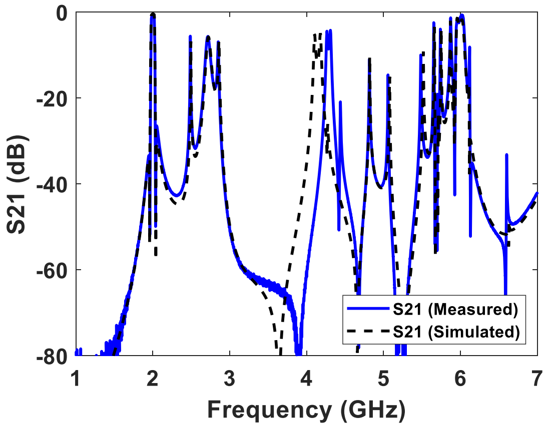

Figure 7.24 Measured and simulated S_{21} over a wide frequency range.

7.5 Conclusion

This chapter presented a fourth-order hybrid coaxial bandpass filter with two symmetrical transmission zeros, where the main-line couplings and input/output coupling are realized using PCB lines, and cross coupling is realized using a capacitive gap. The idea showed that the couplings in a filter can also be achieved using PCB lines, instead of using coupling irises or probes. This will allow different topologies to be designed easily, even a fully canonical filter where direct coupling between source and load is needed.

The filter was designed using coupling matrix theory, where a folded $N+2$ coupling matrix was used, the design procedure was explained in this chapter. The filter was fabricated using stereolithography 3-D printing process, and the fabrication details were provided in this chapter. A good agreement between the measured and simulated results demonstrated the accuracy of the fabrication process.

References

[1] R. Mansour, “Filter technologies for wireless base stations,” *IEEE Microwave Magazine*, vol. 5, no. 1, pp. 68–74, Mar. 2004.

[2] C. Kudsia, R. Cameron, and W.-C. Tang, “Innovations in microwave filters and multiplexing networks for communications satellite systems,” *IEEE Transactions on Microwave Theory and Techniques*, vol. 40, no. 6, pp. 1133–1149, June. 1992.

[3] Y. Wang and M. Yu, “True Inline Cross-Coupled Coaxial Cavity Filters,” *IEEE Transactions on Microwave Theory and Techniques*, vol. 57, no. 12, pp. 2958–2965, Dec. 2009.

[4] M. Hoft and F. Yousif, “Orthogonal Coaxial Cavity Filters With Distributed Cross-Coupling,” *IEEE Microwave and Wireless Components Letters*, vol. 21, no. 10, pp. 519–521, Oct. 2011.

[5] X. Wang, G. Jang, B. Lee, and N. Park, “Compact Quad-Mode Bandpass Filter Using Modified Coaxial Cavity Resonator With Improved Q-Factor,” *IEEE Transactions on Microwave Theory and Techniques*, vol. 63, no. 3, pp. 965–975, Mar. 2015.

[6] M. Yuceer, “A Reconfigurable Microwave Combline Filter,” *IEEE Transactions on Circuits and Systems II: Express Briefs*, vol. 63, no. 1, pp. 84–88, Jan. 2016.

[7] J. Zhan, X. Chen, and L. Gong, “A realization of convenient structure with electrical coupling in coaxial cavity,” *IET International Radar Conference 2013*, Xian, China, 2013, pp. 1-4.

[8] M. Hoft, "Tunable Capacitive Coupling for Cavity Resonator Filters," *2009 German Microwave Conference,* Munich, Germany, 2009, pp. 1-4.

[9] V. K. Dad and S. Gupta, "Novel High Q Coaxial Resonator Filter for Millimeter Wave Application," *2017 IEEE MTT-S International Microwave and RF Conference (IMaRC),* Ahmedabad, India, 2017, pp. 1-4.

[10] J.-S. Hong, *Microstrip filters for RF/microwave applications*. Hoboken, NJ: Wiley, 2011.

[11] R. J. Cameron, C. M. Kudsia, and R. R. Mansour, *Microwave filters for communication systems: fundamentals, design, and applications*. Hoboken, NJ, USA: John Wiley & Sons, Inc., 2018.

[12] Computer Simulated Technology (CST). (2017). Microwave Studio. [Online]. Available: http//www.cst.com/.

[13] M. Höft and S. Burger, "Q-factor improvement of combline resonators", German Microwave Conference 2005, Ulm, Germany, 2005, pp. 53-56.

[14] M. Hoft, T. Magath, O. Bartz, and S. Burger, "Corner rounding for increased quality factor of cavity resonators," *2005 Asia-Pacific Microwave Conference Proceedings,* Suzhou, China, 2005, pp. 1-4.

[15] Rogers Corporation. Accessed: June. 15, 2018. [Online]. Available: https://www.rogerscorp.com/.

[16] 3DDC Ltd. Accessed: Nov. 12, 2018. [Online]. Available: https://www.3ddc.eu/.

[17] G. O. Mallory and J. B. Hajdu, *Electroless plating: fundamentals and applications*. Norwich, NY: Knoyes Publications/William Andrew Publishing, 2009.

[18] X. Shang, P. Penchev, C. Guo, M. J. Lancaster, S. Dimov, Y. Dong, M. Favre, M. Billod, and E. D. Rijk, "W-Band Waveguide Filters Fabricated by Laser Micromachining and 3-D Printing," *IEEE Transactions on Microwave Theory and Techniques,* vol. 64, no. 8, pp. 2572–2580, Aug. 2016.

CHAPTER 8: DESIGN OF 300 GHz WAVEGUIDE BANDPASS FILTER AND FABRICATION BY 3-D SCREEN PRINTING

This chapter presents a fifth-order waveguide bandpass filter with two embedded H-plane waveguide bends. The filter design is completed and is going to be fabricated using 3-D screen printing technique. The 3-D screen printing allows such a filter with complex structure to be fabricated accurately using metallic materials. The filter is designed to operate at a centre frequency of 300 GHz, with a bandwidth of 27 GHz (fractional bandwidth of 9%) and a Chebyshev response. The waveguide filter is designed using coupling matrix theory and the design procedure is already explained in chapter 2, here the design of waveguide bends is explained. The project demonstrates the possibility of using 3-D screen printing in fabrication of terahertz components. This project will be done in collaboration with Fraunhofer IFAM Dresden in Germany [1].

8.1 Introduction

As discussed in chapter 3, the process of 3-D screen printing is a new additive manufacturing technique which was introduced by Fraunhofer IFAM Dresden in Germany and it is a modified process based on classical screen-printing technique [1]. The 3-D screen printing is very suitable for fabrication of high frequency components as it enables complex structures to be fabricated accurately, using a variety of metallic materials. Here, for the first time the process is going to be used to fabricate a terahertz filter, which demonstrates the capability of 3-D screen printing for fabrication of terahertz components.

The filter presented in this chapter is a fifth-order waveguide bandpass filter, designed with a centre frequency of 300 GHz, a fractional bandwidth of 9% and a Chebyshev response. In order to achieve a direct and accurate connection with standard UG387/U waveguide flanges of the network analyser, two embedded H-plane waveguide bends are included in the design. The structure of the filter including waveguide bends consists of four layers, where each layer is going to be fabricated separately using 3-D screen printing. The design of the filter is completed; however, it is still in the fabrication stage.

8.2 Design of Waveguide Bandpass Filter and Waveguide Bends

The filter is a terahertz filter operating at a centre frequency of 300 GHz with a bandwidth of 27 GHz (fractional bandwidth of 9%), a return loss of 20 dB and a Chebyshev response. The filter consists of five rectangular cavity resonators operating in the TE_{101} mode, where the resonators are coupled using asymmetrically placed capacitive irises. The advantage of using asymmetrically placed capacitive irises instead of conventional symmetrically placed capacitive irises is that they offer bigger gap, as reported in [2]. Having a bigger gap is much preferred for high frequency filters, because it is much easier to fabricate. The waveguide filter presented here is designed using coupling matrix theory [3, 4]. The design and physical realization of the waveguide filter was explained in section 2.6 (chapter 2). Figure 8.1 shows internal structure of the designed 300 GHz waveguide bandpass filter, along with internal dimensions after optimisation. Figure 8.2 shows the optimised response of the filter over the frequency range of 220 – 330 GHz. Note that the ideal response of the filter and simulated response of the filter before optimisation along with the design procedure are provided in section 2.6 (chapter 2). Having the designed waveguide filter, the next step is to design waveguide bends which is going to be explained in the next section.

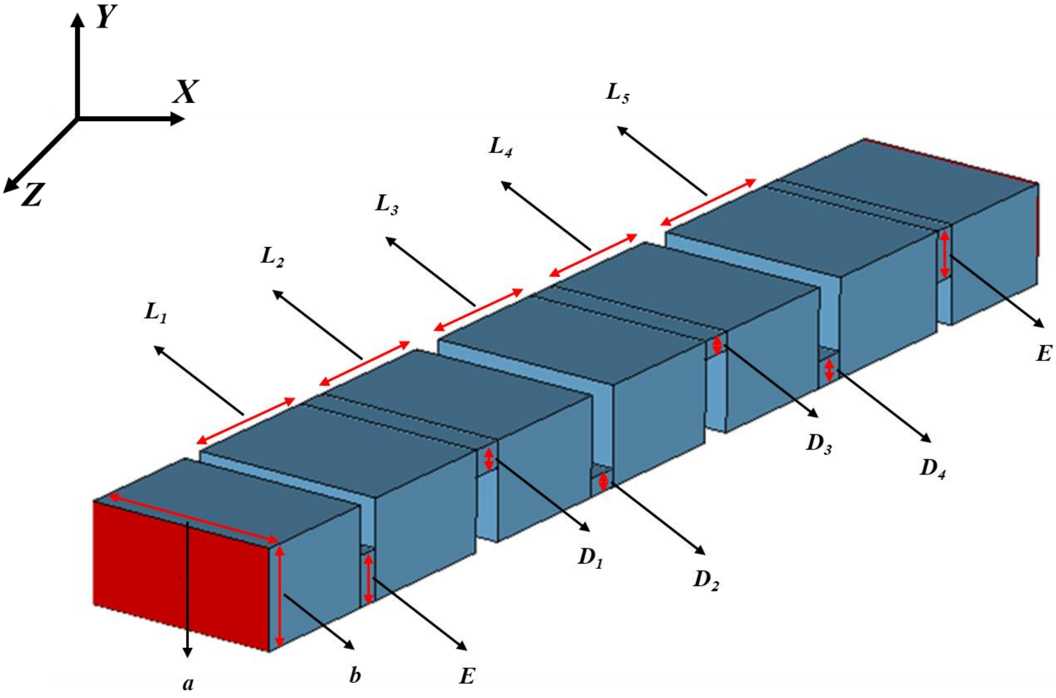

Figure 8.1 Internal structure of the 300 GHz waveguide bandpass filter showing internal dimensions. The dimensions in millimetres are: $L_1 = L_5 = 0.694$, $L_2 = L_4 = 0.644$, $L_3 = 0.639$, $E = 0.258$, $D_1 = D_4 = 0.135$, $D_2 = D_3 = 0.093$, $a = 0.864$ and $b = 0.432$.

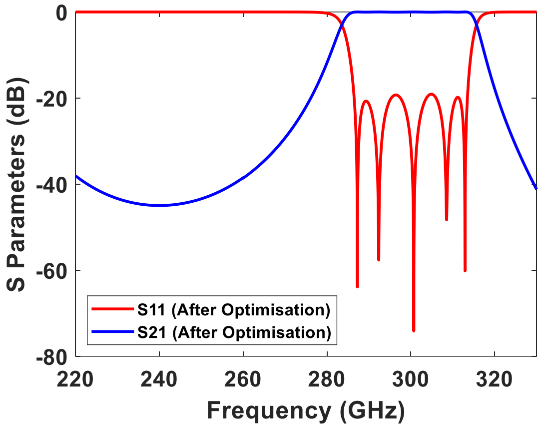

Figure 8.2 Simulated response of the 300 GHz waveguide bandpass filter after optimisation.

8.2.1 Design of Waveguide Bends

In order to achieve an accurate and easy connection between the waveguide filter and standard UG387/U waveguide flanges of the network analyser, two waveguide bends need to be included in the design. Multi-mitred and multi stepped corners are normally used to design a 90° waveguide bend, which is a conventional approach to design a waveguide bend with broadband match [5, 6]. Here, multi-layer waveguide bends are used to facilitate fabrication by 3-D screen printing. As described in chapter 3, in the process of 3-D screen printing, the model structure is divided into layers, where each layer is printed separately using a different screen layout, so the structure of the filter including waveguide bends need to be designed in a multi-layer structural format in order to be fabricated using 3-D screen printing. In this work a novel multi-layer embedded H-plane waveguide bend is designed for the filter, and the waveguide bend is made of three layers with the same layer thickness of 0.432 mm.

Figure 8.3 shows a detailed structure of the H-plane waveguide bend. Such a waveguide bend configuration has been used before and reported in [2], [7], [8] and [9]. To design the waveguide bend, the dimensions are optimised in CST [10] in order to achieve a return loss of 20 dB or better across the frequency range of 240-330 GHz. Figure 8.4 shows simulated response of the designed H-plane waveguide bend. As it can be seen, the simulated results show a return loss of better than 20 dB for frequency range of 240 – 330 GHz. Figure 8.3 provides all optimised dimensions. Matching across the entire WR-3 band (220 – 330 GHz) with return loss of 20 dB or better is also possible by optimising the structure further, as it is done in [9]. However, the waveguide bend in this project is only matched for frequency range of 240-330 GHz, as this frequency range cover the passband of the filter (286.5 – 313.5 GHz). Looking at the simulated response in figure 8.4, the minimum return loss in the passband is 27.16 dB at 313.5 GHz.

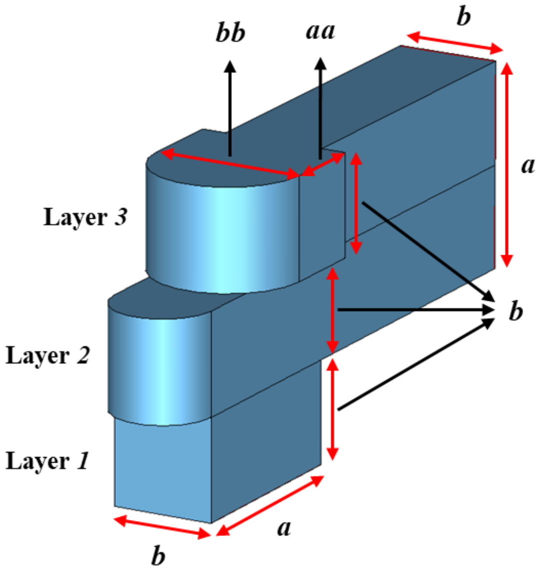

Figure 8.3 Structure of the H-plane waveguide bend, showing the dimensions. The dimensions in millimetres are: a = 0.864, b = 0.432, aa = 0.36 and bb = 0.64.

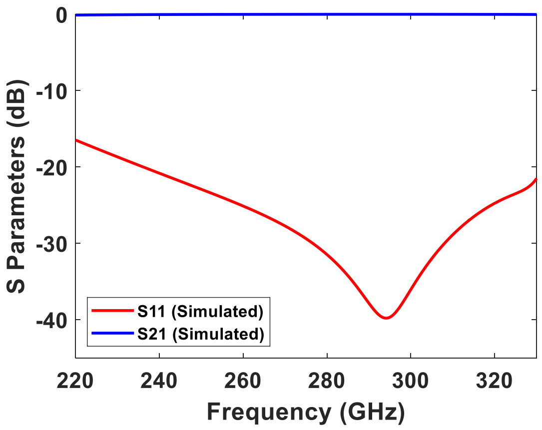

Figure 8.4 Simulated response of the H-plane waveguide bend as shown in figure 8.3.

Figure 8.5 shows structure of a WR-3 waveguide with two back-to back H-plane waveguide bends, which is used to see the simulated response of the designed waveguide bends when embedded in a straight waveguide. Figure 8.6 shows simulated response of the structure shown in figure 8.5. The simulated results show a return loss of better than 15.18 dB for frequency range of 240 – 330 GHz.

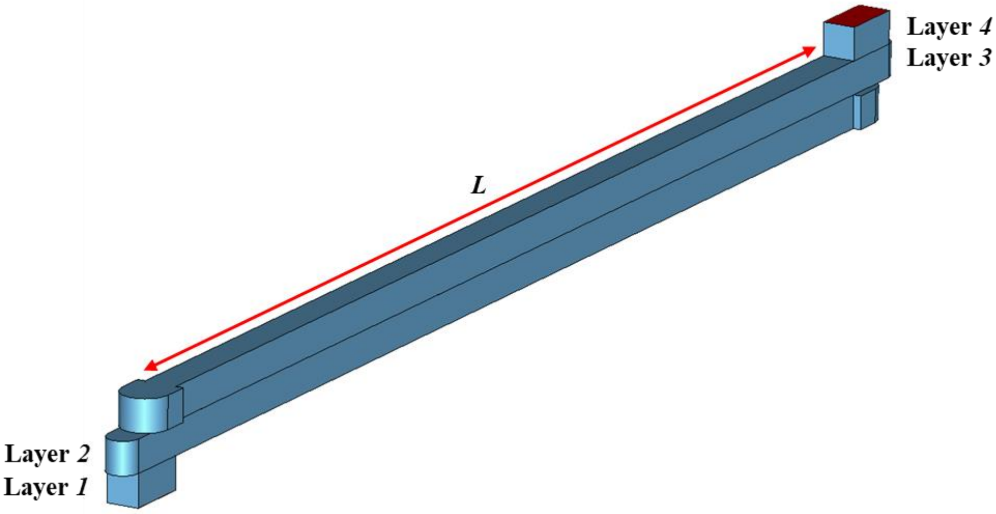

Figure 8.5 Structure of the WR-3 waveguide with two back-to-back H-plane waveguide bends. The length of waveguide is L = 16.087 mm.

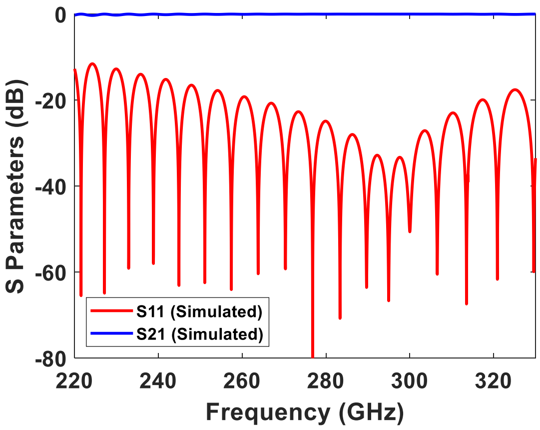

Figure 8.6 Simulated response of the WR-3 waveguide with two back-to-back H-plane waveguide bends as shown in figure 8.5.

8.2.2 Final Physical Design of the Filter

The final step of the design process is to attach the H-plane waveguide bends to the 300 GHz waveguide bandpass filter. Figure 8.7 shows internal structure of the 300 GHz waveguide bandpass filter with embedded H-plane waveguide bends.

The filter is simulated in CST [10] after waveguide bends were added. Figure 8.8 shows simulated response of the filter after adding waveguide bends in comparison with the response before adding waveguide bends. The simulated responses are almost identical with a slight difference in return loss. The dimensions of the filter then further optimised in CST [10] to get a response close to the specification. During optimisation process, optimisation goals are set to be: S_{11} under -20 dB for frequency range of 286.5 GHz to 313.5 GHz, S_{11} more than -20 dB for frequency range of 220 GHz to 286.5 GHz and S_{11} more than -20 dB for frequency range of 313.5 GHz to 330 GHz.

Figure 8.9 shows simulated response of the filter after adding waveguide bends in comparison to the final response after optimisation process. Internal dimensions of the filter after final optimisation are provided in figure 8.7 (a). Figure 8.7 (b) shows all four layers of internal structure, where each layer has a thickness of 0.432 mm.

External design of the 300 GHz waveguide bandpass filter is shown in figure 8.10. Figure 8.10 (a) shows external design of each individual layer and external dimensions. The layers are going to be assembled together using four nuts and bolts, one on each corner. The design also includes standard UG387/U waveguide flange screw holes, alignment pin holes and precision alignment pin holes for both input and output ports as indicated in figure 8.10 (b). This insures accurate connection to the measurement system.

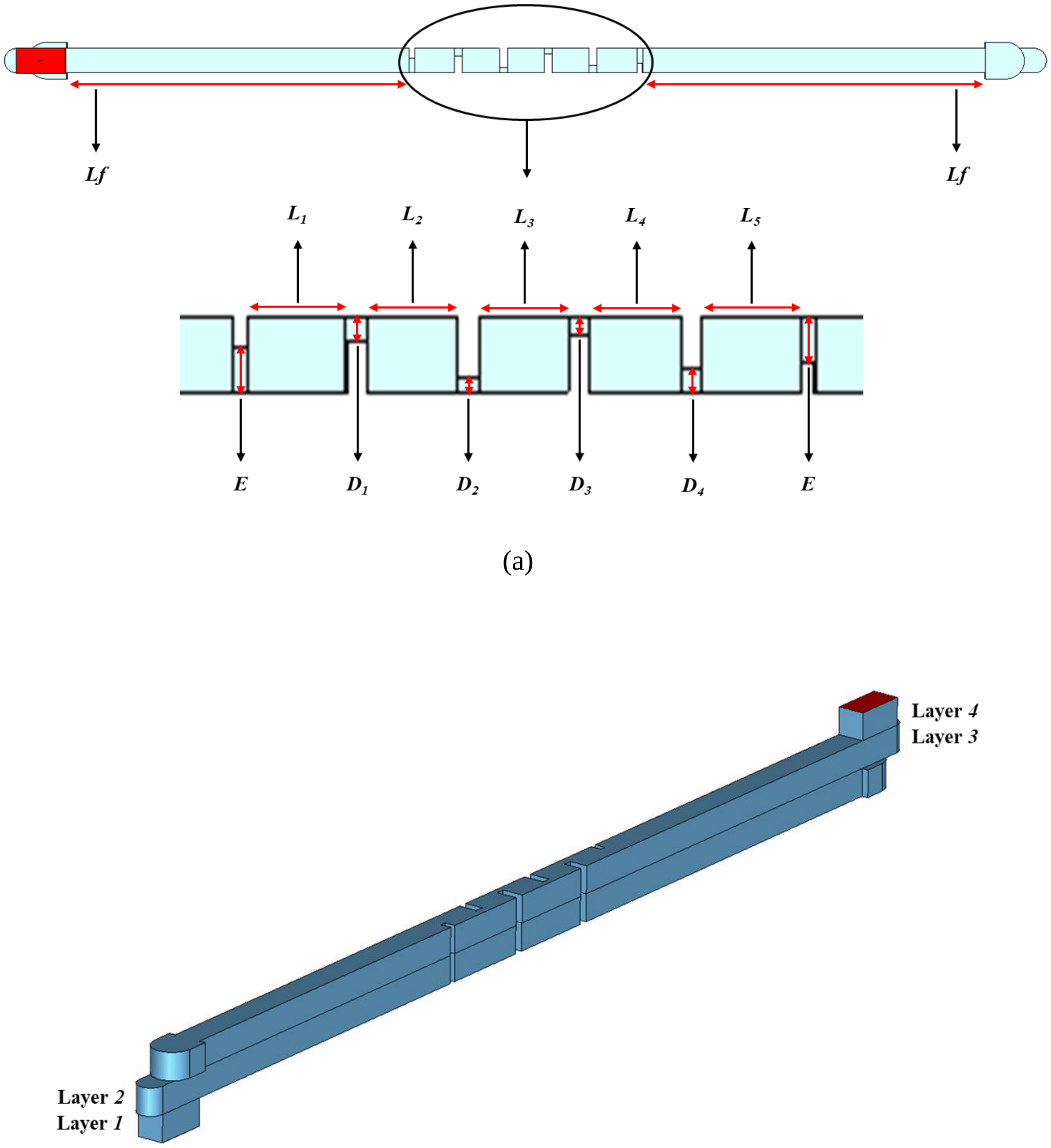

(a)

(b)

Figure 8.7 Internal structure of the 300 GHz waveguide bandpass filter with embedded back-to-back H-plane waveguide bends. (a) Internal structure showing internal dimensions after optimisation. The dimensions in millimetres are: $L_1 = L_5 = 0.696$, $L_2 = L_4 = 0.644$, $L_3 = 0.639$, $E = 0.26$, $D_1 = D_4 = 0.135$, $D_2 = D_3 = 0.094$ and $L_f = 6$. (b) Internal structure showing all four layers.

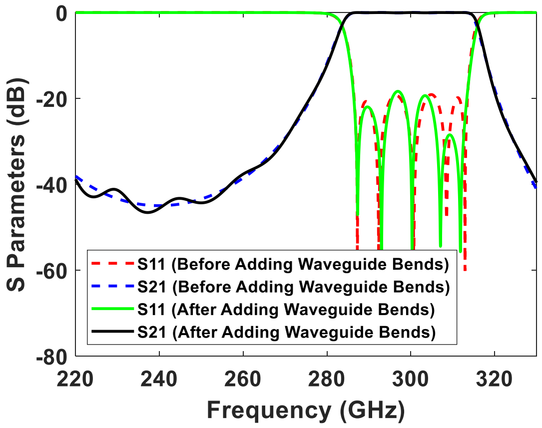

Figure 8.8 Comparison between simulated response of the 300 GHz waveguide bandpass filter before adding waveguide bends and after adding waveguide bends.

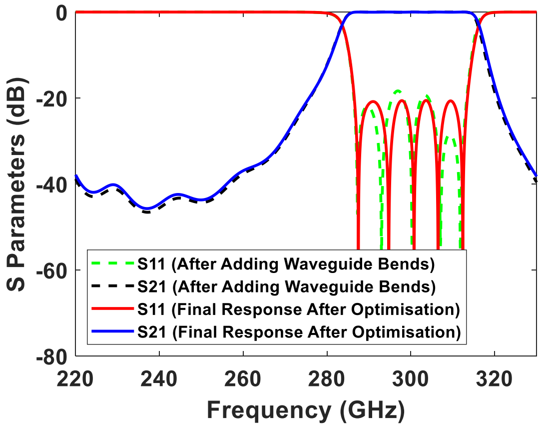

Figure 8.9 Simulated response of the 300 GHz waveguide bandpass filter after adding waveguide bends in comparison to the final response after optimisation.

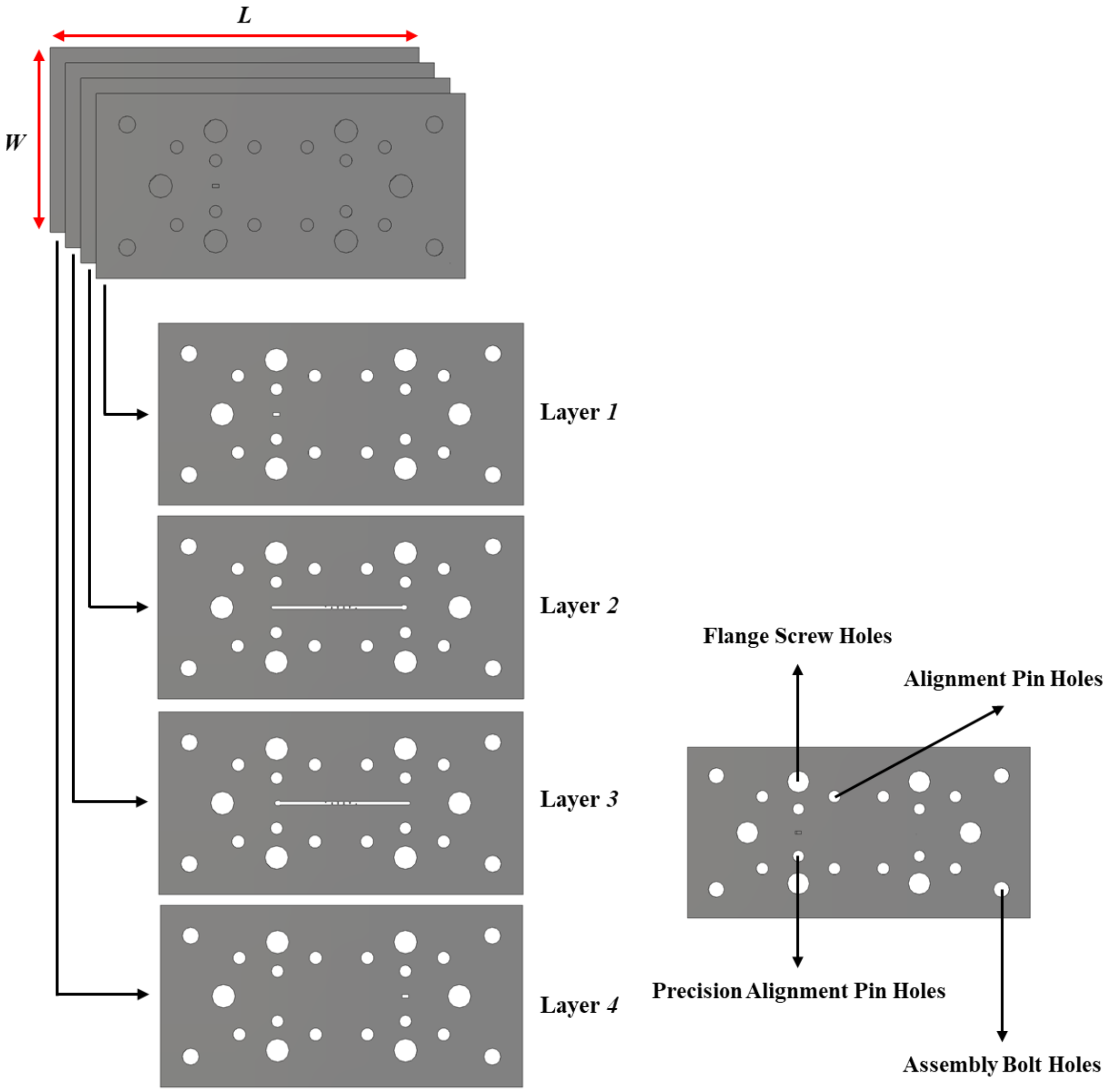

(a) (b)

Figure 8.10 External design of the 300 GHz waveguide bandpass filter. (a) External design, showing all four layers and external dimensions. The dimensions in millimetres are: L = 48 and W = 24. (b) Position of flange screw holes (diameter = 3.048 mm), alignment pin holes (diameter = 1.702 mm), precision alignment pin holes (diameter = 1.6 mm) and assembly bolt holes (diameter = 2.2 mm).

8.3 Discussion and Analysis

As mentioned previously, the 300 GHz waveguide bandpass filter is still in the stage of fabrication. However, the screens are already fabricated by Fraunhofer IFAM Dresden in Germany [1]. Figure 8.11 shows a photograph of the fabricated screens which are going to be used to print the filter. Note, figure 8.11 also provides the zoomed image of screens for each layer of the filter.

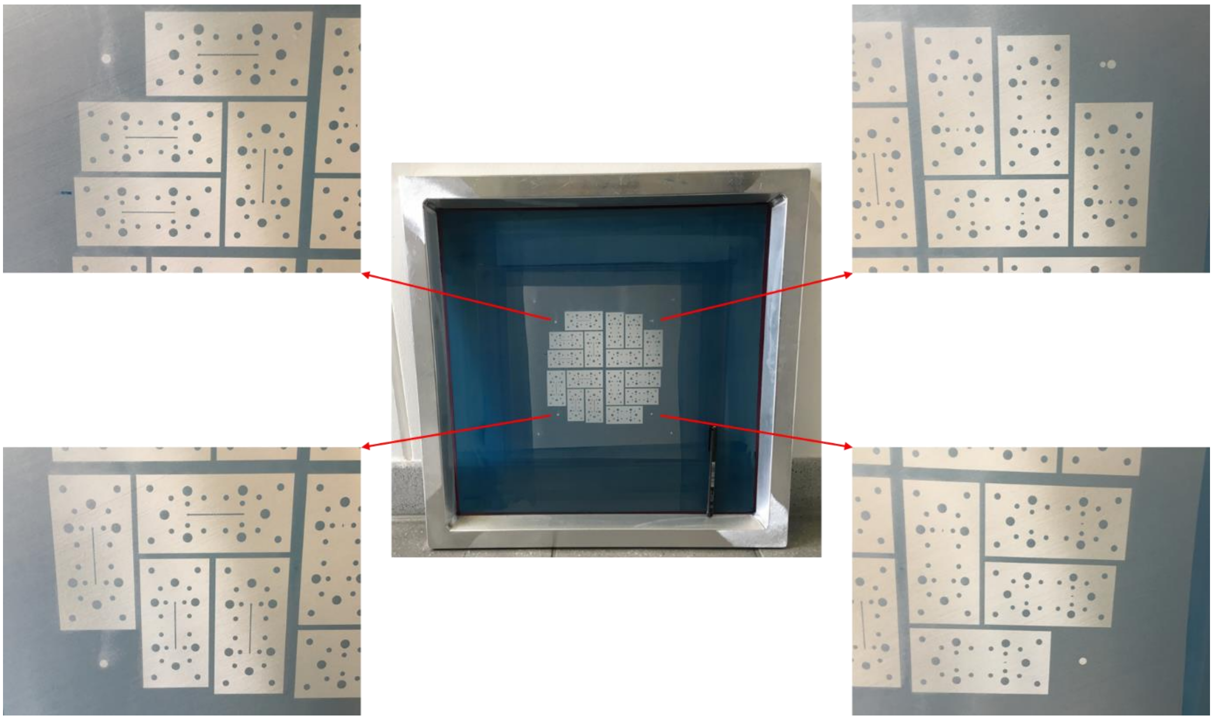

Figure 8.11 Photograph of the fabricated screens.

As the filter is still in the fabrication stage, here the discussion can only be based on simulated results. The discussions below mainly focus on effect of using different materials on insertion loss, dimensional tolerance analysis and effect of waveguide flange misalignment.

The filter is going to be printed using stainless steel material (17-4PH) with electrical conductivity of 1.25×10^7 S/m. However, the filter is simulated in CST [10] using different materials to see the effect on insertion loss. Here, PEC, copper, gold and stainless steel are used for simulations. Figure 8.12 (a) shows simulated response of the filter with PEC, copper, gold and stainless steel over the frequency range of 220 – 330 GHz.

Looking at the expanded view of S_{21} over passband in figure 8.12 (b), it can be seen that the average insertion loss is about 0.41 dB, when using copper with electrical conductivity of 5.96×10^7 S/m, the average insertion loss increases to 0.49 dB, when gold is used with electrical conductivity of 4.1×10^7 S/m, and the average insertion loss will increase further to 0.88 dB when stainless steel is used. Of course, the insertion loss is zero for a perfect electric conductor (PEC), and only the passband ripple of about 0.04 dB can be seen.

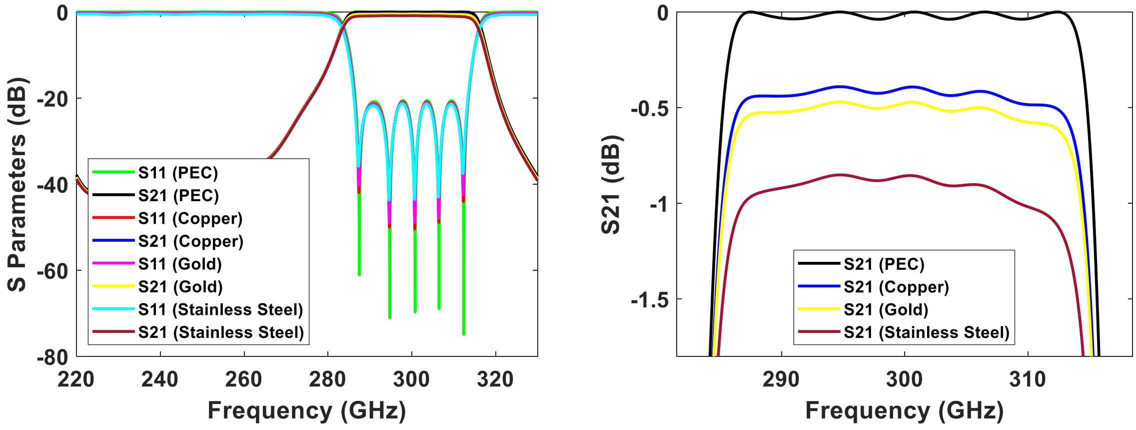

(a) (b)

Figure 8.12 Simulated response of the 300 GHz waveguide bandpass filter with PEC, copper, gold and stainless steel. (a) Simulated response over the frequency range of 220-330 GHz. (b) Expanded view of S_{21} over passband.

A modified model of the filter is simulated in CST [10] by considering dimensional changes of 3 µm, in order to analyse the dimensional tolerances. Figure 8.13 shows variation in S_{11} and S_{21} with a selection of random changes in the size by 3 µm, which shows that even if dimensions are changed by 3 µm, still good results are achievable.

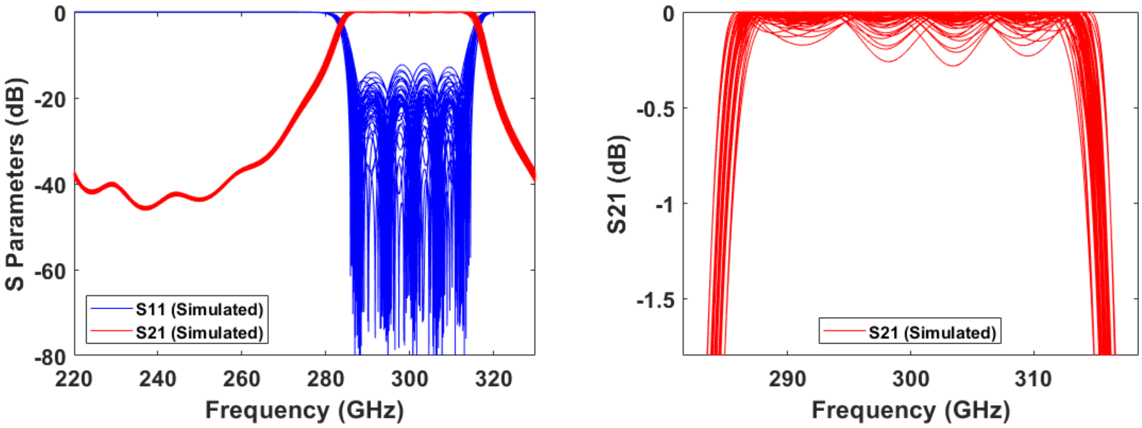

(a) (b)

Figure 8.13 Simulated tolerance analysis of the 300 GHz waveguide bandpass filter. Simulated results are with a selection of random changes in the size by 3 µm. (a) Simulated results over the frequency range of 220 – 330 GHz. (b) Expanded view of S_{21} over passband.

The connection between the filter and measurement system is accomplished using waveguide flanges. Generally, a waveguide flange is aligned using alignment pin holes and precision alignment pin holes. A waveguide flange misalignment is always possible when connecting the waveguide flanges, this is due to fabrication tolerances on pins and holes. Misalignment between two waveguide flanges can occur in many ways, here only four types of waveguide flange misalignments are going to be analysed using simulations in CST [10], these are vertical, horizontal, angular and diagonal waveguide flange misalignments. Figure 8.14 shows the effect of vertical waveguide flange misalignment on response of the filter. Direction of vertical movement of the waveguide flanges is shown in figure 8.14 (a), where dashed rectangular line represents the input/ output waveguide flange of the filter, and solid rectangular line represents the waveguide flange of the measurement system. Simulated responses of the filter are shown in figure 8.14 (b), where both input and output waveguide flanges are moved vertically in the same direction. The position of waveguide flanges is moved vertically from 0 µm to 80 µm in 10 µm steps. The simulated results in figure 8.14 (b) show that the return loss can be affected by vertical waveguide flange misalignment, if the waveguide flanges are moved vertically by more than 20 µm, below which the effect is very small (1.7 dB). The return loss starts to decrease as vertical waveguide flange misalignment increases, where the minimum return loss decreases to about 10 dB as the waveguide flanges move vertically by 80 µm.

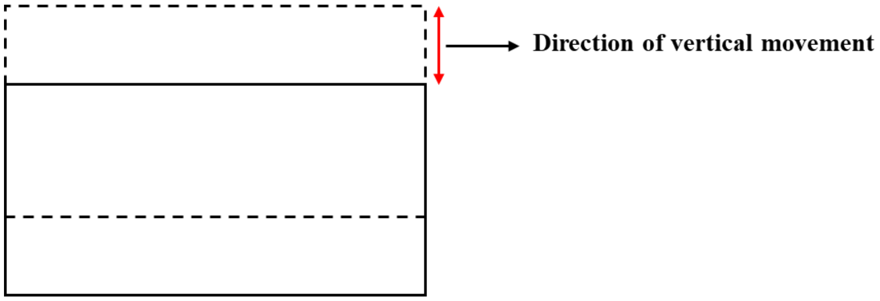

(a)

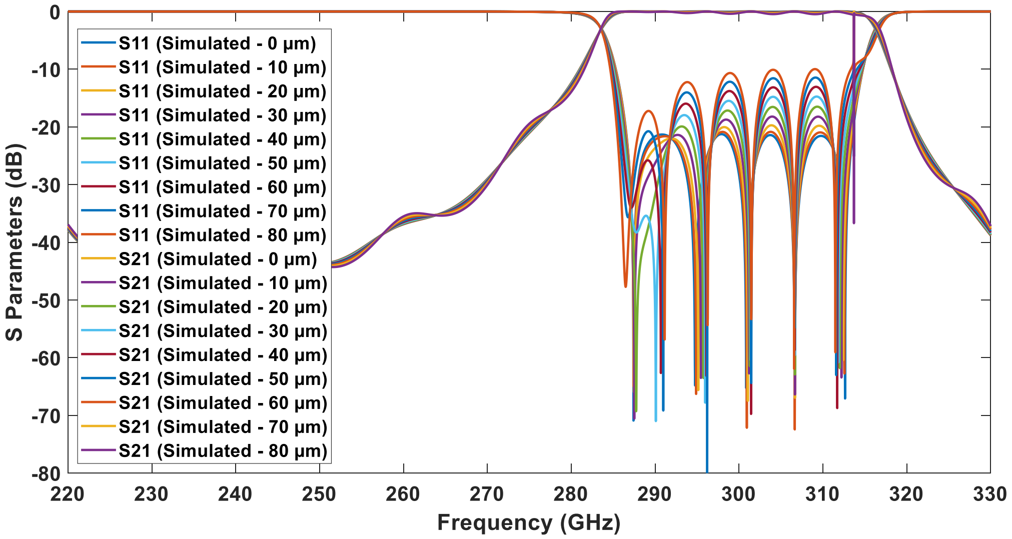

(b)

Figure 8.14 Effect of vertical waveguide flange misalignment on response of the filter. (a) Direction of vertical movement of the waveguide flanges. (b) Simulated responses of the filter when input and output waveguide flanges are moved vertically in the same direction.

The effect of horizontal waveguide flange misalignment on response of the filter is shown in figure 8.15, where direction of horizontal movement of the waveguide flanges, shown in figure 8.15 (a), and simulated responses of the filter, shown in figure 8.15 (b). Both input and output waveguide flanges are moved horizontally in the same direction. The position of waveguide flanges is moved horizontally from 0 µm to 80 µm in 10 µm steps. Looking at the simulated results in figure 8.15 (b), the return loss will be affected if there is a horizontal waveguide flange misalignment. However, the effect on return loss is minimal (1.6 dB) if horizontal movement is less than 30 µm, beyond which the return loss will decrease. The decrease in return loss is mostly noticeable in lower part of the passband. The minimum return loss decreases to about 14.5 dB as the horizontal waveguide flange misalignment increases to 80 µm.

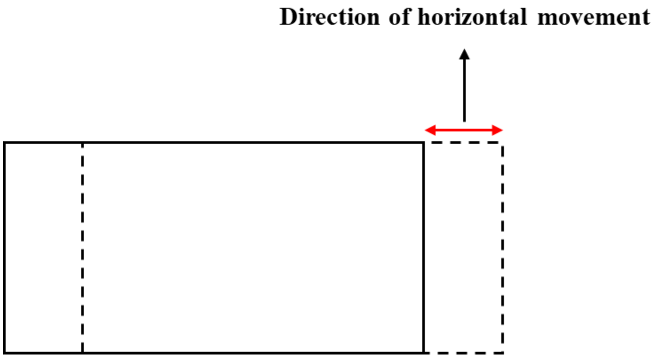

(a)

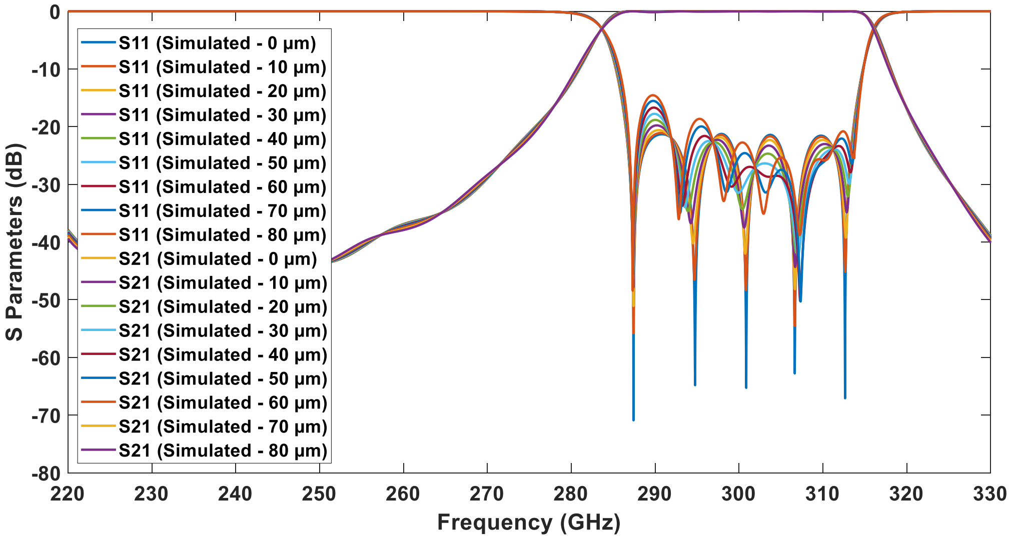

(b)

Figure 8.15 Effect of horizontal waveguide flange misalignment on response of the filter. (a) Direction of horizontal movement of the waveguide flanges. (b) Simulated responses of the filter when input and output waveguide flanges are moved horizontally in the same direction.

Figure 8.16 shows the effect of angular waveguide flange misalignment on response of the filter. Direction of angular movement of the waveguide flanges is shown in figure 8.16 (a), and simulated responses of the filter are shown in figure 8.16 (b). Both input and output waveguide flanges are rotated in the same direction, where the position of the waveguide flanges is rotated from 0° to 16° in 2° steps. The simulated results in figure 8.16 (b) show that if there is an angular waveguide flange misalignment, the return loss will be affected. Looking at the simulated results, the minimum return loss can be decreased by as much as 4 dB as the waveguide flanges are rotated by 16°.

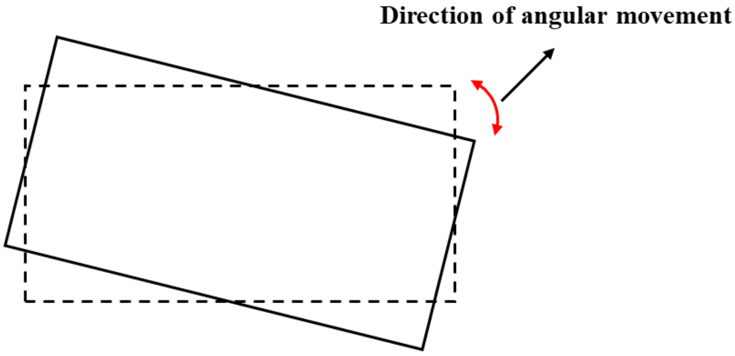

(a)

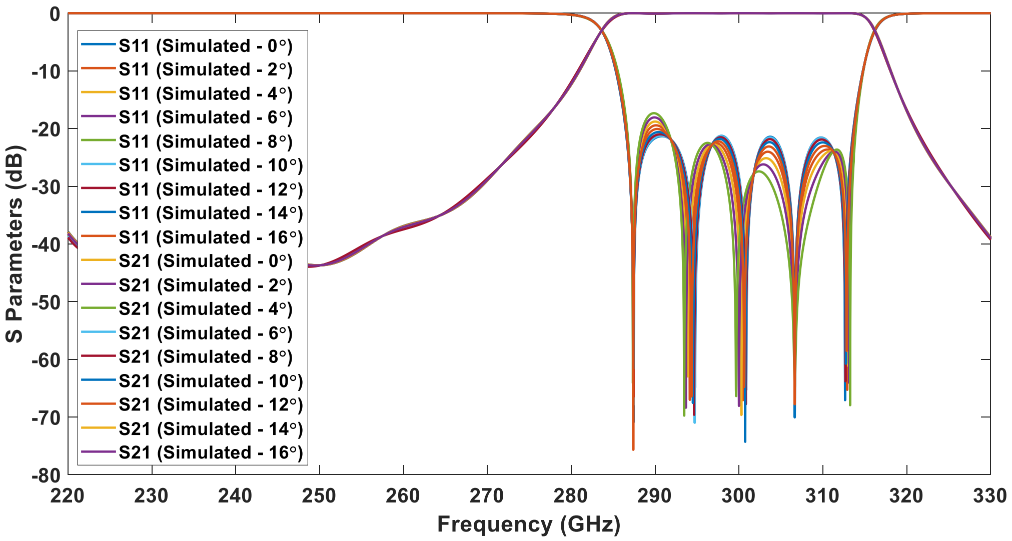

(b)

Figure 8.16 Effect of angular waveguide flange misalignment on response of the filter. (a) Direction of angular movement of the waveguide flanges. (b) Simulated responses of the filter when input and output waveguide flanges are rotated in the same direction.

Finally, figure 8.17 shows the effect of diagonal waveguide flange misalignment on response of the filter. Direction of diagonal movement of the waveguide flanges is shown in figure 8.17 (a), and simulated responses of the filter are shown in figure 8.17 (b). Both input and output waveguide flanges are moved diagonally in the same direction from 0 µm to 80 µm in 10 µm steps. The Simulated results in figure 8.17 (b) show that diagonal waveguide flange misalignment will also affect the return loss. The effect on return loss is very small (2 dB) with diagonal movement of up to 30 µm, and as the diagonal waveguide flange misalignment increases, the return loss decreases. The minimum return loss decreases to about 13 dB as diagonal waveguide flange misalignment increases to 80 µm.

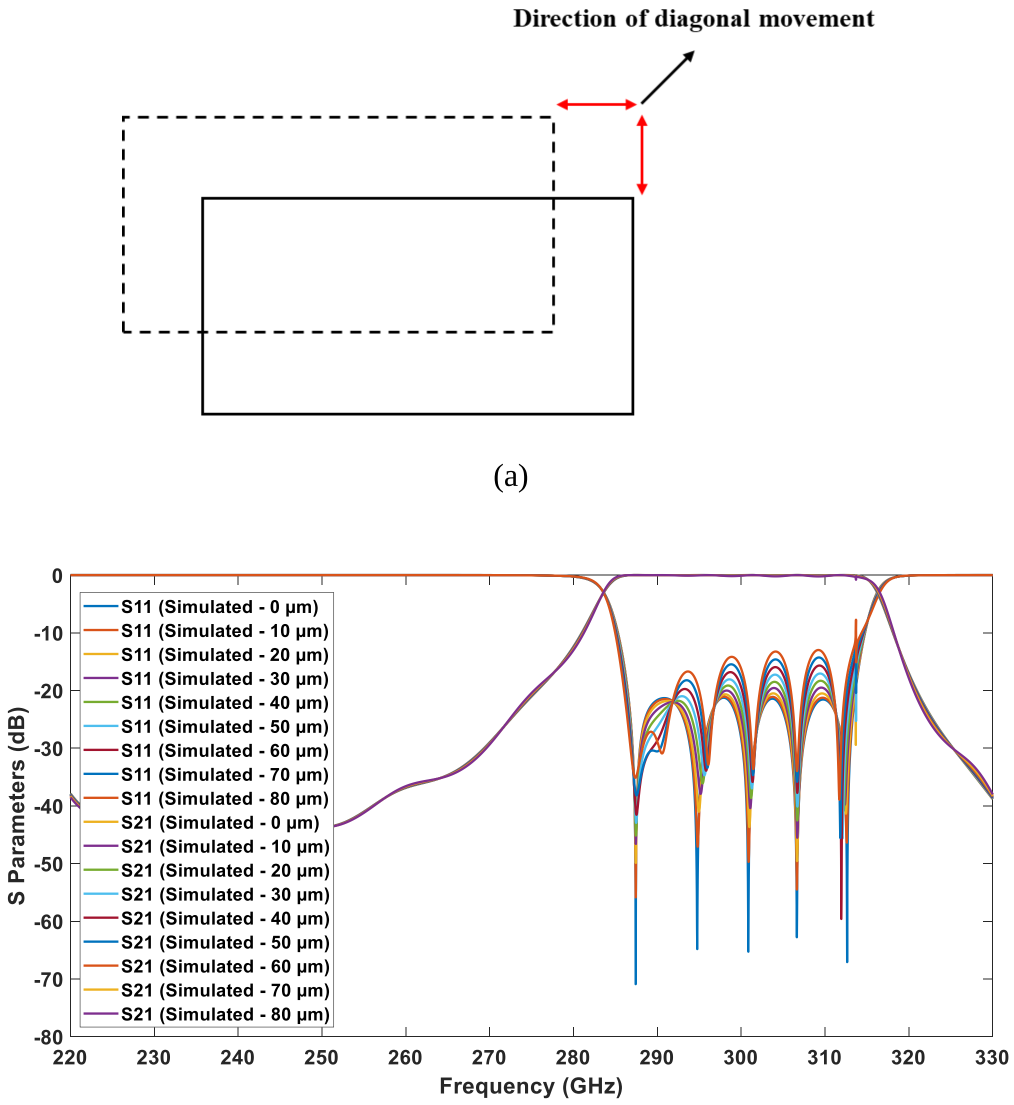

(a)

(b)

Figure 8.17 Effect of diagonal waveguide flange misalignment on response of the filter. (a) Direction of diagonal movement of the waveguide flanges. (b) Simulated responses of the filter when input and output waveguide flanges are moved diagonally in the same direction.

8.4 Conclusion

This chapter presented a fifth-order waveguide bandpass filter with embedded H-plane waveguide bends. As described, the filter is going to be fabricated by Fraunhofer IFAM Dresden in Germany using 3-D screen printing. The project demonstrates the possibility of using 3-D screen printing in fabrication of high frequency components. The design procedure of the waveguide filter using coupling matrix theory, explained in chapter 2, and the design of waveguide bends is explained in this chapter.

Although the filter has not been fabricated yet, a discussion about insertion loss when using different metallic materials, as well as dimensional tolerance analysis and effect of waveguide flange misalignment has been undertaken.

References

[1] “Fraunhofer IFAM Dresden - Fraunhofer IFAM,” *Fraunhofer-Institut für Fertigungstechnik und Angewandte Materialforschung IFAM*. Accessed: Sept. 13, 2018. [Online]. Available: http://www.ifam-dd.fraunhofer.de/.

[2] X. Shang, M. Ke, Y. Wang, and M. Lancaster, “Micromachined W-band waveguide and filter with two embedded H-plane bends,” *IET Microwaves, Antennas & Propagation*, vol. 5, no. 3, p. 334, Feb. 2011.

[3] J.-S. Hong, *Microstrip filters for RF/microwave applications*. Hoboken, NJ: Wiley, 2011.

[4] R. J. Cameron, C. M. Kudsia, and R. R. Mansour, *Microwave filters for communication systems: fundamentals, design, and applications*. Hoboken, NJ, USA: John Wiley & Sons, Inc., 2018.

[5] W. B. Alison, *A handbook for the mechanical tolerancing of waveguide components*. Norwood: Artech House, 1987.

[6] A. Casanueva, J. A. Pereda, and A. L. Mediavilla, “Optimum compact H- and E-plane corners in rectangular waveguide,” *Microwave and Optical Technology Letters*, vol. 42, no. 6, pp. 494-497, July. 2004.

[7] X. Shang, M. Ke, Y. Wang, and M. J. Lancaster, “WR-3 Band Waveguides and Filters Fabricated Using SU8 Photoresist Micromachining Technology,” *IEEE Transactions on Terahertz Science and Technology*, vol. 2, no. 6, pp. 629–637, Nov. 2012.

[8] X. Shang, M. J. Lancaster, M. Ke, and Y. Wang, “Measurements of micromachined submillimeter waveguide circuits,” *2010 76th ARFTG Microwave Measurement Conference*, Clearwater Beach, FL, USA, 2010, pp. 1-4.

[9] X. Shang, M. Ke, Y. Wang, and M. Lancaster, “Micromachined WR-3 waveguide filter with embedded bends,” *Electronics Letters*, vol. 47, no. 9, p. 545, Apr. 2011.

[10] Computer Simulated Technology (CST). (2017). Microwave Studio. [Online]. Available: http//www.cst.com/.

CHAPTER 9: CONCLUSION AND FUTURE WORK

9.1 Conclusion

The work presented in this thesis mainly focused on the design and fabrication of several microwave and terahertz filters, which were fabricated using different types of 3-D printing technology. The work demonstrated the potential of using 3-D printing as an additive manufacturing technique in fabrication of high frequency passive components. The components were fabricated using both non-metallic and metallic materials, where different 3-D printing fabrication processes were used. All the projects presented in the thesis are completed, but one project introduced in chapter 8 is still at the fabrication stage.

The work in this thesis showed that in fact 3-D printing can be used to fabricate high frequency components with complex structures, as conventional manufacturing techniques reach their limits to fabricate complex structures. In chapter 4 a fourth-order 3 GHz coaxial cavity resonator filter was introduced. In this project, the volume and size of the filter reduced by almost half compare to other conventional coaxial filters by fitting one resonator inside another resonator. Because of the complexity of the internal structure, the filter couldn’t be easily fabricated by conventional fabrication techniques, such as CNC milling, and the easiest way was to use 3-D printing to fabricate the filter. The filter was fabricated using stereolithography 3-D printing process and good agreement between measured and simulated *S* parameter results demonstrated the accuracy of the fabrication process. This project demonstrated the advantages of using 3-D printing process to fabricate components with complex structures. This work was published in [1].

In chapter 5, three metal 3-D printed fifth-order 90 GHz waveguide bandpass filters were introduced, which were fabricated using micro laser sintering process. As explained in chapter 5, the micro laser sintering process allows high frequency passive components to be fabricated accurately using metallic materials. Using metallic materials instead of non-metallic materials in fabrication process insures wider working temperature range, better thermal expansion properties, and increasing the strength of components. The filters in chapter 5, were made from stainless steel powder. The measured *S* parameter results of the filters had good agreement with simulated results, which demonstrated the accuracy of the fabrication process.

Extremely close measured results of the two identically designed filters demonstrated the capability of reproducibility of the fabrication process. It is also shown that the insertion loss of the filter can be improved considerably by electroplating the surface of the filter with copper. This project demonstrated the potential of using micro laser sintering process in fabrication of high frequency passive components. This work was published in [2] and [3].

In chapter 6, two identical fifth-order 180 GHz waveguide bandpass filters were introduced, which were fabricated using micro laser sintering process. This work extends the work introduced in chapter 5, and the aim was to show the capability of micro laser sintering process for fabricating filters that operate at much higher frequency. As it is shown in chapter 6, the measured S parameter results of both filters had good agreement with simulated results showing the accuracy of the fabrication process, also measured results of the filters were extremely close, which demonstrated the capability of reproducibility of the fabrication process. These filters are the highest frequency waveguide filters that have ever been fabricated using metallic 3-D printing process.

In chapter 7, a fourth-order 2 GHz hybrid coaxial bandpass filter with two symmetrical transmission zeros was introduced, which was fabricated using stereolithography 3-D printing process. In this work all the main-line couplings and input/output coupling were realized using PCB lines, and a capacitive gap used to realize the cross coupling. Using PCB lines to achieve couplings, instead of coupling irises or probes allows different topologies to be designed by simply changing the PCB layout. This work provided another example of using 3-D printing process to fabricate high frequency passive components with good agreement between the measured and simulated S parameter results.

Finally, in chapter 8, a fifth-order 300 GHz waveguide bandpass filter with embedded H-plane waveguide bends was introduced. The filter is still at the stage of fabrication and it is being fabricated using 3-D screen printing technique. As mentioned, 3-D screen printing is capable of fabricating complex components accurately using a variety of metallic materials. The technique is well suitable for mass production, where different parts with different structures can be made simultaneously [4, 5]. The 3-D screen printing technique is a good choice for fabrication of high frequency passive components, and this project will demonstrate the possibility of using 3-D screen printing technique in fabrication of terahertz passive components.

In summary, the work in this thesis demonstrated the design and fabrication of several high frequency filters, which were fabricated using different types of 3-D printing technology, showing the potential of using 3-D printing as an additive manufacturing for fabrication of high frequency passive components with complex structures.

9.2 Future Work

Some possible future work based on what presented in this thesis are given below.

i. *Electroplating the 180 GHz waveguide bandpass filters with gold and investigate the possible cause of additional losses in the filters*

   As mentioned in chapter 6, the average measured insertion losses of the both waveguide filters are about 2 dB higher than the simulated results. This needs further investigation, and in chapter 6 some of the possible causes were explained. The waveguide filters are going to be gold plated in the near future in order to understand more about the losses. If the insertion loss improved substantially after gold plating that means the main possible cause for the additional insertion loss is because of changes in specified conductivity of the stainless steel due to manufacturing process.

ii. *Improve spurious free performance of the 2 GHz hybrid coaxial bandpass filter*

   In chapter 7, a hybrid coaxial bandpass filter was introduced, where the main-line couplings and input/ output coupling realized using PCB lines. Based on measured *S* parameter results, the filter didn’t have a good spurious free performance. It is mentioned that the length of PCB lines is probably the main cause of poor spurious free performance, which act as resonators. In the future the length of PCB lines can be designed shorter in order to improve the spurious free performance, which can be done by reducing the wall thickness between the resonators.

iii. *Fabrication and testing of the 300 GHz waveguide bandpass filter*

   The filter introduced in chapter 8, is being fabricated soon. The filter needs to be tested once it is fabricated by 3-D screen printing. Successful completion of this project will show the possibility of using 3-D screen printing in fabrication of terahertz passive components.

iv. *Other possible future 3-D printing projects*

A number of projects are still in the design stage, which maybe to be fabricated using 3-D printing process once the design is completed. The first project is a waveguide termination (waveguide load) which uses the property of loss due to conduction loss of waveguide to absorb microwave energy and convert to heat, instead of using resistive tapers at the end of waveguide, as in conventional waveguide terminations. This project would be expected to be fabricated using a metal 3-D printing process, so it can be used in high power applications. Another possible future 3-D printing project is terahertz bandstop filter which can be fabricated using 3-D printing process.

References

[1] M. Salek, X. Shang, and M. J. Lancaster, “Compact S-Band Coaxial Cavity Resonator Filter Fabricated By 3-D Printing,” *IEEE Microwave and Wireless Components Letters*, vol. 29, no. 6, pp. 382-384, June. 2019.

[2] M. Salek, X. Shang, R. C. Roberts, M. J. Lancaster, F. Boettcher, D. Weber, and T. Starke, “W-Band Waveguide Bandpass Filters Fabricated by Micro Laser Sintering,” *IEEE Transactions on Circuits and Systems II: Express Briefs*, vol. 66, no. 1, pp. 61–65, Jan. 2019.

[3] M. Salek, X. Shang, M. J. Lancaster, R. C. Roberts, T. Starke, F. Boettcher, and D. Weber, “90 GHz Micro Laser Sintered Filter: Reproducibility and Quality Assessment,” *2019 49th European Microwave Conference (EuMC),* Paris, France, 2019, pp. 1-4.

[4] P. Brauer, M. Lindner, T. Studnitzky, B. Kieback, J. Rudolph, R. Werner, and G. Krause, “3D Screen Printing technology — Opportunities to use revolutionary materials and machine designs,” *2012 2nd International Electric Drives Production Conference (EDPC),* Nuremberg, Germany, 2012, pp. 1-5.

[5] M. Dressler, T. Studnitzky, and B. Kieback, “Additive manufacturing using 3D screen printing,” *2017 International Conference on Electromagnetics in Advanced Applications (ICEAA),* Verona, Italy, 2017, pp. 476-478.

APPENDIX A: PUBLICATIONS

1. Published: M. Salek, X. Shang, and M. J. Lancaster, “Compact S-Band Coaxial Cavity Resonator Filter Fabricated By 3-D Printing,” *IEEE Microwave and Wireless Components Letters*, vol. 29, no. 6, pp. 382-384, June. 2019.

2. Published: M. Salek, X. Shang, R. C. Roberts, M. J. Lancaster, F. Boettcher, D. Weber, and T. Starke, “W-Band Waveguide Bandpass Filters Fabricated by Micro Laser Sintering,” *IEEE Transactions on Circuits and Systems II: Express Briefs*, vol. 66, no. 1, pp. 61–65, Jan. 2019.

3. Published: M. Salek, X. Shang, M. J. Lancaster, R. C. Roberts, T. Starke, F. Boettcher, and D. Weber, “90 GHz Micro Laser Sintered Filter: Reproducibility and Quality Assessment,” *2019 49th European Microwave Conference (EuMC)*, Paris, France, 2019, pp. 1-4.

4. In preparation: “2 GHz Hybrid Coaxial Bandpass Filter Fabricated by Stereolithography 3-D Printing”: outlining the design and fabrication of the fourth-order 2 GHz hybrid coaxial bandpass filter, which presented in chapter 7.

Note: Papers (1) and (2) are attached to this thesis and are available at *IEEE Xplore Digital Library*. Paper (3) is attached to this thesis, but still not available at *IEEE Xplore Digital Library* as it is accepted recently.

Compact *S*-Band Coaxial Cavity Resonator Filter Fabricated By 3-D Printing

Milan Salek, *Member, IEEE*, Xiaobang Shang, *Senior Member, IEEE*,
and Michael J. Lancaster, *Senior Member, IEEE*

***Abstract*— This letter presents a novel fourth-order coaxial cavity resonator bandpass filter with a Chebyshev response. The filter operates at a center frequency of 3 GHz and has a bandwidth of 90 MHz. The filter is formed of four coupled coaxial cavity resonators. To make the filter compact, the first resonator is embedded inside the inner conductor of the second resonator and the fourth resonator is embedded inside the central conductor of the third resonator. The filter is fabricated stereolithography apparatus 3-D by printing process that allows such a design with a complex structure to be fabricated accurately at a reasonable cost. The filter is tested and good agreement between measured and simulated results is obtained.**

***Index Terms*— 3-D printing, bandpass filter, coaxial cavity resonator, *S*-band, stereolithography.**

I. INTRODUCTION

COAXIAL cavity resonator filters are widely used in radar and communications as they offer a medium to high-quality factor, a low manufacturing cost, a wide tuning range, excellent spurious-free performance, and a compact size [1]. Reducing the size and volume of coaxial cavity resonator filters, while maintaining low loss, is a significant challenge in the field of filter design. In general, the size of low loss filters can be reduced by using dual-mode and multimode resonators [2] or using dielectric resonators [3], but these techniques are not suitable for the coaxial resonator filters here as they are based on different materials and technologies. Several studies have been presented by others on how to reduce the size and volume of coaxial cavity resonator filters. It is reported in [4] that the size of the filter can be reduced by using controlled mixed electric and magnetic couplings to move the resonators closer. In [5], the length of the filter is reduced by changing the orientation of some of the coaxial resonators. It is reported in [6] that the volume of a filter can be reduced by using inner conductive posts within a single cavity, where the coupling between the posts is achieved by adjusting the post positions and dimensions. Altering the coupling properties can, in fact, adjust the filter size by moving the resonators closer together, but the overall effect is limited, as there is always a minimum distance between resonators. Of course, the coaxial resonator can always be reduced in length by increasing the open-end capacitance, but this reduces the quality factor. The concept of using stepped impedance resonators (SIR) to reduce the length of the resonators is also possible and reported in [7]; however, the quality factor of the resonators is again reduced. This letter presents a fourth-order coaxial cavity resonator filter, the novel aspect is where one coaxial resonator is embedded within the second coaxial resonator. Such an arrangement allows the size and volume of the filter to be reduced by approximately a factor of 2. A further novel aspect is that the filter is fabricated by the stereolithography apparatus (SLA) 3-D printing process, which allows such a complex structure to be fabricated easily. The design procedure of the filter is explained briefly in Section II, and Section III gives a brief description of the fabrication process. Measured and simulated results are provided in Section IV with relevant discussion.

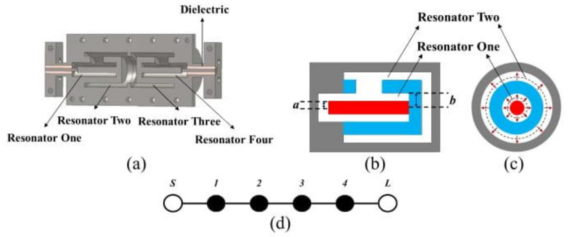

Fig. 1. Configuration of the fourth-order coaxial cavity resonator filter. (a) Cross section view of the filter showing the filter resonators and internal couplings between resonators. (b) Simplified diagram showing resonators one and two. (c) Side view showing the electric field (solid arrows) and magnetic field (dashed lines). (d) Coupling routing diagram of the filter with the black filled circles as the resonators.

II. BANDPASS FILTER DESIGN

The coaxial cavity resonator bandpass filter is designed to have a Chebyshev response with a center frequency of 3 GHz, a bandwidth of 90 MHz (fractional bandwidth of 3%), and a return loss of 20 dB over the passband. The structure of the filter is shown in Fig. 1(a). Each resonator is about a quarter wavelength, being shorted at one end and open at the other.

Fig. 1(b) and (c) shows a pair of resonators, the central conductor of resonator one is represented by the red area and this is inserted inside resonator two. The blue area represents the metal of the outer conductor of resonator 1 and

Manuscript received January 15, 2019; revised February 14, 2019 and April 11, 2019; accepted April 21, 2019. The work was supported by the U.K. Engineering and Physical Science Research Council (EPSRC) under Contract EP/M016269/1. *(Corresponding author: Milan Salek.)*

M. Salek and M. J. Lancaster are with the Department of Electronic, Electrical, and Systems Engineering, University of Birmingham, Birmingham B15 2TT, U.K. (e-mail: mxs1149@bham.ac.uk; m.j.lancaster@bham.ac.uk).

X. Shang was with the Department of Electronic, Electrical, and Systems Engineering, University of Birmingham, Birmingham B15 2TT, U.K. He is now with the National Physical Laboratory, Middlesex TW11 0LW, U.K. (e-mail: xiaobang.shang@npl.co.uk).

Color versions of one or more of the figures in this paper are available online at http://ieeexplore.ieee.org.

Digital Object Identifier 10.1109/LMWC.2019.2913155

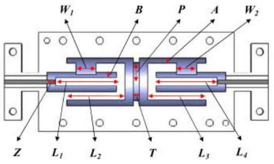

Fig. 2. Illustration of the fourth-order coaxial cavity resonator filter, showing its internal structure with all internal dimensions. The dimensions in millimeter are: $P = 6.759$, $W_1 = W_2 = 7.1054$, $L_1 = L_4 = 21.428$, $L_2 = L_3 = 20.498$, $A = B = 2$, $Z = 2.856$, and $T = 2$.

inner conductor of resonator 2. The field distribution in the resonators is shown in Fig. 1(c), which is the same throughout the filter as all resonators operate in the TEM mode. Note the optimal Q for coaxial resonators can be obtained by making $b/a = 3.59$ (Fig. 1). However, a minimum SLA wall thickness of about 3 mm defines the design making this difficult to achieve. Fig. 1(d) shows the coupling routing diagram of the filter. The design of the filter is based on the coupled resonator approach, which is used extensively in modern filter design [8]. From the specifications above, external Q values and coupling coefficients can be calculated. This calculation gives a value for the external Q at both input and output of $Q_e = 31.05$. The calculated required coupling values between resonators 1 and 2, and 3 and 4 are $M_{12} = M_{34} = 0.0274$, and between the resonators 2 and 3 is $M_{23} = 0.021$. The apertures between resonators need to be set to the correct size to reflect these coupling values. The coupling between resonators 1 and 2, and 3 and 4 are realized by the width of irises that are denoted by W_1 and W_2 in Fig. 2. By adjusting W_1 (or W_2) in an electromagnetic simulation of the two resonators, a relation between the coupling coefficient and the iris width can be obtained as shown in Fig. 3(a). This can be used to find the correct W_1 (or W_2) for the required coupling coefficient M_{12} (or M_{34}). The coupling between resonators 2 and 3 is adjusted by changing the radius of the iris shown as P in Fig. 2. Thus, by altering P in a two-resonator simulation, the relation between the interresonator coupling coefficient and the iris radius can be obtained as shown in Fig. 3(b). This can be used to find the value of P which corresponds to the required coupling coefficient M_{23}. The input–output couplings are realized by adjusting the probe penetration depth located on the end of an SMA (subminiature version A) connector (Z). Changing Z in an electromagnetic simulation results in finding the relation between the external quality factor Q_e and Z as shown in Fig. 3(c). This allows the correct value of Z for the required external quality factor Q_e to be found. Electromagnetic optimization of the filter is performed using CST [9], and are shown together with the measurement results, in Section IV.

III. FILTER FABRICATION

Using additive manufacturing or 3-D printing such as SLA has become very popular for the fabrication of microwave components such as filters, as it enables novel lightweight components with complex structures to be fabricated with excellent surface quality and high resolution. Examples are reported in [10]–[12]. The filter reported here was fabricated using a stereolithography 3-D printing process with a printing resolution of 0.1 mm. The filter was printed out of the nonconductive photocurable polymer resin Accura Xtreme resin, layer by layer using an ultraviolet laser. The filter was subsequently coated with a 20-μm-thick copper layer which was compensated for in the 3-D model of the filter before fabrication. Supporting material was used while the parts were being built using the same polymer material and this was then removed during postprocessing. Fig. 4(a) shows a photograph of the fabricated filter after being copper-plated and assembled. The filter is formed of two symmetrical pieces as shown in Fig. 4(b). The two-piece split is to facilitate the copper plating process after printing which requires access to the internal surfaces. The split is such that there is no current flow across the boundary, so it has little effect on the loss. The good experimental results confirm this. There was no polishing after printing. After the copper plating process, both pieces are assembled using seven nuts and bolts on each side. The connectors are standard female 50-Ω flange mount SMA connectors with a long center conductor surrounded by dielectric (dielectric constant 2.1). Both connectors were bolted on to the flat end of the filter.

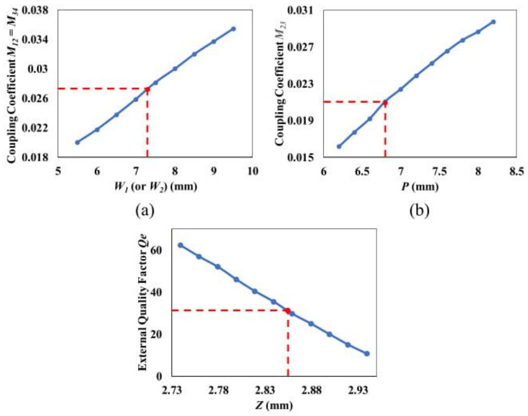

(a) (b)

(c)

Fig. 3. (a) Coupling coefficient $M_{12} = M_{34}$ versus the iris width W. (b) Coupling coefficient M_{23} versus the iris radius P. (c) External quality factor Q_e versus the probe penetration depth Z.

(a) (b)

Fig. 4. Photograph of the fabricated S-band coaxial cavity resonator filter after being copper plated. (a) Fabricated filter with both sides fixed together using nuts and bolts. (b) Left and right side of the fabricated filter.

IV. MEASUREMENT AND DISCUSSION

The S-parameter measurements of the filter were performed on an Agilent E8362C PNA network analyzer. Fig. 5 shows the measured and simulated results of the filter. The measured results are denoted with solid lines and simulated results with dashed lines. As shown in Fig. 5(a), it can be observed that the

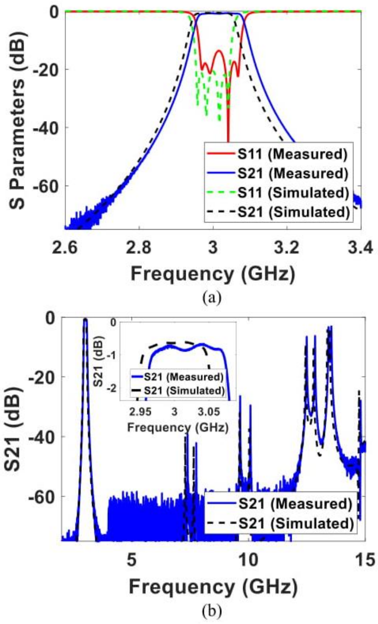

Fig. 5. Measured and simulated results of the coaxial cavity resonator filter. (a) Narrow frequency range. (b) Wide frequency range.

TABLE I

COMPARISON WITH OTHER SLA 3-D PRINTED BANDPASS FILTERS

f_c (GHz)	FBW (%)	IL (dB)	RL (dB)	R.T.	f_c *offset* (%)	Vol/λ_C ($\times 10^6$)	*Ref.*
10	3	0.25	>18	S	<0.01	2.36	[10]
32	1	0.56~0.7	>17	HS	0.04	N/A	[11]
10	5	0.107	>20	S	0.05	11.2	[12]
3.019	3.38	0.7	>13.5	C	0.63	0.749	T.W.

f_c: center frequency; FBW: fractional bandwidth; IL: insertion loss; RL: return loss; R.T.: resonator type (S: spherical; HS: hemispherical; C: coaxial); f_c offset: frequency shift; Vol/λ_C: volume/wavelength at the filter center frequency; T.W.: this work; Ref.: reference.

measured center frequency is shifted up by 19 MHz (0.63% of the simulated center frequency), and there is a minimum return loss of 13.5 dB across the whole passband. Simulations show the 19-MHz frequency shift can be accounted for by a small (0.28 mm) shrinkage of the structure. The dimensional changes are due to final UV curing and over plating the surface, which could be corrected by remanufacturing. The inset in Fig. 5(b) shows a minimum insertion loss of around 0.70 dB for the measured results. The corresponding minimum insertion loss for the simulation with perfectly smooth copper (conductivity 5.96×10^7 S/m) is 0.46 dB. If the copper has a surface roughness of 1 μm, then the effective conductivity reduces to 2.66×10^7 S/m and the loss becomes 0.63 dB. This is also shown on the inset of Fig. 5(b). This low surface roughness is typical of these SLA structures [13]. The simulated and measured results are very close, and the additional insertion loss that cannot be accounted for could be caused by a combination of factors including joints, losses in the connectors, different surface roughness, impurities in the copper, and contamination of the copper surface. Note that we are using minimum insertion losses here, so the effect of the return loss is negligible given it is about 50 dB at 3.041 GHz. The minimum insertion loss corresponds to a resonator unloaded Q value of 987 for the measured result and 1048 for the simulated one [14]. Fig. 5(b) shows the frequency response of the filter over a wide frequency range. The first spurious response appears at about 13 GHz, giving a spurious-free window of about 10 GHz. Table I provides a comparison of the measured performance of bandpass filters that are fabricated using SLA 3-D printing. Note these are different specifications and resonator types. However, the reported filter has a comparable performance in terms of insertion loss whilst having a small size.

V. CONCLUSION

A novel compact fourth-order coaxial cavity resonator filter fabricated by SLA 3-D printing has been presented in this letter. By fitting one resonator inside another resonator, the volume of the filter can be reduced by almost a half. This letter also demonstrates the advantages of 3-D printing in the fabrication of complex microwave filters. Good agreement between the measured and simulated results demonstrates the accuracy of the SLA 3-D printing.

REFERENCES

[1] R. R. Mansour, "Filter technologies for wireless base stations," *IEEE Microw. Mag.*, vol. 5, no. 1, pp. 68–74, Mar. 2004.

[2] M. Memarian and R. R. Mansour, "Quad-mode and dual-mode dielectric resonator filters," *IEEE Trans. Microw. Theory Techn.*, vol. 57, no. 12, pp. 3418–3426, Dec. 2009.

[3] C. Wang and K. A. Zaki, "Dielectric resonators and filters," *IEEE Microw. Mag.*, vol. 8, no. 5, pp. 115–127, Oct. 2007.

[4] H. Wang and Q.-X. Chu, "An inline coaxial quasi-elliptic filter with controllable mixed electric and magnetic coupling," *IEEE Trans. Microw. Theory Techn.*, vol. 57, no. 3, pp. 667–673, Mar. 2009.

[5] M. Hoft and F. Yousif, "Orthogonal coaxial cavity filters with distributed cross-coupling," *IEEE Microw. Wireless Compon. Lett.*, vol. 21, no. 10, pp. 519–521, Oct. 2011.

[6] X. Wang, G. Jang, B. Lee, and N. Park, "Compact quad-mode bandpass filter using modified coaxial cavity resonator with improved Q-Factor," *IEEE Trans. Microw. Theory Techn.*, vol. 63, no. 3, pp. 965–975, Mar. 2015.

[7] H. Aouidad, E. Rius, J.-F. Favennec, A. Manchec, and Y. Clavet, "UHF second order bandpass filters based on miniature two-section SIR coaxial resonators," *Int. J. Microw. Wireless Technol.*, vol. 8, no. 8, pp. 1187–1196, Dec. 2015.

[8] R. J. Cameron, C. M. Kudsia, and R. R. Mansour, *Microwave Filters for Communication Systems: Fundamentals, Design, and Applications*. Hoboken, NJ, USA: Wiley, 2007.

[9] (2017). *Computer Simulated Technology (CST), Microwave Studio*. [Online]. Available: http//www.cst.com/

[10] C. Guo, X. Shang, J. Li, F. Zhang, M. J. Lancaster, and J. Xu, "A lightweight 3-D printedx-band bandpass filter based on spherical dual-mode resonators," *IEEE Microw. Wireless Compon. Lett.*, vol. 26, no. 8, pp. 568–570, Aug. 2016.

[11] J. Li, C. Guo, L. Mao, and J. Xu, "Compact high-Q hemispherical resonators for 3-D printed bandpass filter applications," in *IEEE MTT-S Int. Microw. Symp. Dig.*, Jun. 2017, pp. 1591–1594.

[12] C. Guo, X. Shang, M. J. Lancaster, and J. Xu, "A 3-D printed lightweight X-band waveguide filter based on spherical resonators," *IEEE Microw. Wireless Compon. Lett.*, vol. 25, no. 7, pp. 442–444, Jul. 2015.

[13] X. Shang *et al.*, "W-band waveguide filters fabricated by laser micromachining and 3-D printing," *IEEE Trans. Microw. Theory Techn.*, vol. 64, no. 8, pp. 2572–2580, Aug. 2016.

[14] S. B. Cohen, "Dissipation loss in multiple-coupled-resonator filters," *Proc. IRE*, vol. 47, no. 8, pp. 1342–1348, Aug. 1959.

W-Band Waveguide Bandpass Filters Fabricated by Micro Laser Sintering

Milan Salek, Xiaobang Shang, *Member, IEEE*, Robert C. Roberts, *Member, IEEE*,
Michael J. Lancaster, *Senior Member, IEEE*, Falko Boettcher, Daniel Weber, and Thomas Starke

***Abstract*—This brief presents a fifth-order W-band waveguide bandpass filter with a Chebyshev response, operating at center frequency of 90 GHz and having fractional bandwidth of 11%. The filter is fabricated by micro laser sintering process which is a powder bed based additive manufacturing technology. Use of this technology allows the filter to be made accurately with high resolution and good surface quality in one piece. This results in better performance in term of insertion loss and reproducibility. For the purpose of comparison, two similar filters are presented in this brief with the same structure and specification, one made from stainless steel and the other made from stainless steel coated with copper. Both filters are tested and have excellent agreement between measurements and simulations.**

***Index Terms*—3-D printing, micro laser sintering process, stereolithography, W-band, waveguide bandpass filter.**

I. INTRODUCTION

USING additive manufacturing technologies to fabricate microwave components has become of interest in recent years. Both metallic and non-metallic materials are used in additive manufacturing fabrication processes, but non-metallic materials generally need to be coated with a conductive layer using a surface metallization process to achieve a good electrical conductivity.

Using additive technologies allows components with complex structure to be fabricated at low cost with high accuracy. Many different types of additive manufacturing technologies are available such as stereolithography apparatus (SLA), fused deposition modelling (FDM) and selective laser sintering (SLS) [1]. Fabrication of microwave filters operating at both low and high frequencies (0.5 GHz to 100 GHz) using the stereolithography-based 3-D printing technique is well proven to work with good results as shown in [1]–[11]. Other microwave components produced by stereolithography-based 3-D printing are antennas with examples reported in [12]–[16].

Stereolithography-based 3-D printing makes use of photodefinable plastic materials; so printed filters must be subsequently coated with conductive materials using surface metallization process. This results in an increase in complexity of the fabrication process and cost. However, using the micro laser sintering process allows metallic materials to be used directly. Using a metallic fabrication process increases the strength of components, as well as insuring wider working temperature range and better thermal expansion properties.

This brief describes a W-band waveguide bandpass filter, which is fabricated by micro laser sintering, also known as selective laser sintering or selective laser melting. Using this technique allows the filter to be manufactured with high accuracy, high resolution and good surface quality.

The filter reported here operates at center frequency of 90 GHz with bandwidth of 10 GHz, and to the best of author's knowledge this is the highest frequency filter fabricated by micro laser sintering process. The waveguide bandpass filter design is reasonably conventional, using coupling matrix theory to design a filter based on five rectangular resonators which are coupled using inductive irises [17], [18]. In addition to the waveguide filter, the standard UG387/U flange was included in the fabrication process enabling accurate connection to measurement system.

There are many different types of conductive powder materials that are commonly used in the micro laser sintering process such as stainless steel, molybdenum and tungsten. Stainless steel used in fabrication process of both filters with one being coated with copper to compare insertion loss.

II. BANDPASS FILTER DESIGN

The filter is constructed with five coupled rectangular resonators operating in the TE_{101} mode. The couplings between the resonators as well as input/ output coupling are realized using inductive irises. The filter is specified in terms of the Chebyshev bandpass response with center frequency of

---

Manuscript received February 12, 2018; revised March 22, 2018; accepted April 5, 2018. Date of publication April 10, 2018; date of current version December 20, 2018. This work was supported in part by the U.K. Engineering and Physical Science Research Council under Contract EP/M016269/1 and in part by the 3-D Micro Print Gmbh in Germany and Additive Microfabrication Laboratory, University of Hong Kong. This brief was recommended by Associate Editor I. W. H. Ho. *(Corresponding author: Milan Salek.)*

M. Salek and M. J. Lancaster are with the Department of Electronic, Electrical and Systems Engineering, University of Birmingham, Birmingham B15 2TT, U.K. (e-mail: mxs1149@bham.ac.uk; m.j.lancaster@bham.ac.uk).

X. Shang was with the Department of Electronic, Electrical and Systems Engineering, University of Birmingham, Birmingham B15 2TT, U.K. He is now with the Engineering, Materials and Electrical Science Department, National Physical Laboratory, Middlesex TW11 0LW, U.K. (e-mail: xiaobang.shang@npl.co.uk).

R. C. Roberts is with the Department of Computer Science, University of Hong Kong, Hong Kong (e-mail: rcr8@hku.hk).

F. Boettcher and T. Starke are with 3-D Micro Print Gmbh, 09126 Chemnitz, Germany (e-mail: falko.boettcher@3dmicroprint.com; thomas.starke@3dmicroprint.com).

D. Weber was with the 3-D Micro Print Gmbh, 09126 Chemnitz, Germany. He is now with Freeman Technology, Tewkesbury GL20 8DN, U.K. (e-mail: engineering.daniel.weber@gmail.com).

Color versions of one or more of the figures in this paper are available online at http://ieeexplore.ieee.org.

Digital Object Identifier 10.1109/TCSII.2018.2824898

90 GHz, bandwidth of 10 GHz (fractional bandwidth of 11%) and return loss of 20 dB over the passband. Using coupling matrix theory [17], the filter specification is translated into coupling matrix elements, which are then translated into physical dimensions according to the procedure in [17] and [18].

A coupling routing diagram of the filter can be seen in Fig. 1 (a). The un-normalized non-zero coupling coefficients between resonators are $M_{12} = M_{45} = 0.0961$, $M_{23} = M_{34} = 0.0706$ and the external quality factor of the first (Q_{e1}) and the last (Q_{en}) resonators are calculated to be $Q_{e1} = Q_{en} = 8.76$ [17], [18].

The physical dimensions which correspond to the coupling and Q values are found by the standard technique. Looking at Fig. 1 (b), it can be seen that coupling between resonators is realized by the width of irises, which are denoted by $D_1 = D_4$ and $D_2 = D_3$ and set by coupling coefficients $M_{12} = M_{45}$ and $M_{23} = M_{34}$ respectively. The input/ output coupling is realized by adjusting the width of the iris denoted by E, which is set by external quality factors $Q_{e1} = Q_{en}$. Simulations and final optimization of the filter are carried out in CST Microwave Studio [19] to get the frequency response close to the ideal.

Fig. 1 (c) illustrates the external design of the W-band waveguide bandpass filter, along with its external dimensions in millimeters. Fig. 1 (d) shows a cross section view of the filter with the resonators and all internal couplings between resonators shown. The screw holes, alignment pin holes and precision alignment pin holes are included in both input and output UG387/U waveguide flanges. The filter and flange are designed in the hexagonal shape in order to facilitate fabrication by the micro laser sintering process.

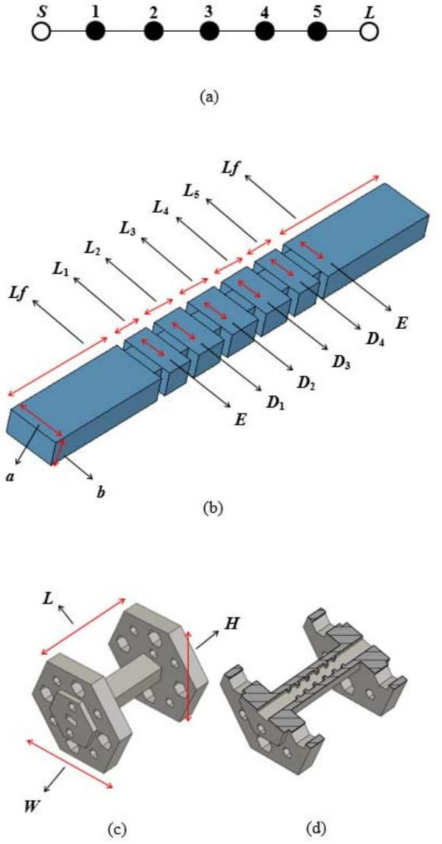

Fig. 1. Illustration of the fifth-order waveguide bandpass filter. (a) Coupling routing diagram of the filter. (b) Internal structure of the filter showing internal dimensions. The dimensions in millimeter are: $Lf = 6.48$, $L_1 = L_5 = 1.317$, $L_2 = L_4 = 1.582$, $L_3 = 1.636$, $E = 1.7$, $D_1 = D_4 = 1.374$, $D_2 = D_3 = 1.291$, $a = 2.54$ and $b = 1.27$. (c) Completed filter, showing external dimensions. The dimensions in millimeter are: $L = 21.4$, $H = 19.05$ and $W = 22$. (d) A cross section view of the filter showing internal couplings between resonators.

III. Micro Laser Sintering Fabrication Process

Micro laser sintering is an additive manufacturing process, which is by far the most accurate sintering fabrication process to 3D print solid metal structures. Using the micro laser sintering process enables parts with complex 3D micro structures to be produced at reasonable costs, where conventional additive manufacturing processes reach their limits. In the process the model structure is divided into layers, and each layer is printed by applying a thin layer of metal powder to a build platform and then, using a laser beam, the powder is selectively fused according to the required layer structure. Once a layer is constructed, the building platform is lowered, and next layer will be constructed with same process as in previous layers. The process continues until all layers are constructed on top of each other according to 3D model structure [20]. The accuracy of micro laser sintering makes this fabrication process attractive for fabricating high frequency waveguide filters, as it enables the production of small filters with complex structures and high strength.

Two similar filters with the same structure and specification were made to compare insertion loss. Both filters made from stainless steel with one being coated with copper. The filters were fabricated by 3D Micro Print Gmbh [20], using their micro laser sintering process in an inert argon atmosphere. The laser source was an IR fiber laser with a 50 W laser average power. The laser spot diameter is focused down to 30 μm and was operated in continuous wave mode. The filters are made from stainless steel powder material with one being coated with a 5μm thick copper layer by electroplating the surface. The type of stainless steel was 1.4542 (17-4PH) according to ASTM 564, which is a chromium nickel copper alloyed stainless steel, containing 17% chromium, 4% nickel, 4% copper and 0.3% niobium. The powder particle sizes were smaller than d_{80} 5μm and had electrical conductivity of 1.25×10^7 S/m. The thickness of each layer in the process was set at 5μm. The print took about 16 hours, but this could be considerably reduced by optimizing the build process further.

Fig. 2 (a) shows photograph of the filter on the support structure after fabrication. Fig. 2 (b) provides a photograph of the fabricated filter made from Stainless Steel and Fig. 2 (c) shows the fabricated filter made from stainless steel after being

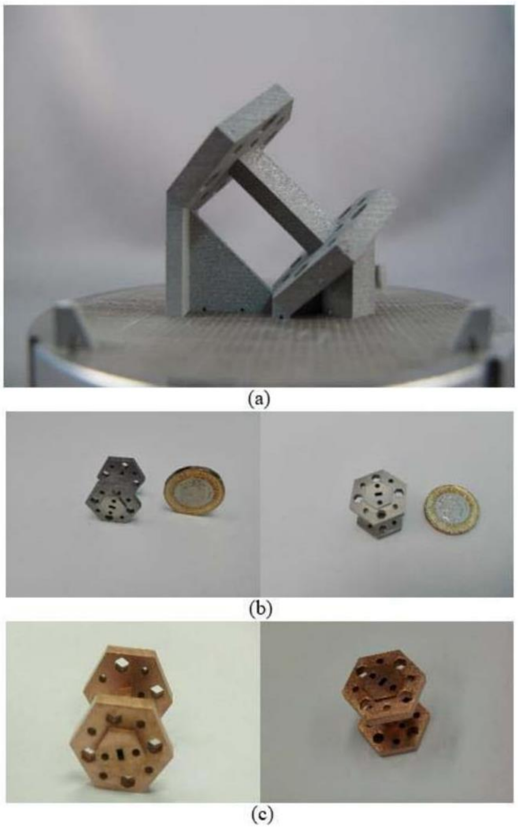

Fig. 2. Photograph of the fabricated W-band waveguide bandpass filter. (a) Filter on support structure after fabrication process. (b) Fabricated filter made from stainless steel. (c) Fabricated filter made from stainless steel, coated with copper.

electroplated with 5μm thick copper layer with electrical conductivity of 5.96×10^7 S/m.

IV. MEASUREMENT AND DISCUSSION

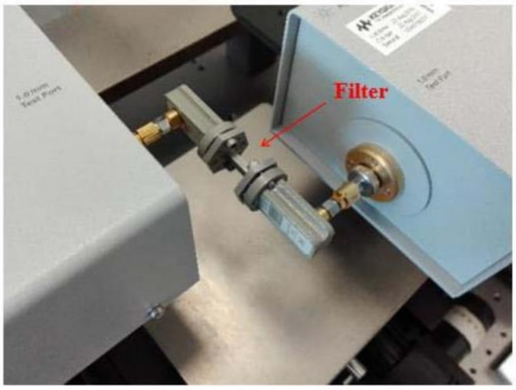

Fig. 3. Photograph of the measurement setup with the filter being placed between two waveguide flanges of the network analyzer.

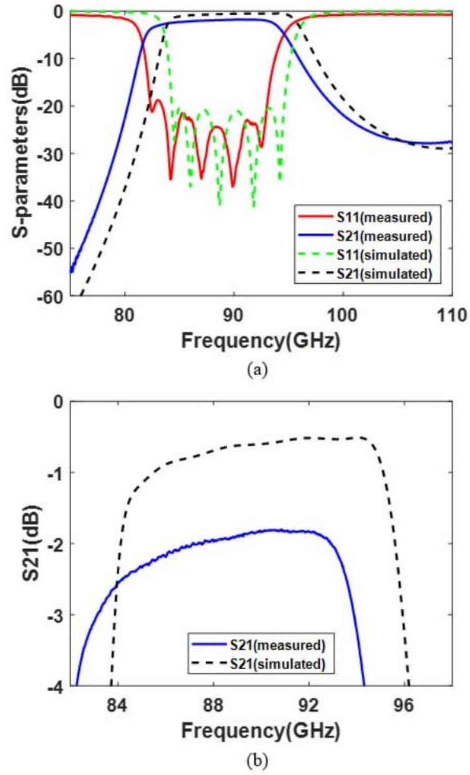

Fig. 4. Measured and simulated results of the W-band waveguide bandpass filter made from stainless steel. (a) Measured and simulated results over the whole W-band. (b) Expanded view of S_{21} over passband.

The *S*-parameter measurements of both filters are performed on Keysight E8361C PNA network analyzer. Fig. 3 shows photograph of the measurement setup. Here the filter is placed between two waveguide flanges of the network analyzer, aligned using four precision alignment pins of the waveguide flanges and tightened using four screws on each side. Fig. 4 and Fig. 5 show the measured and simulated results of both W-band waveguide bandpass filters, where the measured results are denoted with solid lines and simulated results with dashed lines. Looking at the stainless steel filter in Fig. 4 (a), it can be seen that the measured center frequency, shifts down by 1.66 GHz and a minimum return loss of 24.41 dB across the whole passband. Looking at the copper coated filter in Fig. 5 (a), it can be observed that the frequency shift is only 0.9 GHz and a minimum return loss of 26.56 dB across the whole passband. The lower return loss of 15.2 dB at 84.6 GHz in Fig. 5 (a) is caused by slight deviation of the cavity sizes from the design and can be improved by tuning filter. To be clear, there has been no tuning of the filters and these excellent responses show the high quality of the 3D printing.

TABLE I

COMPARISON WITH OTHER WAVEGUIDE BANDPASS FILTERS

f_c (GHz)	FBW	IL (dB)	RL (dB)	Manufacturing techniques	*f_c offset*	*Reference*
107.2	6.34%	0.95	>11	SLA	7.2%	[1]
100	4%	0.5~0.8	>15	Laser micromachining	0%	[10]
87.5	11.5%	0.3~0.5	>18	SLA	2.78%	[10]
88.47	9.7%	0.97~1.1	>15	SU-8 process	1.7%	[21]
102	5%	1.2	>10	SU-8 process	2%	[22]
100	10%	0.6	>18	CNC milling	0%	[23]
92.6	4.53%	0.5	>14	CNC milling	0.02%	[24]
92.45	4.83%	1.1~1.3	>10	DRIE	1.86%	[25]
95	3.68%	3.49	>18	Hot embossing	0.52%	[26]
75.5	5.3%	8	>8	SLM	2.72%	[27]
88.34	12.1%	1.94	>18	MLS	1.84%	T.W. (stainless steel)
89.1	11.07%	1	>15	MLS	1%	T.W. (copper coted)

f_c: center frequency of the filter; FBW: fractional bandwidth; IL: passband insertion loss; RL: passband return loss; f_c offset: frequency shift; T.W.: this work.

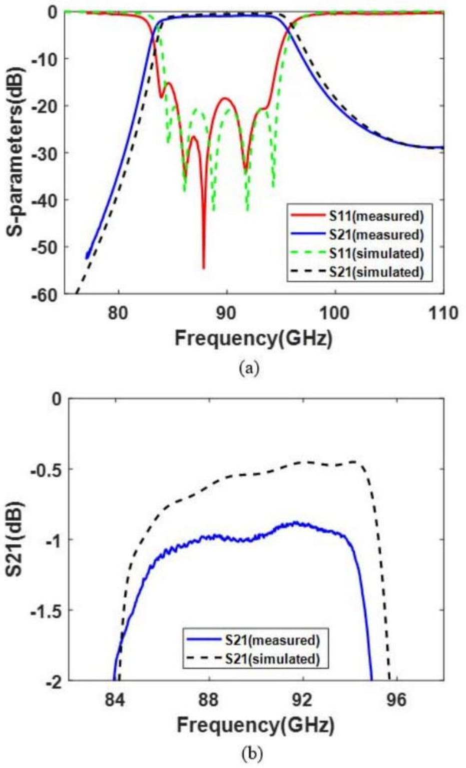

(a)

(b)

Fig. 5. Measured and simulated results of the W-band waveguide bandpass filter made from stainless steel coated with 5μm thick copper layer. (a) Measured and simulated results over the whole W-band. (b) Expanded view of S_{21} over passband.

The unwanted frequency shifts in the filters is believed to be caused by small dimensional inaccuracies, as a result of expansion in length of resonators, which could be corrected by remanufacturing. It has been found that such an expansion of dimensions is repeatable and as both filters have small frequency shift, the model could be adjusted accordingly to compensate during the remanufacturing.

Careful examination of the expanded view of S_{21} in Fig. 4 (b) shows an average insertion loss of around 1.94 dB over the passband for the measured results, which is 1.34 dB higher than the simulated results. The expanded view of S_{21} in Fig. 5 (b) shows an average insertion loss of around 1 dB over the passband for the measured results, which is 0.47 dB higher than simulated results. Note, the copper plated filter has 0.94 dB lower measured insertion loss in comparison to the filter made from stainless steel showing the advantages of the copper coating.

The typical surface roughness values of the filters measured with Mitutoyo SurfTest SV-3000 CNC surface roughness tester is about 2 μm. This reduces effective conductivity of stainless steel to 3.19×10^6 S/m and copper to 14.97×10^6 S/m. According to calculations [19] this results in additional loss of 0.456 dB for the filter that is not coated with copper and 0.453 dB for the copper coated filter, however this loss is already reflected in the CST simulated results. The loss in the waveguide jointing the filter to the flanges (0.075dB) is also included in the simulations. In addition, small misalignments during measurements also contribute to the difference in insertion loss but show up in the return loss. The 20 dB return loss contributes about 0.1 dB to the insertion loss.

The additional difference in insertion loss between simulation and measurement is probably caused by a combination of factors including the estimate of the conductivity of the stainless steel and copper which may not be as specified due to impurities, surface contaminates, or oxidation. There may be effects because of the granular nature of the surface formed from the powder as well as changes from the specified stainless steel conductivity because of the manufacturing process. Because of the high frequency and the small skin depth, the loss is highly dependent on these surface effects. A further detailed study is required here to understand these losses. The insertion loss can be improved by electroplating the surface (as we have seen), laser polishing, chemical polishing and using higher conductivity powder materials.

Table I provides a comparison of measured performance of waveguide bandpass filters that are fabricated using different types of manufacturing technique.

V. CONCLUSION

A metal 3D printed W-band waveguide bandpass filter fabricated by micro laser sintering process has been presented in this brief. This is the highest frequency metal 3D printed filter so far reported. Good agreement between the measured and simulated results demonstrate that micro laser sintering process can be used to fabricate filters with complex structures, that operate at high frequencies accurately. The micro laser sintering technique not only offers accuracy, but it also enables the whole structure, including flanges, to be made in a single piece. In addition, using electroplated copper demonstrates, it can improve the insertion loss of the filter considerably.

REFERENCES

[1] M. D'Auria *et al.*, "3-D printed metal-pipe rectangular waveguides," *IEEE Trans. Compon. Packag. Manuf. Technol.*, vol. 5, no. 9, pp. 1339–1349, Sep. 2015.

[2] X. Shang, J. Li, C. Guo, M. J. Lancaster, and J. Xu, "3-D printed filter based on helical resonators with variable width," in *Proc. IEEE MTT-S Int. Microw. Symp. (IMS)*, 2017, pp. 1587–1590.

[3] C. Guo, J. Li, J. Xu, and H. Li, "An X-band lightweight 3-D printed slotted circular waveguide dual-mode bandpass filter," in *Proc. IEEE Int. Symp. Antennas Propag. USNC/URSI Nat. Radio Sci. Meeting*, 2017, pp. 2645–2646.

[4] L. Araujo *et al.*, "3-D printed band-pass combline filter," *Microw. Opt. Technol. Lett.*, vol. 59, no. 6, pp. 1388–1390, 2017.

[5] C. Guo, X. Shang, M. J. Lancaster, and J. Xu, "A 3-D printed lightweight X-band waveguide filter based on spherical resonators," *IEEE Microw. Wireless Compon. Lett.*, vol. 25, no. 7, pp. 442–444, Jul. 2015.

[6] C. Guo *et al.*, "A lightweight 3-D printed X-band bandpass filter based on spherical dual-mode resonators," *IEEE Microw. Wireless Compon. Lett.*, vol. 26, no. 8, pp. 568–570, Aug. 2016.

[7] C. Guo *et al.*, "Ceramic filled resin based 3D printed X-band dual-mode bandpass filter with enhanced thermal handling capability," *Electron. Lett.*, vol. 52, no. 23, pp. 1929–1931, Oct. 2016.

[8] J. Li, C. Guo, L. Mao, and J. Xu, "Compact high-Q hemispherical resonators for 3-D printed bandpass filter applications," in *Proc. IEEE MTT-S Int. Microw. Symp. (IMS)*, 2017, pp. 1591–1594.

[9] J. Li, C. Guo, J. Xu, and L. Mao, "Lightweight low-cost Ka-band 3-D printed slotted rectangular waveguide bandpass filters," in *Proc. IEEE Int. Symp. Antennas Propag. USNC/URSI Nat. Radio Sci. Meeting*, 2017, pp. 2647–2648.

[10] X. Shang *et al.*, "W-band waveguide filters fabricated by laser micromachining and 3-D printing," *IEEE Trans. Microw. Theory Techn.*, vol. 64, no. 8, pp. 2572–2580, Aug. 2016.

[11] G. Venanzoni, M. Dionigi, C. Tomassoni, D. Eleonori, and R. Sorrentino, "3D printing of X band waveguide resonators and filters," in *Proc. 32nd Gen. Assembly Sci. Symp. Int. Union Radio Sci. (URSI GASS)*, 2017, pp. 1–2.

[12] M. V. D. Vorst and J. Gumpinger, "Applicability of 3D printing techniques for compact Ku-band medium/high-gain antennas," in *Proc. 10th Eur. Conf. Antennas Propag. (EuCAP)*, 2016, pp. 1–4.

[13] F. Bongard, M. Gimersky, S. Doherty, X. Aubry, and M. Krummen, "3D-printed Ka-band waveguide array antenna for mobile SATCOM applications," in *Proc. 11th Eur. Conf. Antennas Propag. (EUCAP)*, 2017, pp. 579–583.

[14] K. F. Brakora, J. Halloran, and K. Sarabandi, "Design of 3-D monolithic MMW antennas using ceramic stereolithography," *IEEE Trans. Antennas Propag.*, vol. 55, no. 3, pp. 790–797, Mar. 2007.

[15] B. Liu, X. Gong, and W. J. Chappell, "Applications of layer-by-layer polymer stereolithography for three-dimensional high-frequency components," *IEEE Trans. Microw. Theory Techn.*, vol. 52, no. 11, pp. 2567–2575, Nov. 2004.

[16] J. S. Silva, E. B. Lima, J. R. Costa, C. A. Fernandes, and J. R. Mosig, "Tx-Rx lens-based satellite-on-the-move Ka-band antenna," *IEEE Antennas Wireless Propag. Lett.*, vol. 14, pp. 1408–1411, 2015.

[17] R. J. Cameron, C. M. Kudsia, and R. R. Mansour, *Microwave Filters for Communication Systems: Fundamentals, Design and Applications*. Hoboken, NJ, USA: Wiley, 2007.

[18] J.-S. Hong, *Microstrip Filters for RF/Microwave Applications*. Hoboken, NJ, USA: Wiley, 2011.

[19] Computer Simulated Technology. (2017). *Microwave Studio*. [Online]. Available: http//www.cst.com/

[20] *3D Micro Print Gmbh*. Accessed: Jan. 10, 2018. [Online]. Available: http://www.3dmicroprint.com/

[21] X. Shang, M. Ke, Y. Wang, and M. Lancaster, "Micromachined W-band waveguide and filter with two embedded H-plane bends," *IET Microw. Antennas Propag.*, vol. 5, no. 3, pp. 334–339, Feb. 2011.

[22] C. A. Leal-Sevillano *et al.*, "A pseudo-elliptical response filter at W-band fabricated with thick SU-8 photo-resist technology," *IEEE Microwave Wireless Compon. Lett.*, vol. 22, no. 3, pp. 105–107, Mar. 2012.

[23] C. A. Leal-Sevillano, J. R. Montejo-Garai, J. A. Ruiz-Cruz, and J. M. Rebollar, "Low-loss elliptical response filter at 100 GHz," *IEEE Microw. Wireless Compon. Lett.*, vol. 22, no. 9, pp. 459–461, Sep. 2012.

[24] X. Liao, L. Wan, Y. Zhang, and Y. Yin, "W-band low-loss bandpass filter using rectangular resonant cavities," *IET Microw. Antennas Propag.*, vol. 8, no. 15, pp. 1440–1444, Sep. 2014.

[25] Y. Li, P. L. Kirby, and J. Papapolymerou, "Silicon micromachined W-band bandpass filter using DRIE technique," in *Proc. Eur. Microw. Conf.*, 2006, pp. 1271–1273.

[26] F. Sammoura *et al.*, "A micromachined W-band iris filter," in *13th Int. Conf. Solid-State Sensors Actuators Microsyst. Dig. Tech. Papers. (TRANSDUCERS)*, 2005, pp. 1067–1070.

[27] B. Zhang and H. Zirath, "3D printed iris bandpass filters for millimetre-wave applications," *Electron. Lett.*, vol. 51, no. 22, pp. 1791–1793, Oct. 2015.

90 GHz Micro Laser Sintered Filter: Reproducibility and Quality Assessment

Milan Salek, Xiaobang Shang, Michael J. Lancaster, Robert C. Roberts, Thomas Starke, Falko Boettcher, Daniel Weber
Emerging Device Technology, School of Electronic, Electrical and Systems Engineering,
The University of Birmingham, Birmingham, B15 2TT, U.K.
mxs1149@bham.ac.uk, xiaobang.shang@npl.co.uk, m.j.lancaster@bham.ac.uk, rcr8@hku.hk, thomas.starke@3dmicroprint.com,
falko.boettcher@3dmicroprint.com, engineering.daniel.weber@gmail.com

Abstract — **This paper presents reproducibility and quality assessment of two identical 90 GHz micro laser sintered waveguide bandpass filters. Both filters operating at center frequency of 90 GHz, with bandwidth of 10 GHz and return loss of 20 dB. The filters are fabricated by micro laser sintering process which is a metal 3-D printing technique, allowing the components to be fabricated in a single piece with high resolution and good surface quality accurately. This paper shows that micro laser sintering can be used to reproduce high frequency filters repeatedly with almost identical responses. The micro laser sintering process can provide reproducibility for small to medium batch size production of high frequency components. The paper discusses the quality of both filters by comparing the measured results with simulated results and providing the surface roughness measurements. Both filters are tested, and measurement results have excellent agreement with simulated results.**

Keywords — **waveguide bandpass filter, W-band, micro laser sintering process, 3-D printing.**

I. INTRODUCTION

In recent years, using 3-D printing or additive manufacturing has become of interest in fabrication of passive microwave components. Using additive manufacturing allows complex 3-D structures to be fabricated accurately at a reasonable cost. In general, additive manufacturing allows components to be fabricated using many different types of materials, with a number of different types of printing process. For example, microwave components have been made with fused deposition modelling (FDM), stereolithography apparatus (SLA) and selective laser sintering (SLS) [1]. Using 3-D printing or additive manufacturing in the fabrication of microwave components such as filters [1] – [7] and antennas [8, 9] is well documented. This paper presents a 90 GHz filter fabricated using micro laser sintering, discussing its reproducibility and quality. Using the micro laser sintering process, also known as selective laser melting or selective laser sintering, allows components to be fabricated using metallic materials with high accuracy, high resolution and good surface quality. Reproducibility of a process is an important factor, especially when components need to be produced in quantities. It is important that a process to be capable of producing components that fit with the required specification across a required batch. This paper shows capability of micro laser sintering process on reproducing microwave filters. Two identical waveguide bandpass filters with centre frequency of 90 GHz and bandwidth of 10 GHz, fabricated by micro laser sintering are presented here. As it is shown in this paper, both filters have the very close agreement in measured *S*-parameter, indicating that micro laser sintering can in fact reproduce high frequency filters with very high accuracy. In addition, this paper also accesses the quality of the filters, by providing detailed surface roughness measurements and showing impact of this on insertion loss. Measured and simulated results are compared throughout.

II. FILTER DESIGN

The waveguide bandpass filter is designed with a center frequency of 90 GHz, a bandwidth of 10 GHz (fractional bandwidth of 11%) and a return loss of 20 dB over the passband. The filter is specified in terms of the Chebyshev response and is constructed with five rectangular resonators operating in TE_{101} mode. The couplings between resonators and input/ output coupling are realized using inductive irises. The filter is designed using coupling matrix theory [10], where the filter specification is translated into coupling matrix elements, which are then translated into physical dimensions following the procedure explained in [10]. Based on coupling matrix theory [10], the un-normalized non-zero coupling coefficients between resonators and external quality factor of the first (Q_{e1}) and the last (Q_{en}) resonators are calculated as $M_{12} = M_{45} = 0.0961$, $M_{23} = M_{34} = 0.0706$ and $Q_{e1} = Q_{en} = 8.76$. These are then used to extract the physical dimensions of the filter. Fig. 1 (a) shows the internal structure of the filter. The coupling between resonators 1 and 2 and resonators 4 and 5 are realized by the width of irises denoted by D_1 and D_4, which set by coupling coefficients M_{12} and M_{45}. The coupling between resonators 2 and 3 and resonators 3 and 4 are realized by the width of irises denoted by D_2 and D_3 and set by coupling coefficients M_{23} and M_{34}. The input/ output coupling is realized by adjusting the width of iris denoted by E and set by external quality factors $Q_{e1} = Q_{en}$. Electromagnetic simulations of the filter are performed using CST Microwave Studio [11]. Fig. 1 (b) illustrates external design of the filter and its external dimensions. Fig. 1 (c) shows a cross section view of the filter with all internal couplings between resonators. Both input and output UG387/U waveguide flanges have screw holes, alignment pin holes and precision

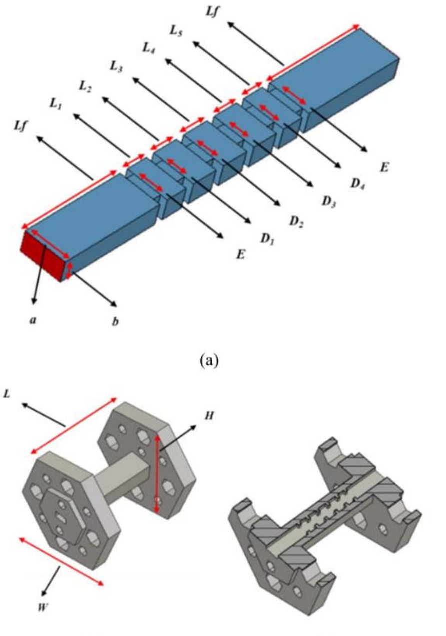

(a)

(b) (c)

Fig. 1. Illustration of the 90 GHz waveguide bandpass filter. (a) Internal structure of the filter showing internal dimensions. The dimensions in millimetre are: $Lf = 6.48$, $L_1 = L_5 = 1.317$, $L_2 = L_4 = 1.582$, $L_3 = 1.636$, $E = 1.7$, $D_1 = D_4 = 1.374$, $D_2 = D_3 = 1.291$, $a = 2.54$ and $b = 1.27$. (b) External design of the filter, showing external dimensions. The dimensions in millimetre are: $L = 21.4$, $H = 19.05$ and $W = 22$. (c) A cross section view of the filter showing internal couplings between resonators.

alignment pin holes, and they all are designed in the hexagonal shapes in order to facilitate fabrication by the micro laser sintering process.

III. FABRICATION PROCESS

The filters reported here were fabricated by 3D Micro Print Gmbh [12] using micro laser sintering process. Micro laser sintering is an additive manufacturing process which can print complex solid metal 3-D micro structures accurately at a reasonable cost. Details of micro laser sintering process is already provided in [12]. The filters are fabricated layer by layer, where the powders are selectively fused using IR fiber laser with 50 W laser average power. During the process the laser spot diameter was focused down to 30 µm and was operated in continuous wave mode. The thickness of each layer in the process was 5 µm and the printing time for each filter was about 16 hours. Both filters are made from stainless-steel powders with powder particle sizes of smaller than d_{80} 5µm and electrical conductivity of 1.25×10^7 S/m. The type of stainless-steel was 1.4542 (17-4PH), which is a chromium nickel copper alloy. Fig. 2 (a) shows photograph of the filter on the support structure after fabrication. The support structure used in order to print the filter in 60° from the vertical, which prevents any overhang during printing.

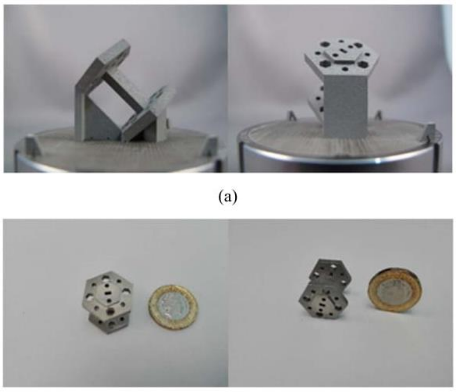

(a)

(b)

Fig. 2. Photograph of the fabricated 90 GHz waveguide bandpass filter. (a) Filter on support structure after fabrication process. (b) One of the samples made from stainless-steel.

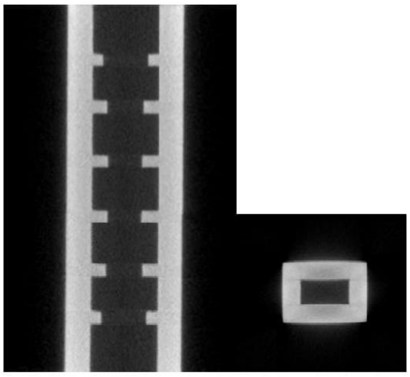

(a) (b)

Fig. 3. CT scan image of the waveguide bandpass filter. (a) Cross section of the waveguide bandpass filter. (b) End on view of the input waveguide.

The support structure is cut off by an Electrical Discharge Machine (EDM) wire during post processing. Fig. 2 (b) shows photograph of one of the samples, which is the same as the other sample. A Bruker SkyScan 1076 MicroCT system was used to obtain a view of the internal structure of the filter, non-destructively in order to detect any defects, voids or cracks. Fig. 3 shows this CT scan, with Fig. 3 (a) showing the cross section of the waveguide filters, and the end on view of the input waveguide is shown in Fig. 3 (b).

IV. MEASUREMENT AND DISCUSSION

The *S*-parameter measurements of the filters were performed on Keysight E8361C PNA network analyzer. Fig. 4 shows the measured and simulated results of both filters. Looking at *S*-parameter response of the first sample in Fig. 4 (a), it can be observed that the measured center frequency is shifted down by 1.66 GHz and the minimum return loss is about 24.41 dB in the passband.

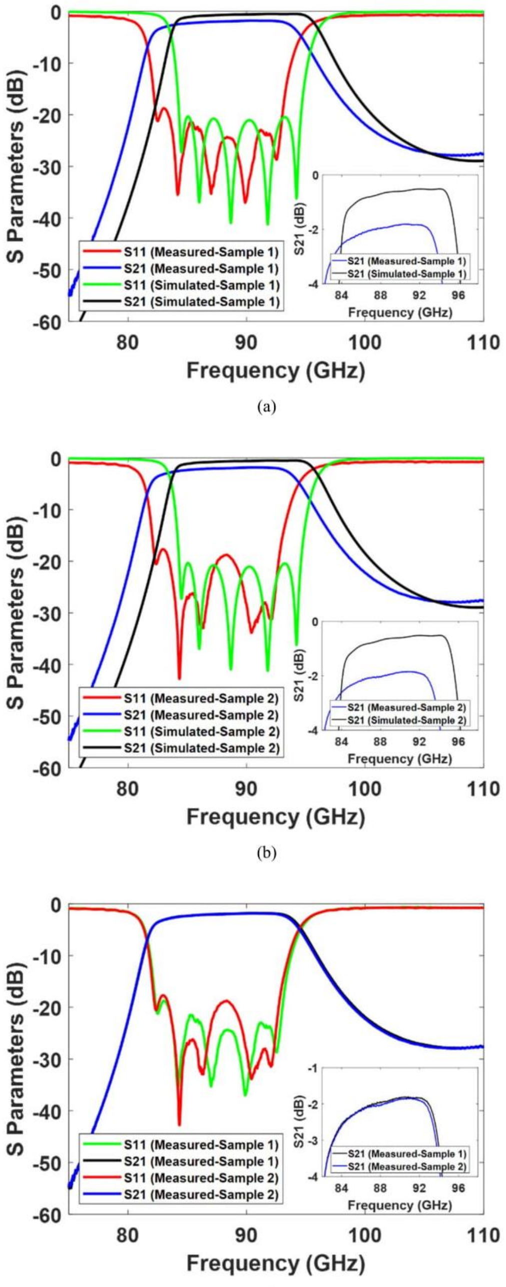

(a)

(b)

(c)

Fig. 4. Measured and simulated results of 90 GHz waveguide bandpass filters. (a) Measured and simulated results of the first sample over the whole W-band. (b) Measured and simulated results of the second sample over the whole W-band. (c) Measured results of both samples over the whole W-band.

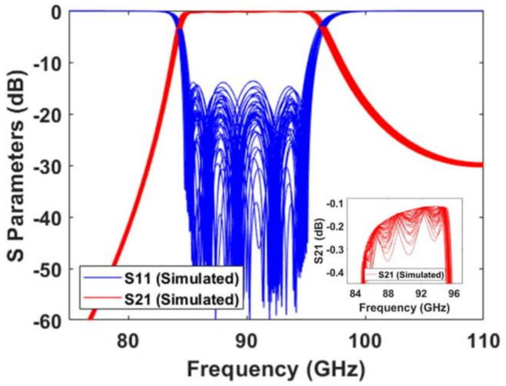

Fig. 5. Simulated tolerance analysis of 90 GHz waveguide bandpass filter. Simulated results are with a selection of random changes in the size by 10 µm.

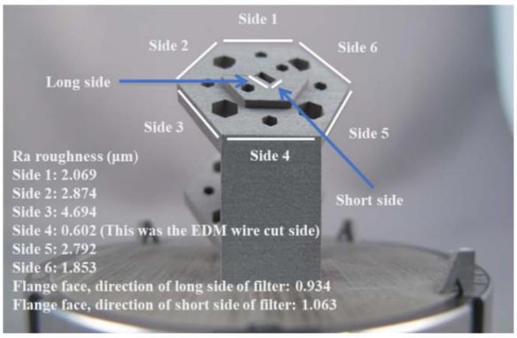

Fig. 6. The surface roughness measurements at various position on the structure.

The *S*-parameter response of the second sample in Fig. 4 (b) shows that the frequency shift is about 1.68 GHz and the minimum return loss is about 28 dB in the passband. Simulations show the small unwanted frequency shifts in the filters can be accounted for by a small (0.09 mm) expansion in length of resonators during manufacturing. Both samples have a very similar frequency shift; this repeatable frequency shift could be corrected by remanufacturing the filter and adjusting the model accordingly to compensate for frequency shift during the remanufacturing. It would be interesting to simulate the filter with measured dimensions however, the CT scan in Fig. 3 is not accurate enough. The return loss of both filters is very close to the designed 20 dB and the 5 poles are visible on both filters. This shows the excellent accuracy of the process. Return loss is a very sensitive measurement of the dimensional accuracy and the errors can be attributed to small dimensional inaccuracies. Fig. 4 (c) shows the measured results of both samples on the same plot. As it can be seen, on this scale, both filters have close identical results, except for the return loss described above. A modified model of the filter considering dimensional changes of 10 µm is simulated in CST [11]. The graph in Fig. 5 shows variation in S_{11} and S_{21} with a selection of random changes in the size by 10 µm. The results indicate that even if dimensions are changed by 10 µm during the manufacturing process, good results will be achieved. The expanded view of S_{21} in Fig. 4 (c) shows an average measured insertion loss of about 2 dB over the passband for both samples. The reproducibility between the two samples is very striking from this figure, with less than 0.055 dB between the two insertion loss values. This maximum difference is at 88.19 GHz and is accounted for by the difference in S_{11} of the two filters at this frequency. Both samples have an average insertion loss about 1.4 dB larger than the simulated. There have been detailed surface roughness measurements of the filters using a Mitutoyo SurfTest SV-3000 CNC surface roughness tester. Fig. 6 shows the results of some of the measurements at various position on the structure. The base for the growth of the components can be seen and side 4 represents a side grown vertically, however this is the side cut by an Electrical Discharge Machine (EDM) wire and has a very low Ra surface roughness of about 0.6 µm. The other vertical sides (2, 3, 5, 6) have a roughness of between 2–5 µm. These values are very small, but nevertheless larger than the 475 nm skin depth (using stainless-steel conductivity 1.25×10^7 S/m). The flange face in Fig. 6 is not vertically grown and has a roughness of about 1 µm. Of course, these measurements are not inside the waveguide, but the expectation is that the surface roughness here is similar. For simulation purposes an average roughness of 2.1 µm used. This reduces effective conductivity of stainless-steel to 3.19×10^6 S/m, which results in additional loss of 0.456 dB. However, this loss is already reflected in the simulated results of both filters. The loss of 0.075 dB which is caused by the conduction loss of the 12.96 mm long waveguides joining the filter to flanges is also reflected in simulated results. The additional difference in insertion loss between simulated and measured results is caused by a combination of factors including; impurities of powder material used, contamination of the stainless-steel surface, changes in the specified stainless-steel conductivity due to the manufacturing process and the effect of the granular nature of the surface which is formed from the powder. Further investigation is required here. The insertion loss of the filters can be improved further by electroplating the surface with a good conductor. Additionally, higher conductivity powder materials are available and there are polishing techniques to further reduce the surface roughness. Table 1 provides a comparison of measured performance of waveguide bandpass filters that are fabricated using different types of 3-D printing technique. Note, filters provided in table 1, operate in W-band frequency range (75 - 110 GHz).

V. CONCLUSION

Two similar metal 3-D printed 90 GHz waveguide bandpass filters fabricated by micro laser sintering process have been presented in this paper. The filters have extremely close measured results that match the simulated results. This shows the capability of micro laser sintering process on reproducing microwave filters and makes this process suitable for small to medium batch size production of high frequency filters with complex structures. Measurements of the surface roughness show that in the micro laser sintering process it is very low and around 1-5 µm.

Table 1. Comparison with other 3-D printed waveguide bandpass filters. (*f_c*: centre frequency; FBW: fractional bandwidth; IL: insertion loss; RL: return loss; *f_c* offset: frequency shift; T.W.: this work; *Ref.*: reference.)

f_c (GHz)	**FBW (%)**	**IL (dB)**	**RL (dB)**	**3-D printing technique**	***f_c offset* (%)**	***Ref.***
107.2	6.34	0.95	>11	SLA	7.2	[1]
87.5	11.5	0.3~0.5	>18	SLA	2.78	[5]
75.5	5.3	8	>8	SLM	2.72	[6]
89.1	11.07	1	>15	MLS	1	[7]
88.34	12.1	1.94	>18	MLS	1.84	T.W. (sample 1)
88.32	11.9	1.995	>17	MLS	1.87	T.W. (sample 2)

REFERENCES

[1] M. Dauria, W. J. Otter, J. Hazell, B. T. W. Gillatt, C. Long-Collins, N. M. Ridler, and S. Lucyszyn, “3-D Printed Metal-Pipe Rectangular Waveguides,” *IEEE Trans. Compon., Packag., Manuf. Technol.*, vol. 5, no. 9, pp. 1339–1349, 2015.

[2] G. Venanzoni, C. Tomassoni, M. Dionigi, and R. Sorrentino, “Stereolitographic 3D printing of compact quasi-elliptical filters,” *2017 IEEE MTT-S Int. Microwave Workshop Series on Advanced Materials and Processes for RF and THz Applications (IMWS-AMP)*, 2017.

[3] C. Guo, X. Shang, J. Li, F. Zhang, M. J. Lancaster, and J. Xu, “A Lightweight 3-D Printed X-Band Bandpass Filter Based on Spherical Dual-Mode Resonators,” *IEEE Microw. Wireless Compon. Lett.*, vol. 26, no. 8, pp. 568–570, 2016.

[4] C. Guo, X. Shang, M. J. Lancaster, and J. Xu, “A 3-D Printed Lightweight X-Band Waveguide Filter Based on Spherical Resonators,” *IEEE Microw. Wireless Compon. Lett.*, vol. 25, no. 7, pp. 442–444, 2015.

[5] X. Shang, P. Penchev, C. Guo, M. J. Lancaster, S. Dimov, Y. Dong, M. Favre, M. Billod, and E. D. Rijk, “W-Band Waveguide Filters Fabricated by Laser Micromachining and 3-D Printing,” *IEEE Trans. Microw. Theory Techn.*, vol. 64, no. 8, pp. 2572–2580, 2016.

[6] B. Zhang and H. Zirath, “3D printed iris bandpass filters for millimetre-wave applications,” *Electron. Lett.*, vol. 51, no. 22, pp. 1791–1793, 2015.

[7] M. Salek, X. Shang, R. C. Roberts, M. J. Lancaster, F. Boettcher, D. Weber, and T. Starke, “W-Band Waveguide Bandpass Filters Fabricated by Micro Laser Sintering,” *IEEE Trans. Circuits Syst. II, Exp. Briefs*, pp. 1–1, 2018.

[8] M. V. D. Vorst and J. Gumpinger, “Applicability of 3D printing techniques for compact Ku-band medium/high-gain antennas,” *2016 10th Eur. Conf. Antennas Propag. (EuCAP)*, 2016.

[9] F. Bongard, M. Gimersky, S. Doherty, X. Aubry, and M. Krummen, “3D-printed Ka-band waveguide array antenna for mobile SATCOM applications,” *2017 11th Eur. Conf. Antennas Propag. (EUCAP)*, 2017.

[10] R. J. Cameron, C. M. Kudsia, and R. R. Mansour, *Microwave filters for communication systems: fundamentals, design, and applications*. Hoboken, NJ, USA: John Wiley & Sons, Inc., 2018.

[11] Computer Simulated Technology (CST), Microwave Studio. Available at http://www.cst.com/.

[12] 3D Micro Print Gmbh. [Online]. Available: http://www.3dmicroprint.com/.